

Formability of AA7075 Aluminum Sheet at Elevated  
Temperatures for Automotive Hot Stamping  
Applications

Formability of AA7075 Aluminum Sheet at Elevated Temperatures for  
Automotive Hot Stamping Applications

By

Cameron Oud, B. Eng.

A Thesis Submitted to the School of Graduate Studies in Partial Fulfillment of  
the Requirements for the Degree Master of Applied Science

McMaster University © Copyright by Cameron Oud, 2019

Master of Applied Science (2019)

McMaster University

(Mechanical Engineering)

Hamilton, Ontario

TITLE: Formability of AA7075 Sheet at Elevated Temperatures  
for Automotive Hot Stamping Applications

AUTHOR: Cameron Oud, B. Eng.  
McMaster University

SUPERVISOR: Professor Mukesh K. Jain  
Department of Mechanical Engineering  
McMaster University

NUMBER OF PAGES: xxvii, 212

# ABSTRACT

Sheet metal forming is a process in which sheet materials are stretched, drawn and bent into complex shapes by use of a forming press fitted with a die set and punch suitable for forming a part. There are several ways to form sheet including hot and cold stamping. If the material to be formed is ductile, commonly, the cold stamping process is utilized. However, if the material has low formability in its room temperature state, hot stamping can be employed to avoid fracture and significant part spring-back. In this thesis the hot stamping feasibility of aluminum AA7075-F (as-fabricated temper) was investigated.

The formability of AA7075-F sheet was assessed for elevated temperature forming by means of the in-plane Marciniak test. Although common at room temperature, development of an elevated temperature Marciniak test was necessary. ABAQUS® FE suite was used to create an accurate finite element model (FEM) to assist in understanding material flow during experimental testing. Upon development of an elevated temperature Marciniak test, strain maps were produced through digital image correlation (DIC) to create forming limit curves (FLC). In addition, the resulting samples were observed for their microstructure, plastic flow, necking and fracture behaviour. Macroscopic strain field inhomogeneity, surface roughening characteristics, and ductile void damage as a function of strain, strain path

and temperature were also analyzed in an attempt to correlate formability and fracture behaviour to the material microstructural, damage development and surface characteristics in the deformed state.

FLC prediction of AA7075-F sheet were made using the laboratory-based FE simulation models of in-plane Marciniak test. For this purpose, strain-rate dependant data for AA7075-F sheet was obtained through elevated temperature tensile tests for use as material model input data. The predicted FLCs were compared with the experimental FLCs, and good general agreement was observed.

Lastly, a die was designed to replicate the hot stamping die quenching process through forming annealed AA7075 sheet. Tensile samples were cut from hot stamped parts to evaluate the process feasibility. Supplementary tests were performed to evaluate the impact of cooling rate on material strength.

# ACKNOWLEDGEMENTS

I want to thank my supervisor, Dr. Mukesh Jain, and express my gratitude for his continuous support and expertise. His breadth of knowledge and willingness to help were major contributors to the project's success.

I would also like to thank my research team for their help, especially Dr. Mike Bruhis and Dr. Zhutian Xu for their time and willingness to help. Jim Cleaver and Martin Wensveen in the McMaster prototype machine shop for their support in sample preparation. As well as Farhad Molaikiya and Dr. Stephen Veldhuis for access to McMaster Manufacturing Research Institute (MMRI) and aid in completing surface roughness measurements.

I would like to thank our industry partner Novelis Aluminum Company for their technical support and supply of AA7075 sheet material, the Natural Science and Engineering Research Council for their financial support, and McMaster University for its research facilities without which this research would not have been possible.

Lastly, I would like to thank my parents, family and friends for their continuous support, guidance and understanding throughout the course of this thesis.

# Table of Contents

Chapter 1 .....	1
1.1 Background .....	1
1.2 Objectives .....	6
Chapter 2 .....	8
2.1 General Formability of Sheet Materials .....	8
2.2 Forming Limit Curve as a Measure of Formability.....	10
2.2.1 Factors Effecting Formability.....	14
2.3 Experimental Techniques for FLC Determination .....	17
2.3.1 Out-of-Plane Nakazima Method.....	17
2.3.2 In-Plane Marciniak Method .....	21
2.3.3 Methods for Determining Onset of Localized Necking .....	26
2.4 Prediction of Forming Limits and FLDs.....	32
2.4.1 Marciniak-Kuczynski Method .....	32
2.4.2 FE Simulations of Laboratory-Based Forming Tests.....	37
2.5 Aluminum Alloys .....	41
2.5.1 Composition and Strength of Aluminum Alloy Series.....	41
2.5.2 Characteristics of Precipitation Hardenable Aluminum Alloys.....	43
2.5.3 Mechanical Properties of AA7075 Sheet.....	48
2.5.4 Microstructure, Damage Development, and Room and Elevated Temperature Formability and Fracture of AA7075 Sheet.....	51
2.6 Summary .....	54
Chapter 3 .....	55
3.1 Introduction.....	55
3.2 Material.....	56
3.3 Uniaxial Tensile Test .....	56
3.4 Elevated Temperature Marciniak Test Development .....	60
3.4.1 Elevated Temperature Forming Test System.....	69
3.4.2 DIC Methodology for Full-Field Strain Measurement and Necking Determination .....	70
3.4.3 Methodology for Fracture Strain Determination .....	74
3.4.4 Forming Test Sample Geometry .....	75
3.5 Hot Stamping Experiments .....	77

3.5.1 Forming Test System.....	79
3.5.2 Die Design and Manufacturing .....	79
3.5.3 Temperature Data Acquisition During Forming .....	82
3.5.4 Tensile Test Sample Acquisition After Hot Stamping .....	83
3.5.5 Cooling Rate Study.....	84
3.6 Microstructure Analysis .....	87
3.6.1 Sample Preparation for Microscopy Work.....	88
3.6.2 SEM Analysis .....	91
3.6.3 FLD Sample Surface Roughening Characteristics .....	93
Chapter 4 .....	94
4.1 Model Setup .....	94
4.2 Model Geometry.....	94
4.3 Material Model and Input Data .....	95
4.4 Boundary Conditions.....	98
4.5 Meshing .....	100
4.6 Mass Scaling.....	102
4.7 Modelling Data Analysis Methodology .....	103
Chapter 5 .....	105
5.1 Uniaxial Tensile Test Results .....	105
5.2 Marciniak Test Results .....	108
5.2.1 Load versus displacement .....	108
5.2.2 Deformed Sample Geometries .....	111
5.2.3 Full-field Strain Distributions .....	112
5.2.4 Strain Paths and Necking Characteristics.....	115
5.2.5 FLDs at Elevated Temperatures.....	118
5.2.6 Fracture Limit Curves at Elevated Temperatures .....	121
5.2.7 Microstructural Damage from Deformed Samples .....	123
5.2.8 EDS Analysis of Precipitates in the Fractured Samples .....	131
5.2.9 Neck and Fracture Characteristics .....	138
5.2.10 EDS Analysis of Precipitates from Neck and Fracture Regions of LT polished sections.....	154
5.2.11 Surface Roughness Development in Deformed Specimens .....	159
5.3 Marciniak Test FE Simulation Results .....	166

5.3.1 Load versus Displacement Curves .....	167
5.3.2 Deformed Samples Characteristics and Strain Maps.....	169
5.3.3 Strain Paths and Necking Characteristics .....	171
5.3.4 Model FLD .....	176
5.4 Hot Stamping Results .....	176
5.4.1 Cooling Rates .....	177
5.4.2 Post-ageing Strength .....	179
5.4.3 Part Surface Quality .....	181
5.5 Supplementary Cooling Rate Study.....	183
5.6 Summary .....	185
Chapter 6 .....	188
Chapter 7 .....	192
Appendix A .....	202
Appendix B .....	205
Appendix C .....	207

# LIST OF FIGURES

Figure 1.1.1 Historical fleet CO <sub>2</sub> emissions performance and current standards (gCO <sub>2</sub> /km normalized to NEDC) for passenger cars (Yang, 2018) .....	1
Figure 1.1.2 The new Audi A8 L – Audi Space Frame (ASF) (“Audi MediaCenter,” 2017) .....	2
Figure 1.1.3 ‘Banana’ chart showing inverse relationship between strength and elongation (“Steel Definitions   WorldAutoSteel,” 2018).....	4
Figure 1.1.4 Hot stamping processes: a) conventional hot stamping process b) adapted hot stamping for age-hardenable aluminum alloys (Adapted from Merklein et al, 2008).....	5
Figure 2.1.1 Strain paths observed in cup forming operations (Marciniak & Duncan, 1992) .....	10
Figure 2.2.1 Forming limit curve showing various strain paths as well as fracture limits.....	11
Figure 2.2.2 Forming Window for Plane Stress Sheet Forming (Marciniak & Duncan, 1992) .....	14
Figure 2.2.3 Increasing n-value raises FLC (Marciniak & Duncan, 1992). ...	16
Figure 2.2.4 The effect of sheet thickness on the FLC of AA2024-T4 (Dilmec et al., 2013).....	16
Figure 2.3.1 Out-of-plane Nakazima test method (BHF-blank holder force; PF-punch force) (Hsu et al, 2008) .....	18
Figure 2.3.2 Typical specimen geometry corresponding to strain paths for FLC (Shao et al., 2018) .....	20
Figure 2.3.3 Cross-section of Marciniak sheet metal test (Hsu et al, 2008). ..	22
Figure 2.3.4 Elevated temperature failure modes for Marciniak samples (Hsu et al, 2008).....	24
Figure 2.3.5 FLDs of AA7075-T6 at forming temperatures between 100-250°C (Huang et al, 2010) .....	26

Figure 2.3.6 1mm diameter dot pattern etched onto aluminum grid at 2mm x 2mm (Zdravecky, 2007) .....	28
Figure 2.3.7 Test blank with speckle (stochastic) pattern applied through high temperature paint .....	29
Figure 2.3.8 Time-dependent method for analysis of limiting strain (Martinez-Donaire et al, 2014).....	32
Figure 2.4.1 Thickness imperfection used in MK method (Marciniak & Duncan, 1992) .....	33
Figure 2.4.2 Strain evolution in imperfection region versus safe zone (Marciniak & Duncan, 1992) .....	34
Figure 2.4.3 Effect of imperfection factor on FLD (Marciniak & Duncan, 1992) .....	34
Figure 2.4.4 Flow chart of computing process of FLCs with the M-K model (Ding et al., 2015) .....	36
Figure 2.5.1 Strengthening mechanism illustrated through, (a) shearing of particles by dislocations, (b) bypassing of particles by dislocations (Gerold, 1979), and (c) critical precipitate radius for particle shearing or bypassing (Polmear, 2006) .....	44
Figure 2.5.2 CCT curve for AA7075 (Li, Bin, Zhao, & Wang, 2011) .....	46
Figure 2.5.3 Thermal processing of AA7075 sheet.....	47
Figure 2.5.4 Influence of particle size on strength, a) large precipitate interacting with minimal slip planes, and b) finely dispersed precipitates interacting with a larger number of slip planes.....	48
Figure 2.5.5 Ductile fracture timeline showing progression of fracture stages (Anderson, 2005).....	52
Figure 2.5.6 Main micro-mechanisms of fracture observed in metals a) ductile b) trans-granular (cleavage) and c) inter-granular (Anderson, 2005) .....	52

Figure 3.3.1 Standard AA7075 tensile sample for elevated temperature testing (all dimensions are in inches; * reference dimension) .....	57
Figure 3.3.2 (a) MTS tensile testing frame with furnace enclosure, (b) cooling system, and (c) high temperature tensile clamps. ....	58
Figure 3.3.3 Aramis setup utilizing 2 cameras through the furnace window	60
Figure 3.4.1 MACRODYNE press and forming setup with high temperature capability .....	61
Figure 3.4.2 Testing blanks with riveted thermocouples for temperature uniformity study .....	62
Figure 3.4.3 Blank failure due to pinching .....	63
Figure 3.4.4 Specimen fracture characteristics, (a) edge fracture due to small punch radius, and (b, c) fracture due to stress concentration around carrier hole reaching punch radius apex .....	64
Figure 3.4.5 Upper and lower die designs and final punch design with holes (all dimensions are in inches) .....	65
Figure 3.4.6 Teflon lubricant and blank placement for high temperature Marciniak test with alignment pins .....	66
Figure 3.4.7 Limiting strain experienced by carrier blank around hole (uniaxial tension) versus test blanks for balanced biaxial strain path testing.....	68
Figure 3.4.8 Impact of carrier surface roughness on strain translation.....	69
Figure 3.4.9 MACRODYNE built-in 2-camera Aramis setup .....	71
Figure 3.4.10 Lines perpendicular to necking region used to gather major strain data .....	72
Figure 3.4.11 Limiting strain calculation utilizing a second-order parabola, showing major and minor limiting strains at apex .....	73
Figure 3.4.12 Facet size 13x13 with step size of 9 applied over stochastic speckle grid at high magnification for DIC-based strain measurement .	74

Figure 3.4.13 Blank geometries for achieving strain paths from uniaxial tension to balanced biaxial tension.....	76
Figure 3.4.14 Carrier blank geometries for tension-tension side of FLD.....	77
Figure 3.5.1 Experimental hot stamping die quenching setup .....	78
Figure 3.5.2 Hot stamping die quenching die geometry .....	81
Figure 3.5.3 Hot stamping blank with thermocouple ports for temperature measurement.....	83
Figure 3.5.4 Thermocouple placement into hot stamping blank for forming temperature measurement.....	83
Figure 3.5.5 ASTM standard E8 for sub-size tensile samples .....	84
Figure 3.5.6 Setup capable of variable forced air and LN <sub>2</sub> cooling .....	85
Figure 3.5.7 Tensile sample with k-type thermocouple inserted .....	86
Figure 3.5.8 Tensile testing setup with 1-inch gauge length extensometer .	87
Figure 3.6.1 Fracture surfaces cut from formed Marciniak test for fractography .....	88
Figure 3.6.2 STRUERS Secotom-50 precision cut-off machine .....	89
Figure 3.6.3 STRUERS Tegramin-25 semi-automatic polishing machine .....	90
Figure 3.6.4 Epoxy-mounted fracture sample with carbon coating and nickel-based paint.....	91
Figure 3.6.5 JOEL-6610LV SEM in CCEM laboratory.....	92
Figure 3.6.6 Alicona InfiniteFocus G5 .....	93
Figure 4.2.1 (a) Uniaxial tension, (b) plane strain and (c) balanced biaxial tension model geometries .....	95
Figure 4.3.1 Ludwik equation fitted to experimental tensile data at 400°C..	97
Figure 4.4.1 ABAQUS finite element model boundary conditions for plane strain condition.....	99
Figure 4.5.1 Effect of element size on punch force versus displacement of plane strain model .....	101

Figure 4.6.1 Plane strain model with mass scaling factor of 100,000 showing, (a) a comparison of kinetic and internal energy contributions as a function of forming process time, and (b) ratio of kinetic/internal energies .....	103
Figure 5.1.1 Effect of test speed on true stress versus true strain for AA7075-F at 300°C .....	107
Figure 5.1.2 Effect of test speed on true stress versus true strain for AA7075-F at 400°C .....	107
Figure 5.1.3 Effect of test speed on true stress versus true strain for AA7075-F at 500°C .....	108
Figure 5.2.1 Punch load versus displacement traces from Marciniak tests at 300°C for specimens of various widths .....	109
Figure 5.2.2 Punch load versus displacement traces from Marciniak tests at 350°C for specimens of various widths .....	110
Figure 5.2.3 Punch load versus displacement traces from Marciniak tests at 400°C for specimens of various widths .....	110
Figure 5.2.4 Material flow-in and locking causing increase in punch forming force. Rectangular shaped cut-out at the centre of the specimen is from removal of material for microstructural observation.....	111
Figure 5.2.5 Deformed Marciniak test samples; sample geometry from uniaxial tension to balanced biaxial tension (left to right) and 300°C to 400°C (top to bottom).....	112
Figure 5.2.6 Dome height taken from image before fracture showing effects of temperature and specimen geometry.....	112
Figure 5.2.7 Full-field strain plot overlay on deformed Marciniak specimen geometries showing major logarithmic strain components of uniaxial, plane strain and biaxial tension test specimens (left to right) at 300°C. Maximum strain corresponds to central region of full-field strain distribution. ....	114

Figure 5.2.8 Full-field strain plot overlay on deformed Marciniak specimen geometries showing major logarithmic strain components of uniaxial, plane strain and biaxial tension test specimens (left to right) at 350°C. Maximum strain corresponds to central region of full-field strain distribution. .... 114

Figure 5.2.9 Full-field strain plot overlay on deformed Marciniak specimen geometries showing major logarithmic strain components of uniaxial, plane strain and biaxial tension test specimens (left to right) at 400°C. Maximum strain corresponds to central region of full-field strain distribution. .... 114

Figure 5.2.10 Marciniak sample strain paths at 300°C of a material point in the neck region..... 116

Figure 5.2.11 Marciniak sample strain paths at 350°C of a material point in the neck region..... 117

Figure 5.2.12 Marciniak sample strain paths at 400°C of a material point in the neck region..... 117

Figure 5.2.13 Bragard’s method applied to a Marciniak sample having undergone uniaxial strain path (0.5-inch wide geometry) showing fitting to one section line (left). Positioning of 3 section lines for capturing strain gradient along sample (right) ..... 118

Figure 5.2.14 Bragard’s method applied to a Marciniak sample having undergone plane strain path (3-inch wide geometry) showing fitting to one section line (left). Positioning of 3 section lines for capturing strain gradient along sample (right) ..... 119

Figure 5.2.15 Bragard’s method applied to a Marciniak sample having undergone biaxial strain path (7.5-inch wide geometry) showing fitting to one section line (left). Positioning of 3 section lines for capturing strain gradient along sample (right) ..... 119

Figure 5.2.16 Marciniak (in-plane) forming limit curves for AA7075-F at elevated temperatures..... 121

Figure 5.2.17 Fracture forming limit diagram (FFLD) and FLC for elevated temperatures ..... 122

Figure 5.2.18 0.5-inch width sample fracture surfaces of specimens deformed at room temperature (20°C) and observed at magnifications of x50, x500, x2,500 and x5,000 (left to right). Top and bottom rows of fractographic images of the same region were obtained under backscatter electron (BEC) diffraction and secondary electron (SEI) modes ..... 125

Figure 5.2.19 0.5-inch width sample deformed at 300°C and observed at magnifications of x50, x500, x2,500 and x5,000 (left to right). Top and bottom rows of fractographic images of the same region were obtained under backscatter electron (BEC) diffraction and secondary electron (SEI) modes..... 126

Figure 5.2.20 3-inch width sample deformed at 300°C and observed at magnifications of x50, x500, x2,500 and x5,000 (left to right). Top and bottom rows of fractographic images of the same region were obtained under backscatter electron (BEC) diffraction and secondary electron (SEI) modes..... 126

Figure 5.2.21 7.5-inch diameter sample deformed at 300°C and observed at magnifications of x50, x500, x2,500 and x5,000 (left to right). Top and bottom rows of fractographic images of the same region were obtained under backscatter electron (BEC) diffraction and secondary electron (SEI) modes..... 127

Figure 5.2.22 0.5-inch width sample deformed at 350°C and observed at magnifications of x50, x500, x2,500 and x5,000 (left to right). Top and bottom rows of fractographic images of the same region were obtained

under backscatter electron (BEC) diffraction and secondary electron (SEI) modes.....	128
Figure 5.2.23 3-inch width sample deformed at 350°C and observed at magnifications of x50, x500, x2,500 and x5,000 (left to right). Top and bottom rows of fractographic images of the same region were obtained under backscatter electron (BEC) diffraction and secondary electron (SEI) modes.....	128
Figure 5.2.24 7.5-inch diameter sample deformed at 350°C and observed at magnifications of x50, x500, x2,500 and x5,000 (left to right). Top and bottom rows of fractographic images of the same region were obtained under backscatter electron (BEC) diffraction and secondary electron (SEI) modes.....	129
Figure 5.2.25 0.5-inch width sample deformed at 400°C and observed at magnifications of x50, x500, x2,500 and x5,000 (left to right). Top and bottom rows of fractographic images of the same region were obtained under backscatter electron (BEC) diffraction and secondary electron (SEI) modes.....	130
Figure 5.2.26 3-inch width sample deformed at 400°C and observed at magnifications of x50, x500, x2,500 and x5,000 (left to right). Top and bottom rows of fractographic images of the same region were obtained under backscatter electron (BEC) diffraction and secondary electron (SEI) modes.....	130
Figure 5.2.27 7.5-inch diameter sample deformed at 400°C and observed at magnifications of x50, x500, x2,500 and x5,000 (left to right). Top and bottom rows of fractographic images of the same region were obtained under backscatter electron (BEC) diffraction and secondary electron (SEI) modes.....	131

Figure 5.2.28 SEM fractographic image from fracture surface of 0.5-inch wide sample (uniaxial tension strain path) deformed at room temperature and marked with regions analyzed with EDS .....	133
Figure 5.2.29 EDS point analysis of 0.5-inch sample tested at room temperature a) Spectrum 1 – Cu-Al-Mg precipitate b) Spectrum 2 -Al-Zn-Cu-Mg precipitate c) Spectrum 3 – Zn-Al-Mg-Cu d) Spectrum 4 – matrix make up, mainly consisting of Al with fine Zn-Mg precipitate make up .....	133
Figure 5.2.30 SEM fractographic image from fracture surface of 7.5-inch diameter sample (balanced biaxial tension strain path) deformed at 300°C and marked with regions analyzed with EDS .....	134
Figure 5.2.31 EDS point analysis of 7.5-inch diameter fractured sample tested at 300°C a) Spectrum 5 – Zn-Cu-Mg-Al precipitate, b) Spectrum 6 – Al matrix composition .....	135
Figure 5.2.32 SEM fractographic image from fracture surface of 7.5-inch diameter sample (balanced biaxial tension strain path) deformed at 350°C and marked with regions analyzed with EDS .....	135
Figure 5.2.33 EDS point analysis of 7.5-inch diameter sample tested at 350°C a) Spectrum 7 – Al matrix b) Spectrum 8 – Zn-Mg-Cu-Al precipitate .....	136
Figure 5.2.34 SEM fractographic image from fracture surface of 7.5-inch diameter sample (balanced biaxial tension strain path) deformed at 400°C and marked with regions analyzed with EDS .....	137
Figure 5.2.35 EDS point analysis of 7.5-inch diameter sample tested at 400°C a) Spectrum 9 – Al-Zn matrix .....	137
Figure 5.2.36 SEM micrographs from polished LT section near fracture surface of 0.5-inch wide sample (uniaxial tension strain path) deformed at 300°C at magnifications of x50, x200 and x2,500. Backscatter electron mode (BEC) .....	140

Figure 5.2.37 SEM micrographs from polished LT section near fracture surface of 3.0-inch wide sample (plane strain tension strain path) deformed at 300°C at magnifications of x50, x200 and x2,500. Backscatter electron mode (BEC) ..... 141

Figure 5.2.38 SEM micrographs from polished LT section near fracture surface of 7.5-inch diameter sample (balanced biaxial tension strain path) deformed at 300°C at magnifications of x50, x200 and x2,500. Backscatter electron mode (BEC) ..... 142

Figure 5.2.39 7.5-inch diameter sample secondary fracture region for 300°C at magnifications of x35 and x250. Backscatter electron mode (BEC) 143

Figure 5.2.40 SEM micrographs from polished LT section near fracture surface of 0.5-inch wide sample (uniaxial tension strain path) deformed at 350°C at magnifications of x50, x200 and x2,500. Backscatter electron mode (BEC) ..... 144

Figure 5.2.41 SEM micrographs from polished LT section near fracture surface of 3.0-inch wide sample (plane strain tension strain path) deformed at 350°C at magnifications of x50, x200 and x2,500. Backscatter electron mode (BEC) ..... 145

Figure 5.2.42 SEM micrographs from polished LT section near fracture surface of 7.5-inch diameter sample (balanced biaxial tension strain path) deformed at 350°C at magnifications of x50, x200 and x2,500. Backscatter electron mode (BEC) ..... 146

Figure 5.2.43 SEM micrographs from polished LT section near fracture surface of 0.5-inch wide sample (uniaxial tension strain path) deformed at 400°C at magnifications of x50, x200 and x2,500. Backscatter electron mode (BEC) ..... 147

Figure 5.2.44 SEM micrographs from polished LT section near fracture surface of 3.0-inch wide sample (plane strain tension strain path)

deformed at 400°C at magnifications of x50, x200 and x2,500.	
Backscatter electron mode (BEC) .....	148
Figure 5.2.45 3-inch wide sample secondary fracture region for 400°C at x2,500 magnification showing fractured particle. Backscatter electron mode (BEC) .....	149
Figure 5.2.46 SEM micrographs from polished LT section near fracture surface of 7.5-inch diameter sample (balanced biaxial tension strain path) deformed at 400°C at magnifications of x50, x200, x2,500 and x5,000. Backscatter electron mode (BEC) .....	151
Figure 5.2.47 7.5-inch diameter sample secondary fracture region for 400°C test. Images acquired at magnifications of x45 (left) and x200 (right). Backscatter electron mode (BEC) .....	151
Figure 5.2.48 Fracture region of polished LT section of balanced biaxial tension sample tested at 400°C showing image processing for void fraction calculation where red regions indicate significant voids (14.2% void fraction).....	154
Figure 5.2.49 Relationship between void fraction, Von Mises equivalent strain, and temperature from uniaxial, plane strain, and balanced biaxial tension specimens.....	154
Figure 5.2.50 BSE image of fracture region for 0.5-inch wide sample tested at 300°C. This specimen region was chosen for EDS mapping data shown in Figure 5.2.51 .....	156
Figure 5.2.51 EDS maps of 0.5-inch wide sample at 300°C from BSE fracture region image .....	156
Figure 5.2.52 BSE image of fracture region for 0.5-inch wide sample at 350°C. This specimen region was chosen for EDS mapping data shown in Figure 5.2.53.....	157
Figure 5.2.53 EDS maps of 0.5-inch wide sample at 350°C from BSE fracture region image .....	157

Figure 5.2.54 BSE image of fracture region for 0.5-inch wide sample at 400°C. This specimen region was chosen for EDS mapping data shown in Figure 5.2.55..... 158

Figure 5.2.55 EDS maps of 0.5-inch wide sample at 400°C from BSE fracture region image ..... 158

Figure 5.2.56 3D surface roughness graphs for as-received AA7075-F. Rolling direction (RD) and transverse direction (TD) shown. 1.6 x 1.6 mm..... 162

Figure 5.2.57 3D surface roughness graphs for uniaxial tension strain path at 300°C, 350°C, and 400°C (top to bottom). Direction of applied stress parallel to TD direction. 1.6 x 1.6 mm ..... 163

Figure 5.2.58 3D surface roughness graphs for plane strain path at 300°C, 350°C, and 400°C (top to bottom). Direction of applied stress parallel to TD direction. 1.6 x 1.6 mm ..... 164

Figure 5.2.59 3D surface roughness graphs for balanced biaxial tension strain path at 300°C, 350°C, and 400°C (top to bottom). Direction of applied stress parallel to TD direction. 1.6 x 1.6 mm ..... 165

Figure 5.2.60 Relationship between average roughness (Ra), Von Mises equivalent technical strain, and temperature for as-received sheet as well as uniaxial, plane strain, and biaxial tension specimens..... 166

Figure 5.3.1 Force versus displacement curves comparing experimental and simulation test results for 0.5-, 3-, and 7.5-inch sample geometries at 400°C..... 168

Figure 5.3.2 Simulated Marciniak uniaxial tension strain path test at 400°C showing the principal logarithmic strain for 0.5-inch wide geometry at punch displacement of 0.67-inches ..... 170

Figure 5.3.3 Simulated Marciniak plane strain tension strain path test at 400°C showing the principal logarithmic strain for 3.0-inch wide

geometry at punch displacement of 1.21-inches. The strain distribution in the carrier blank is shown on the bottom right .....	170
Figure 5.3.4 Simulated Marciniak balanced biaxial tension strain path test at 400°C showing the principal logarithmic strain for 3.0-inch wide geometry at a punch displacement of 1.39-inches. The strain distribution in the carrier blank is shown on the bottom right .....	171
Figure 5.3.5 Marciniak sample strain paths at 400°C of a material point in the neck or highest strained region for both experimental and FE simulation .....	172
Figure 5.3.6 Time-dependent method (Martinez-Donaire et al., 2014) for calculating limiting strain for simulated Marciniak uniaxial strain path (0.5-inch geometry) at 400°C .....	173
Figure 5.3.7 Time-dependent method (Martinez-Donaire et al., 2014) for calculating limiting strain for simulated Marciniak plane strain path (3-inch geometry) at 400°C .....	174
Figure 5.3.8 Full-field major strain maps of experimental (left column) and FE simulations (right column) for: (a) uniaxial tension, (b) plane strain, and (c) balanced biaxial tension strain paths at 400°C.....	175
Figure 5.3.9 Experimental FLC in the tension-compression region and FE simulation based forming limit strains for uniaxial and plane strain paths at 400°C.....	176
Figure 5.4.1 Cooling rate curves from 5 different positions in hot stamping blank during formation process.....	179
Figure 5.4.2 Locations of tensile samples taken from hot stamped part ...	180
Figure 5.4.3 Post-artificial ageing stress versus strain curves from uniaxial tensile test samples cut from various regions along the hot stamped part .....	181
Figure 5.4.4 Post hot stamping blank surface features for, a) Fuchs RENOFORM 10 ALWF applied to blank before heating, b) Fuchs	

RENOFORM 10 ALWF applied to die surface, c) Silicon lubricant applied to die surface, and d) Teflon film applied to die surface .....	182
Figure 5.5.1 Tensile sample cooling rates after solutionizing samples for 1 hour and after post quench T6 tempering .....	184
Figure 5.5.2 Engineering stress versus strain curves from uniaxial tensile test samples after solutionizing, quenching at various quench rates and artificial ageing to T6 temper state.....	184
Figure 5.5.3 Effect of cooling rate on ultimate tensile strength (UTS) of AA7075 .....	185

## LIST OF TABLES

Table 2.4.1 FE Investigations for FLD Determination .....	38
Table 2.5.1 Strength and compositions of various wrought aluminum alloys (Davis, 2001) .....	42
Table 2.5.2 Role of alloying elements in Al-7XXX series alloys .....	42
Table 2.5.3 Room temperature tensile properties of AA7075 .....	50
Table 3.2.1 Elemental composition of supplied sheet studied through ICP- OES. ....	56
Table 3.4.1 Macrodyne press parameter settings for a range of temperature and test geometries .....	70
Table 3.5.1 Forming cycle parameters for laboratory hot stamping tests....	79
Table 3.6.1 Polishing and lubricant settings .....	90
Table 4.3.1 Ludwik equation fitting parameters .....	97
Table 5.2.1 Surface roughness measurements on deformed Marciniak samples in the vicinity of surface fracture (or crack).....	162

# NOMENCLATURE

A	Atomic mass
AA	Aluminum Association
CCT	Continuous cooling transformation
$c_d$	Current effective dilatational wave speed
DIC	Digital image correlation
e	Engineering strain
E	Youngs modulus
$E_0$	Accelerating voltage
FE	Finite element
$F_N$	Normal force
$F_f$	Frictional force
$f_0$	Inhomogeneity factor
HTPP	High-temperature pre-precipitation
K	Strength coefficient
$L_e$	Characteristic element dimension
m	Strain rate sensitivity
n	Strain hardening exponent
N	Newton (unit of force)
Pa	Pascal (unit of stress)
Q	Related activation energy
r	Plastic anisotropy

R	Gas constant
RRA	Retrogression and re-aging
$R_a$	Average surface roughness
$R_q$	Root mean square roughness
$R_z$	Average maximum height of profile
S	Engineering stress
SCC	Stress corrosion cracking
T	Temperature
$t_0$	Initial thickness
$t_f$	Thickness at fracture
$t_{a0}$	Initial nominal thickness
$t_{b0}$	Initial imperfection thickness
$\nu$	Poisson's ratio
Z	Atomic number, Zener-Hollomon parameter
$\rho$	Density
$\rho^*$	Strain ratio (for proportional loading condition)
$\sigma$	True stress
$\sigma_y$	Yield stress
$\mu$	Coefficient of friction
$\bar{\epsilon}$	Equivalent strain
$\epsilon$	True strain
$\dot{\epsilon}$	Strain rate
$\epsilon_p$	Plastic strain

$\epsilon_1, \epsilon_2, \epsilon_3$	Principal strains
$\lambda$	Plastic multiplier
$\beta$	Strain ratio
$\omega$	Frequency

# Chapter 1

## Introduction

### 1.1 Background

The push for increased fuel efficiency of automotive vehicles and reduction in greenhouse gases (GHG) has resulted in substantial investment in new technology development by the automotive industry. Environment Canada has currently targeted an annual reduction of 3.5% and 5% in GHG for 2017 to 2021 and 2021 to 2025, respectively (“Canada: Light-duty: Fuel Consumption and GHG | Transport Policy,” 2018) corresponding to a fuel efficiency of 6.5 L/100km by 2021 and 4.7 L/100km by 2025 (Beene et al, 2018). As fuel standards become more stringent as seen in Figure 1.1.1, vehicle manufacturers must invest in research related to light-weighting of vehicles among other environmentally friendly technologies.

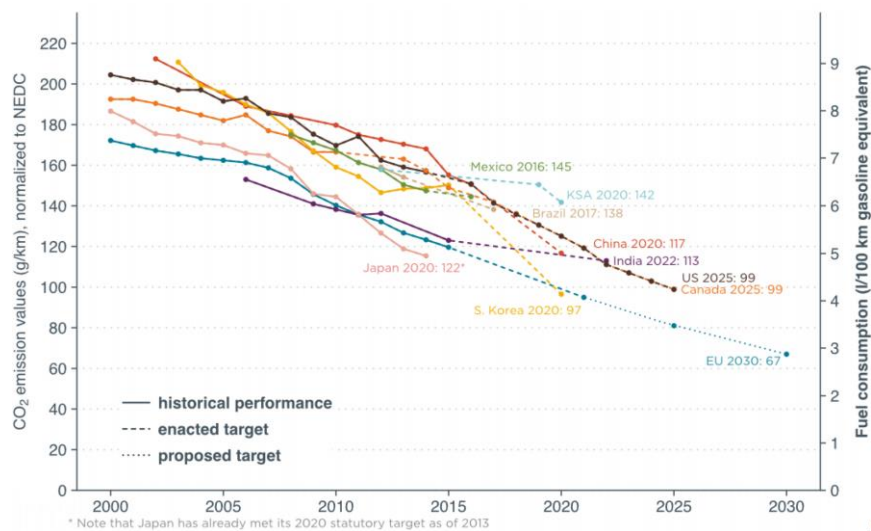


Figure 1.1.1 Historical fleet CO<sub>2</sub> emissions performance and current standards (gCO<sub>2</sub>/km normalized to NEDC) for passenger cars (Yang, 2018)

One way automakers can improve vehicle efficiency is by reducing the weight of the vehicles body-in-white (BIW), the stage when only the frame of the vehicle is assembled in a process known as light-weighting. Light-weighting not only reduces fuel costs by lowering the weight of the vehicle but also allows for utilization of smaller components such as engines, brakes, suspension, etc. - creating a domino effect of weight savings.

Light-weighting is done by using materials with increased strength-to-weight ratios in the car body. Light-weight materials such as aluminum, carbon-fibre reinforced plastics (CFRP) and magnesium alloys have already made their debut in vehicles such as Audi's A8, Alfa Romero's 4C and BMW's 7-series sedan (Berman, 2015). As seen in Figure 1.1.2, Audi's Space Frame (ASF) utilizes a large amount of aluminum alloy sheet material.

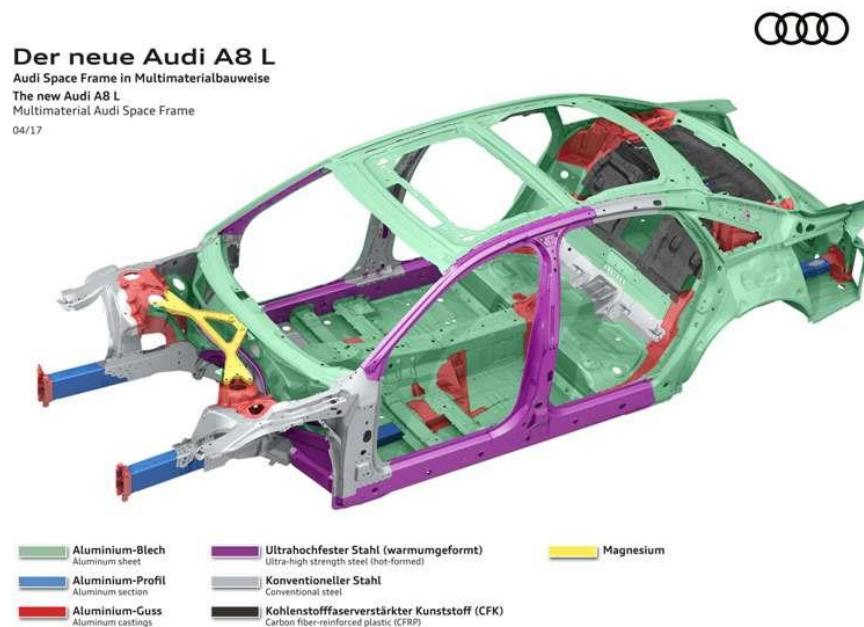


Figure 1.1.2 The new Audi A8 L – Audi Space Frame (ASF) ("Audi MediaCenter," 2017)

Although it takes significantly more energy to produce virgin aluminum than steel, its lifetime energy savings outweigh that of steel through emissions savings and its comparative recyclability (Ungureanu et al, 2007). Its comparative cost can also be outweighed by the expected fuel savings and extended vehicle life. With aluminum weight percent in vehicles expected to increase from 6% in 2015 to 26% in 2025 (Trefis Team, 2018). The optimal vehicle design moving forward will most likely consist of multiple materials as to provide optimal crash performance and fuel-efficiency.

Currently, the material of choice for automotive companies is steel, accounting for over 60% of vehicle weight (Trefis Team, 2018). However, even with some third-generation advanced high strength steels (AHSS) having strengths above 1500 MPa's (Yi et al, 2018), AA7075's low density, about one-third that of steel, put it in a comparable strength-to-weight ratio. In its strongest temper (T6) AA7075 can achieve an ultimate strength of approximately 600 MPa, significantly higher than other automotive aluminum alloys used today and mainly attributed to its classification as an age hardenable alloy (J.R, 2001).

Unfortunately, a typical feature accompanying many high strength steels and aluminum alloys is their low formability at room temperature. As seen in Figure 1.1.3, the strength of an alloy is inversely proportional to its formability or elongation. To increase formability and the complexity of parts

that can be produced by stamping, the hot stamping die quenching (HSDQ) process is utilized.

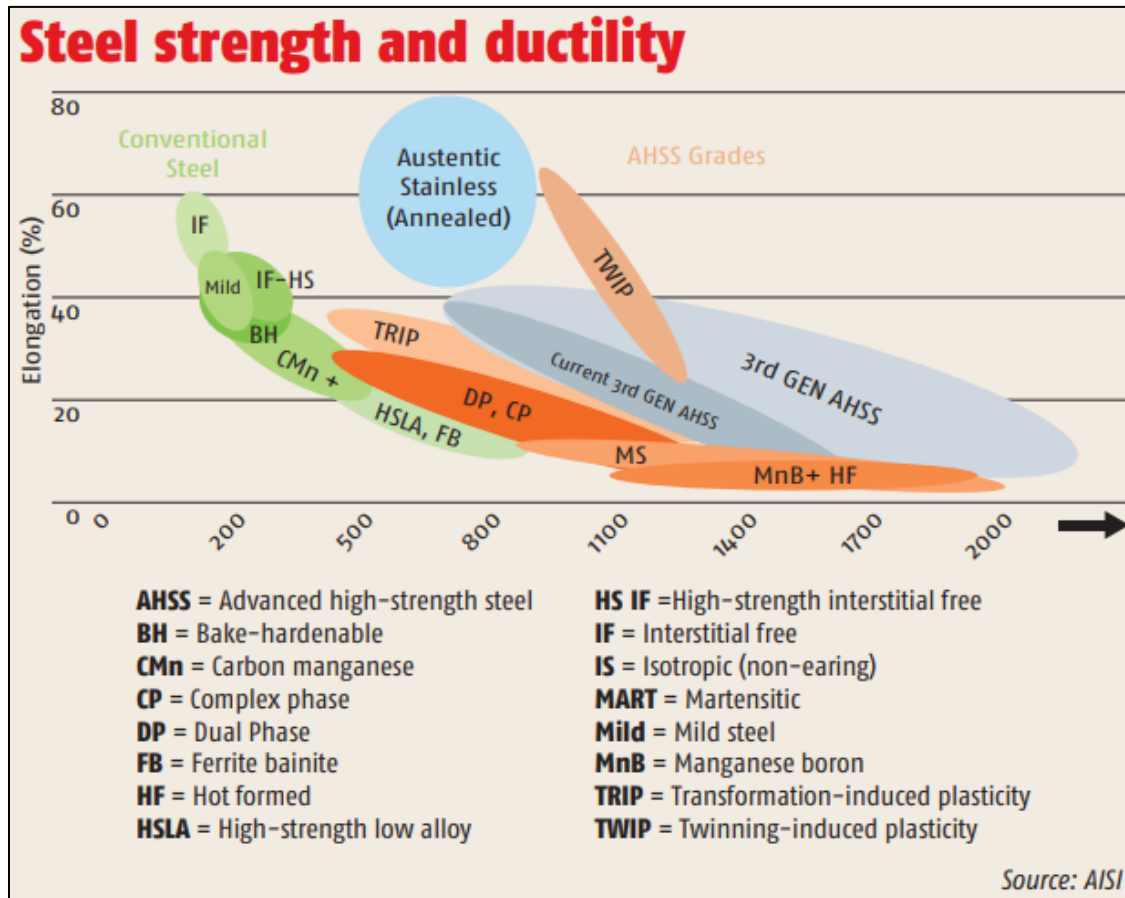


Figure 1.1.3 'Banana' chart showing inverse relationship between strength and elongation ("Steel Definitions | WorldAutoSteel," 2018)

Originally developed for stamping of press-hardenable AHSS steels, the process has since been adapted for age hardenable aluminum sheet materials (see Figure 1.1.4). The typical process involves the heating of the blank to the solutionizing temperature of the aluminum alloy of interest. By heating the aluminum sheet to its solutionizing temperature above 460°C, precipitates go into solution, decreasing strength and increasing formability. The blank is then transferred to be formed at elevated temperatures and simultaneously

quenched in the die. It is these process parameters and cooling rates that will have a significant effect on the parts final strength among other characteristics as the quenching acts as a mechanism to lock precipitates into super-saturated solid solution (SSSS). Unlike press-hardenable steels that gain peak strength post quenching, age-hardenable aluminum alloys require an additional step to regain their initial strength properties. These alloys must be artificially aged in a furnace to avoid a lengthy natural aging process that can take weeks to produce satisfactory properties. This aging step provides the thermal energy to form fine strengthening precipitates on the order of 1-100 nm in size that are uniformly dispersed within the matrix material and cause significant strengthening of the formed and quenched part.

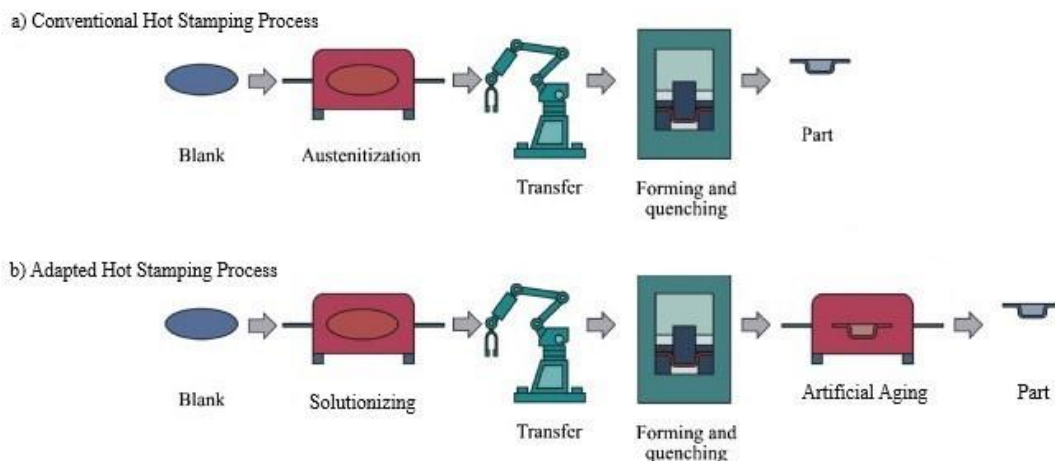


Figure 1.1.4 Hot stamping processes: a) conventional hot stamping process b) adapted hot stamping for age-hardenable aluminum alloys (Adapted from Merklein et al, 2008)

Typically, stamping operations rely on an understanding of a materials formability so that they can be successfully formed into complex parts. By analysing the various strain paths typically encountered in sheet metal

forming, the well-known forming limit diagram (FLD) can be produced - giving the capability to predict where the formability of the material will be exceeded, and a stamped part may fail. Although typically obtained at room temperature through an out-of-plane (Nakazima) deformation method, more insight into the material's intrinsic characteristics can be achieved through an in-plane (Marciniak) method which minimizes the effect of tool-sheet contact and friction on forming limits. Although the Marciniak test is more complex, the advantage of this test outweighs the associated cost.

## **1.2 Objectives**

The objectives of the following research are to assess the aluminum alloy AA7075-F for its feasibility for use in hot stamping applications in the automotive industry. This research focuses on the strength and formability of AA7075 at elevated temperatures primarily between 300°C and 400°C. It is at these temperatures that formability during the hot stamping processes will be mimicked. The following sub-objectives are addressed in the present research:

1. Development of an elevated temperature in-plane formability (Marciniak) test for high strength precipitation-hardenable AA7075 aluminum sheet in the as-fabricated temper (F).
2. Relate formability and forming limit diagram (FLD) to microstructural damage and deformed surface characteristics after forming.

3. Development of a finite element (FE) model of elevated temperature Marciniak test that utilizes a constitutive material model to aid in the development of the test method and prediction of forming limits. The model provides a better understanding of material flow behavior during elevated temperature through various in-plane loading conditions.
4. Design of a lab-based hot stamping and die quenching test set-up for a simpler, small-scale, AA7075 sheet component resembling the cross-section of an automotive B-pillar component, and assess part strength after forming, quenching and post-formed artificial ageing. Specifically, investigating the effect of blank cooling rate in the die after forming by conducting tensile tests on quenched and aged material taken from the formed component along with supplemental cooling rate studies on un-formed sheet.

## Chapter 2

# Literature Review

### 2.1 General Formability of Sheet Materials

Sheet metal forming process studies investigate a sheet material's ability to be formed into useful but complex 3D components and consumer products. The process predominantly involves large out-of-plane plastic deformation of a flat sheet by employing large presses and component-specific tooling. The forming of a sheet metal is done through three main forming modes: (i) stretching, (ii) drawing and (iii) bending. The forming modes in combination allow for the formation of complex parts such as vehicle structural pillars, fenders, doors and enclosures. Often under multi-axial, out-of-plane loading conditions, forming tools are used to induce stress states that allow the material to be shaped into desired parts. However, due to complexity and material limitations, parts can be susceptible to failure during production experiencing localized necking and component fracture.

As previously observed in Figure 1.1.3, a reciprocal relationship exists between a materials strength and formability. That is, a higher strength material may typically initiate failure and fracture at a smaller elongation (or lower formability) than a lower strength material. Along with strength dependency, a materials failure can depend greatly on its strain state.

The axisymmetric cup drawing process will be analysed below to show how various strains develop in the different regions of the part during the automotive stamping process. In Figure 2.1.1 (a), a standard cup drawing process is shown where a circular blank is clamped between a die (or bottom circular plate with a central circular hole) and a blank holder (or upper circular plate with a central circular hole) around its periphery. A circular punch with a flat head is then moved downwards in a process that draws the circular blank into the die cavity to form an axisymmetric cup. The process of drawing involves several forming sub-modes such as radial drawing of the blank into the die, bending and un-bending of the blank around the die profile radius, plane strain tension of the cup wall, stretch-bending over the punch profile radius, and in-plane balanced-biaxial stretching of the bottom of the cup. A pie section of a partially formed cup is shown in Figure 2.1.1(b) where six points along the cup line profile from the outer edge to the centre of the cup are analyzed for two principal surface strain components ( $\varepsilon_1$  and  $\varepsilon_2$ ) and plotted as a schematic in Figure 2.1.1 (c) for two different cup heights. The two strain contours in Figure 2.1.1(c) covering a range of strain states from pure shear along the cup edge to a plane strain state in the cup wall to balanced-biaxial tension state at the centre of the cup base can be observed (Marciniak & Duncan, 1992). These correspond to two different cup heights with the higher strain contour corresponding to the greater cup height. Even more complex strain signatures result when complex automotive components are formed.

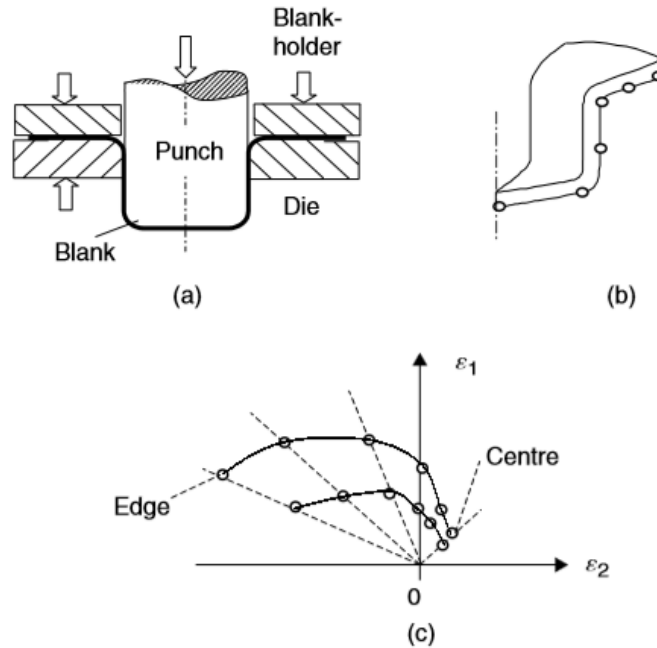


Figure 2.1.1 Strain paths observed in cup forming operations (Marciniak & Duncan, 1992)

## 2.2 Forming Limit Curve as a Measure of Formability

The forming limit curve (FLC) was originally introduced in 1964 by Keeler-Backofen as a measure of formability of a sheet material. This single representation is perhaps the most widely accepted measure of onset of plastic instability (or onset of localized necking, a precursor to material failure by fracture) in sheet materials ever since. A FLC is a V-shaped curve in 2D principal surface strain space (also called major and minor strain space) that represents the locus of various possible 'necked' states in a sheet material that arise from various idealized forming modes such as uniaxial tension, plane strain tension, balanced-biaxial tension etc., as noted earlier. These forming modes are also referred to as strain paths and shown by radial lines

emanating from the zero minor strain point in the 2D strain state, as shown in Figure 2.2.1 below.

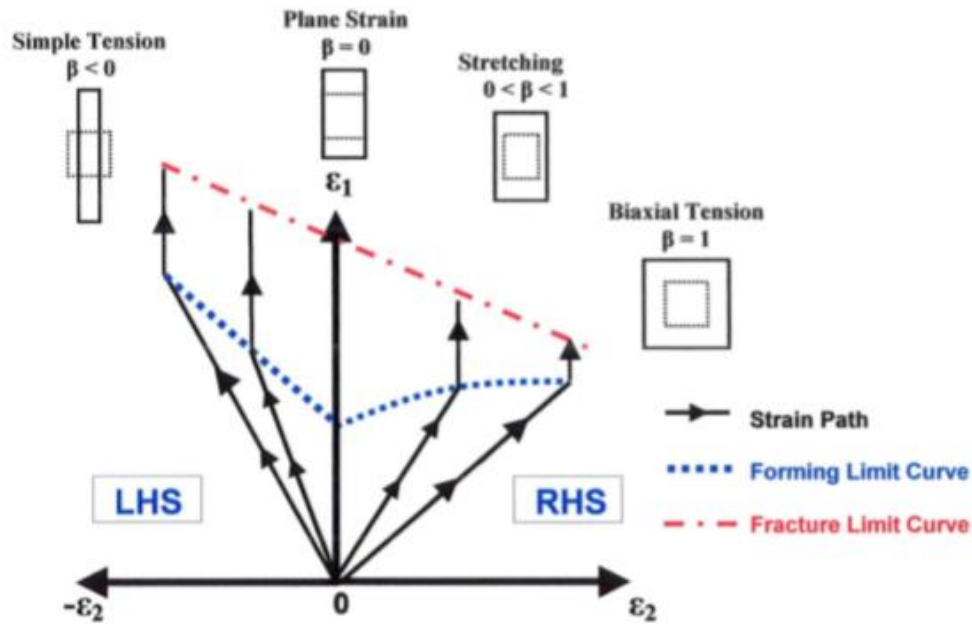


Figure 2.2.1 Forming limit curve showing various strain paths as well as fracture limits

The original FLC looks at paths that are most typical of forming operations and quantifies strain values before localized necking occurs. These strain paths are often assumed to be linearly proportional (straight lines) and as such are defined by strain ratios of minor to major strain as follows:

$$\beta = \frac{\epsilon_2}{\epsilon_1} \quad (2.1)$$

Through the analysis of the major ( $\epsilon_1$ ) and minor principal strain ( $\epsilon_2$ ) paths taken by a sheet material until localized necking, a materials formability can be mapped through the FLC. The concept of FLC has been subsequently

extended to include the forming limit stress diagram (FLSD), introduced by Arriuex et al. (1982).

The assumption of linear proportionality holds largely true for in-plane forming while the strain paths can deviate from linearity during out-of-plane forming typical of real forming operations that involve dies and punches and will be discussed later (Chen & Fang, 2018; Gutierrez et al., 2012). As seen in Figure 2.2.1, the black lines denote the different strain paths taken through various processes. The right-hand side (RHS) corresponds to stretching and positive minor strain such as biaxial tension ( $\beta=1$ ) and plane strain ( $\beta=0$ ); while the left-hand side (LHS) corresponds to negative minor strains such as uniaxial tension ( $\beta=-1/2$ ) and plane strain ( $\beta=0$ ). It is important to note that major strain is always considered the larger positive quantity. As the magnitude of strain increases beyond the forming limit, localized necking occurs, and the strain increment ratio approaches a zero value, typically under plane strain conditions.

$$\frac{d\varepsilon_2}{d\varepsilon_1} \rightarrow 0 \quad (2.2)$$

Outside of the described strain paths, various failure mechanisms such as wrinkling, shear and fracture can occur. The cross hatched region in Figure 2.2.2 signifies the forming window; strain paths inside this region are safe for forming operations, while strain paths outside are prone to failure. It should also be noted that as strains localize to fracture, another limit curve, the so-

called forming limit curve at fracture (FLCF) may become a better measure of formability. Depending on the materials ductility the FLCF may lie below the FLC for less ductile materials, especially in the tension-tension region of the FLC space. In other words, FLCF may intersect the FLC, causing premature fracture without localized necking. Due to the importance of FLC as determinant of localized deformation in a sheet material, effort has been made to obtain it experimentally via controlled experiments in a laboratory setting and use it in conjunction with strain signatures from forming trials of real parts to analyze and optimize component as well as die design for formability. Also, by implementing material specific FLC into FE models of component forming, it has become possible to more effectively and cheaply carry out virtual die stamping tryout and optimize die design for specific part forming with a certain sheet material of interest before costly die manufacturing.

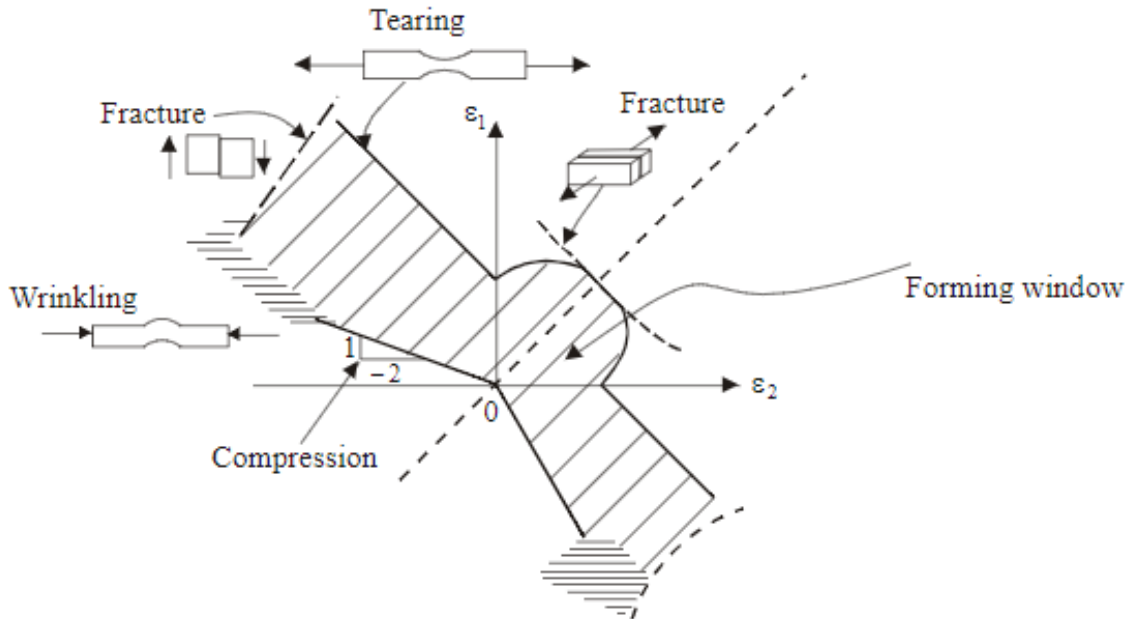


Figure 2.2.2 Forming Window for Plane Stress Sheet Forming (Marciniak & Duncan, 1992)

### 2.2.1 Factors Effecting Formability

A materials formability/FLC depends on many parameters including: basic material property parameters, sheet microstructure and crystallographic texture, sheet surface characteristics, tool geometric parameters, and tool/sheet contact conditions and friction. Basic material property parameters that primarily come from uniaxial tension test include its: strain hardening exponent (or n-value), strain rate sensitivity (or m-value), plastic strain anisotropy (or r-value), and sheet nominal thickness among many others (Hosford & Caddell, 2011). The n, m and r values can be easily measured and therefore are often used to select or specify material for forming applications. Many of the material property parameters, especially the n, m and r values, are also dependent on sheet orientation, strain, strain rate, and temperature.

Therefore, it is often more valuable and efficient from the point of view of formability assessment and FLC prediction to develop material and forming process appropriate constitutive material models. Such material models are then used in conjunction with elastoplastic mechanics of sheet metal forming to analyze the intrinsic formability of the sheet for a specific sheet metal forming process. Because of the vast number of parameters associated with each material and the knowledge necessary to choose a suitable constitutive material model other approaches have been undertaken in recent years. One interesting approach that has been utilized is that of artificial neural network (ANN) modelling (Kotkunde et al, 2014; Mohamed et al, 2016). By utilizing existing FLCs Mohamed et al (2016) were able to predict FLCs for AA5754 at additional temperatures with some accuracy.

Intrinsic properties of a material such as the  $n$ -value can often give insight into a materials formability. A material with a high  $n$ -value, indicative of increased strain hardening and larger uniform deformation prior to diffuse necking of the sheet will typically prolong localized necking. Marciniak & Duncan (1992) showed a higher  $n$ -values correlation with an increased FLC in general (Figure 2.2.3). The same relationship of increased FLC can be seen for  $m$ -value, contributed primarily by the delayed growth of necking beyond maximum tension.

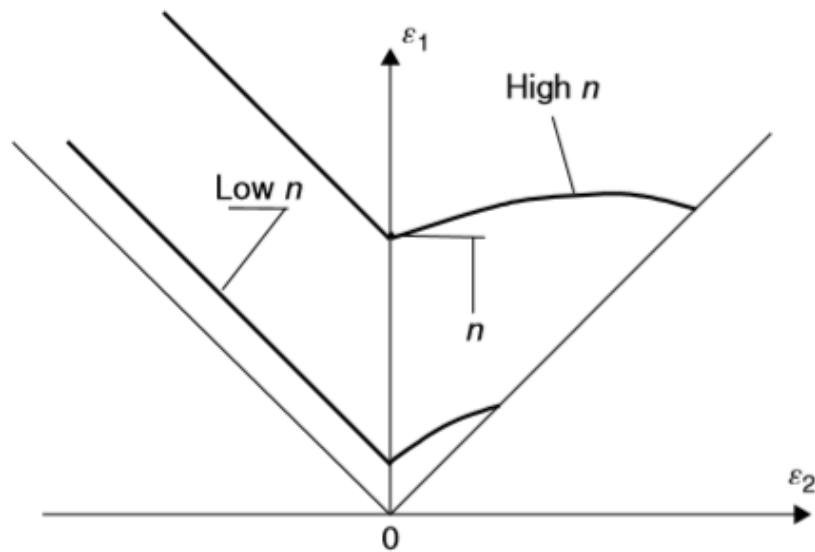


Figure 2.2.3 Increasing  $n$ -value raises FLC (Marciniak & Duncan, 1992).

In addition, it is known that the FLC will increase with increased sheet thickness. Using the Nakazima test method, Dilmeç et al. (2013) concluded that as AA2024-T4 sheet thickness increased from 1 mm to 2 mm the limiting strain also increased as shown in Figure 2.2.4.

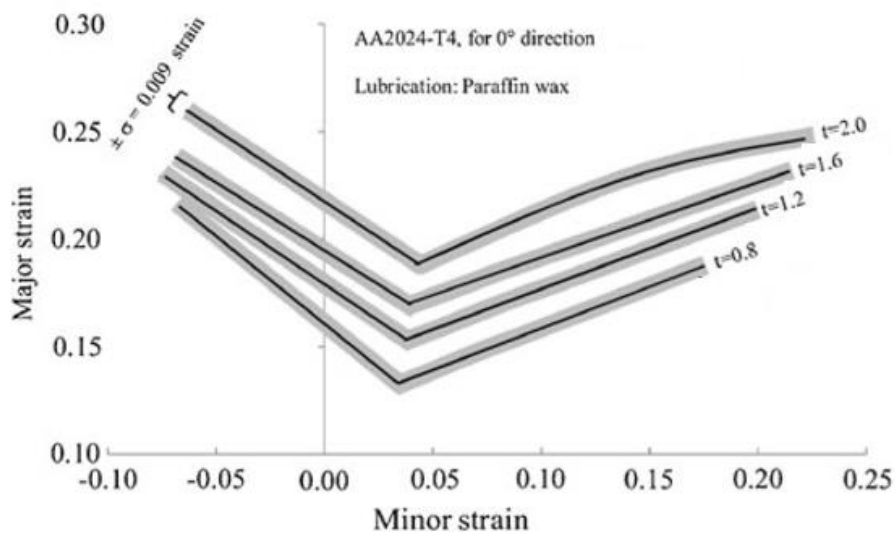


Figure 2.2.4 The effect of sheet thickness on the FLC of AA2024-T4 (Dilmeç et al., 2013)

## **2.3 Experimental Techniques for FLC Determination**

### **2.3.1 Out-of-Plane Nakazima Method**

While numerous methods have been proposed for theoretically obtaining a materials formability by utilizing basic material properties and analyzing mechanics of hemispherical punch stretching, experimental methods are still considered to be the most reliable means of obtaining accurate FLCs. One of the most commonly used tests is the out-of-plane sheet stretching test, using a cylindrical punch with a hemispherical head, called the Nakajima test (Affronti et al, 2018). In this test, a sheet metal blank is held by its edges using a circular lock-bead in a die set, and centre region of the blank is formed into a dome shape with the hemispherical punch head until the onset of necking or fracture. Figure 2.3.1 shows a schematic diagram of the die region where the blank is being held by lock beads to prevent the flow of material outside of the lock bead. Typically, the Nakazima test requires a forming test system with two separate vertical motions, typically performed by servo-hydraulic actuators, one to securely clamp the test blank between the upper die and the lower blank holder, and second motion to move the punch upwards (or downwards, as per the test design configuration) to stretch the test blank. The rigid punch is moved until localized necking or failure (i.e., a crack) occurs at some location over the dome surface. The Nakazima test has been standardized in recent years for obtaining room temperature FLCs

by ISO and other national technical societies (*International Standard ISO 12004-2:2008*, 2008). However, draw bead design can vary, consisting of knurled or roughened surfaces, to effectively prevent any flow of material from outside the clamped region into the die cavity. The Nakajima test is a robust test that allows for assessment of formability and FLC determination of a range of sheet materials of different strengths, tempers and thicknesses completed in a single setup. In-situ (or continuous) image capturing of the deforming dome specimen can be implemented into the test set-up to better detect the onset of necking and later analysis of images for strain mapping and FLC construction.

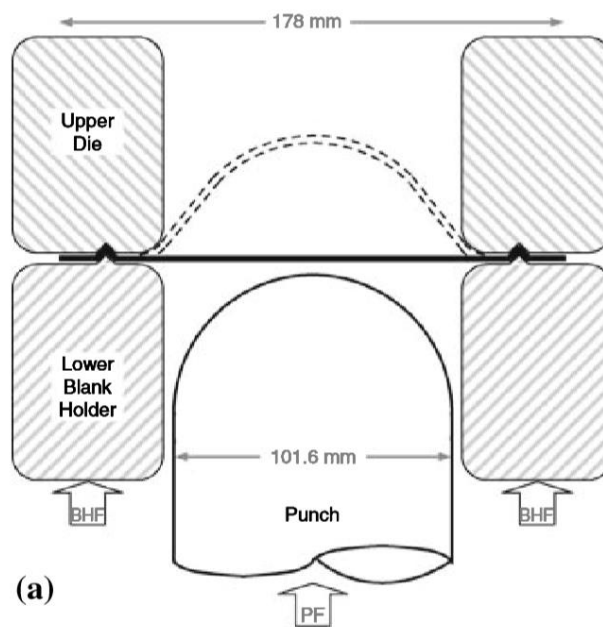


Figure 2.3.1 Out-of-plane Nakajima test method (BHF-blank holder force; PF-punch force) (Hsu et al, 2008)

Using various blank geometries, strain paths from simple uniaxial tension to balanced biaxial tension, analogous to those found in automotive

stampings, can be mimicked to create the previously discussed FLCs. Figure 2.3.2 shows the various blank geometries and their corresponding strain paths. Narrower widths at the centre region of the blank correspond to strain paths on the left-side (or the tension-compression side) of FLD strain space while wider blanks correspond to strain paths on the right-side (or the tension-tension side). Typically, to obtain various tension-tension strain paths, full dome specimen geometry with a range of punch-sheet friction conditions are needed. This is achieved by using dry (or no lubricant providing a large friction at the punch/sheet interface) to highly effective lubricants (providing a very low friction value). A combination of grease, liquid lubricants, and polymer films can also be used to generate a range of friction conditions that lead to a range of strain paths. Typically, the location of localized neck or failure is friction-dependent with dry conditions leading towards a strain path closer to plane strain and the neck or failure location farthest from the pole of the dome, and *vice versa* for the well lubricated punch-sheet contact conditions (i.e., strain path closer to balanced biaxial tension and neck/failure location at the pole). It is to be noted that the blanks shown in Figure 2.3.2 are the geometries utilized by Shao et al. (2018). Actual blank dimensions used by the various researchers are often presented in the experimental section of their papers.

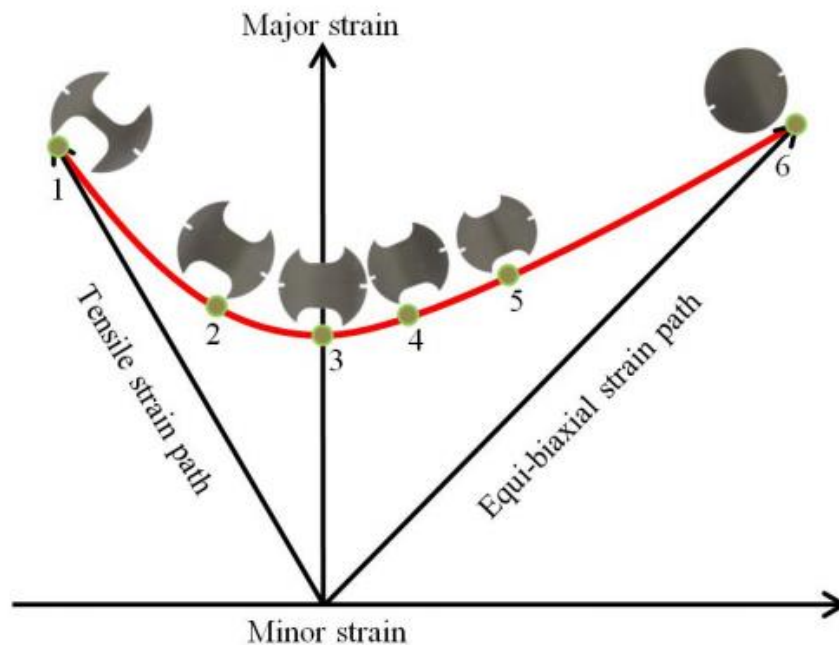


Figure 2.3.2 Typical specimen geometry corresponding to strain paths for FLC (Shao et al., 2018)

As noted earlier, the out-of-plane test method, as the name suggests, induces bending stresses in the material during forming. Charpentier (1975) noted the test's susceptibility to punch geometry and observed that the limit strains increased with a reduction in hemispherical punch head radius. Ghosh and Hecker (1974) also noted the bending stress variation with punch radius as well as changes to the friction, normal pressure, and instability conditions with punch radius. It was shown that a smaller radius punch contributes to the prolonging of localized necking and fracture, and, as a result, raises the FLC compared to an in-plane stretching method. As shown in the next section, an in-plane method does not suffer from the effect of punch geometry, contact and friction on the FLC. However, the out-of-plane method is easier and more

practical in that the resulting FLCs correlate well with the strains associated with necked and fractured regions of actual automotive stampings. In-plane test method, on the other hand, offers advantages when intrinsic formability of a sheet material is desired independent of the die design parameters.

### **2.3.2 In-Plane Marciniak Method**

Another test akin to the Nakajima test is the in-plane Marciniak test first introduced by Marciniak and Kuczynski (1973). The method uses a cylindrical punch with a flat head as opposed to a hemispherical head. As mentioned earlier, this method seeks to remove the effects of bending (or through-thickness stress variation) and friction observed in the Nakajima test and is not susceptible to punch diameter. However, this test typically requires two overlapping blanks (a carrier blank and a test blank) and is somewhat harder to implement for less tried materials and can be more time consuming. A carrier blank is inserted into the die set between the test blank and punch to remove frictional effects. The carrier blank is manufactured with a hole in the center to allow for expansion, this expansion along with the radial friction between the blanks translates strain to the test blank, promoting fracture in the unsupported central region of the test blank. According to ISO 12004-2:2008 recommendations, the carrier blank is to be manufactured from a material that is more formable than the test blank as well as at least 80 percent of its thickness to promote fracture in the test piece (*International*

*Standard ISO 12004-2:2008*, 2008). A successful test results when the specimen fails in the unsupported central region of the test blank.

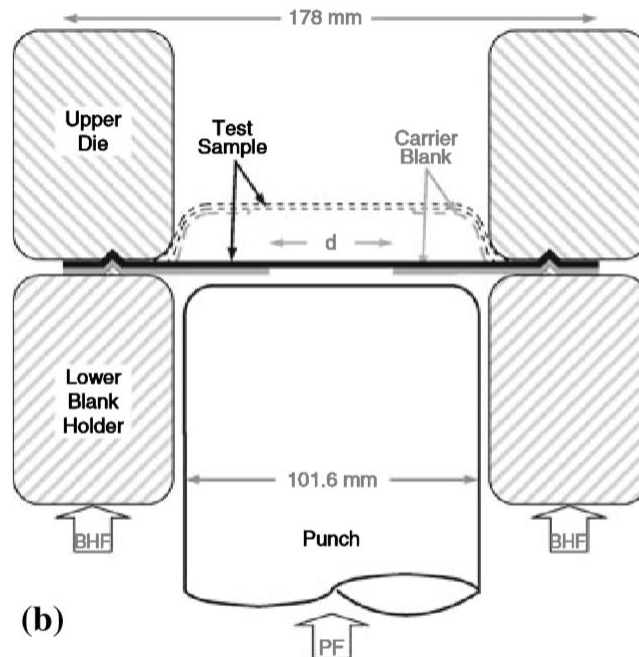


*Figure 2.3.3 Cross-section of Marciniak sheet metal test (Hsu et al, 2008)*

The in-plane test is often considered to be more conservative than the out-of-plane test as its unsupported regions make it more susceptible to inhomogeneities and imperfections in the material. Also, the in-plane tests show more linearly proportional strain paths when compared with their out-of-plane counterpart (Gutierrez et al, 2010). Because of these differences the Marciniak test is often considered to be a more accurate representation of a material's intrinsic properties (Chen & Fang, 2018). Although it is considered more accurate, this test requires a lot of effort to find a suitable carrier blank material and hole size compared to Nakazima, and, as a result, is comparatively less preferred.

In this thesis, the elevated temperature formability of AA7075 sheet was assessed with the in-plane Marciniak test method. No known standards for FLC determination at elevated temperature through either Nakajima or Marciniak method exist. Therefore, multiple papers that attempted to produce elevated temperature FLD through Marciniak method will be briefly reviewed below.

Heating methods typically consisted of using cartridge heaters located inside the punch to heat the metal after prior annealing in furnace (Hsu et al, 2007). It is critical that the punch temperature is maintained constant and close to the blank test temperature to ensure isothermal test conditions and that the failure does not occur outside of the unsupported central blank region due to thermal gradients in the test blank. If the punch temperature is too low compared to the clamping surface, the blank will have higher flow stress at its centre and the failure will be shifted toward the clamped region making the test invalid.

Typically, boron nitride (BN) and graphite sheet were used as lubricant between the punch and carrier blank. Hsu et al. (2007) applied the lubricant, in some cases, to both sides of the carrier blank which seemed to be counter intuitive, being unable to effectively transfer the force of the carrier blank to the test blank.

Many failure modes were evident in the tests conducted by Hsu et al. (Figure 2.3.4). Some of those observed were crack initiation in plane-strain region of cup wall, along the upper die entry radius which is consistent with too high friction at the radius. Failure also initiated along the edge of the carrier blank as it over expanded causing high stresses. Proper hole diameter selection could have avoided this issue. None of the elevated temperature tests with either AA5754 aluminum or with AZ31B magnesium sheets were successful in obtaining failure in the unsupported central region of the test blank. The authors utilized 10 mm radius punch but noted that a larger punch radius may have led to more suitable neck or fracture location. The samples were held at temperature for 4 minutes before initiating the test.

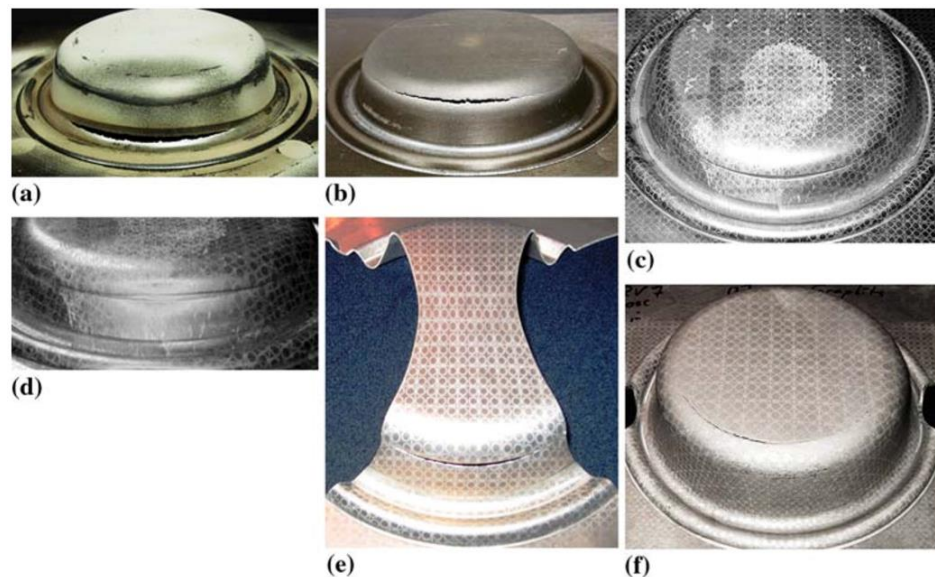


Figure 2.3.4 Elevated temperature failure modes for Marciniak samples (Hsu et al, 2008)

Zhang et al. (2014) investigated the effects of temperature and strain rate on the forming limit curves of AA5086 sheet. Although they investigated

these effects, it is unclear whether experimental testing was completed at elevated temperature or the results were entirely based on the numerical modeling study. They did not utilize the carrier blank but machined a decreased thickness in the unsupported central region of the blank to promote failure in that region. This approach was perhaps chosen due to the difficulty of finding a suitable carrier blank at elevated temperatures. Unfortunately, use of a machined surface in the critical unsupported central region of the blank took away the characteristic surface microstructure and surface roughness features that evolve and cause flow localization and plastic instability. Chu et al. (2014) also used the same approach while investigating the effect of temperature on FLD of AA5086 aluminum sheet.

Huang et al. (2010) investigated the FLD of AA7075-T6 sheet for warm forming at temperatures ranging from 100°C-250°C; strain rate and thermal history details were not provided. Figure 2.3.5 shows a drastic increase in formability when transitioning from 150°C to 200°C but no explanation for this increase was provided. However, it should be noted that the lower warm forming temperature range used by Huang et al. in their study is not a useful range for hot stamping. Higher temperatures above at least 300°C should be considered from the hot stamping die quenching perspective.

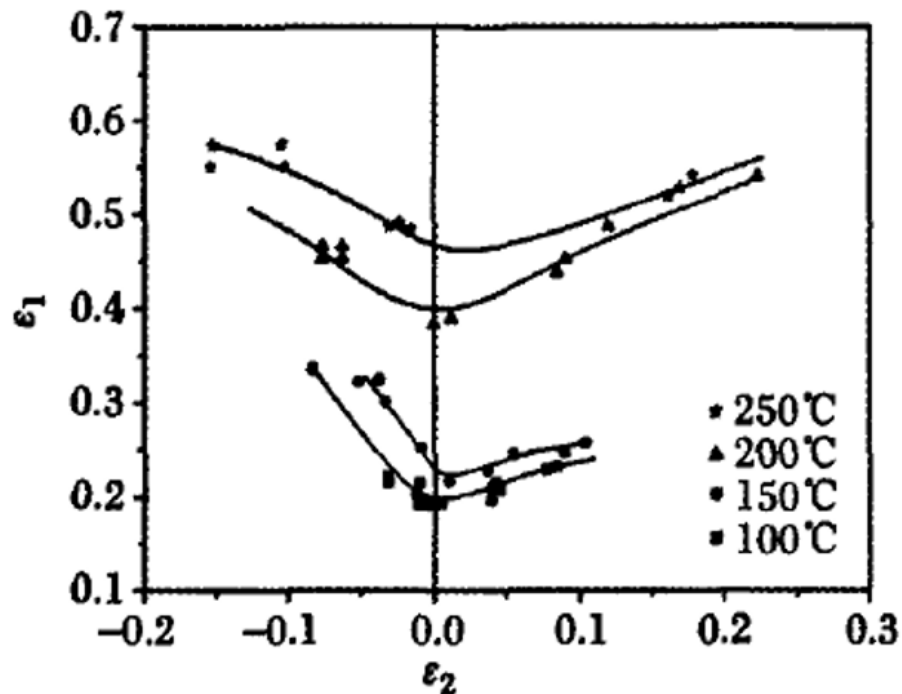


Figure 2.3.5 FLDs of AA7075-T6 at forming temperatures between 100-250°C (Huang et al, 2010)

Lastly, typical carrier blanks used in room temperature in-plane Marciniak testing consist of low carbon or IF steels. However, such carrier materials do not see a significant increase in formability when heated to hot stamping temperatures for aluminum sheet in the 400°C range. They often fail prematurely in elevated temperature testing or fail to provide the desired strain path to the test blank.

### 2.3.3 Methods for Determining Onset of Localized Necking

Observation and interpretation of the localized neck region and its vicinity is critical to understanding when forming limits are reached. Although it is possible to visually determine when a neck has occurred, the subjective

nature of what constitutes a localized neck often depends on the observer and leads to differing results. To reduce or eliminate this ambiguity, conventionally, gridded dots are etched onto the samples and strain measurements in and around the localized neck region are taken after the test is completed (Figure 2.3.6). The post-test strain measurements from deformed periodic grids on necked specimens are limited in terms of data for truly establishing the limit strains compared to the real-time strain measurement over large dome surface area with online camera system. Firstly, the necked dome specimens are in different stages of necking which introduces considerable variability from sample-to-sample in strain distribution in and around the neck. Secondly, in some cases, it is nearly impossible to capture a neck due to the catastrophic nature of failure, so no useful limit strain data can be extracted from such specimens. Thirdly, the specimen test speeds are deliberately reduced towards the end of the test to enable neck capture which introduces another variability in the process. Moreover, in the post-test strain measurement, no information is gained about strain path followed by the material that eventually becomes the site of the localized neck. This information is often valuable in designing specimen geometry for specific strain paths. Also, if the test is being simulated with FE analysis, strain path agreement between the experiment and model results, in addition to the limit strains, can be a valuable model validation method. Lastly, the periodic grid-based post-test strain measurements are susceptible

to information loss as limiting strain determination depends on the dot size, dot spacing, number of dots available for the narrow width specimens, and dot position compared to the neck. The resolution of the measurements may also be insufficient. More recent Digital Image Correlation (DIC) methods of full-field continuous strain mapping eliminates many of these limitations of determining the onset of localized necking as discussed below.

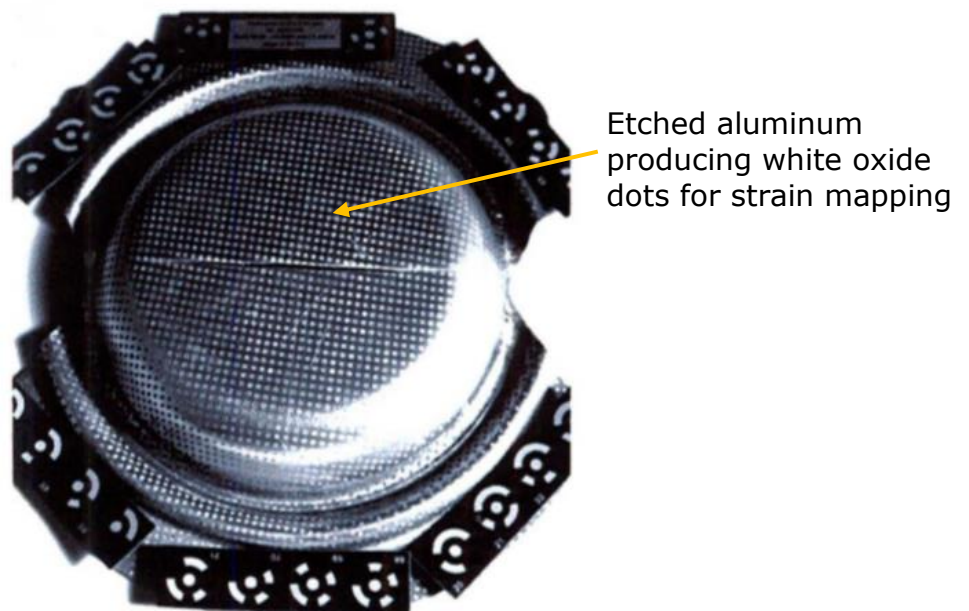


*Figure 2.3.6 1mm diameter dot pattern etched onto aluminum grid at 2mm x 2mm (Zdravecky, 2007)*

DIC has been employed by many researchers (for example, Situ et al., 2011; Urbánek et al., 2018), giving high resolution strain data of the sample surfaces during deformation. Aramis<sup>®</sup> system, based on DIC technique, with its dedicated camera and software has become commonplace for analyzing macroscopic strain fields in inhomogeneously deformed specimens. The

samples are first cleaned with ethanol before applying a high temperature (up to 900°C) peel resistant paint. A stochastic (or random) speckle pattern is applied to the sheet specimen by spraying black paint or ink onto a white backdrop with a fine spray nozzle to give maximum contrast (Figure 2.3.7). Unfortunately, the high temperature testing can degrade image contrast and accuracy of the strain data.

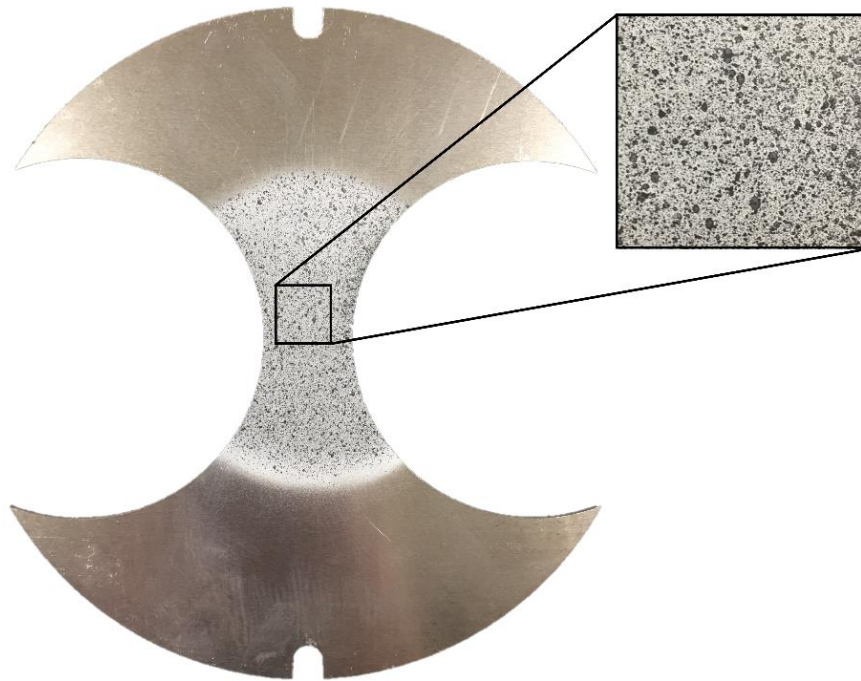


*Figure 2.3.7 Test blank with speckle (stochastic) pattern applied through high temperature paint*

Through DIC, high resolution full-field strain maps can be produced and used to determine the onset of necking. Various criteria have been set forth for limiting strain determination. Banabic et al. (2004) assumed necking to have occurred when the major strain increment between the neck region and

a safe zone away from the neck had reached 10, while Barata De Rocha et al. (1985) assumed this ratio to be closer to 7. Ding et al. (2015) showed there to be little difference between ratios of 7 and 15 as strain progressed quickly once necking initiated. This method is quite subjective when applied to experimental incremental strain data where data quality and frequency can vary significantly and is usually only considered in the MK analysis for theoretical prediction of FLCs which will be discussed in the next chapter.

ISO 12004-2:2008 lays out several techniques based on continuous online strain data as well as offline (post-test) data. Although the online imaging approach can capture the entire process and encompasses more data, there is not currently a well-defined approach for determining limiting strain at elevated temperatures. Several methods have been proposed to capture the moment of limit strain. The first approach is position-dependent which plots strain progress, utilizing strain history from points along a line perpendicular to the length of the crack. Bragard et al. (1972) proposed a method where a quadratic curve is fit to the major and minor strain plots on the image just before fracture, considering a sufficiently high frame rate is used. The vertex of the curves fitted to the major and minor strains are classified as the limiting strains and provide a point at the end of strain path. Although this method can be used on both deformed periodic gridded and speckle-patterned samples various phenomenon such as multiple necking points can make this method error prone.

Situ et al. (2011) determined the localized necking from an analysis of strain history. By taking the first and second order derivatives of major strain versus time data, the major strain rate and major strain acceleration versus time curves are obtained. They considered localized necking had been achieved once inflection of the major strain rate or a maximum in the major strain acceleration had occurred. This method proved difficult when computing second derivatives due to noise in the experimental data. However, the procedure could be readily applied to the curve fitted experimental data.

Lastly, Figure 2.3.8 shows a time-dependent method known as the necking-zone method has been proposed by Martinez-Donaire et al. (2014) which used a similar approach to that of Situ et al. (2011). Taking the major strain rate of a point just outside of the necking zone and recording its major strain through the process, they were able to identify the occurrence of necking at an inflection point in major strain or major strain rate maximum. Dicecco et al. (2016) noted while testing the warm forming behaviour of AA6013-T6 that the necking-zone method predicted slightly higher limiting strains on the biaxial side of the FLD than the position-dependent ISO methods.

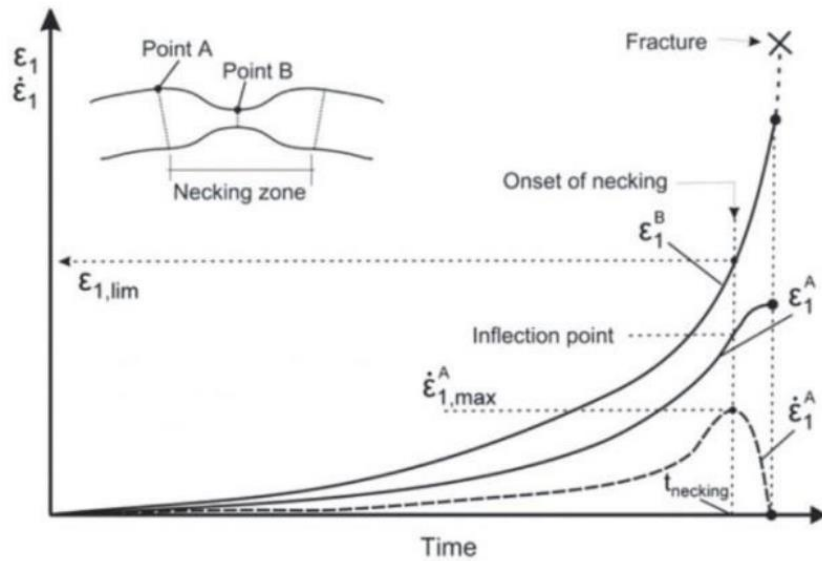


Figure 2.3.8 Time-dependent method for analysis of limiting strain (Martinez-Donaire et al, 2014)

## 2.4 Prediction of Forming Limits and FLDs

### 2.4.1 Marciniak-Kuczynski Method

Although there are many methods for predicting the failure limits of a sheet metal by numerical methods in the literature, it is useful here, for brevity, to review a well-accepted theoretical approach, first published by Marciniak and Kuczynski (M-K) (1967). This method predicts the necking instability for a range of linear proportional strain paths applicable to sheet metal forming. The M-K method assumes an initial imperfection of the sheet. These imperfections attempt to imitate natural imperfections observed in materials such as voids, material texture/grain orientation, and/or surface roughness. The latter can be represented in the form of slightly reduced sheet thickness as shown in Figure 2.4.1. It is this imperfection or inhomogeneity,

normally located perpendicular to the largest principal stress direction, which causes instability and subsequent localized necking and fracture in the sample.

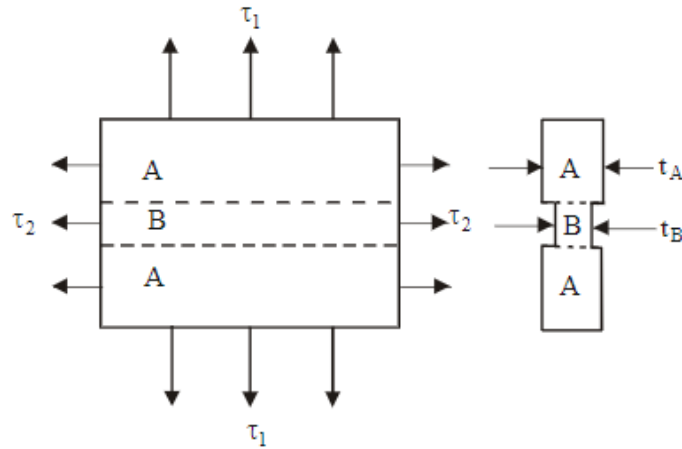


Figure 2.4.1 Thickness imperfection used in MK method (Marciniak & Duncan, 1992)

The inhomogeneity factor,  $f_0$ , as seen in Equation 2.3, is a ratio of initial imperfection thickness,  $t_{b_0}$ , to initial nominal thickness,  $t_{a_0}$ , of the rest of the sheet, considered as a “safe” region.

$$f_0 = \frac{t_{b_0}}{t_{a_0}} \quad (2.3)$$

As the sheet deforms, the thickness values evolve, calculated through incompressibility assumption, and their current values, designated as  $t_b$  and  $t_a$  respectively. The deformation of the sheet is governed by a proportional loading condition in the safe zone,  $\rho^*$  as seen in Equation 2.4, which is the ratio of the incremental minor strain,  $\Delta\varepsilon_{22}^a$ , to incremental major strain,  $\Delta\varepsilon_{11}^a$ .

$$\rho^* = \frac{\Delta\varepsilon_{22}^a}{\Delta\varepsilon_{11}^a} \quad (2.4)$$

As the forming process approaches necking, the imperfection zone approaches the plane strain condition, and the safe region ceases to strain further. In a material with zero surface roughness, the inhomogeneity factor would be equal to one ( $f_0=1$ ). Thus, any  $f_0$  value lower than unity shows early separation of the imperfection zone from the linear strain resulting in a lowered FLD as seen in Figures 2.4.2 and 2.4.3.

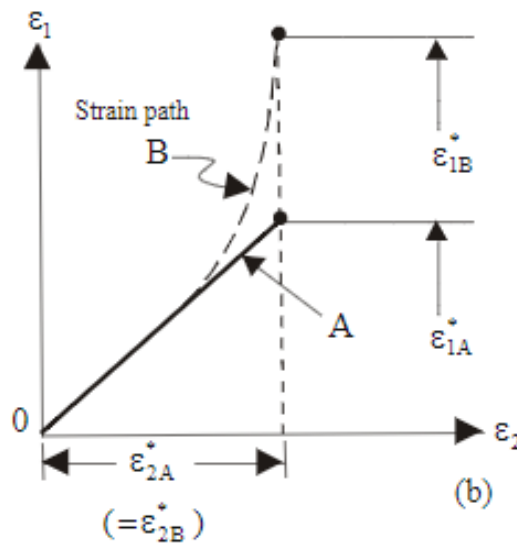


Figure 2.4.2 Strain evolution in imperfection region versus safe zone (Marciniak & Duncan, 1992)

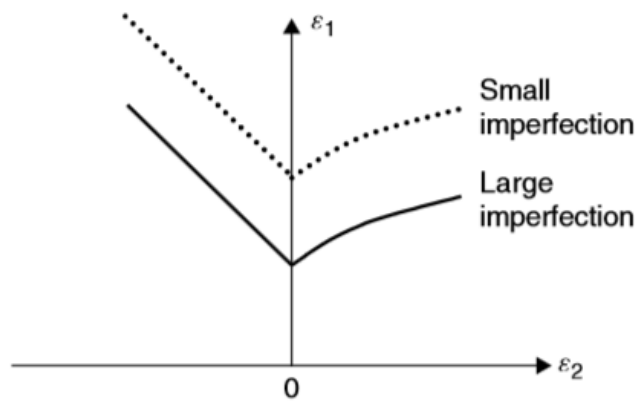


Figure 2.4.3 Effect of imperfection factor on FLD (Marciniak & Duncan, 1992)

It is important to note several assumptions of the M-K method such as the system is assumed to be in a plane stress state as well as the strain component in the minor direction of both the imperfection and safe zone are held equal during deformation. As the deformation progresses the entire system is updated including the stress, strain, thickness values, depending on the complexity of the model. While typically done with an initial groove orientation perpendicular to the maximum stress, in recent years researchers have begun implementing less restrictive assumptions in their versions of M-K model. These attempts to improve the M-K theory include adding the effects of strain rate, temperature, anisotropic yield criterion as well as a more realistic physical basis for the inhomogeneity factor. Ding et al (2015) have shown there to be an influence of the initial groove angle on limiting strain predominantly lowering the FLD. They were also able to show the effect of various constitutive material models, yield criteria, and imperfection factor on the FLD. Figure 2.4.4 shows a typical iterative process of the M-K method as it runs through various strain paths to form a complete FLD. A M-K method code was produced during the course of this thesis utilizing Python and Newton-Raphson method but will not be presented.

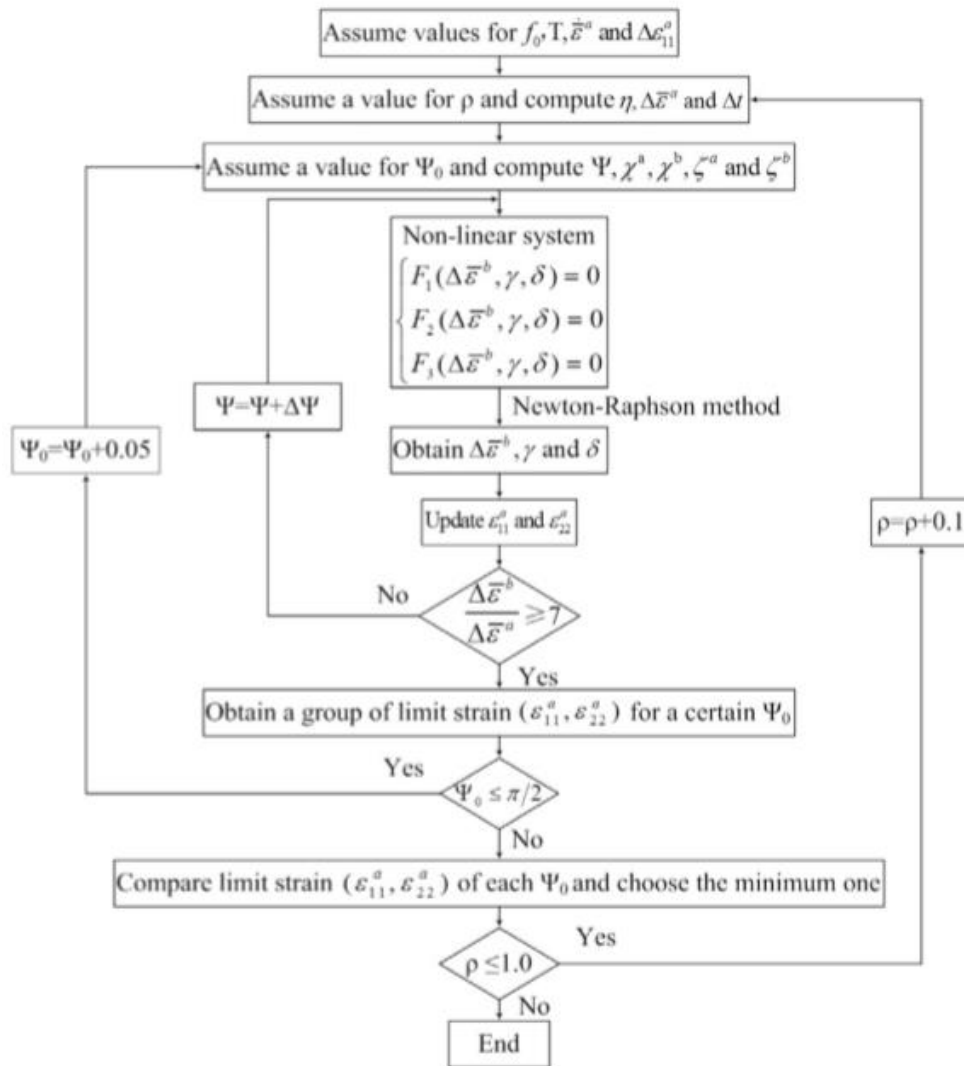


Figure 2.4.4 Flow chart of computing process of FLCs with the M-K model (Ding et al., 2015)

FLD prediction using the M-K theory are relatively easier, quicker, and more cost effective compared to the experimental methods discussed earlier. However, the method relies critically on suitable description of anisotropic yield criterion, hardening law, and appropriate consideration of thickness inhomogeneity factor. Also, the most common experimental method based on Nakazima test involves out-of-plane deformation and non-linear strain paths whereas the conventional M-K theory assumes in-plane deformation and linear

proportional strain paths. Considering all these complexities, the numerical prediction of FLCs using the M-K method and other theoretical approaches still fall short in accurately predicting FLCs of many commercially produced automotive sheet materials. This is especially true involving strain rate and temperature dependent material behavior typical of elevated temperature forming and hot stamping. This is an active area of research where material microstructure, crystallographic texture, and even ductile damage criterion are being introduced in the M-K analysis to obtain FLC characteristics closer to the experiments. The above new considerations add considerable complexity to the analysis, cost of additional material data generation and data inputs into the models as well as the added computational cost.

#### **2.4.2 FE Simulations of Laboratory-Based Forming Tests**

With the recent rapid advances made in computer processing, considerable effort is being devoted by the scientific community to implement complex constitutive models, fracture criteria, and yield criteria into FE models of sheet forming processes. This is often done first at the laboratory-scale where the experiments are conducted in a well-controlled and rigorous manner while measuring multiple forming process and material parameters for model validation. FE based approach is a very useful and cost-effective method for testing various tool geometries, friction effects, and other test parameters.

As mentioned earlier, the theoretical M-K method has been the main tool in FLD prediction until now. Some researchers have recently begun to utilize advanced FE codes with superior material constitutive models to accurately simulate the lab experiments and to predict FLDs. Recent work in this area is summarized in Table 2.4.1. As shown, friction models based on Coulomb law in many of the FE models are still quite primitive and do not accurately reflect the lubricated contact conditions that exist in the laboratory-based dome test experiments.

Table 2.4.1 FE Investigations for FLD Determination

<b>Researcher</b>	<b>FEM Code</b>	<b>Material</b>	<b>Test Type</b>	<b>Element Type</b>	<b>Yield Criteria</b>	<b>Constitutive Model</b>	<b>Friction (carrier-to-blank)</b>
(D'Amours and Ilinich, 2018)	LS-DYNA	AA7075	Nakazima	3D Solid	Hill 1948	User Data	N/A
(Kumar, Amjith, & Anjaneyulu, 2016)	Pam-Stamp 2G	AA2014	Nakazima	4 Node Rectangular, 3 Node Triangular	Hill 48, Hill 90, Barlat 89	Hollomon	N/A
(Abovyan, Kridli, Friedman, & Ayoub, 2015)	LS-DYNA	AA5182-O	Nakazima	Belytschko-Tsay Shell	N/A	Hockett-Sherby	Coulomb (0.2)
(Chung, Lee, & Kim, 2014)	ABAQUS/Explicit	TWIP Steel DP980	Nakazima	3D Continuum	Isotropic Hill 1948	Voce-Swift	Coulomb
(Zhang et al., 2014)	ABAQUS/UHARD	AA5086	Marciniak	N/A	N/A	Lin-Voce	Coulomb (0.1)
(Safari, Hosseinipour, & Azodi, 2011)	ABAQUS/Standard	AA3105	Nakazima	N/A	Hosford	Swift	Coulomb (0.11)
(Pepelnjak & Kuzman, 2007)	ABAQUS	AA3003	Marciniak	Shell	N/A	Hollomon	Coulomb

When using FE analysis to simulate laboratory experiments, there are many geometric, material constitutive, process parameters and other

computational considerations. One of the most influential consideration is the choice of FE code and its intrinsic computational formulation. Typically, implicit/standard or explicit formulations are available in the various general-purpose commercial FE codes. Standard formulation is commonly used for quasi-static or smooth nonlinear problems that have minimal boundary contact due to its need to ensure equilibrium at the end of each iteration. In contrast, an explicit (also called dynamic) formulation can be used to analyze high strain rate problems involving more complex multi-body contact conditions such as in tool sheet contact or crash simulations where wave propagation through the material comes into effect, and there is no requirement to maintain between each calculation step. Thus, in explicit FE simulations of high strain rate forming problems, the model is typically converted back after the forming step to a standard model for accurate modelling of elastic spring-back.

When deciding between implementing the FE model in either standard or explicit formulation code, it is important to check the so-called stability limit of the model. This limit is defined in terms of the highest frequency of the system as seen in Equation 2.5. Decreasing stable time increment becomes exponentially more expensive when utilizing standard solver, and explicit solver should be considered if time increment is substantially small.

$$\Delta t_{stable} \leq \frac{2}{\omega_{max}} \quad (2.5)$$

Another important factor when implementing FE code in sheet metal forming operations is the use of mass scaling. The stable time increment discussed above can be expressed as:

$$\Delta t_{stable} = \frac{L_{emin}}{c_d} \quad (2.6)$$

Where  $L_e$  is the characteristic element dimension and  $c_d$  is the current effective dilatational wave speed of the material. Given that  $c_d$  is related to Young's modulus and inversely related to material density as expressed by Equation 2.7, an increase in density effectively increases the stable time increment.

$$c_d = \sqrt{\frac{E}{\rho}} \quad (2.7)$$

If inertial effects are minimized, an explicit solution can be extremely effective in reducing computation time. Determining whether an acceptable mass scaling factor has been chosen can be confirmed by keeping the kinetic energy of the system to below 10 percent of the total system energy. An agreement of the punch force versus displacement data from the simulations with that of experiments can also provide confidence in the strain data obtained from FE simulations ("Abaqus/CAE User's Guide", 2016).

In the present work, FE simulations of in-plane Marciniak tests were carried out using the ABAQUS-Explicit FE code.

## **2.5 Aluminum Alloys**

Aluminum alloys are known for their high strength to weight ratio as well as their superior corrosion resistance which arises due to their high reactivity with atmospheric air that results in the formation of a hard aluminum oxide layer which strongly binds to the base metal. However, forming of aluminum alloys into parts can be difficult due to their high strength and limited formability at room temperature. Strength and formability vary with the alloy type and temper. In the next sub-section, aluminum alloy designations from Aluminum Association are briefly presented.

### **2.5.1 Composition and Strength of Aluminum Alloy Series**

As seen in Table 2.5.1, aluminum can be categorized into series based upon the main alloying element used. For instance, 1XXX-series belonging to aluminum that is greater than 99.0% pure, containing no alloying elements. This usually produces a low strength alloy, used mainly for its high conductivity. This differs from 2XXX-series aluminum, where its main alloying element is copper – making it an age-hardenable alloy. The series 2XXX, along with 6XXX and 7XXX-series aluminum alloys fall under the category of age hardenable alloys. These alloys gain their strength as they “age” post-heat treatment, the process of which will be further discussed in the next section.

Table 2.5.1 Strength and compositions of various wrought aluminum alloys (Davis, 2001)

Aluminum Association series	Type of alloy composition	Strengthening method	Tensile strength range	
			MPa	ksi
1xxx	Al	Cold work	70–175	10–25
2xxx	Al-Cu-Mg (1–2.5% Cu)	Heat treat	170–310	25–45
2xxx	Al-Cu-Mg-Si (3–6% Cu)	Heat treat	380–520	55–75
3xxx	Al-Mn-Mg	Cold work	140–280	20–40
4xxx	Al-Si	Cold work (some heat treat)	105–350	15–50
5xxx	Al-Mg (1–2.5% Mg)	Cold work	140–280	20–40
5xxx	Al-Mg-Mn (3–6% Mg)	Cold work	280–380	40–55
6xxx	Al-Mg-Si	Heat treat	150–380	22–55
7xxx	Al-Zn-Mg	Heat treat	380–520	55–75
7xxx	Al-Zn-Mg-Cu	Heat treat	520–620	75–90
8xxx	Al-Li-Cu-Mg	Heat treat	280–560	40–80

Some of the alloying elements used in 7XXX-series aluminum alloys such as AA7075 used in this work are shown in Table 2.5.2.

Table 2.5.2 Role of alloying elements in Al-7XXX series alloys

Alloying Element	Effects of Alloying Elements
Zinc & Magnesium	<ul style="list-style-type: none"> <li>Responsible for the age hardening characteristics of AA7075 and its strength properties</li> </ul>
Copper	<ul style="list-style-type: none"> <li>Increase the aging rate through increased supersaturation</li> <li>Increases quench sensitivity</li> <li>Decreases general corrosion resistance while increasing SCC resistance</li> </ul>
Chromium, Manganese & Zirconium	<ul style="list-style-type: none"> <li>Small compositional percentage to prevent grain growth</li> </ul>
Iron & Silicon	<ul style="list-style-type: none"> <li>Typically, contaminant elements – also prevent grain coarsening</li> </ul>

It is important to note the variance in tensile strength reported in Table 2.5.1. Although this is due to the difference in tensile strength as a result of chemical composition in the alloy series, the strength of aluminum alloys can display dependency on temper as well. The main temper that will be studied in this thesis is AA7075-F or 'as fabricated' temper. This temper is a combination of hot and cold rolling and is a result of the final processing of material from the mill. The processed AA7075-F sheet was received from Novelis, Inc., for the present research work.

## **2.5.2 Characteristics of Precipitation Hardenable Aluminum Alloys**

Age-hardenable or precipitate hardening alloys were first discovered by Alfred Wilm in 1901 where he noticed the increase in material hardness after heating, quenching and subsequent aging (Polmear, 2004). As mentioned previously, 7XXX-series aluminum alloys are age-hardenable, defined by their primary alloying element, Zinc. Specifically, alloy AA7075 is alloyed with zinc, magnesium and copper in composition range of 5.6-6.1%, 2.1-2.5% and 1.2-1.6% respectively (Davis, 2001). These are the main alloying elements in addition to others such as silicon, iron, chromium, manganese, etc. The role of these elements in the aluminum alloy are each very different.

The strengthening mechanisms seen in age-hardenable aluminum alloys work by impeding the movement of dislocations through the matrix crystal

structure, typically, by the presence of precipitates that form during the artificial aging process. Figure 2.5.1 (a) depicts highly idealized interaction of a dislocation (line defects) with spherical precipitates during plastic deformation step causing shearing of the precipitate. When the particle size increases the energy needed for the dislocations to shear through the particle also increases resulting in an increase in material strength (Figure 2.5.1 (c)). However, when the particle size becomes too large, the dislocation-precipitate interaction mechanism changes, where instead of shearing the precipitate, dislocations now by-pass the particle leaving a dislocation loop in its wake (Figure 2.5.1 (b)). For optimal strength, a combination of both mechanisms is targeted during alloy design and development.

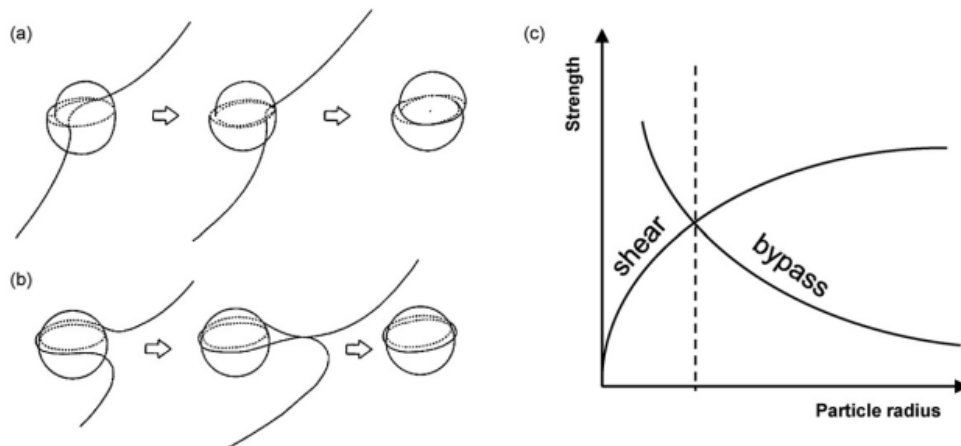


Figure 2.5.1 Strengthening mechanism illustrated through, (a) shearing of particles by dislocations, (b) bypassing of particles by dislocations (Gerold, 1979), and (c) critical precipitate radius for particle shearing or bypassing (Polmear, 2006)

The three main type of particles present in AA7XXX alloys, and including AA7075 alloy, are: constituent particles, dispersoid particles, and precipitate particles.

Constituent particles are large intermetallic particles in the size range 1-50  $\mu\text{m}$  that are known to form during alloy casting, and due to their high melting temperature, rarely go back into solution. These particles are known for pinning grain growth as well as reducing the fracture toughness of aluminum (Jordon et al., 2009). In contrast, the smaller dispersoid particles, in the size range 0.2-3  $\mu\text{m}$ , aid in controlling grain recrystallization, grain orientation as well as grain growth (Bretz et al, 1981). Lastly, the finest are precipitate particles on the order of 1-100 nm consisting of elements Zn, Mg, Al and Cu in their stoichiometric compositions. These contribute to strengthening through dislocation pinning, as discussed earlier (Jacumasso et al., 2016).

To obtain abundant precipitates necessary for increased strength, AA7075 must undergo thermal processing (or heat-treatment) which involves heating of aluminum sheet to temperatures between 470°C and 520°C for a short time. Holding at this temperature is known as solutionizing as it allows for the precipitates consisting of Zn, Cu & Mg to be dissolved into solution. Solutionizing is followed by rapid quenching of the sheet where alloying elements are locked-in the aluminum unit cell, a state referred to as supersaturated solid solution (SSSS). This step is critical to ensure enough alloying elements are present later in SSSS to form hardening precipitates necessary for material strength during the aging process. By using continuous cooling transformation (CCT) diagrams (Figure 5.2.2), one can better

understand the cooling rates that must be obtained to form and/or avoid specific phases within a material.

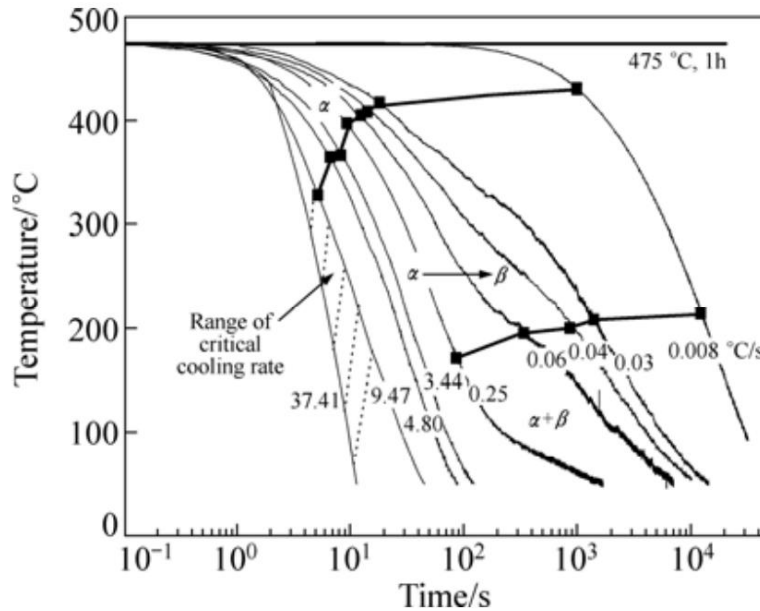


Figure 2.5.2 CCT curve for AA7075 (Li, Bin, Zhao, & Wang, 2011)

The SSSS state obtained after quenching is unstable at room temperature or higher and undergoes several stages of phase transformation as the alloy is heated (or aged). Different ageing treatments (or tempers) in especially designed furnaces are imparted to the sheet depending on the desired strength and ductility. The tempering temperatures usually vary between 120°C-165°C with tempering times between 1-30 hours depending on the required temper (Li et al., 2008; Clark et al., 2005). Tempering is accompanied by dissolution of the SSSS into well-known Guinier-Preston zones (GP zones), followed by formation of metastable (semi-coherent)  $\eta'$  phase, and finally the formation of stable (incoherent)  $\eta$  phase precipitates, where the metastable  $\eta'$  phase is thought to be responsible for the majority of

the hardening effect (Wang et al, 2008). The  $\eta$  phase is typically associated with a reduction in strain energy from over-aging, resulting in lowered peak-strength due to incoherency with the matrix lattice. The various steps associated with the precipitation from SSSS state and heat treatment processes are illustrated in Figure 2.5.3.

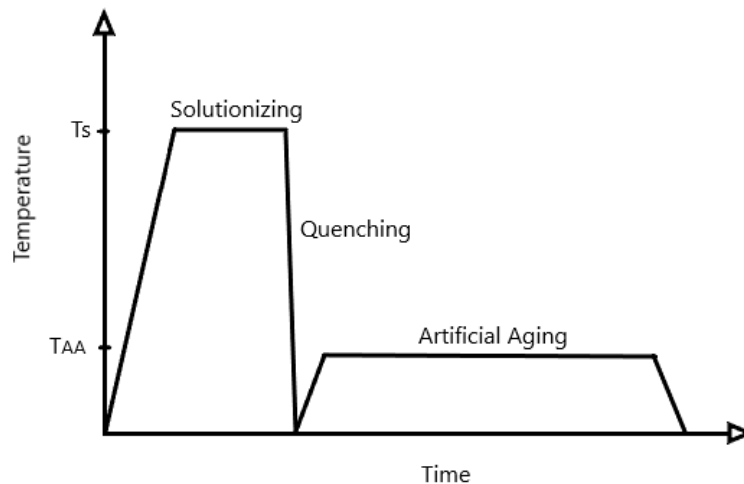
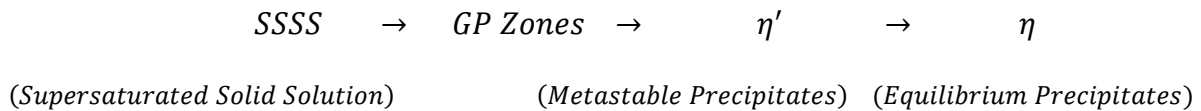
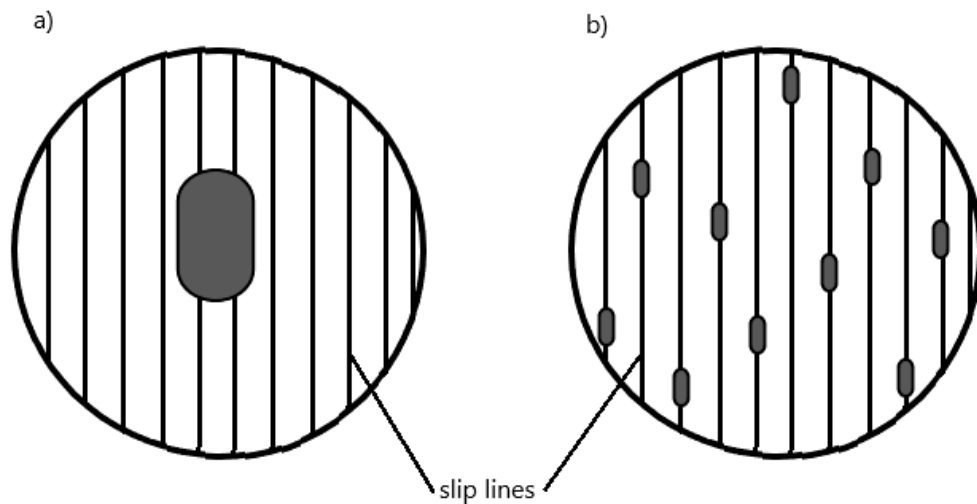


Figure 2.5.3 Thermal processing of AA7075 sheet

In AA7075, it is the addition of Zn and Mg in the approximate ratio of 1:2 that allows for the formation of finely spaced  $MgZn_2$  precipitates (Olawale et al, 2012) where Zn can be substituted for Al or Cu producing  $MgAl_2$  or  $MgCu_2$  (Wang et al., 2013). Figure 2.5.4 shows how a larger number of finely dispersed precipitates interfere with an increased number of slip planes, increasing strength, as opposed to fewer but larger precipitates which are not as effective for strengthening of the alloy.



*Figure 2.5.4 Influence of particle size on strength, a) large precipitate interacting with minimal slip planes, and b) finely dispersed precipitates interacting with a larger number of slip planes*

### **2.5.3 Mechanical Properties of AA7075 Sheet**

As previously mentioned, temper and service temperatures have a significant effect on the mechanical properties of 7XXX-series aluminum alloys. Treatments such as annealing produce O-temper, resulting in significant reduction in dislocation density due to recovery of the cold worked microstructure, grain recrystallization, coarsening of the recrystallized grain structure from grain growth as well as coarsening of hardening precipitates to make them less effective as strengthening agents. The above microstructural changes give AA7075 sheet lower strength but higher formability in room temperature forming. The peak-aged temper T6, on the other hand, gives the alloy its peak yield and ultimate strengths but considerably reduced strain hardening behaviour. There is also increased propensity to fracture due to

increased void induced damage development by precipitate/matrix decohesion and break-up of constituent particles in room temperature forming. T6 temper is achieved by heating the AA7075 sheet to 480°C, rapidly quenching in water, and subsequent artificial ageing for 24 hours at 120°C in a furnace. Sheet materials are rarely formed in T6 temper state due to their very poor formability and large spring-back.

A study by Li et al (2007) investigated several other aging treatments and their effects on mechanical properties. They noted that treatments such as retrogression and re-aging (RRA), T73, T6I6 and high-temperature pre-precipitation (HTPP) were all able to increase resistance to stress corrosion cracking (SCC), while only RRA and T6I6 were able to maintain strength similar to that of T6-temper. Abachi et al (2016) showed the over-aging of AA7075 into the T73 temper corresponded to a decrease in strength of 10-15%. This is due to the vastly different microstructures (grain and precipitate morphology) that occur not only through different tempers but at various temperatures. Table 2.5.3 shows the dependency of AA7075 uniaxial tensile properties on tempers and temperature; particularly the annealed (O), as-fabricated (F) and peak-strengthened (T6) tempers. The F-temper is of interest as this is the temper in which the sheet is supplied by sheet producers to its automotive customers for stamping applications.

Table 2.5.3 Room temperature tensile properties of AA7075

<b>Temper</b>	<b>Process</b>	<b>Yield Strength (MPa)</b>	<b>Tensile Strength (MPa)</b>	<b>Total Elong. (%)</b>	<b>Reference</b>
<b>O (annealed)</b>	Solution-treatment at 470°C for 1 hr, furnace cooled to room temperature	203-263	221-276	19-25	Hashimoto, 1986
<b>F (as-fabricated)</b>	Combination of hot and cold rolling resulting in final sheet produced from mill	260	305	8-10	N/A
<b>T6</b>	Solution-treatment at 470°C for 1 hr, quenching in cold water, aging at 120°C for 24 hrs	406-559	504-620	2-10	Ortiz et al., 2006; Li et al., 2008
<b>T73</b>	Solution-treatment at 470°C for up to 1 hr, quenching in cold water, aging at 120°C for 24 hrs, and aging at 160°C for 30 hrs	434-464	503-527	13	Abachi et al., 2016; Li et al., 2008
<b>RRA</b>	Solution-treatment at 470°C for 1 hr, quenching in cold water, aging at 120°C for 24 hrs, retrogression at 203°C for 10 min, and re-aging at 120°C for 24 hrs	511	568	N/A	Li et al., 2008
<b>T6I6</b>	Solution-treatment at 470°C for 1 hr, quenching in cold water, pre-aging at 130°C for 80 min, interrupted aging at 65°C for 240 hrs and re-aging at 130°C for 18 hrs	507	563	N/A	Li et al., 2008
<b>HPP aging</b>	Solution-treatment at 470°C for 1 hr, cooling to 445°C in resistance oven and maintaining for 30 min for pre-precipitation, quenching in cold water, and aging at 120°C for 24 hrs	468	538	N/A	Li et al., 2008

## **2.5.4 Microstructure, Damage Development, and Room and Elevated Temperature Formability and Fracture of AA7075 Sheet**

Fractography is the field that investigates the fracture surfaces of highly deformed and subsequently failed materials. The microstructure and failure mechanisms can be observed through three basic steps: (i) observing, (ii) describing, and (iii) measuring and interpreting (Hull, 1999). Observing is typically done using scanning electron microscopy (SEM) due to its large depth of field and ability to identify specific elements through SEM-based energy-dispersive spectroscopy (EDS).

Under the presence of large strains typical of forming, sheet metal typically fractures in a ductile manner through void initiation, void growth, strain localization, and void coalescence. These processes can occur sequentially or concurrently and accentuated by the presence of precipitates, dispersoids and constituent particles. The processes of void initiation, growth, strain localization, and void coalescence are shown schematically in Figure 2.5.5. Once physical separation of the sheet material occurs and the fracture surfaces have become visible from above, they can be investigated for more detailed fracture characteristics via fractography (Figure 2.5.6) such as transgranular and/or intergranular fracture.

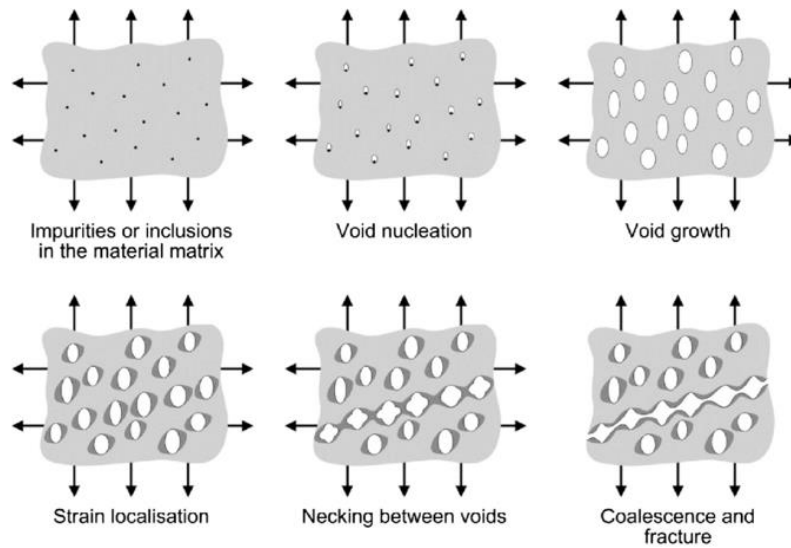


Figure 2.5.5 Ductile fracture timeline showing progression of fracture stages (Anderson, 2005)

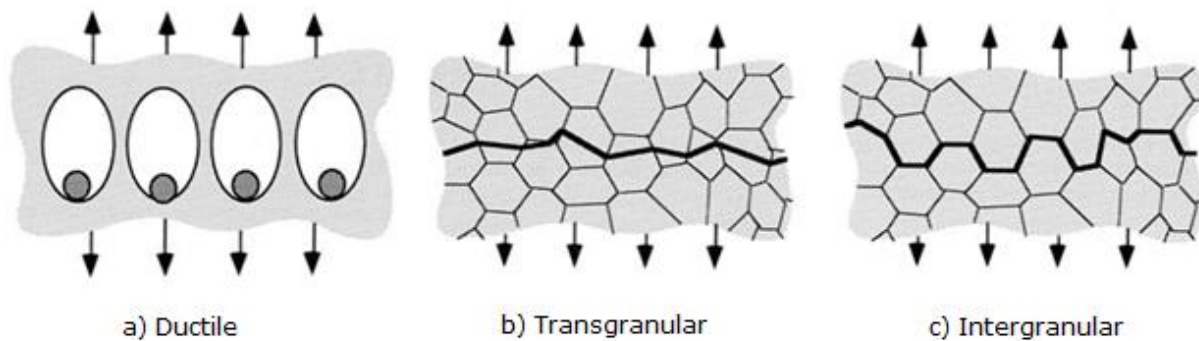


Figure 2.5.6 Main micro-mechanisms of fracture observed in metals a) ductile b) transgranular (cleavage) and c) inter-granular (Anderson, 2005)

Jordon et al. (2009) investigated the damage characterization of 7075-T651 aluminum plate deformed at room temperature confirming that intragranular fracture was the primary failure mechanism with void nucleation initiating at constituent and dispersoid ( $\text{Al}_3\text{Ti}$ ,  $\text{Al}_6\text{Mn}$ ,  $\text{Al}_{20}\text{Cu}_2\text{Mn}_3$  and  $\text{Al}_3\text{Zr}$ ) particles.

Leong (2008) characterized fracture surfaces of 7075-T6 rod under uniaxial tension at elevated temperatures ranging from ambient to 204°C. Leong stated that due to the high fracture toughness of the material, failure was expected to occur by shear stress as opposed to normal stresses seen in brittle fracture. However, on observation, the fracture appeared brittle in nature, exhibiting cleavage and trans-granular fracture. As temperature increased, the primary failure mode became ductile micro-void coalescences, as expected.

Hu et al. (2007) examined AA7050 alloy deformed in uniaxial tension at strain rates of  $1.0 \times 10^{-4}$ ,  $1.0 \times 10^{-3}$ ,  $1.0 \times 10^{-2}$ ,  $0.1 \text{ s}^{-1}$  and temperatures of 340, 380, 420, 460°C. Noting that fracture surface characteristics depended strongly on thermomechanical conditions. Ductile trans-granular fracture was observed with dimples of different sizes at 340°C for strain rate of  $1.0 \times 10^{-2} \text{ s}^{-1}$ , whereas ductile inter-granular fracture was observed 460°C for both at  $0.1 \text{ s}^{-1}$  and  $1.0 \times 10^{-4} \text{ s}^{-1}$  revealing the initial grain structure. The testing was limited to uniaxial strain path in the above study.

As noted earlier, sheet forming operations can involve a combination of biaxial strain paths that can lead to different void-induced damage characteristics as well as roughening of the surface prior to strain localization and fracture. A surface condition known as “orange peeling” involving larger grains that undergo grain rotation can lead to earlier onset of necking as well as unaesthetic surfaces that remain visible even after painting

(Wilson, 1997). Surface roughening induced by in-plane biaxial straining of unsupported surfaces is more pronounced and can be effectively investigated through use of Marciniak method mentioned earlier. As noted earlier, this method provides a range of strain paths that take the material to necking and fracture.

## **2.6 Summary**

In this chapter general formability of aluminum alloys, experimental techniques for forming limit determination as well as well-known M-K analytical method for FLD prediction are briefly reviewed. Also reviewed was the role of microstructure and surface characteristics of sheet on formability and fracture characteristics of aluminum alloys including AA7075. One of the main objectives of the present work is to assess the formability, fracture and surface roughness characteristics of AA7075 in the as-fabricated temper at elevated temperatures. Therefore, development of an elevated temperature Marciniak test was completed and this test was subsequently utilized to assess forming limits of the material at several isothermal temperatures ranging from 300-400°C. This test was also chosen for its ability to show surface features and its sensitivity to material inhomogeneities. DIC method was used to continuously map the evolving strain field over the deforming planar Marciniak test sample surface for strain inhomogeneity, strain path and FLD determination at all chosen temperatures. The various experimental methodologies are described in the next chapter.

## Chapter 3

# Experimental Methods

### 3.1 Introduction

The experimental work consisted of the analysis of AA7075-F sheet for formability at a range of elevated temperatures. Development of an elevated temperature Marciniak test methodology was completed utilizing mechanical engineering design principles and FE models of the Marciniak test with material data obtained separately from elevated temperature uniaxial tensile tests for input. A subsequent forming study was completed in a laboratory sized, in-house designed, hot stamping die. Hot stamped parts were successfully made and their strength characteristics from different regions of the part were analyzed after hot stamping, die quenching, and aging treatment. Similar testing was completed outside of the die to analyze strength characteristics dependant on cooling rate for benchmarking. Fractography and surface roughness measurements were completed on the Marciniak samples to qualitatively correlate strain path dependent void induced damage and surface roughness characteristics to strain distribution, forming and fracture limit strains.

### 3.2 Material

AA7075 sheet in the F-temper (as-fabricated) were utilized in the present research. Commercial quality sheets were received from aluminum company Novelis in the 2 mm nominal gauge thickness. The specific elemental composition of the material utilized in this study was studied through Inductively Coupled Plasma – Optical Emission Spectrometer (ICP-OES). Its composition is presented in Table 3.2.1 below.

*Table 3.2.1 Elemental composition of supplied sheet studied through ICP-OES.*

<b>Element</b>	<b>Cr</b>	<b>Cu</b>	<b>Fe</b>	<b>Mg</b>	<b>Mn</b>	<b>Si</b>	<b>Ti</b>	<b>Zn</b>	<b>Al</b>
<b>Weight (%)</b>	0.192	1.662	0.163	2.605	0.02	0.02	0.022	5.829	Bal.

### 3.3 Uniaxial Tensile Test

The uniaxial tensile tests were performed at three elevated temperatures: 300°C, 400°C and 500°C to obtain input stress-strain data for FE modelling. All specimens were machined in the rolling direction to the geometric specifications shown in Figure 3.3.1.

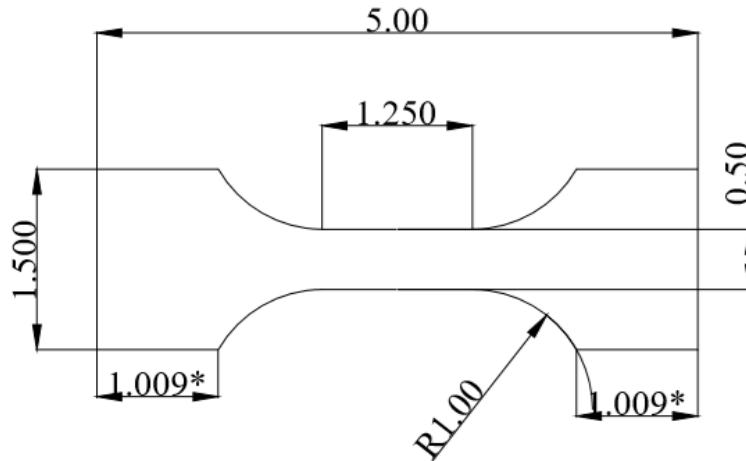
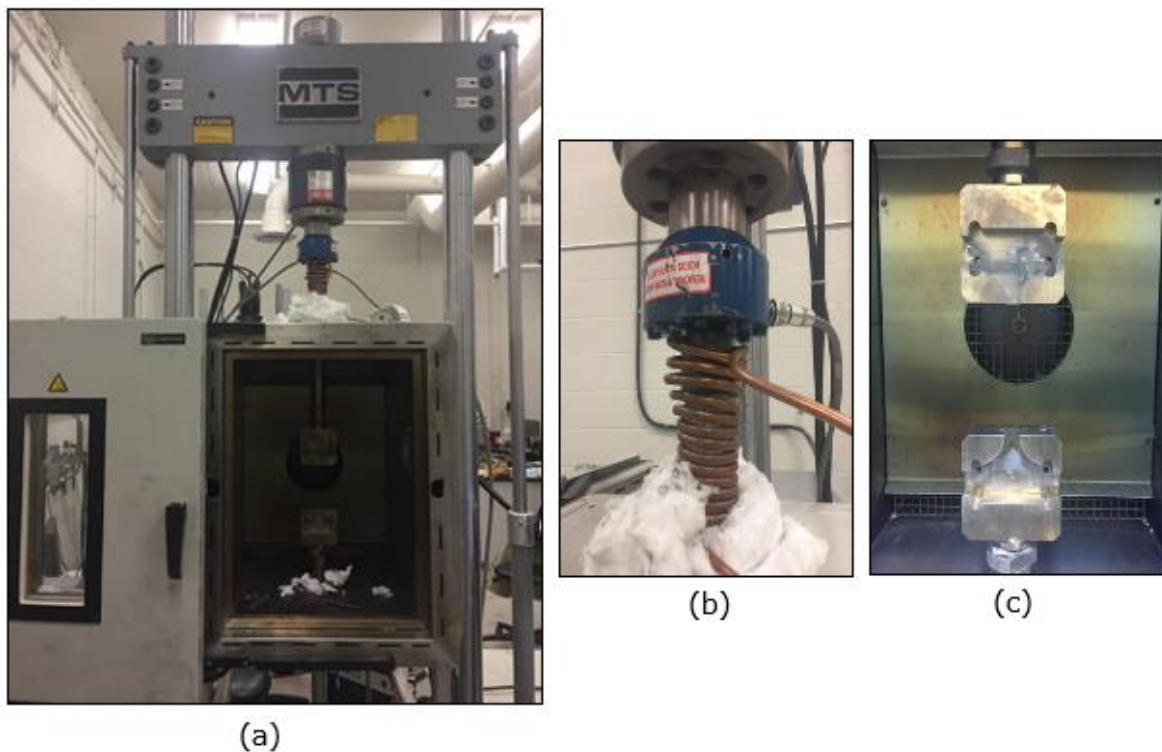


Figure 3.3.1 Standard AA7075 tensile sample for elevated temperature testing (all dimensions are in inches; \* reference dimension)

The tensile testing was conducted on the 250 kN MTS 810 servo-hydraulic mechanical test system coupled with Instron 8800 control and data acquisition system. Tests were performed at 300°C, 400°C, and 500°C and at speeds of 5, 10, 50, 100 and 500 mm/min, corresponding to initial strain rates of 0.002, 0.004, 0.018, 0.04, and 0.19 s<sup>-1</sup> respectively, for each of the three temperatures. The loading train and the grips of the mechanical test system were enclosed in an environmental chamber as shown in Figure 3.3.2 (a). The chamber was held at test temperature, and, additionally, a tensile sample with an attached thermocouple was used to ensure that specimen temperature did not differ from the furnace temperature. The additional thermocouple also provided the time needed to reach the test temperature prior to testing. A HH12C handheld thermometer was used with type K thermocouples for sample temperature measurement. The thermocouple was attached to the tensile sample by aluminum rivets, the riveting process consisted of drilling

holes, inserting the thermocouple wire and subsequent pressing of a soft aluminum rivet into the hole to hold the wires in place. A Lytron chiller unit and copper tubing was positioned around the top tensile rod to cool it and protect the load cell from heat damage (Figure 3.3.2 (b)). The specimen clamping grips were designed in-house and made from Inconel 718 alloy to withstand high test temperatures (Figure 3.3.2 (c)).



*Figure 3.3.2 (a) MTS tensile testing frame with furnace enclosure, (b) cooling system, and (c) high temperature tensile clamps.*

The strain data was obtained by use of a 2 camera Amaris system. The cameras were mounted on a tripod and positioned outside of the quartz observation window of the environmental chamber as shown in Figure 3.3.3. The gauge region of the uniaxial tensile test sample was coated with a speckle

pattern for Aramis dual cameras imaging of the specimen for strain measurement. High temperature white and black paint were used for backdrop and speckling respectively to provide good contrast for the DIC analysis of the camera images. As noted earlier in Chapter 2, high temperature paint was necessary to avoid delamination of the speckle pattern from the specimen surface under high temperature and large deformation during the test. The load and strain from the test were converted to true stress versus true strain data after receiving engineer data by use of a virtual extensometer feature in the Aramis software. This relationship is seen through Equations 3.1 and 3.2 where  $S$  is engineering stress,  $\sigma$  is true stress,  $e$  is engineering strain, and  $\varepsilon$  is true strain.

$$\sigma = S(1 + \varepsilon) \quad (3.1)$$

$$\varepsilon = \ln(1 + e) \quad (3.2)$$

Tensile data was also received separately from Novelis on the same material with testing performed at strain rates of 0.1, 1, and 5 s<sup>-1</sup> at temperatures of 25, 200, 300, and 400°C (see Appendix B). However, this data was obtained after solutionizing, therefore, it was not directly applicable to our experimental and simulated Marciniak testing.

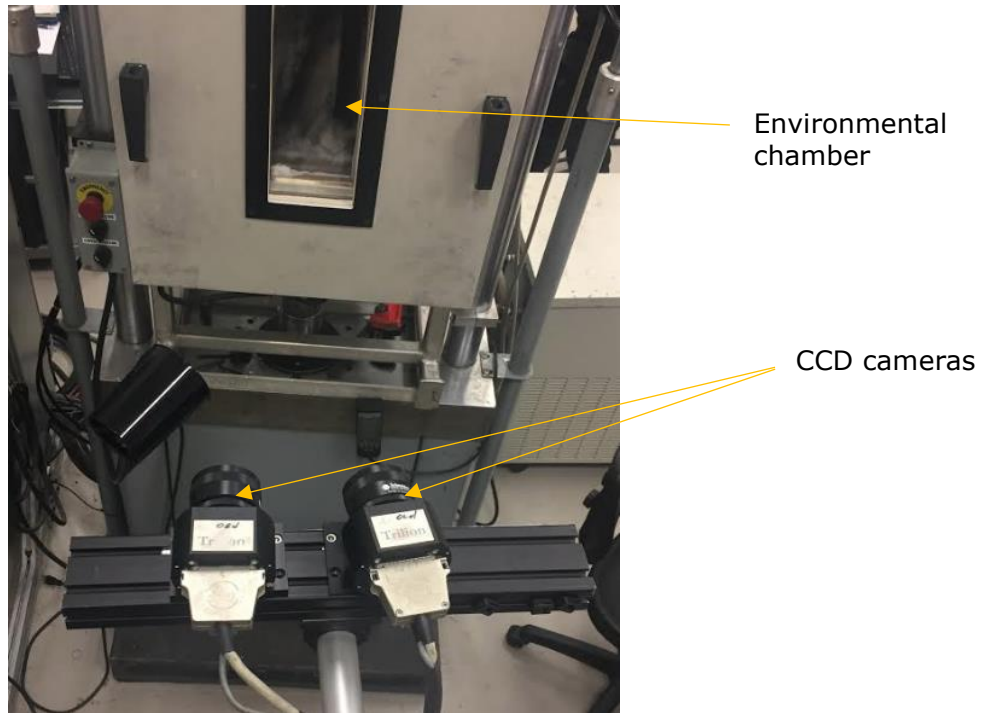


*Figure 3.3.3 Aramis setup utilizing 2 cameras through the furnace window*

### **3.4 Elevated Temperature Marciniak Test Development**

To assess material flow, surface roughness and fracture characteristics under in-plane biaxial straining conditions and to obtain strain inhomogeneity data and FLDs of AA7075-F sheet at elevated temperatures, Marciniak test was developed using the 150 Ton hydraulic driven double action MACRODYNE servo-press already available in the Metal Forming Laboratory of McMaster University. This press was chosen for Marciniak experiments as it is custom fitted with a large box furnace surrounding the forming chamber. The furnace is designed to be heated uniformly up to 700°C with a circulation fan for temperature uniformity. The forming process consisted of heating the entire Marciniak die-set to test temperature. The temperature data was obtained

additionally by thermocouples attached to the blanks as well as to the punch. Figure 3.4.1 shows the MACRODYNE press and forming setup located inside the box furnace. The punch is raised during pre-heating to ensure temperature uniformity of the punch as well as the rest of the tooling during testing. Alignment pins were used to ensure sample alignment was consistent across all test samples. The specimen geometry will be presented and discussed in a later sub-section.



*Figure 3.4.1 MACRODYNE press and forming setup with high temperature capability*

Since temperature could not be measured on the surface of the blank during testing so as not to alter the necking instability, a test sample fitted with 32 AWG type-k thermocouples riveted to the blank with aluminum rivets was used to capture the thermal history without the deformation of the

sample. Holes were drilled in 0.5-inch increments in the test blank moving outwards in the shaft direction with the first hole in the centre of the blank (Figure 3.4.2). Once the furnace was preheated to temperatures of 300°C, 350°C, and 400°C the blank was inserted to ensure uniform temperature along the blank was met. After 10 minutes this was achieved, and it was selected as preheating time for all blanks prior to forming. It is to be noted that the blanks were not solutionized prior to forming.

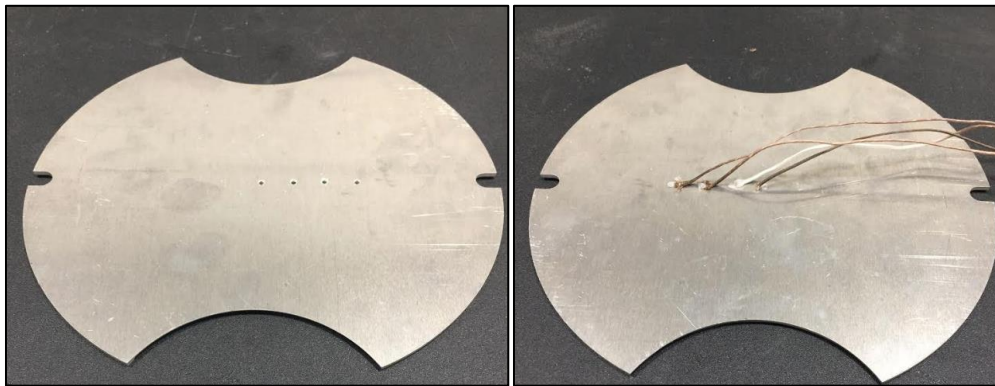


*Figure 3.4.2 Testing blanks with riveted thermocouples for temperature uniformity study*

ISO standard 12004-2008 was followed in the selection of the carrier blanks when applicable, however, due to differences in the elevated temperatures, forming process deviations were necessary. ISO suggests the use of a carrier material with thickness of at least 80 percent of the forming blank. Due to the limitations in the inner hole diameter of the die, pinching occurred when using a carrier blank with this thickness, and, as a result, blank failure occurred (Figure 3.4.3). A similar failure type occurred when the punch was not raised up to the die region during preheating and maintained a lower

temperature, causing the unsupported region of the test blank to have higher strength at lower temperatures, again promoting similar failure as shown in Figure 3.4.3.

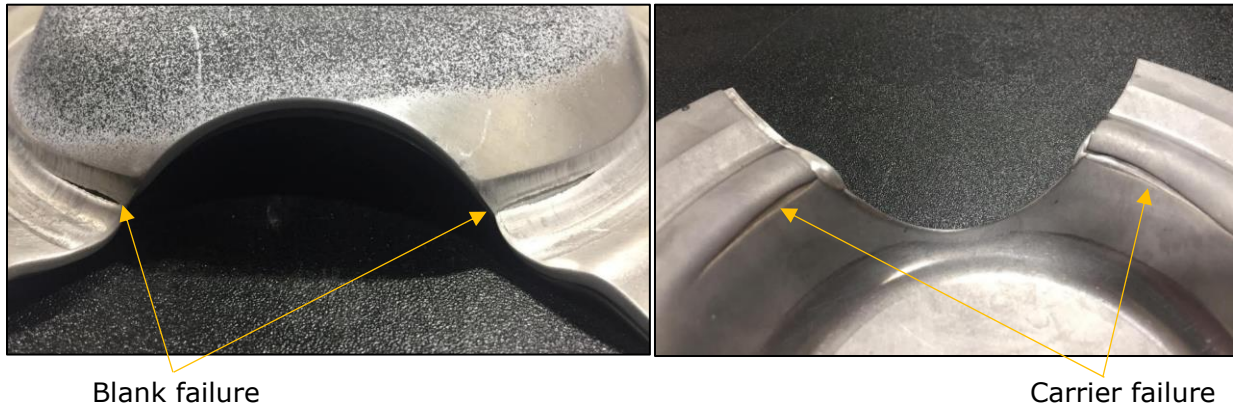


*Figure 3.4.3 Blank failure due to pinching*

Trials were conducted with thinner carrier blanks of several materials, however, due to the lower forming limit apparent in thinner sheet the carrier blank fracture proceeded the fracture of the test blank making the test invalid. Consequently, the upper die radius was increased to allow for the ease of material flow and use of thicker carrier blanks. This new radius required the manufacturing of new upper and lower clamping plates, moving the draw beads outward to compensate for the larger inlet radius.

The selection of a proper punch radius was also critical to avoiding fracture. The radius of the punch could not be too small to induce large frictional forces, causing fracture at the edge (Figure 3.4.4 (a)). While too large of a punch radius, the carrier blank hole expansion would reach the punch radius profile earlier causing stress concentration and fracture (see Figure 3.4.4 (b) and (c)).



*Figure 3.4.4 Specimen fracture characteristics, (a) edge fracture due to small punch radius, and (b, c) fracture due to stress concentration around carrier hole reaching punch radius apex*

The punch final, upper and lower die designs are present in Figure 3.4.5. This 3.75 inch diameter punch was manufactured from hardened H13 tool steel. It was equipped with a ceramic ring between the hydraulic piston and punch to mitigate temperature loss of the punch. Cavities were also drilled into the punch from below to reduce the weight of the punch and allow for easier heating.

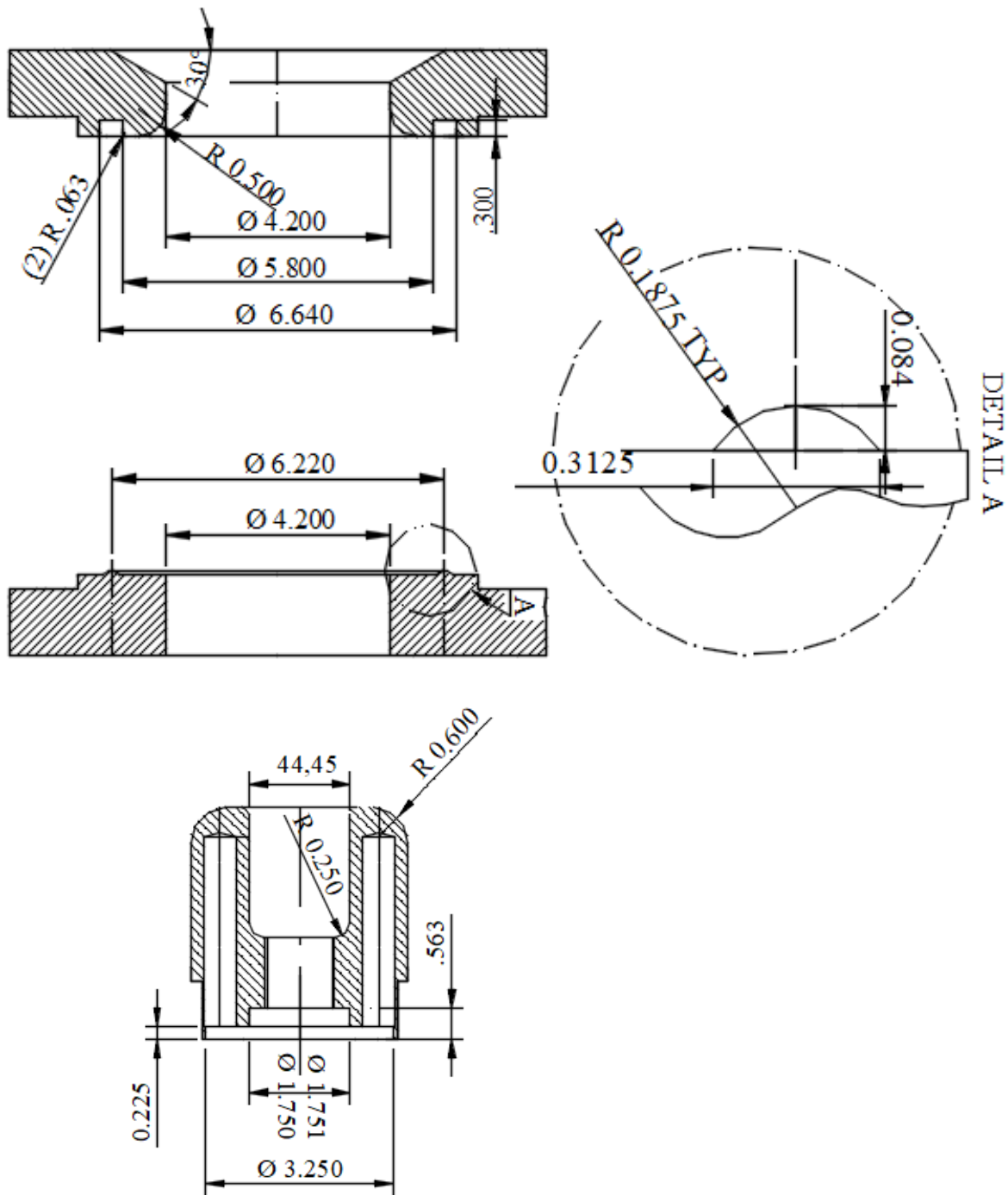


Figure 3.4.5 Upper and lower die designs and final punch design with holes (all dimensions are in inches)

A variety of methods for reducing the friction between the carrier blank and punch were attempted to improve carrier blank material flow. For improved lubrication, 0.15 mm thick Teflon (PTFE) film was placed between the punch and carrier blank. The Teflon sheet was able to greatly reduce frictional effects around the punch radius and was used in subsequent testing by placing it under the carrier blank before testing commenced (Figure 3.4.6). Also, Boron Nitride (BN) was sprayed on contacting punch and carrier blank surface to improve carrier material flow.



*Figure 3.4.6 Teflon lubricant and blank placement for high temperature Marciniak test with alignment pins*

The role of carrier blank in affecting the test material flow during the elevated temperature Marciniak test was also assessed. The candidate materials selected for carrier blank selection were IF steel (0.75 mm sheet thickness), 430SS (0.75 mm sheet thickness), AA5182 (1.5 mm sheet thickness). All of the above materials were chosen for their superior formability characteristics at room temperature. AA5182, additionally, offered

a thickness closer to the the thickness of the test blank, as suggested by the ISO standard for room temperature Marciniak tests. All carrier blanks were tested through hole expansion of the 7 inch specimen with 1.3 inch hole at 300°C. However, none of the materials performed satisfactorily for all strain paths that utilize the carrier blank. Many failed prematurely at the hole, and initiated artificial fracture in the test blank at the fracture location of the carrier blank. The final material tested for carrier blank material was AA7075-F, the same material as the test material. Figure 3.4.7 shows schematically the different strain paths taken by the carrier and test blank of AA7075-F at 300°C. Through initial testing it was shown that the uniaxial strain path taken by the carrier blank could sustain higher strain paths compared to the right side of the FLD, as desired. AA7075 also showed the highest formability at elevated temperature, while IF steel formability was much too low and relatively unaffected at temperatures of 400°C. AA7075-F sheet thus proved quite effective and was readily available in sufficient quantity in the laboratory. As a result, AA7075 was chosen as a suitable driver material.

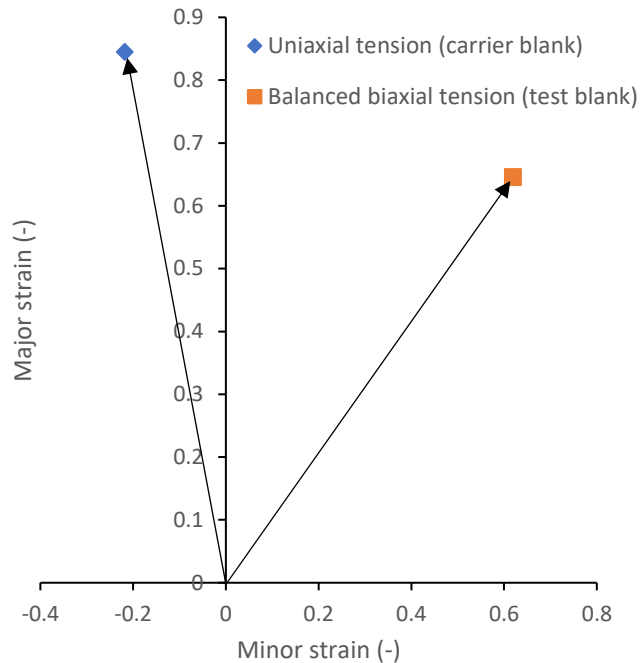


*Figure 3.4.7 Limiting strain experienced by carrier blank around hole (uniaxial tension) versus test blanks for balanced biaxial strain path testing*

Due to the high formability evident in AA7075 at elevated temperatures it was critical that all of the deformation from the carrier blank was translated to the test blank. This was achieved by increasing friction between the carrier and test blanks. The carrier and test blanks surfaces were roughened using 320-grit Silicon Carbide sandpaper in the areas away from the unsupported centre region of the test blank so as not to affect strain localization and fracture. The effect of roughening on flow localization and fracture is shown in Figure 3.4.8 where rough, high friction, carrier and test blanks helped with punch load transfer from carrier blank to the test blank, and promoted necking or fracture of the test blank in the unsupported flat region. While each test had the same dome height (~2 inches) the unroughened sample exhibited a substantially larger hole and the corresponding test blank did not experience fracture

whereas the roughened sample experienced fracture with a smaller hole expansion of the carrier blank. Noting this, the carrier blanks were roughened and not the test blank.

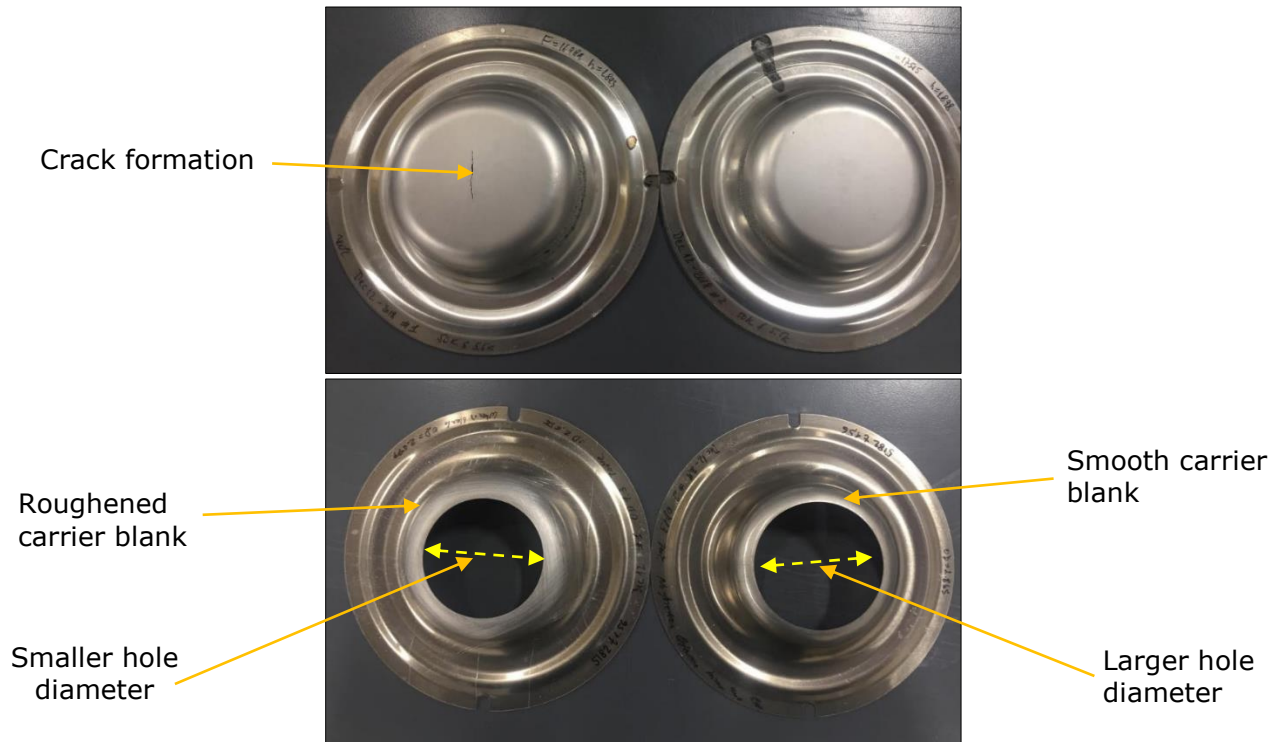


Figure 3.4.8 Impact of carrier surface roughness on strain translation

### 3.4.1 Elevated Temperature Forming Test System

The forming parameters of a Marciniak test can vary considerably between each strain path tested from uniaxial tension (0.5-inch wide specimen at its narrowest location) to balanced biaxial tension (7.5-inch diameter specimen). Other than the punch speed which was held constant at 2.4 inches per minute (1 mm/sec), many other parameters were adjusted. Each of these tests required adjustment of the clamping load to ensure that no material from outside of the lock-bead could flow towards the die opening

during the test. The clamping load was adjusted to compensate for the varying clamping area between tests. The tests were stopped when fracture was detected using a break-load detector. The break-load detector checked for a specified load drop in the punch force while forming. This drop would vary drastically between strain paths as well as temperatures. Break-load and clamping forces are presented for each temperature and geometry in Table 3.4.1.

*Table 3.4.1 Macrodyne press parameter settings for a range of temperature and test geometries*

Sample geometry (inches)	Clamp load (kips)			Breaking load (lbs.)			Max punch force (lbs.)		
	300°C	350°C	400°C	300°C	350°C	400°C	300°C	350°C	400°C
0.5	20	20	10	150	150	150	624	452	324
1	20	20	10	300	300	200	1,450	928	547
2	20	20	20	300	300	250	3,360	2,487	1,697
3	25	20	20	500	500	300	12,589	9,495	7,312
4	50	50	50	1,250	500	500	14,747	10,841	8,012
5	50	50	50	1,800	1,250	1,250	13,945	10,488	7,304
full	50	50	50	5,800	5,500	4,000	14,693	10,603	7,561

### **3.4.2 DIC Methodology for Full-Field Strain Measurement and Necking Determination**

The blanks were imaged from a built-in ARAMIS camera system located directly above the central column of the MACRODYNE press frame shown in

Figure 3.4.9. The online strain measurement system consisted of two dedicated 5-megapixel CCD cameras with 50 mm lens as part of the Aramis system. The cameras imaged down through a window located on top of the furnace. Initially, the high thermal gradients coming from the top of the furnace through the glass produced large refraction of light rays, making accurate strain recording difficult due to image fluctuation from frame-to-frame. To alleviate this problem, a fan was mounted above the window that circulated cool air and kept the hot air from rising towards the cameras, thus keeping the thermal gradients down and avoiding this affect. Imaging of a stationary blank was used to verify image to image accuracy.

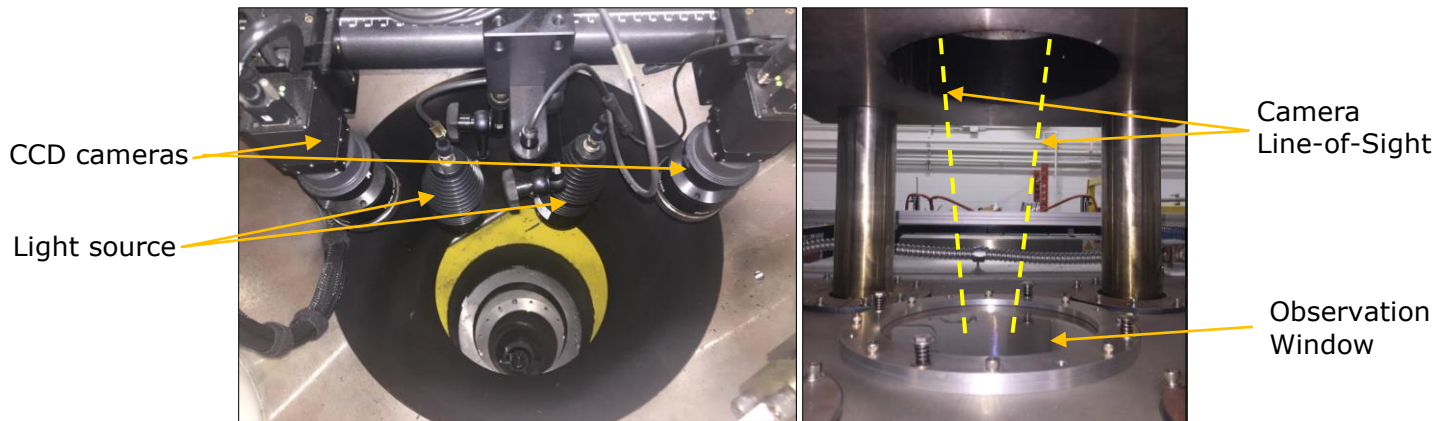


*Figure 3.4.9 MACRODYNE built-in 2-camera Aramis setup*

The frame rate was kept consistent with ISO 12004-2 recommendation of 10 frames per second to ensure accurate capture of fracture. After obtaining the first image after fracture, the position-dependent method was used to calculate the limiting strains in both the major and minor directions. For limit

strain determination, three parallel lines, perpendicular to the fracture line with a line-to-line spacing of 2 mm were drawn, as shown in Figure 3.4.10.

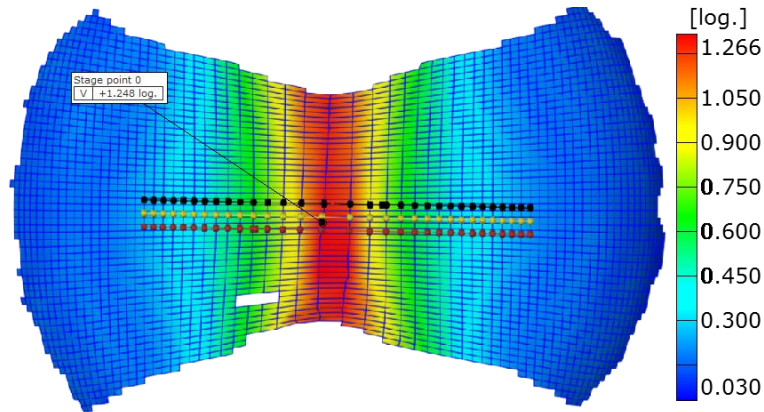
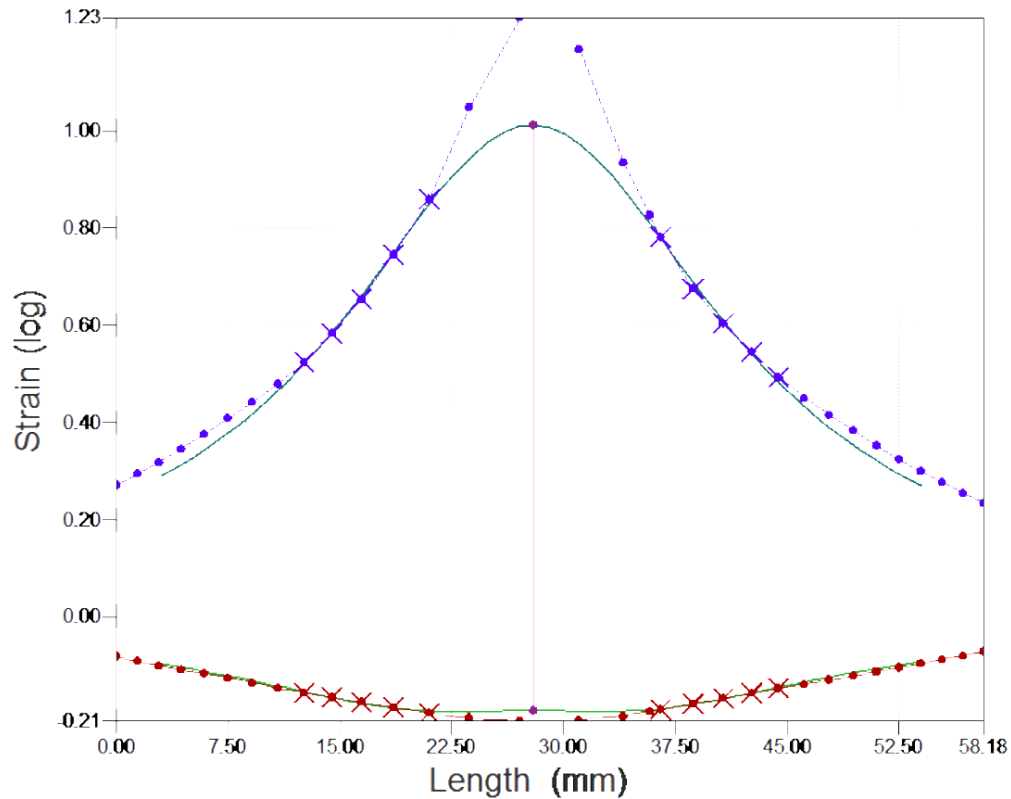


Figure 3.4.10 Lines perpendicular to necking region used to gather major strain data

To detect the onset of necking, Bragard’s graphical curve fitting method from ISO 12004:2008 was adopted. The major strain data on either side of the crack was used to fit a best fit second-order inverse parabola of the form:

$$f(x) = 1/(ax^2 + bx + c) \quad (3.3)$$

For illustration, the parabola fit to the neck strain data from present work is shown below in Figure 3.4.11. The apex of the parabola was taken as the major forming-limit strain value. The process was then repeated for minor strain for a minimum of 2 samples. Samples showing multiple necking regions near fracture made sizing of the fitting window difficult and significantly altered the fit of the second order parabola.



*Figure 3.4.11 Limiting strain calculation utilizing a second-order parabola, showing major and minor limiting strains at apex*

A facet size of 13 x 13 with a step size of 9 pixels was selected to calculate all strain data based on prior experience in the lab analyzing ARAMIS strain data along with its ability to calculate the strain efficiently with the applied random speckle sizing. With too small a facet size, there was insufficient data to capture strain progression, while too large a facet size resulted in the loss of strain resolution. Figure 3.4.12 below shows the placement of facets over a characteristic speckle pattern.

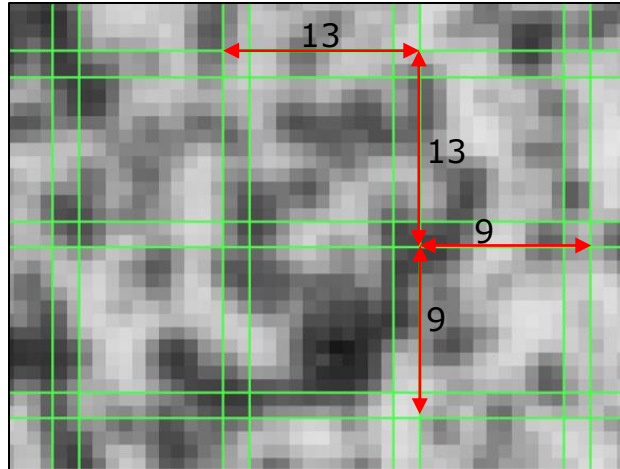


Figure 3.4.12 Facet size 13x13 with step size of 9 applied over stochastic speckle grid at high magnification for DIC-based strain measurement

### 3.4.3 Methodology for Fracture Strain Determination

Fracture strain was determined through measurement of neck region thickness at fracture. Although it was possible to analyze the major and minor strains obtained directly from ARAMIS data, due to the resolution available from the speckle pattern and camera setup, major strain ( $\epsilon_1$ ) calculations led to large errors close to fracture. However, since minor strain ( $\epsilon_2$ ) is typically in the plane strain state once necking has occurred, it can be measured with minimal error. By calculating thickness strain and taking into consideration the volume constancy Equation 3.4, one can back calculate major strain to identify the point of fracture.

$$\epsilon_1 + \epsilon_2 + \epsilon_3 = 0 \quad (3.4)$$

Thickness strain was measured using an optical microscope image of the fracture surface, taking the average fracture thickness measurement

along the edge. The following equation for thickness strain calculation was utilized:

$$\varepsilon_3 = \ln\left(\frac{t_f}{t_o}\right) \quad (3.5)$$

where  $t_o$  and  $t_f$  are the initial and fracture thickness values.

### **3.4.4 Forming Test Sample Geometry**

To obtain a representative and reliable FLD of a sheet material, testing of at least 5 different blank geometries/strain paths is recommended. Initial test blanks and carrier blanks were produced through machining to receive a high-quality edge finish; however, waterjet machining was used for final testing as it was more economical and efficient. Edge quality was closely monitored before testing of specimens. Water jet edges of the test blanks exhibited burrs that that may cause premature failure. Therefore, burrs were removed by sanding with a fine grit sandpaper. Test blanks used to produce limiting strain paths on the left-hand side of the FLD included shaft widths of 0.5", 1" and 2", while shafts of 3", 4", 5" and 7.5" widths (Figure 3.4.13) were used to produce limiting strains on the right-hand side of the FLD. Strain paths on the right-hand side required the use of a carrier blank (Figure 3.4.14). A balanced biaxial tension test was conducted to identify the preferred failure orientation with respect to the sheet rolling direction (RD). Limiting strains of 1" and 2" samples in both the rolling direction (RD) and transverse direction (TD) were also compared to confirm preferred failure orientation. The TD

orientation showed a more conservative limiting strain in the specimens tested as well as being the preferred failure orientation. Therefore, TD orientation was used for all further test blanks to obtain a conservative FLD.

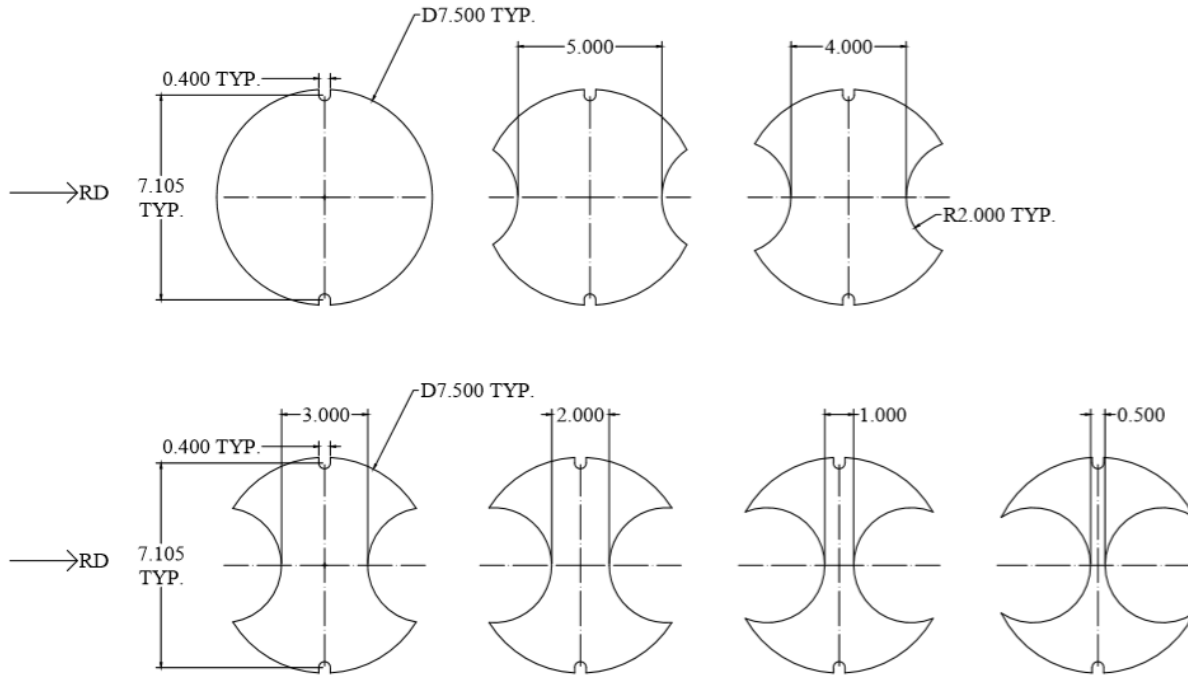


Figure 3.4.13 Blank geometries for achieving strain paths from uniaxial tension to balanced biaxial tension

All carrier blank holes were machined, instead of waterjet cut, to ensure a high-quality surface finish to avoid premature failure at the hole. Due to the higher FLD observed in the RD, carrier blanks were machined in this orientation to give greater compliance to the carrier blank before fracture.

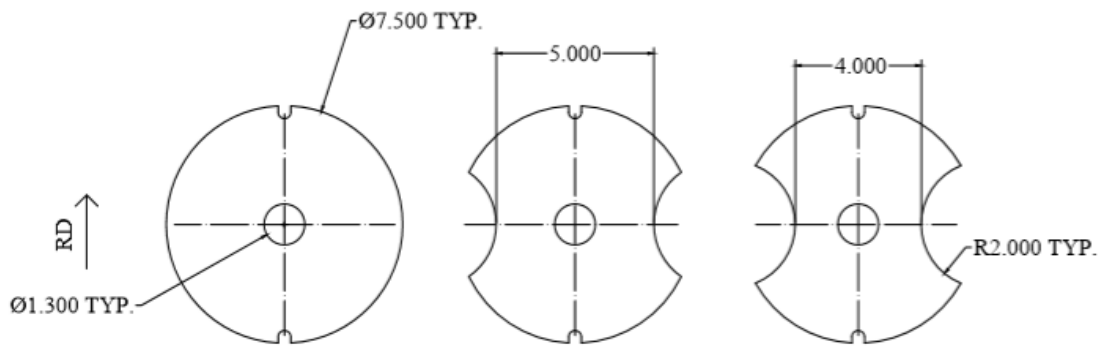


Figure 3.4.14 Carrier blank geometries for tension-tension side of FLD

When the use of a carrier blank was necessary, as noted earlier for specimen sizes of 3", 4", 5" and 7.5", a carrier blank larger than test blank was utilized to avoid premature failure due to the smaller carrier cross section, i.e., 3" test blank used a 5" wide carrier blank whereas 4", 5" and 7.5" test blanks used a 7.5" (full size) carrier blank.

### 3.5 Hot Stamping Experiments

The hot stamping experiments using a custom hot stamping die were conducted on a servo-hydraulic 150 Ton double action press from Interlaken Technologies (model SP150). The die was mounted to the press in a manner that allowed for the quenching of the part during forming. The complete laboratory setup similar to an industrial hot stamping die quenching line is shown in Figure 3.5.1. A separate Nabertherm LT15/11 furnace with a vertical lifting door was placed in close vicinity of the press and utilized for blank heating (i.e., for solutionizing during pre-forming). A Lytron chiller unit was used to keep temperature of the die constant throughout all tests as well as

to increase the quenching rate. The chiller unit was set to 10°C to minimize condensation on the die surface. Various types of lubricant including industry recommended Fuchs Renoform 10 ALWF and Teflon film were utilized on the die before stamping as well as on the blank before solutionizing for 1 hour. AA7057-F 2mm gauge thickness blanks with dimensions of 8.5" x 4" were solutionized at 480°C for 1 hour. The blanks were then transferred by hand using needle nose pliers to the die and placed against alignment shims. The press clamping surface subsequently lifted the blank close to the upper die without clamping force and the blank was punched at a rate of 1.75 inches per second to ensure system stability.

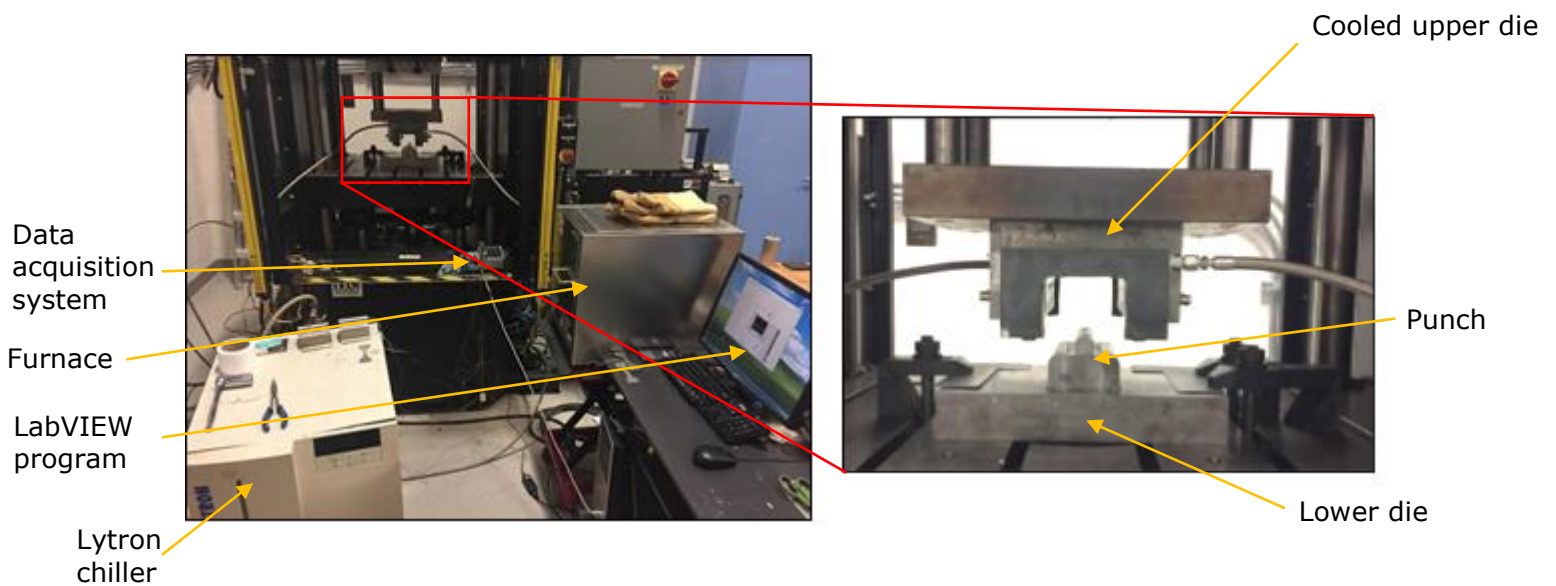


Figure 3.5.1 Experimental hot stamping die quenching setup

### 3.5.1 Forming Test System

The Interlaken Servo-Press Forming Software was used to create a forming cycle specific to the hot stamping experiment. The data acquisition system acquired continuous punch force and displacement data during the test. The forming program was created to follow velocity and position profiles, and to avoid inherent instability of the system when programmed to follow force input.

*Table 3.5.1 Forming cycle parameters for laboratory hot stamping tests*

<b>Process Stage</b>	<b>Punch-Die Clearance (mm)</b>	<b>Clamp-Clearance (mm)</b>	<b>Punch Velocity (in/sec)</b>	<b>Clamp Velocity (in/sec)</b>	<b>Duration (sec)</b>
Blank placement	203	101	0	0	5
Clamp blank	104.5	2.5	1.75	1.75	5
Hot stamping	2	2.5	1.75	0	2.25
Cooling	2	2.5	0	0	25
Part release	152	152	1	1	6

### 3.5.2 Die Design and Manufacturing

The die design was completed to mimic the shape and process of forming of a typical hat shaped B-pillar part (Figure 3.5.2). The cooling channel diameter that would allow for optimal number of channels while maintaining turbulent flow for effective heat transfer was chosen. The chiller flow rate of 4.3 GPM was used as a constraint for this calculation which can be found in Appendix A. Several redesigns of the die were necessary after preliminary testing to correct for the punch and inlet radii that were sufficiently

large enough to avoid fracture and excessive galling. A 1° taper angle was used on the top die to ensure easy removal of samples after hot stamping. The selected material was 1045 steel for its high strength, hardening capabilities, and low relative cost when compared with commonly used tool steel. Due to limited amount of planned testing and experimental part production, 1045 steel for the die material was a good economical choice.

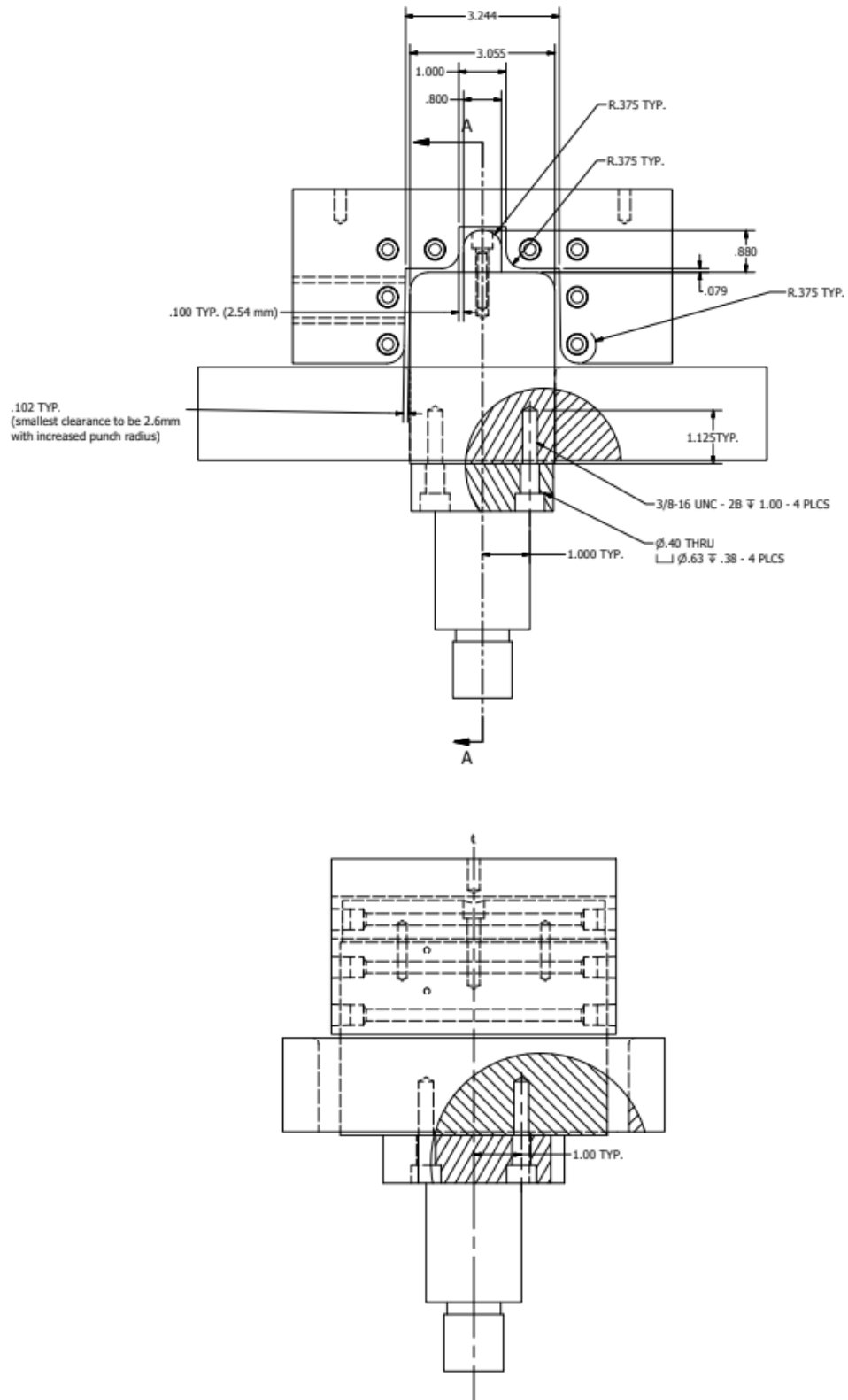


Figure 3.5.2 Hot stamping die quenching die geometry

### **3.5.3 Temperature Data Acquisition During Forming**

The blank temperature profile during forming was measured using 32 AWG type-k thermocouples inserted along the edge of the blank into 1 mm diameter holes drilled to 0.6" deep (Figure 3.5.3). This was the maximum depth that such a small hole could be drilled before excessive drill fracture in the hole became an issue. The thermocouples were connected to a National Instruments cDAQ-9174 data acquisition system with a built-in cold junction compensation. Readings were recorded starting while the blank was still in furnace using a custom-built LabVIEW program that operated on high speed mode - taking temperature measurements on every channel at a frequency of 5 Hz.

The thermocouple ends were inserted and held in place through a small indent to the end of the hole to hold the thermocouples rigidly in place while plastically deforming the blank (Figure 3.5.4).

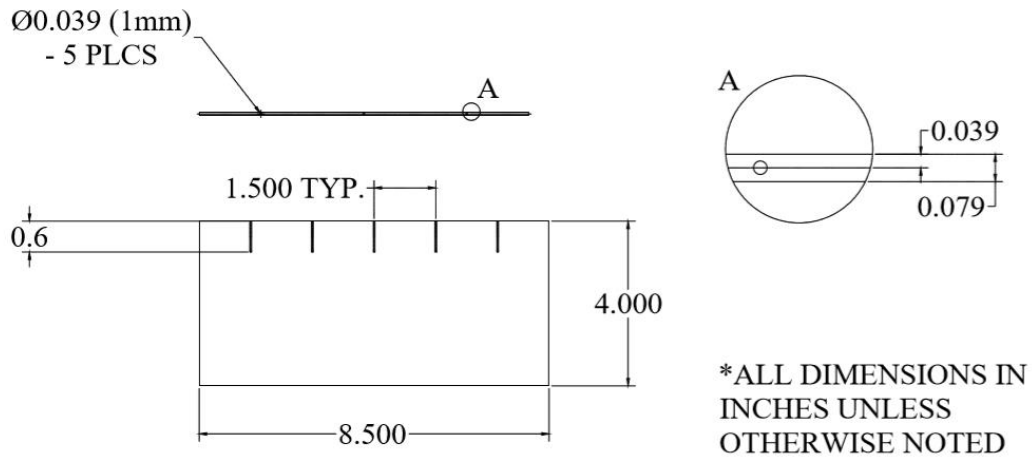


Figure 3.5.3 Hot stamping blank with thermocouple ports for temperature measurement

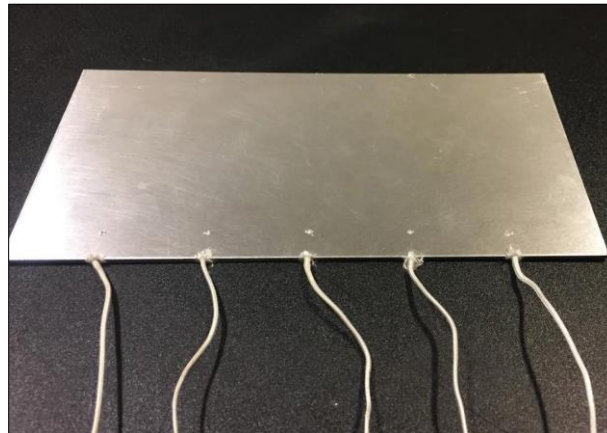
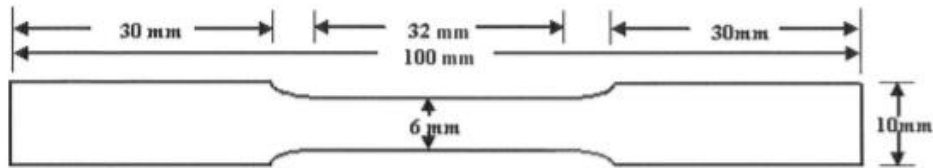


Figure 3.5.4 Thermocouple placement into hot stamping blank for forming temperature measurement

### 3.5.4 Tensile Test Sample Acquisition After Hot Stamping

After hot stamping, the resulting parts were cut into segments with a vertical band saw and tensile samples were taken from each of the areas where cooling rate data was acquired during testing. Tensile samples were

machined following ASTM standard E8 sub-size (E28 Committee, 2013) tensile samples of dimensions shown in Figure 3.5.5.



*Figure 3.5.5 ASTM standard E8 for sub-size tensile samples*

### **3.5.5 Cooling Rate Study**

To obtain an understanding of the cooling rates necessary to provide target strength characteristics, tensile samples separated from those used in the hot stamping trials were machined and subjected to various cooling rates. Tensile specimen geometry was consistent with that of Figure 3.3.1 from Section 3.3. Cooling rates were obtained through various methods such as water quenching, clamping, forced-air quenching, and air cooling to obtain different rates. For forced air quenching, a custom quenching unit consisting of a tube furnace and a translating specimen holder stage mounted on a linear bearing that moved in and out of the heated tube furnace was utilized. The pressurized air was passed through a rigid independently supported aluminum block with 100 or so fine ports that released pressurized air jets over the specimen coupon held by the translating stage (see Figure 3.5.6). The specimen coupon was first placed in the specimen holder stage and the stage

was inserted into the tube furnace for specimen heating at the desired temperature. The stage was then quickly pulled out of the tube furnace and the specimen was subjected to controlled force air quenching by placing the stage and specimen directly below the air jets.

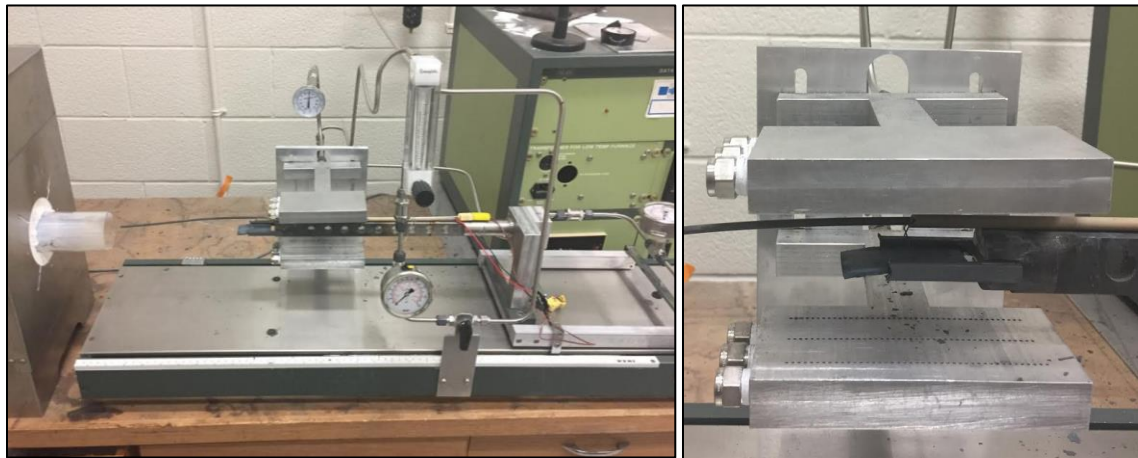


*Figure 3.5.6 Setup capable of variable forced air and LN<sub>2</sub> cooling*

Since the cooling rate of the tensile samples was required, a thermocouple was inserted into the middle of a sacrificial tensile specimen (Figure 3.5.7). Multiple trials of each experiment were completed with the tensile sample capable of measuring temperature. Once a consistent temperature profile was obtained final testing was completed using a tensile specimen without the hole for the thermocouple so as not to cause premature fracture during the tensile test.

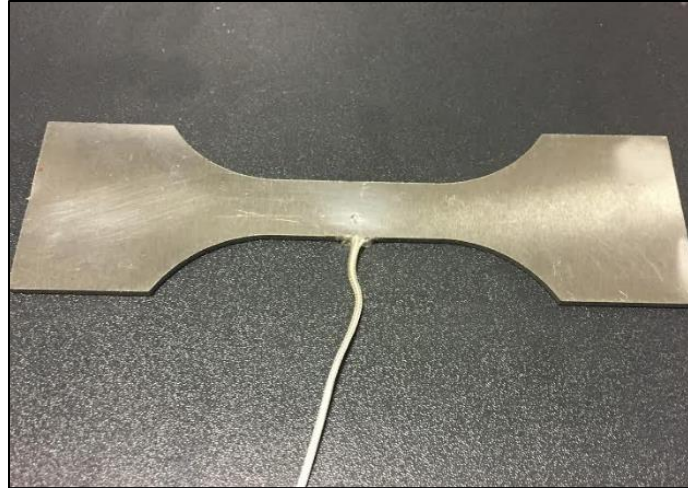


*Figure 3.5.7 Tensile sample with k-type thermocouple inserted*

After tensile samples were cooled, they were kept frozen (below  $-40^{\circ}\text{C}$ ) in a dry ice container to effectively halt any precipitate formation. Once all samples were quenched, they were subjected to T6 aging treatment to attain peak strength typical of a hot stamping and aged part. The samples were then tested in uniaxial tension to obtain their post-aging strength and other mechanical properties. Tensile testing was carried out on a 100 kN MTS 810 mechanical test system equipped with an Instron 8800 test controller. Strain measurements were taken by using a 1-inch gauge length extensometer (see Figure 3.5.8).

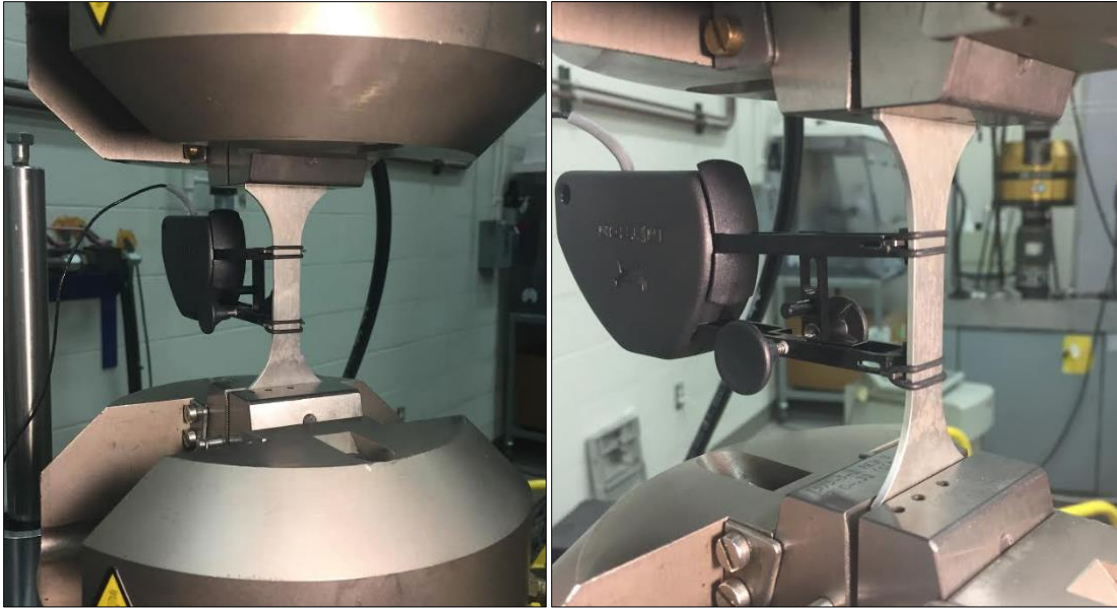


*Figure 3.5.8 Tensile testing setup with 1-inch gauge length extensometer*

### **3.6 Microstructure Analysis**

Microstructural and surface studies were carried out to characterize ductile void damage development, fracture topography and surface roughening of formed and fractured Marciniak specimens. These included: (i) polished through-thickness section analysis of microstructure from the fracture region using SEM, (ii) fracture surface analysis using SEM, and (iii) surface roughening characteristics using a surface roughness measurement equipment. Samples investigated were taken from Marciniak test blanks to investigate effect of temperature, strain and strain path on fracture. Specimens subjected to three strain paths were utilized for microstructure analysis; uniaxial tension (0.5" wide specimens), plane-strain (3" wide specimens) and balanced biaxial tension (7.5" circular specimen) at each of

the three test temperatures of 300°C, 350°C and 400°C. The tests were conducted at a constant speed of 1 mm/sec corresponding to a strain rate range of 0.1-0.2 s<sup>-1</sup>.

### 3.6.1 Sample Preparation for Microscopy Work

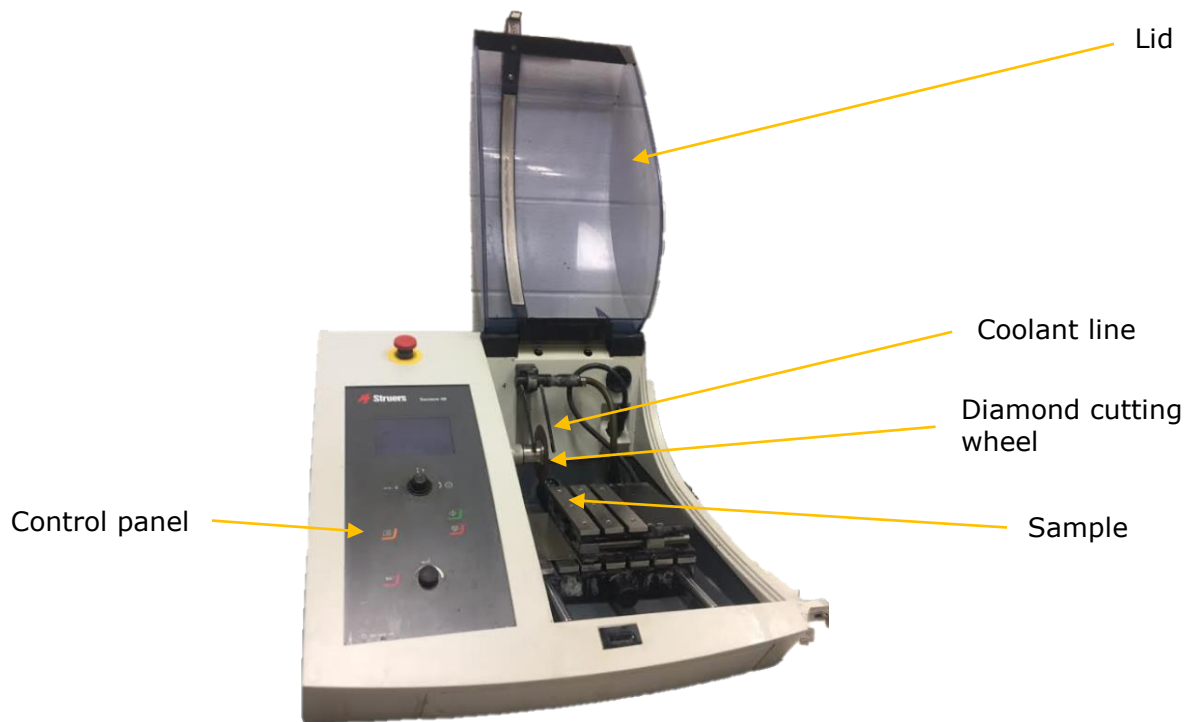
Figure 3.6.1 shows the regions of the Marciniak test sample that were sectioned for microscopy work. The red dashed lines mark the cut away square region for the 3 type of samples: uniaxial tension, plane strain and balanced biaxial tension. High speed abrasive cutting blades were used for initial sample cutting. The samples were then placed into a vacuum tight box with desiccant to avoid surface contamination.



Figure 3.6.1 Fracture surfaces cut from formed Marciniak test for fractography

After fracture surface imaging was completed, the samples were further sectioned using a STRUERS Secotom-50 precision cut-off machine (Figure 3.6.2). The samples were then cold mounted in Epoxy Resin with 20:3 grams

of epoxy to hardening agent. After mounting, samples were polished using the STRUERS Tegramin-25 semi-automatic polishing machine capable of polishing 6 samples at a time (Figure 3.6.3). The polishing abrasives and procedure are presented in Table 3.6.1.



*Figure 3.6.2 STRUERS Secotom-50 precision cut-off machine*

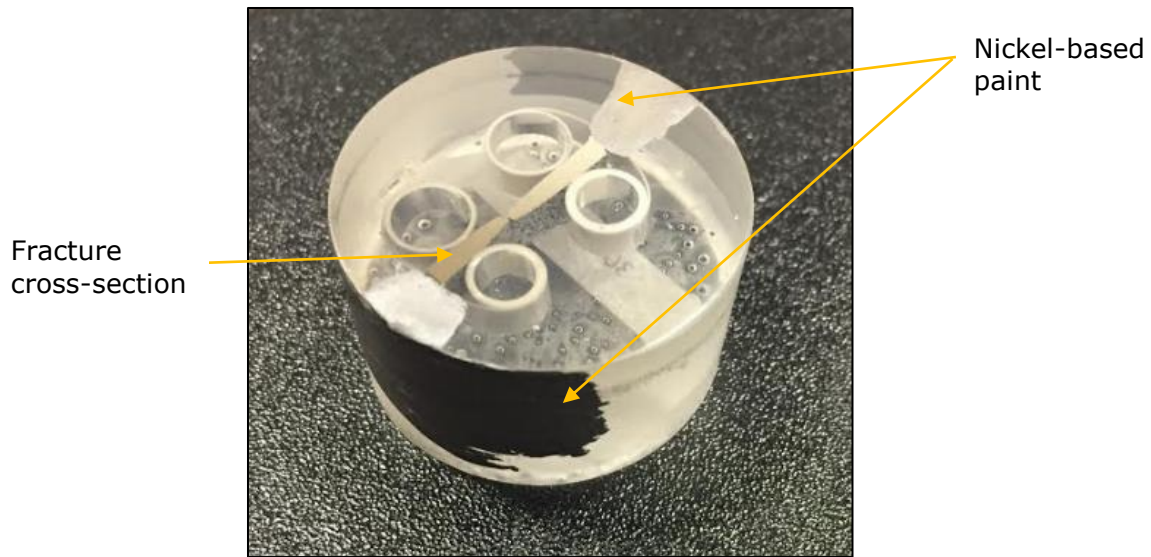


Figure 3.6.3 STRUERS Tegramin-25 semi-automatic polishing machine

Table 3.6.1 Polishing and lubricant settings

Step	Abrasive	Lubricant	Suspension	Holder Speed (RPM)	Bed Speed (RPM)	Load per Sample (N)	Time (min.)
1	SiC 320	Water	N/A	150	150	15	1:30
2	SiC 500	Water	N/A	150	150	15	1:30
3	SiC 800	Water	N/A	150	150	10	1:30
4	SiC 1200	Water	N/A	150	150	15	4:00
5	Mol	Green	DP-P 6 $\mu\text{m}$	150	150	25	4:00
6	Mol	Green	DP-P 3 $\mu\text{m}$	150	100	25	4:00
7	Nap	Green	DP-P 1 $\mu\text{m}$	150	120	25	3:50
8	Chem	N/A	OP-S	150	90	15	2:20

The samples were then placed in a vacuum tight container with desiccant to avoid surface contamination. Prior to imaging via SEM, the samples were painted with a nickel-based paint to allow for the flow of excess electrons away from the sample surface, and thereby avoiding sample charging. Figure 3.6.4 shows an epoxy mounted fractured sample with nickel paint and carbon deposition for imaging via SEM.



*Figure 3.6.4 Epoxy-mounted fracture sample with carbon coating and nickel-based paint*

### **3.6.2 SEM Analysis**

All SEM analyses were conducted using the JOEL-6610LV scanning electron microscope equipped with energy-dispersive spectroscopy (EDS) for measurement of elemental composition. This microscope is capable of 3, 8 and 15 nm resolution at 30, 3 and 1 kV, respectively with a magnification capability of 300,000x. A conductive 32 mm sample stage was used for mounting of the fracture samples. The microscope was equipped with auto contrast/brightness, auto stigmatism, and auto focus modes. Along with dual observation mode, quick setup and viewing of samples was possible. The dual observation mode was useful when identifying areas to investigate for compositional make-up using both secondary (SEI) and backscatter (BEC) electron modes simultaneously. The advantage of BEC mode lies with its ability to differentiate between particles with differing atomic mass, showing

heavier elements as whiter (such as Fe) compared to lighter weight elements (such as Mg and Zn). The topographic nature and fine features of the fracture surfaces made the SEM a better choice over light microscope for fractography work. This was due to much higher range of magnification as well as its much higher depth of field. One drawback of the SEM, however, was the inherent shadowing effect when the electron detector was unable to see the point of interest on the workpiece. As such, observation areas were chosen keeping this in mind. Figure 3.6.5 shows the exact setup of the JOEL-6610LV as utilized in the Canadian Centre for Electron Microscopy (CCEM) laboratories at McMaster University.

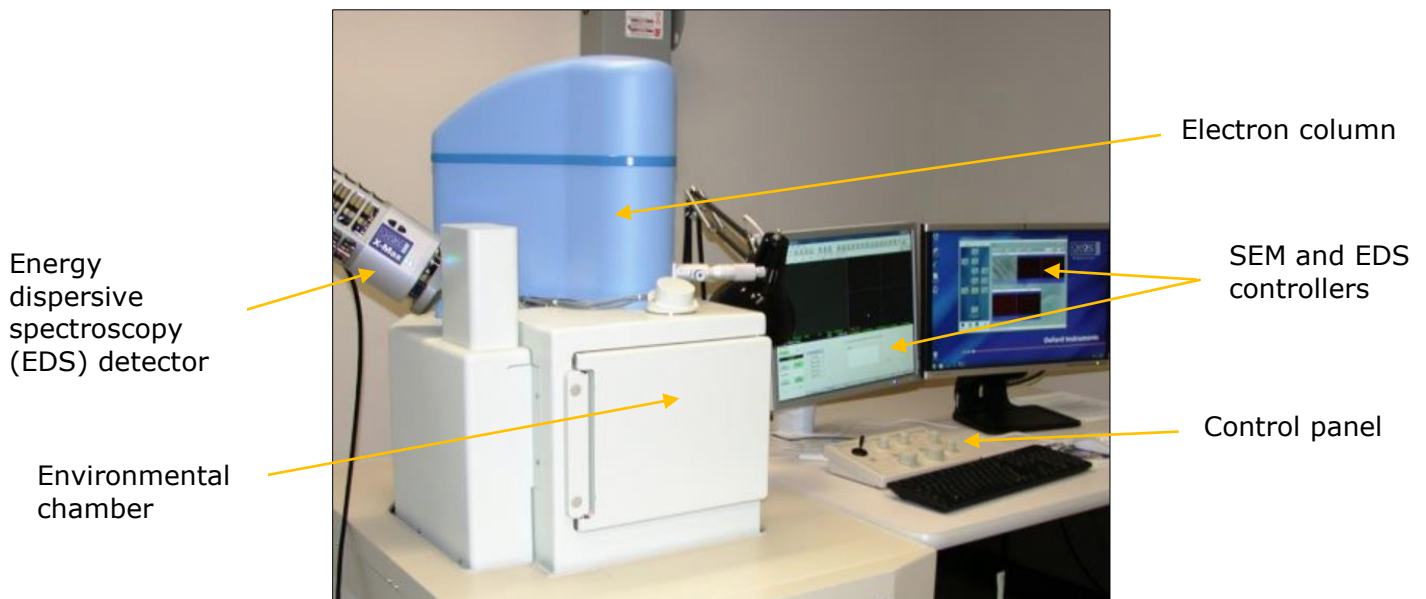


*Figure 3.6.5 JOEL-6610LV SEM in CCEM laboratory*

### 3.6.3 FLD Sample Surface Roughening Characteristics

The surface roughness was characterized on the as-received sheets (F temper) before deformation as well as after undergoing Marciniak testing. Three strain paths including uniaxial tension (0.5" specimen), plane-strain (3") and balanced biaxial tension (7.5") were investigated at each of the three test temperatures of 300°C, 350°C and 400°C. Measurements were carried out using an Alicona InfiniteFocus G5 surface roughness measurement system (see Figure 3.6.6). The system is a non-contact optical 3D system with 120 nm vertical resolution and 400 nm lateral resolution. Each sample was measured with a 1.6 mm x 1.6 mm spot size and 50  $\mu\text{m}$  virtual stylus diameter adjacent to the crack initiation site. Various surface roughness parameters  $R_a$ ,  $R_z$ , and  $R_q$  are measured from the Alicona system, where they are defined as arithmetic average, roughness height and root mean square roughness respectively.



Figure 3.6.6 Alicona InfiniteFocus G5

## Chapter 4

# **FE Modelling Methodology for Isothermal Marciniak Tests**

### **4.1 Model Setup**

The experimental FE work was completed with general purpose ABAQUS 6.14 finite modelling software for solving solid mechanics problems. Explicit solver was utilized due to its ability to solve large non-linear quasi-static sheet metal forming problems. Explicit solver is typically well suited for problems with complex tool-sheet contact problems during forming as seen during the Marciniak test. Aspects such as model geometry, boundary conditions, meshing, material model, and mass scaling are discussed below.

### **4.2 Model Geometry**

Three geometries were modelled for simulation of the Marciniak test including 0.5", 3" and 7.5" (full size) with no carrier blank, 5" carrier blank and 7.5" carrier blank respectively (Figure 4.2.1). Quarter geometries were used due to symmetry of the operation, reducing computational cost. The FE model geometries and dimensions were equivalent to those used for experimental testing in the laboratory. All model geometries were built using the ABAQUS solid modelling environment. An initial imperfection factor of 0.998, based on evolved surface roughness of 2  $\mu\text{m}$ , was applied to the initial

2 mm thickness geometry to initiate necking in the middle region of each of the test specimen geometries.

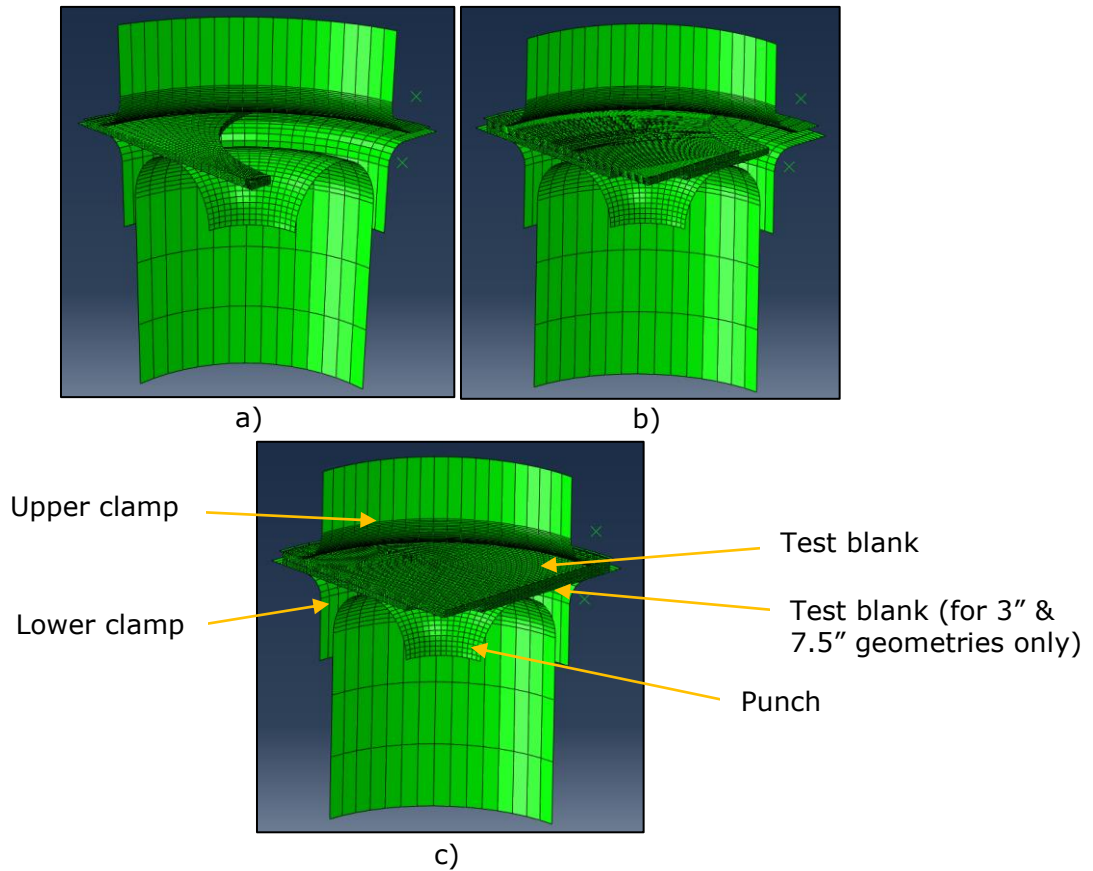


Figure 4.2.1 (a) Uniaxial tension, (b) plane strain and (c) balanced biaxial tension model geometries

### 4.3 Material Model and Input Data

Since the die, clamp and punch were made from hardened steel they were defined as rigid bodies to reduce computational cost of the model. The AA7075-F test blank and carrier blank, also made of AA7075-F, were modelled as elastic-plastic material. Hardening law were fitted to the tensile data produced at 400°C at different strain rates, assuming the test to be isothermal. Ludwik's equation (Eqn. 4.1) (Marciniak & Duncan, 1992) was

fitted to the tensile test data at various strain rates to reduce noise in the input signal. Fitting parameters are presented in Table 4.3.1.

$$\sigma = \sigma_y + K \varepsilon_p^n \quad (4.1)$$

where  $\sigma_y$ ,  $K$ , and  $n$  are defined as true yield strength, strength coefficient and strain hardening exponent respectively. Coulomb friction (Eqn. 4.2) (“Abaqus/CAE User’s Guide”, 2016) along with penalty contact method was used for friction input with different values chosen for the various contacting surfaces. The penalty contact method approximates hard contact by searching for node-into-face and edge-into-edge penetrations between the deformable sheet and the tool. Coefficients of friction between punch-to-carrier blank, carrier blank-to-test blank (Teflon) and die-to-blank were chosen as 0.05, 1.2 and 0.5, respectively based on previous works of Zhang et al. (2009).

$$F_f = \mu \cdot F_N \quad (4.2)$$

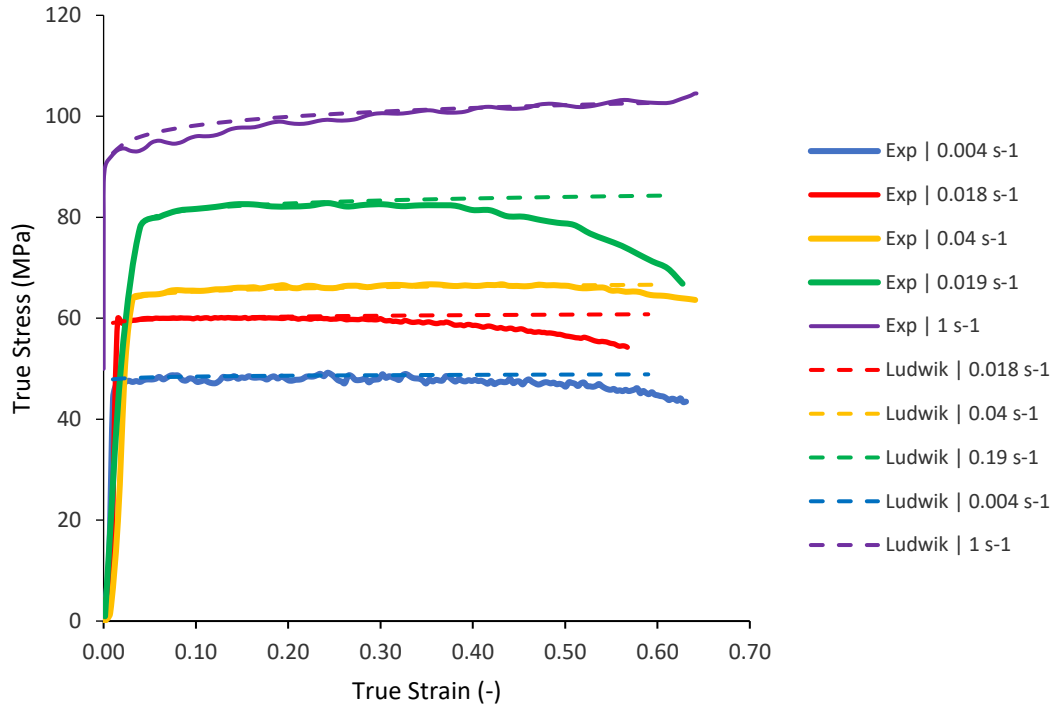


Figure 4.3.1 Ludwik equation fitted to experimental tensile data at 400°C

Table 4.3.1 Ludwik equation fitting parameters

Strain Rate	<b>1 s<sup>-1</sup></b>	<b>0.19 s<sup>-1</sup></b>	<b>0.04 s<sup>-1</sup></b>	<b>0.018 s<sup>-1</sup></b>	<b>0.004 s<sup>-1</sup></b>
<b>Yield Strength, <math>\sigma_y</math></b>	93.5 MPa	80.5 MPa	64.5 MPa	58 MPa	47.5 MPa
<b>Strength Coefficient, <math>K</math></b>	105 MPa	82.5 MPa	67 MPa	60 MPa	49 MPa
<b>Strain hardening exponent, <math>n</math></b>	0.025	0.015	0.01	0.007	0.005

The material was assumed to follow Von Mises isotropic yield criterion of the form shown in Equation 4.3 where  $\sigma_1$ ,  $\sigma_2$ , and  $\sigma_3$ , represent principal stresses.

$$\sigma = \left[ \frac{1}{2}(\sigma_1 - \sigma_2)^2 + \frac{1}{2}(\sigma_2 - \sigma_3)^2 + \frac{1}{2}(\sigma_1 - \sigma_3)^2 \right]^{\frac{1}{2}} \quad (4.3)$$

And the hardening law obeys Prandtl-Reuss associative flow rule:

$$d\varepsilon_p = d\lambda \frac{\delta f}{\delta \sigma} \quad (4.4)$$

where  $d\varepsilon_p$ ,  $d\lambda$ , and  $\frac{\delta f}{\delta \sigma}$  refer to the plastic strain increment, plastic multiplier, and increment in the yield function with respect to current flow stress.

#### **4.4 Boundary Conditions**

Application of boundary conditions is critical in ensuring that the model follows the experimental conditions of the laboratory set-up. Figure 4.4.1 shows the various boundary conditions applied to the FE model. The BC's applied through each of the models are similar, and therefore, only the boundary conditions associated with the plane strain model are presented below, for brevity. In the ABAQUS FE code, for parts defined as rigid, all elements refer to a master node known as a reference point (RP). Also, the displacements U1, U2, U3 correspond to the displacements in X, Y, and Z directions respectively. The references points are shown in Figure 4.4.1 on the right side of the model for the upper die, lower die and punch. Although the experimental Marciniak test method utilized a lock-bead to clamp the test blank, it was not included in the present FE models as it added a significant amount of unstable kinetic energy to the system upon application of mass scaling. Instead, in the model, the encastre BC was applied to the outer edges of the carrier and test blanks to avoid any movement or drawing in of the blank from the outer edges. Also, the upper and lower dies were constrained

with encastre BC in which all axes and rotations were fixed ( $U_1 = U_2 = U_3 = UR_1 = UR_2 = UR_3 = 0$ ). The punch was applied with a velocity BC in the Y direction and was fixed in all directions for the initial step. It was later applied with a smoothed ramp up step, reaching the same velocity of 2.4 inch/minute as in experimental testing. This acceleration was applied over 3 seconds to minimize contact instability in the in model. Without the smoothed step, mass scaling proved ineffective due to instabilities.

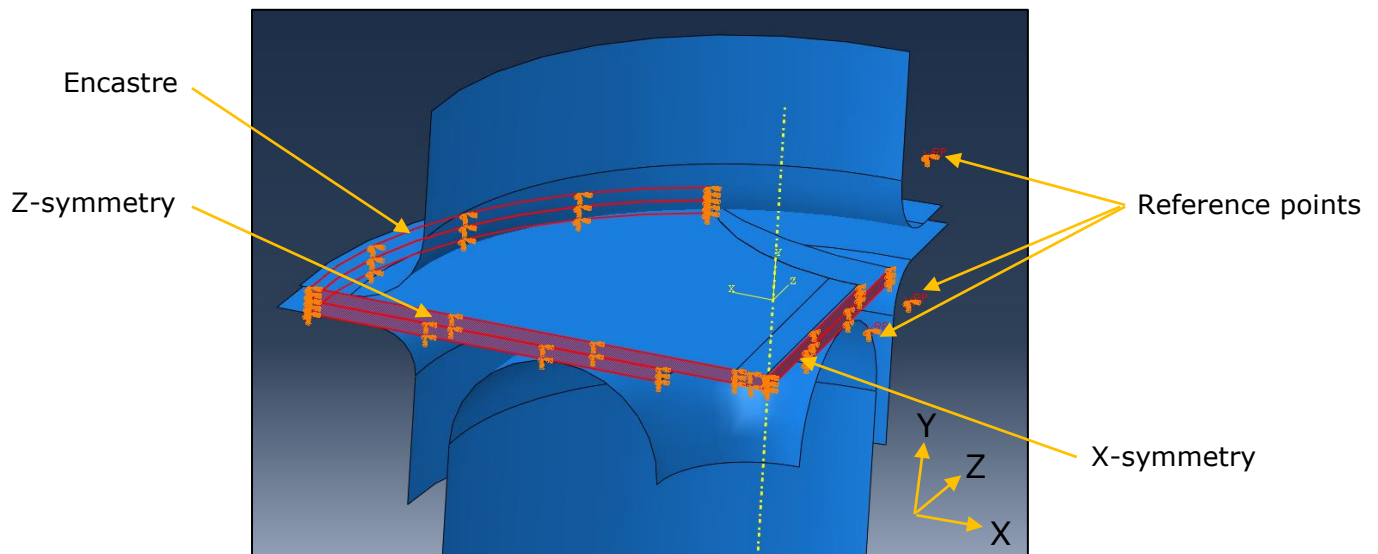


Figure 4.4.1 ABAQUS finite element model boundary conditions for plane strain condition

Boundary conditions seen in red were also applied to the edges of the carrier and test blanks. Along the X-Y plane both carrier and test blank had Z-symmetry applied ( $U_3 = UR_1 = UR_2 = 0$ ). Similarly, along the Y-Z plane both blanks had X-symmetry applied ( $U_1 = UR_2 = UR_3 = 0$ ).

## 4.5 Meshing

It is well known that the size of mesh greatly affects the computation cost and accuracy of the results in a model. Due to the geometry of the model it was possible with careful planning to mesh all blanks with structured hexagonal elements as these elements are well known for their ability to produce accurate results compared to tetrahedral elements which can experience locking phenomenon. The C3D8R 8-node linear brick elements with reduced integration and enhanced hourglass control were utilized in all simulations. A mesh study was completed to balance computation time and accuracy. A mesh of 5 elements through the thickness of the sheet was used to accurately capture bending in the model. Mesh size varied throughout the model, increasing as it approached the non-critical clamping area. Mesh in the area of interest was  $0.4 \times 0.4$  mm to capture necking phenomenon where it transitioned to a global mesh size of 1 mm towards the clamping region; corresponding to a total of 20,489 elements used to construct the plane strain model.

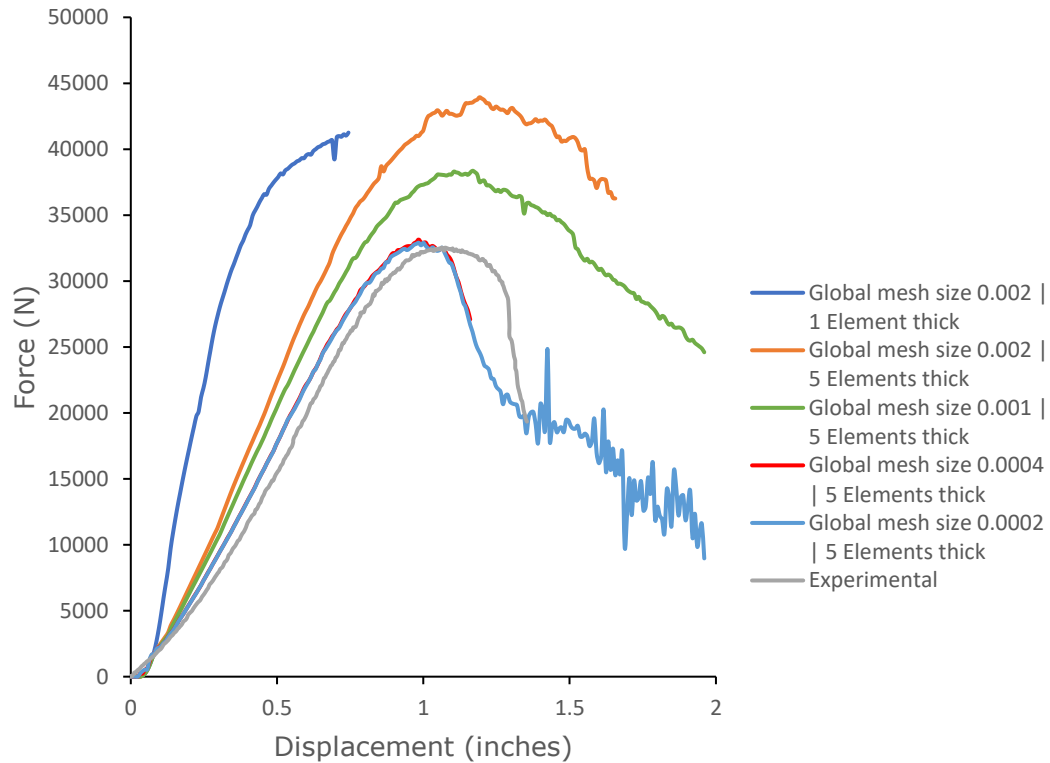


Figure 4.5.1 Effect of element size on punch force versus displacement of plane strain model

Figure 4.5.1 shows the progression of the mesh study showing a relationship between punch force versus punch displacement. Initial meshes corresponded to 0.002 m global mesh size with a 1 element through thickness which amplified forces and did not capture bending stresses. As global element size decreased results began to converge to experimental test also shown in Figure 4.5.1. A mesh size of 0.0004 m was deemed acceptable for further tests to accurately capture the system dynamics as it was the largest mesh that converged with experiments. It also showed the least amount of noise, where mesh sizes of 0.002 m became unstable after necking. Mesh size of 0.0002 m shows a largely unstable system after a punch displacement of 33

mm which was acceptable as the system dynamics under investigation had already been captured.

## **4.6 Mass Scaling**

Mass scaling proved to be extremely important in the FE simulation of Marciniak test as discussed below. With no mass scaling applied, computational time increased to over a week and appeared unrealistic in terms of the overall scope of the modeling work. Typically, models can have their time scaled to take place in a fraction of a second, even if the actual event is much longer when strain rate dependent materials are not used. Essentially having the same effect as mass scaling. However, when strain rate effects are taken into consideration like in the proposed model, this approach is unsatisfactory. Therefore, the entire time period of simulation of forming of a test blank, up to 45 seconds, was required to be calculated and significant mass scaling was necessary. Mass scaling factors up to 100,000 were applied to the plane strain model case and analyzed for ratio of kinetic to internal energies; often an indicator of a systems stability and the impact of inertial effects of mass scaling. Figure 4.6.1 shows even with the highest mass scaling factor that kinetic energies only surpass the suggested 10% for a very small increment of forming and could be ignored.

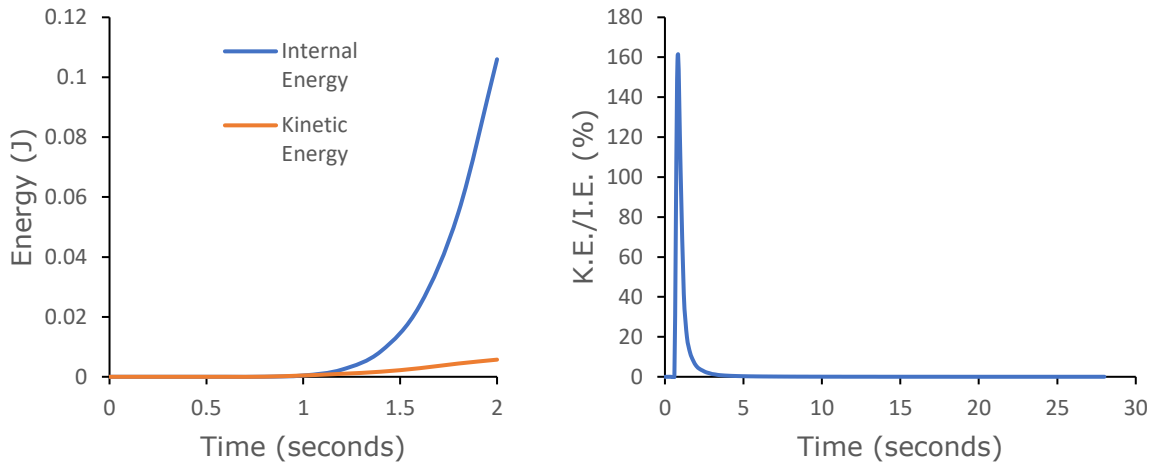


Figure 4.6.1 Plane strain model with mass scaling factor of 100,000 showing, (a) a comparison of kinetic and internal energy contributions as a function of forming process time, and (b) ratio of kinetic/internal energies

## 4.7 Modelling Data Analysis Methodology

Several parameters were analyzed in the simulation of Marciniak tests including force versus displacement curves of the punch, kinetic versus internal energy, strain distribution over the unsupported test blank region, and limit strains.

The punch force versus displacement response of the model was compared to experimental response at 400°C for similar cases. Force data was taken from the model through field output data at the punch reference point, which encapsulates the force felt by the entire punch. Since the model was a quarter geometry, this force was multiplied by four to compare with the experiments.

Model kinetic versus internal energies are also important as the strain energy in the part must be significantly larger than the kinetic energy imposed

by inertial forces from the mass scaling effects. Since kinetic and internal energies of the model output only that of the instances with associated mass, only the blanks were taken into consideration.

As previously discussed, limit strain can be calculated in a variety of ways. However, since no fracture criteria was implemented in the model, it was not possible to use the position-dependent method as it analyzes the strain distribution directly after fracture has occurred. Therefore, the time-dependent method was used.

## Chapter 5

# Results and Discussion

This chapter presents the experimental and simulation results. It is divided into six sub-sections which cover the following test results and associated discussion in a sequential order: elevated temperature tensile tests, Marciniak tests, post-deformation sample surface features, post-fracture microstructural damage on Marciniak test samples, FE simulation results on Marciniak test sample geometries and hot stamping trial results.

### 5.1 Uniaxial Tensile Test Results

As previously mentioned, tensile testing of AA7075-F was completed using the 250 kN MTS 810 hydraulic tensile frame at various temperatures and test speeds. The result in the form of true stress – true strain curves for 300°C, 400°C and 500°C are shown in Figures 5.1.1, 5.1.2 and 5.1.3 respectively. The effect of test speed (or initial strain rate) and the strain softening was more pronounced at 300°C compared to the two higher temperatures. The stress strain data at 400°C was used as input for the FE model. Additional uniaxial tensile test data obtained with Gleeble thermo-mechanical simulator at Novelis at strain rates  $0.1 \text{ s}^{-1}$ ,  $1.0 \text{ s}^{-1}$  and  $5 \text{ s}^{-1}$  are presented in Appendix B at the end of the thesis. The general trends in the shape of the stress strain curves showed that more softening of the material occurred at 300°C compared to at 400°C and 500°C possibly due to its higher dislocation density and dynamic recovery. Flow stress decreased with increase

in temperature and increased with increase in the test speed (or strain rate). This is consistent with thermally activated flow at elevated temperatures in AA7075-F sheet. Some softening occurred in tests conducted at all test speeds at 300°C in the in-house tests whereas work hardening was achieved at all strain rates at 300°C in Novelis Gleeble tests. This is due to difference in test setup when using Gleeble testing as samples were solutionized before being cooled to the test temperature and subsequent testing.

Guo et al. (2018) tested Al-Zn-Mg-Cu alloy between RT and 400°C and observed strain softening at 200°C; with a competition between work hardening (WH), dynamic recrystallization (DRX), and dynamic recovery (DRV) making this the transition temperature for the alloy with WH dominating below, and DRX/DRV above.

In the present work, significant strain softening was observed at higher test speeds (or higher initial strain rates) at 300°C while stress saturation occurred at the lower range of initial strain rates at the same temperature. However, the extent of softening was remarkably less for temperatures of 400°C and 500°C for all initial strain rates. The strain at fracture of the samples between strain rates was subject to a larger variance in the 300°C when compared with other test temperatures.

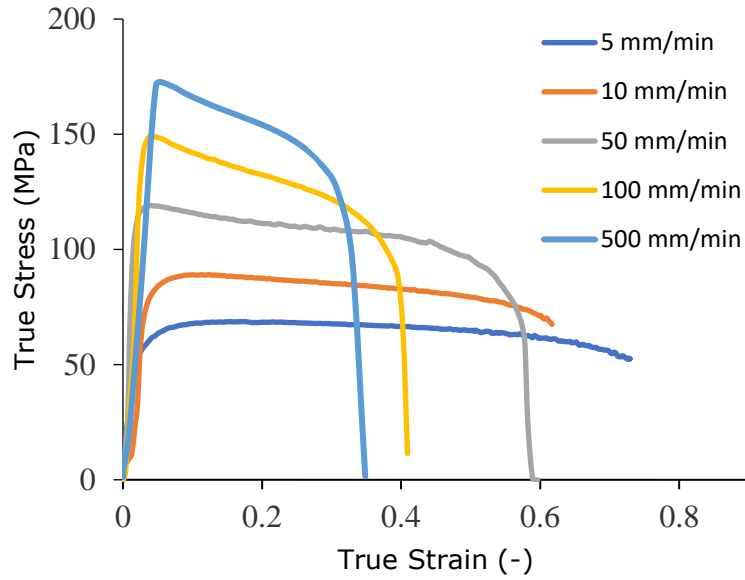


Figure 5.1.1 Effect of test speed on true stress versus true strain for AA7075-F at 300°C

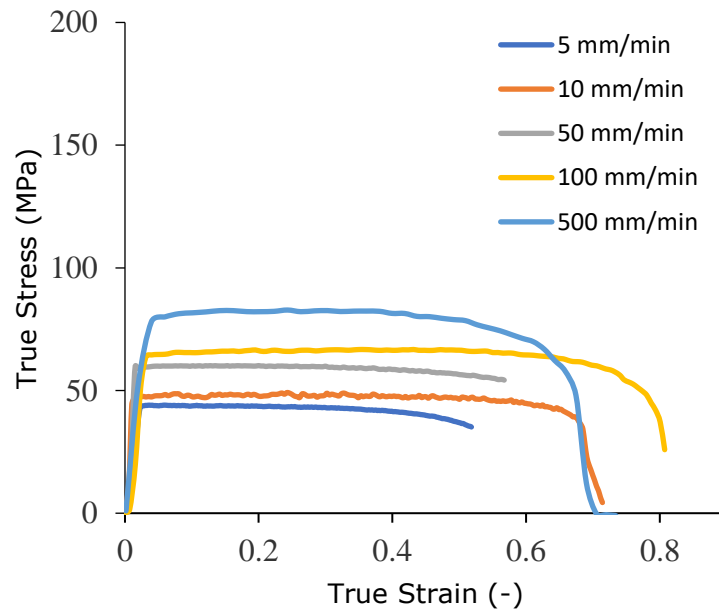


Figure 5.1.2 Effect of test speed on true stress versus true strain for AA7075-F at 400°C

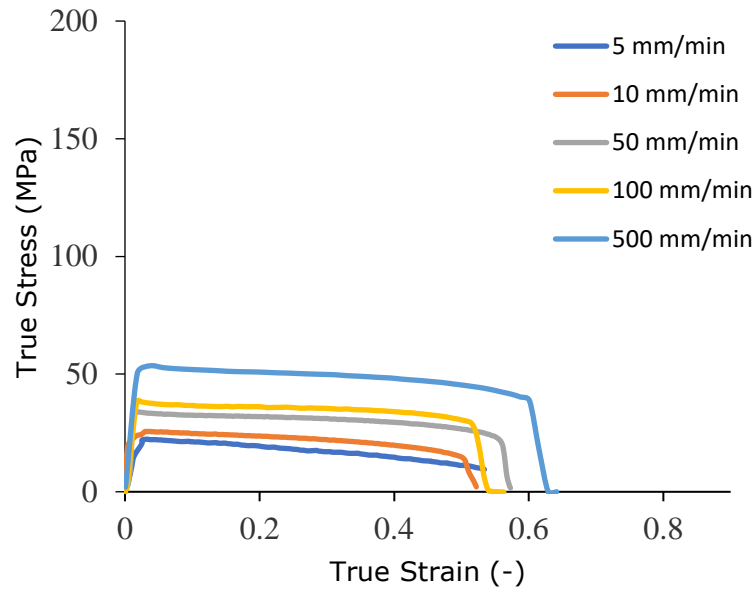


Figure 5.1.3 Effect of test speed on true stress versus true strain for AA7075-F at 500°C

## 5.2 Marciniak Test Results

### 5.2.1 Load versus displacement

The continuously recorded punch load versus displacement traces during the Marciniak test for all specimen geometries can be seen in Figures 5.2.1, 5.2.2, and 5.2.3. All data was calibrated to compensate for the weight of the punch and load cell so that all loads are solely due to material deformation. Figures show an initial gradual increase in punch load to an inflection point (i.e., the point of curvature reversal). Up to this point the load rate increases and beyond which the load rate starts to decrease until a load maximum is reached and subsequent fracture of the specimen occurs. Specimen geometries above 3-inches typically experience a maximum punch load before fracture occurs. In these cases, the maximum load can be

attributed to lower punch load needed once carrier blank hole reaches a critical value of expansion. The 3- and 4-inch specimen geometries tend to show a larger punch load than expected but like other blanks that used a driver were expected to result in higher punch forces than 1-inch samples and below. In the 350°C and 400°C case the 4-inch sample experiences a larger load than the 5- and 7.5-inch geometries. This can be attributed to a locking phenomenon, where the carrier blank material is pushed into the open area of the test blank, creating a stiffer dynamic and a higher punch load (Figure 5.2.4). Much lower punch loads were consistent with the results of the uniaxial tension testing, in that a load drop in the Marciniak test and a flow stress drop in the uniaxial tension test occurred with an increase in temperature. It is to be noted that the direction of applied stress was in the TD direction during testing.

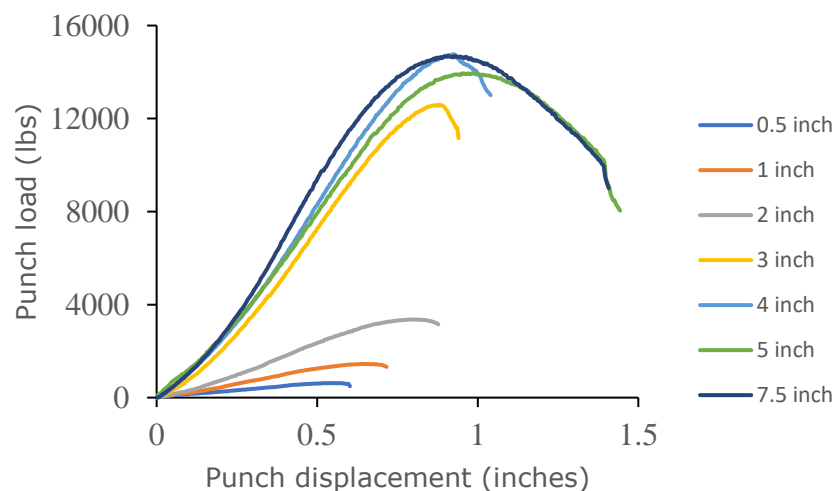


Figure 5.2.1 Punch load versus displacement traces from Marciniak tests at 300°C for specimens of various widths

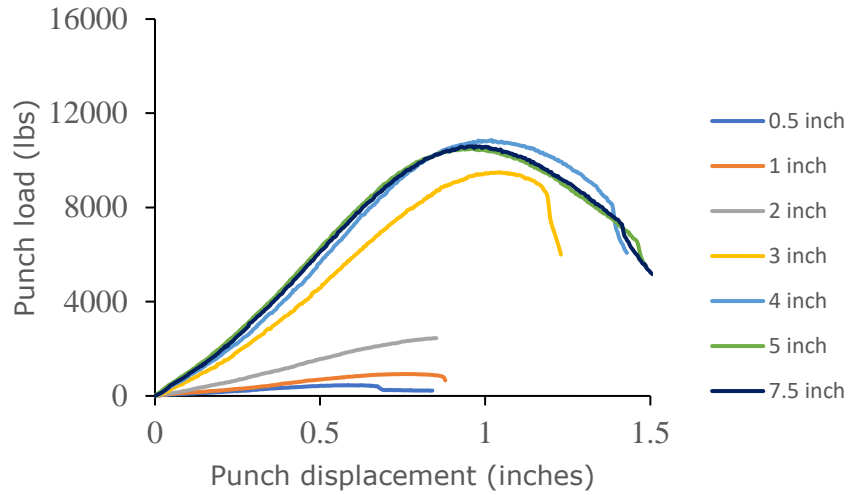


Figure 5.2.2 Punch load versus displacement traces from Marciniak tests at 350°C for specimens of various widths

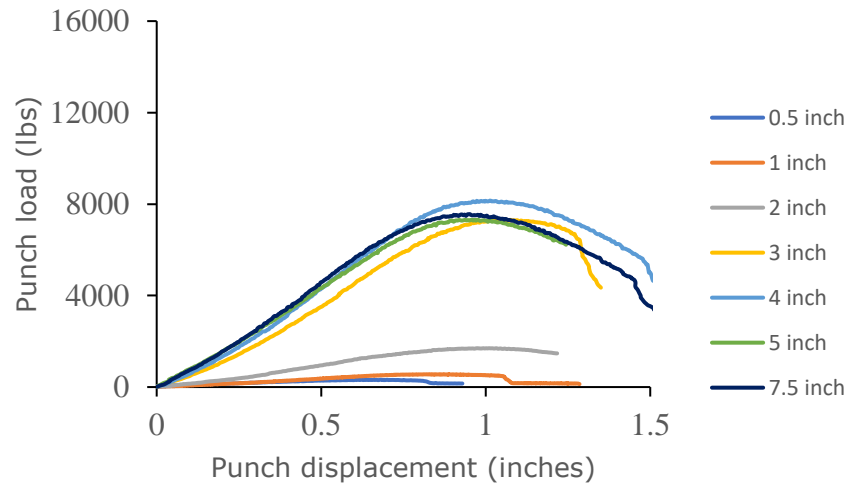
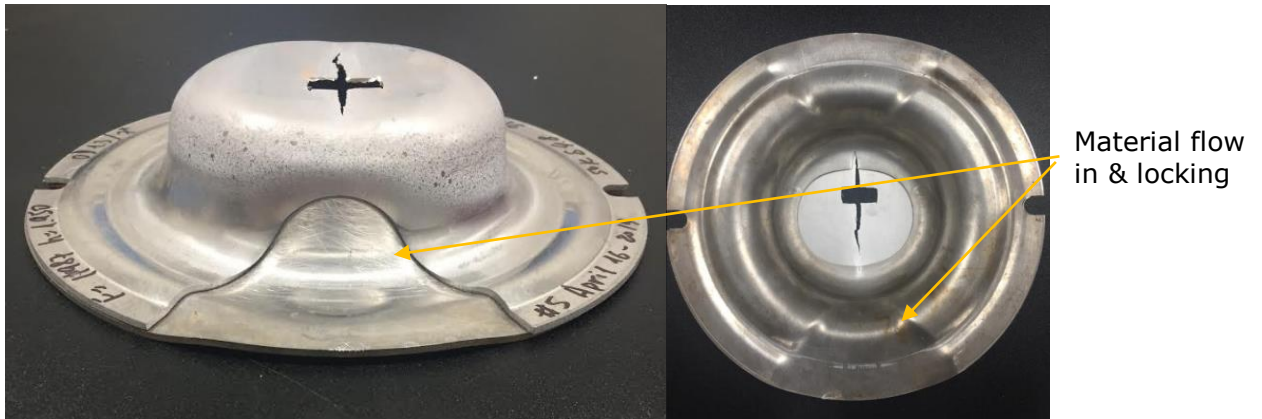


Figure 5.2.3 Punch load versus displacement traces from Marciniak tests at 400°C for specimens of various widths



*Figure 5.2.4 Material flow-in and locking causing increase in punch forming force. Rectangular shaped cut-out at the centre of the specimen is from removal of material for microstructural observation*

## **5.2.2 Deformed Sample Geometries**

Photographs of various Marciniak deformed samples corresponding to different strain paths from tests carried out at 300°C, 350°C and 400°C are presented in Figure 5.2.5. All the test samples exhibited crack formation in the unsupported flat region near the center of the test specimen. The specimen height was measured using the Aramis (DIC) software, where specimen height data was taken from the image frame just before fracture. The dome height at fracture versus sample width are shown in Figure 5.2.6 for a set of samples shown in Figure 5.2.5. A trend towards saturation in dome height at fracture can be observed at each test temperature. An increase in specimen height was evident moving from uniaxial tension to balanced biaxial tension (left to right) as well as from 300°C to 400°C.



Figure 5.2.5 Deformed Marciniak test samples; sample geometry from uniaxial tension to balanced biaxial tension (left to right) and 300°C to 400°C (top to bottom)

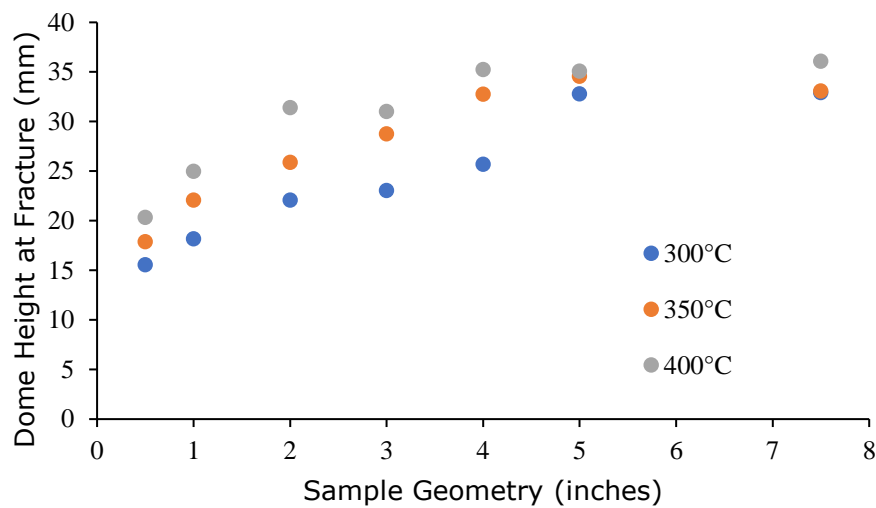


Figure 5.2.6 Dome height taken from image before fracture showing effects of temperature and specimen geometry

### 5.2.3 Full-field Strain Distributions

The full field strain data obtained through Aramis DIC based strain analysis is presented in Figures 5.2.7 – 5.2.9. These figures show typical localization in the stages before fracture as observed in the principal strain direction. As expected, and required for a successful test, strain localization

occurs in the unsupported centre of the flat region in the Marciniak testing setup. The increase in temperature resulted in an increase in maximum major strain value for all geometries. Also, localized necking was more pronounced with the increase in temperature, and especially for the uniaxial strain path geometry, perhaps due to higher strain rate sensitivity (or  $m$ -value) exhibited by AA7075 with increasing temperature as observed by Guo et al. (2018).

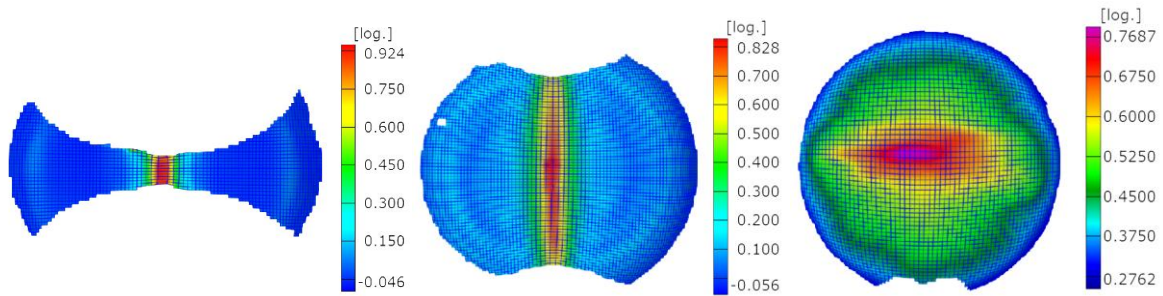


Figure 5.2.7 Full-field strain plot overlay on deformed Marciniak specimen geometries showing major logarithmic strain components of uniaxial, plane strain and biaxial tension test specimens (left to right) at 300°C. Maximum strain corresponds to central region of full-field strain distribution.

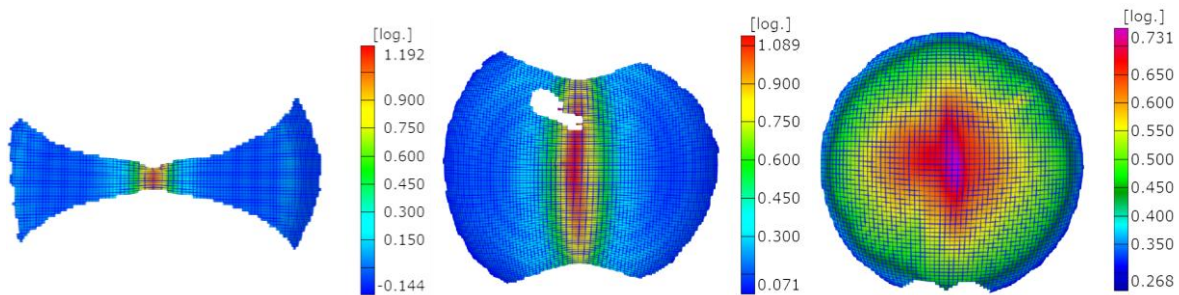


Figure 5.2.8 Full-field strain plot overlay on deformed Marciniak specimen geometries showing major logarithmic strain components of uniaxial, plane strain and biaxial tension test specimens (left to right) at 350°C. Maximum strain corresponds to central region of full-field strain distribution.

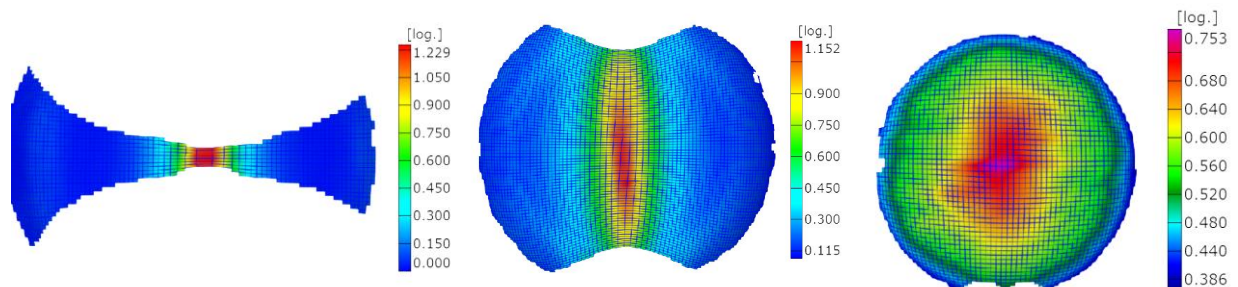


Figure 5.2.9 Full-field strain plot overlay on deformed Marciniak specimen geometries showing major logarithmic strain components of uniaxial, plane strain and biaxial tension test specimens (left to right) at 400°C. Maximum strain corresponds to central region of full-field strain distribution.

## **5.2.4 Strain Paths and Necking Characteristics**

Sample strain paths were extracted from the region of each of the specimens that eventually became the site of the neck formation and fracture. The strain paths are plotted for each of the tested blank geometries at each of the three test temperatures in Figures 5.2.10 - 5.2.12. Strain paths were observed to be linear for the most part other than for the 4-inch geometry which showed a minor inflection. This is in good correlation with expected results as linear strain paths tend to occur when using the in-plane forming methodology. The deviation towards biaxial strain path seen in the 4-inch sample could be due to the increasing contact forces observed as the test progressed and oversized carrier blank. Friction forces increase as a result of increased contact, forcing the test blank to follow the path of the carrier, which tends towards the biaxial strain path.

Strain paths of 0.5-, 1-, 2- and 3-inch geometries tended to cluster together on the tension-compression side of the FLD while paths of 4-, 5- and 7.5-inch geometries tended to cluster on the tension-tension side. Leaving a large region from plane strain towards balanced biaxial tension where limited data was provided. Additional test geometries such as 3.5-inch should be tested in the future to firmly establish the FLD shape in this region.

Strain paths on the left-hand side corresponding to uniaxial tension show separation towards plane strain as local necking occurred while those on

the right-hand side such as for balanced biaxial tension strain path show only a very slight (or incomplete) or drastic transition towards the plane strain state. This will be further discussed later when presenting the various fracture limit curves.

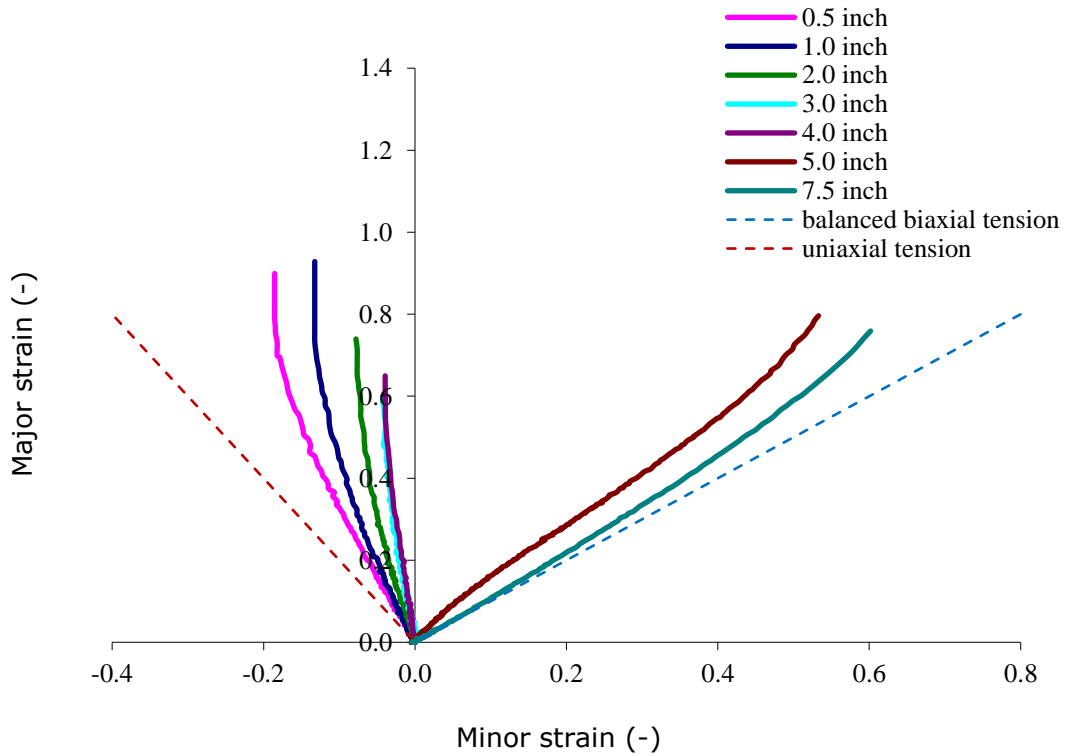


Figure 5.2.10 Marciniak sample strain paths at 300°C of a material point in the neck region

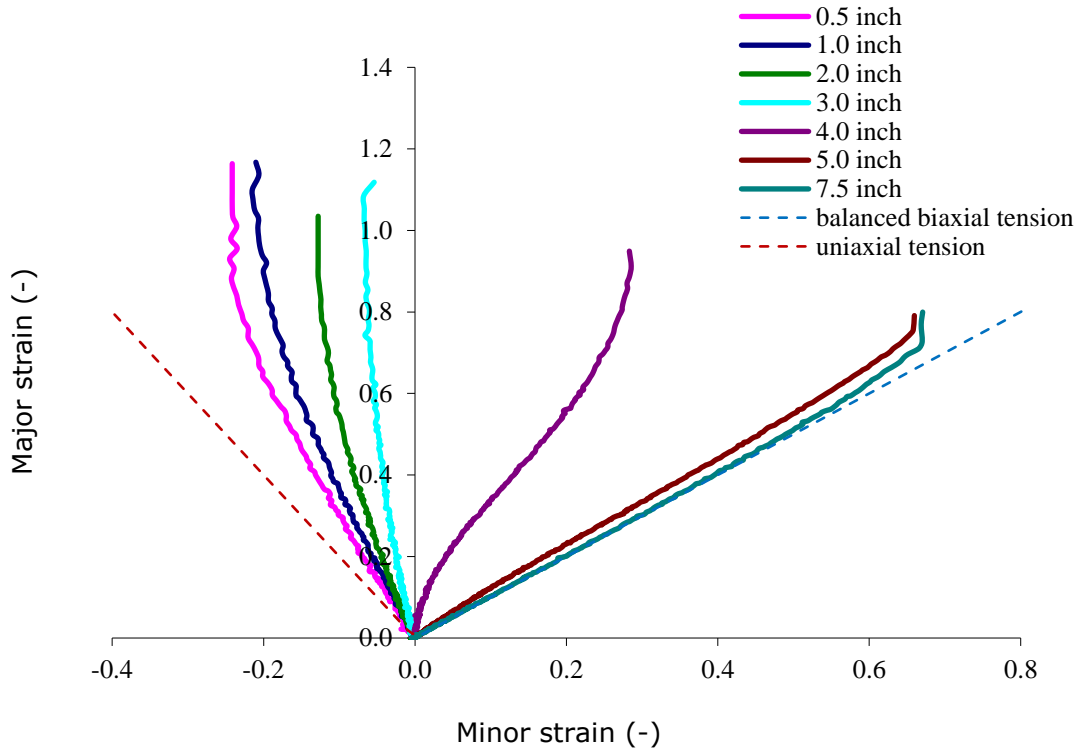


Figure 5.2.11 Marciniak sample strain paths at 350°C of a material point in the neck region

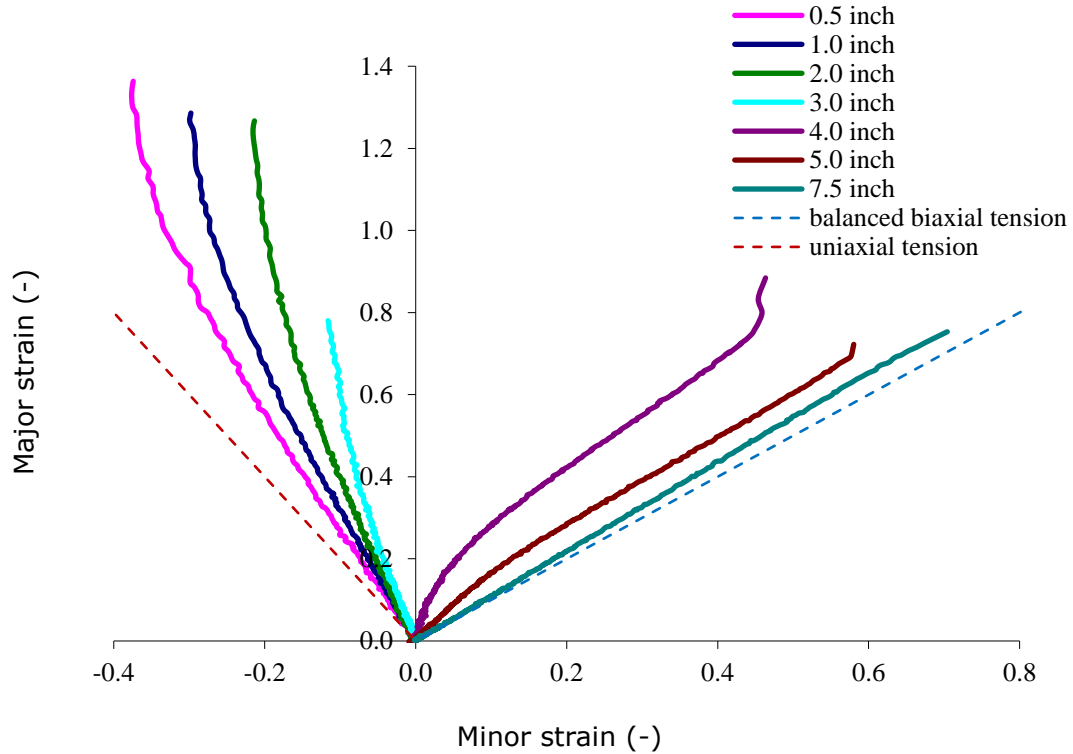


Figure 5.2.12 Marciniak sample strain paths at 400°C of a material point in the neck region

## 5.2.5 FLDs at Elevated Temperatures

The forming limit strains were determined based on ISO 12004-2:2008 methodology and using Bragard’s method for capturing the strain gradient in the localized neck, as discussed earlier in Chapter 3. The curve fitting used in Bragard’s method is shown for 3 different strain paths at 300°C only for illustrative purposes (Figures 5.2.13 – 5.2.15).

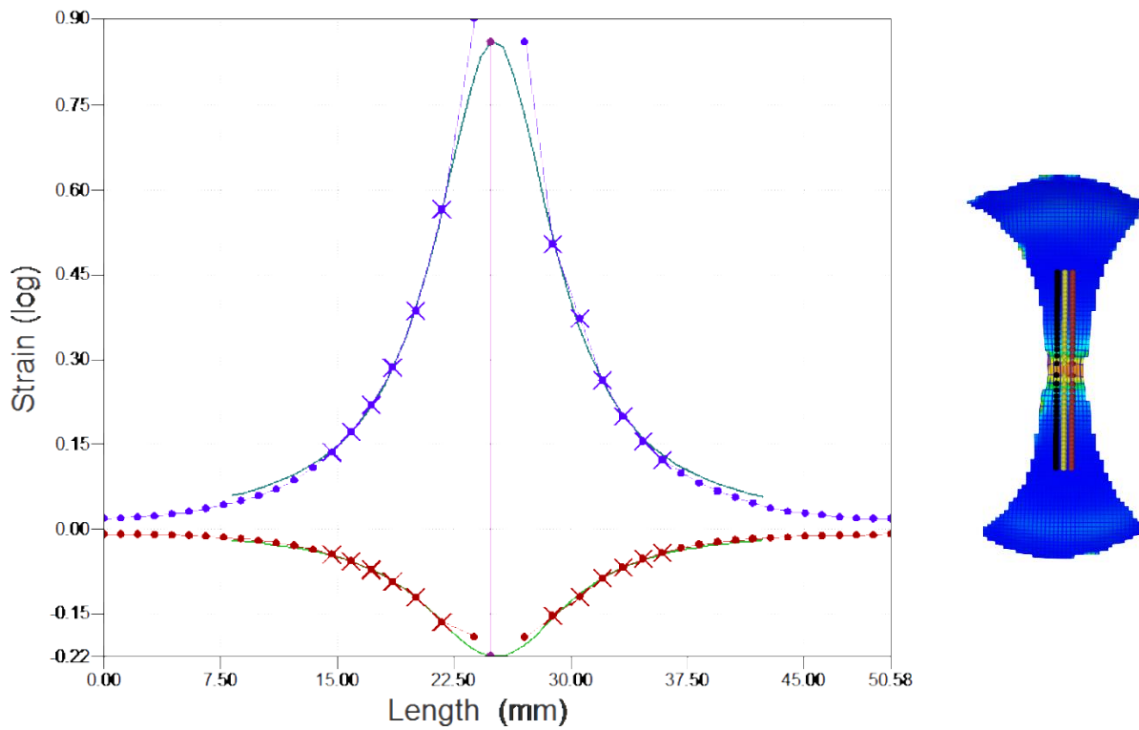


Figure 5.2.13 Bragard’s method applied to a Marciniak sample having undergone uniaxial strain path (0.5-inch wide geometry) showing fitting to one section line (left). Positioning of 3 section lines for capturing strain gradient along sample (right)

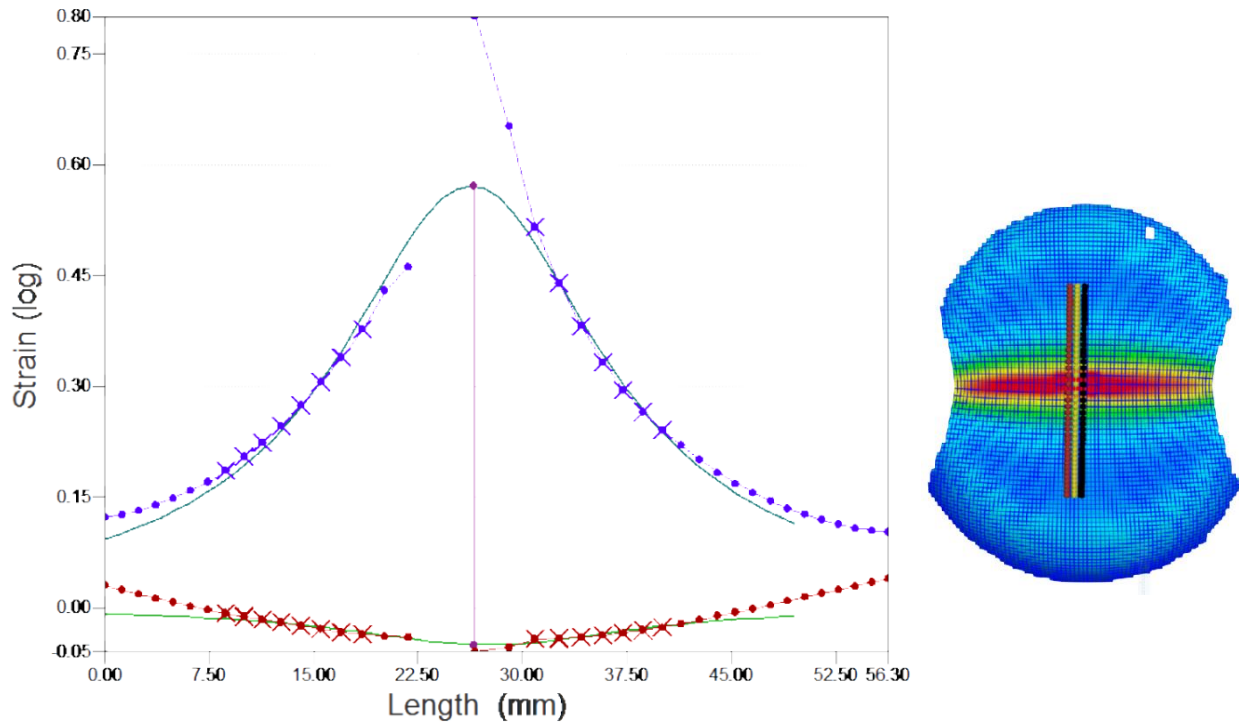


Figure 5.2.14 Bragard's method applied to a Marciniak sample having undergone plane strain path (3-inch wide geometry) showing fitting to one section line (left). Positioning of 3 section lines for capturing strain gradient along sample (right)

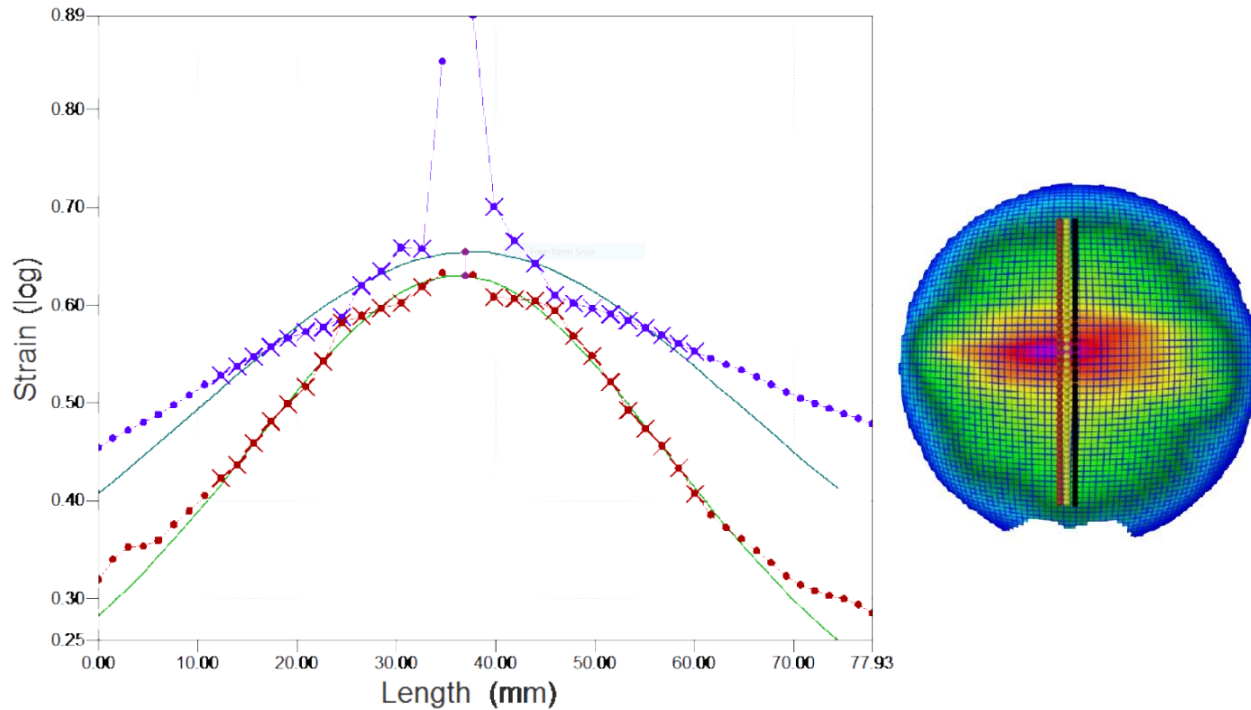


Figure 5.2.15 Bragard's method applied to a Marciniak sample having undergone biaxial strain path (7.5-inch wide geometry) showing fitting to one section line (left). Positioning of 3 section lines for capturing strain gradient along sample (right)

Figure 5.2.16 shows data points for all strain paths and temperatures with corresponding fitted forming limit curves. Fitting was completed on the left-hand side of the FLD through data points, extending the fit line to approximately plane strain. Due to the minimal amount of data on the right-hand side of the FLD lines were linearly interpolated from this point.

An increase in formability can be observed in the FLCs as temperature increases from 300°C to 400°C. This increase is more pronounced on the left-hand side of the FLD where temperature increase appears to have a near proportional effect on limiting strain increase. However, on the right-hand side of the FLD there appears to be only a marginal increase in major limit strain when moving from 300°C to 400°C. It is difficult to draw conclusion on the shape of the FLC on the right-hand side due to the lack of data between plane and balanced biaxial strain paths.

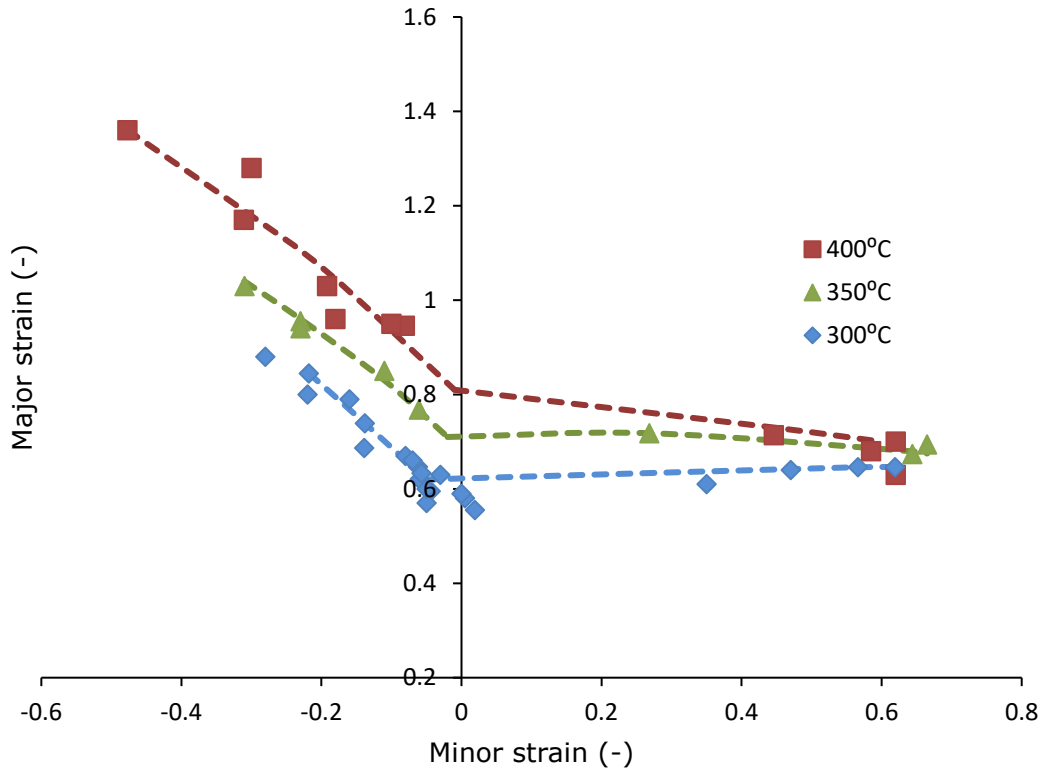


Figure 5.2.16 Marciniak (in-plane) forming limit curves for AA7075-F at elevated temperatures

### 5.2.6 Fracture Limit Curves at Elevated Temperatures

The fracture limit curves were also determined using the methodology described in Chapter 3 (sub-section 3.4.3). The fracture limit curves are also referred to as fracture forming limit diagram (or FFLD) and appear as dashed lines with symbols corresponding to experimental data points, in Figure 5.2.17. As shown, FFLD were mostly straight lines with a negative slope. In other words, the fracture limit decreased with increased biaxiality of the strain path. This was consistent with void damage observations, to be presented later. The earlier FLDs from the previous sub-section are also included in Figure 5.2.17. The intersection of the two sets of curves under balanced biaxial

strain path demonstrate the competition between the localized necking and ductile fracture processes for this strain path. Again, this was consistent with the microstructural damage observations as presented later.

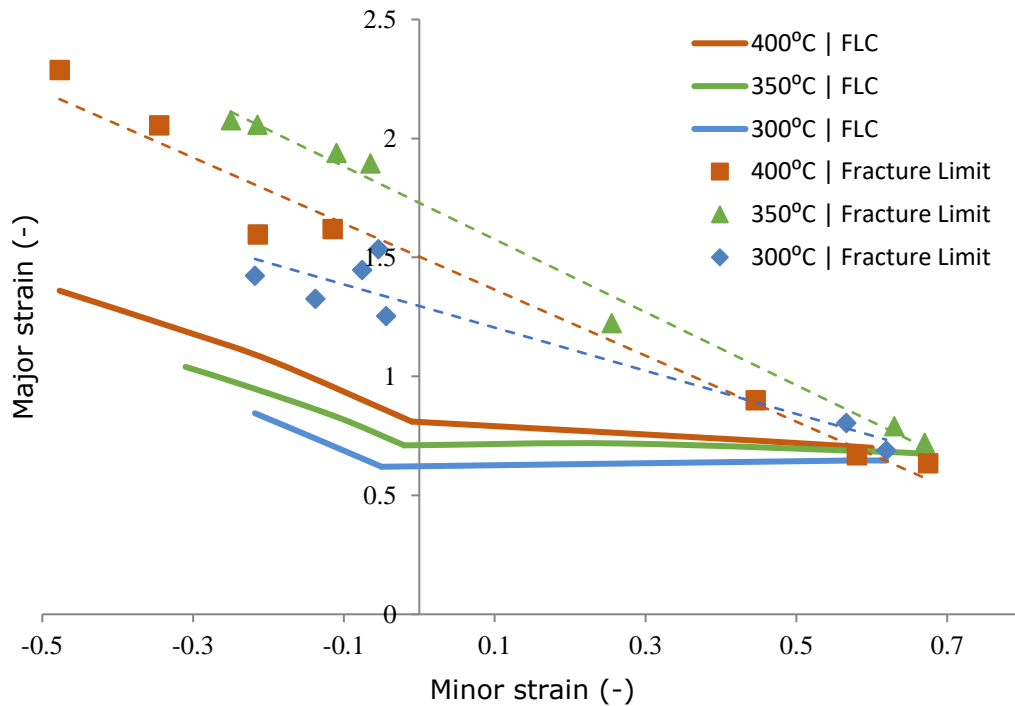


Figure 5.2.17 Fracture forming limit diagram (FFLD) and FLC for elevated temperatures

It should be noted that the major fracture strains were considerably higher than the necking limit strains for all strain paths on the tension-compression side and reflect the extent of localized necking, under plane strain path transition, prior to fracture. However, the fracture limit strains were lower at 400°C compared to 350°C on the tension-compression side and slightly lower than for 300°C and 350°C for balanced biaxial tension strain path. This can be explained by analyzing the void fraction in the sectioned fracture samples. Since a large amount of voiding occurred under balanced biaxial tension and at 400°C, the assumption of volume constancy became

increasing inaccurate at higher temperatures for obtaining the fracture limit values. In other words, the fracture limit values under balanced biaxial strain path as presented in Figure 5.2.17 represent an under-estimation of the major strain as the representative volume is smaller than portrayed due to void formation. Since void fraction increases towards 400°C and biaxial strain states, these fracture limits will see the largest increase with all other fractures with voids present increasing but by lesser amounts. The presence of vast amounts of voids before fracture in AA7075-F sheet also suggests that fracture criteria based on nucleation and growth of voids such as from Gurson (1977) or from McClintock (1968) may be more appropriate in the calculation of the fracture strain limits.

The FLCs and FLCF for all temperatures clearly show an intersection of the two curves under balanced biaxial tension strain path. This is consistent with the observations on sectioned and polished LT sections of balanced biaxial tension strain path fractured test specimens showing little or no necking prior to fracture, as presented later.

### **5.2.7 Microstructural Damage from Deformed Samples**

The focus of the present work is on elevated temperature deformation of AA7075-F sheet. However, microstructural damage under room temperature deformation of a 0.5-inch wide AA7075-F specimen was also investigated. The damage was first characterized in the form of fractographic images of fractured specimens at different magnifications (50X to 5,000X) to

obtain baseline data for comparison with the data from elevated temperature Marciniak tests (see Figure 5.2.18). The lower magnification (50X) provided a general sense of fracture of the entire specimen whereas the highest magnification (5,000X) provided the best image of the individual void shapes and particles present inside many of them.

Figure 5.2.18 (column 1, from left) shows room temperature 50X magnification images that show what appears as brittle fracture with large faceted surfaces. However, at higher magnification of 2,500X and 5,000X (columns 3 and 4, from left) it becomes clear that fracture is ductile, and the voids are nucleated at the matrix-particle interface and grow during the straining process. At room temperature, the voids are expected to nucleate, grow and coalesce earlier due to poor ductility of the matrix phase and limited flow around the particles prior to fracture. Although it appears that most, but not all dimples have a corresponding precipitate (white region on backscatter images), it is likely that the mating half of the fracture surface contains precipitates in those dimples which appear to have linked catastrophically. Voids appear to primarily nucleate at particles consistent in size with that of constituent and dispersoid particles. This interpretation is consistent with that of Abachi et al. (2016) and Jordon et al. (2009) who observed fracture of 7075 alloy at room temperature in T651 temper. It should be noted that the fracture surface was angled at 45° to both the gauge width and gauge thickness during the room temperature test.

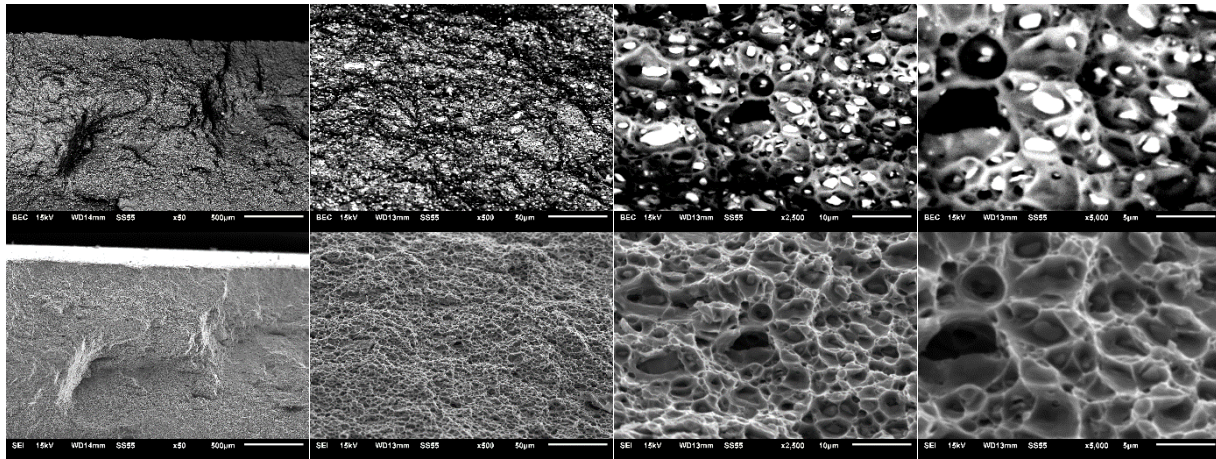


*Figure 5.2.18 0.5-inch width sample fracture surfaces of specimens deformed at room temperature (20°C) and observed at magnifications of x50, x500, x2,500 and x5,000 (left to right). Top and bottom rows of fractographic images of the same region were obtained under backscatter electron (BEC) diffraction and secondary electron (SEI) modes*

The fractographic images of fractured Marciniak test specimens subjected to uniaxial, plane strain, and balanced biaxial strain paths at 300°C, 350°C and 400°C, at four different magnifications, are shown in Figures 5.2.19 – 5.2.27. Figures 5.2.19-5.2.21 show fractographs of uniaxial, plane strain and balanced biaxial tension strain path samples respectively at 300°C. The fracture exhibits dimpled rupture commonly observed in metallic materials at large plastic strains. Voiding is similar to the earlier room temperature test, however, due to the increased matrix ductility at elevated temperature, the matrix phase flows around the precipitates easily and less precipitates are observed at the base of voids. It is possible the decrease in matrix strength could be attributed to dynamic recovery of the matrix at 300°C. A mix of large and small voids are observed at large magnifications with some evidence of stringer-like voids associated with similar particle distributions. Under balanced biaxial tension (Figure 5.2.21), the voids are smaller and more

uniformly distributed through the sheet thickness compared to the other two strain paths. There is more shearing of the voids which possibly led to void-sheeting and catastrophic fracture of the specimen.

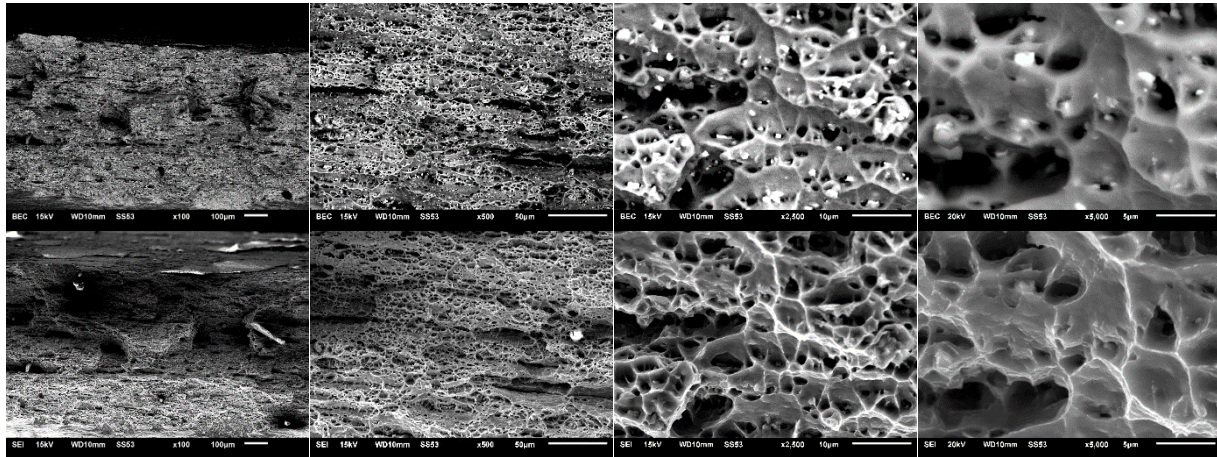


*Figure 5.2.19 0.5-inch width sample deformed at 300°C and observed at magnifications of x50, x500, x2,500 and x5,000 (left to right). Top and bottom rows of fractographic images of the same region were obtained under backscatter electron (BEC) diffraction and secondary electron (SEI) modes*

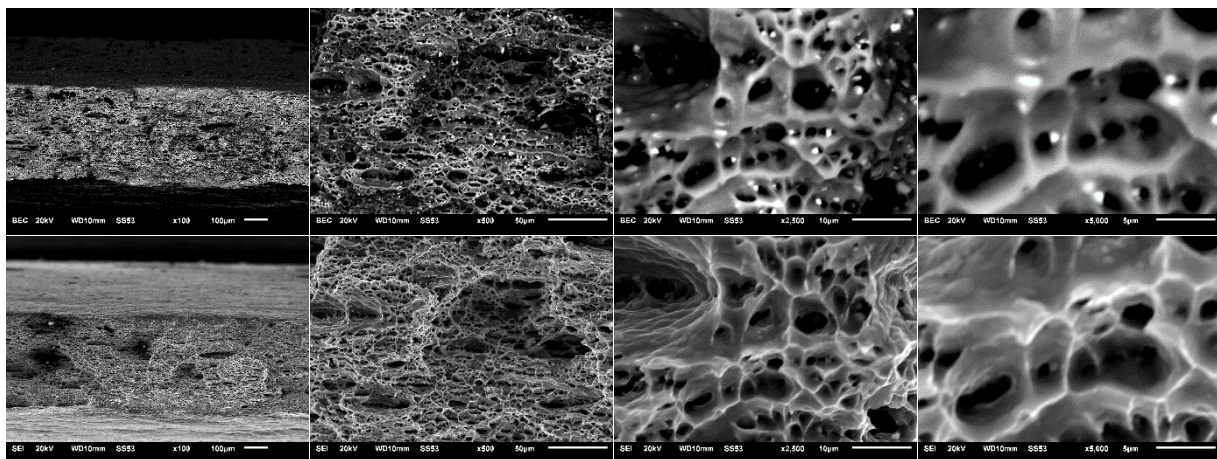


*Figure 5.2.20 3-inch width sample deformed at 300°C and observed at magnifications of x50, x500, x2,500 and x5,000 (left to right). Top and bottom rows of fractographic images of the same region were obtained under backscatter electron (BEC) diffraction and secondary electron (SEI) modes*

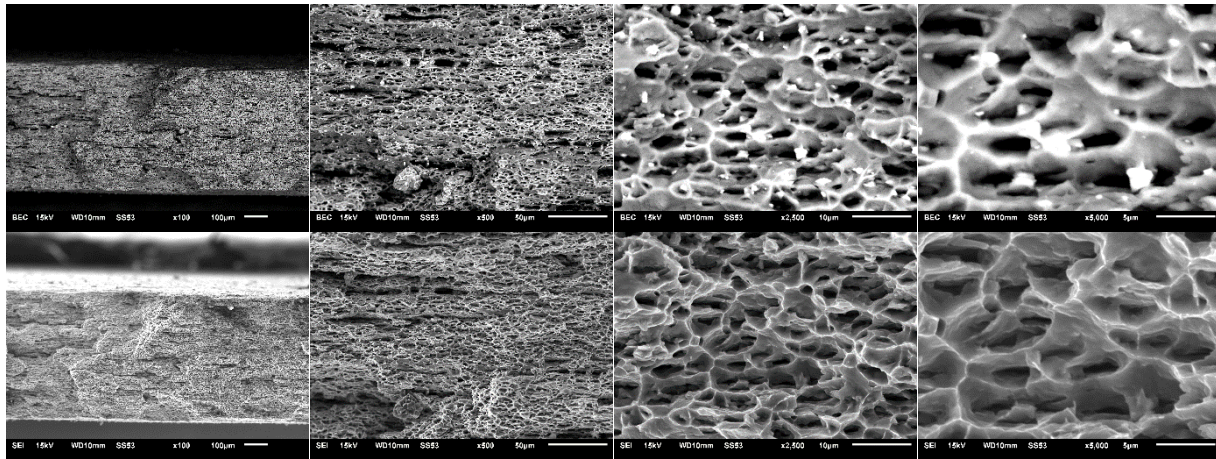


*Figure 5.2.21 7.5-inch diameter sample deformed at 300°C and observed at magnifications of x50, x500, x2,500 and x5,000 (left to right). Top and bottom rows of fractographic images of the same region were obtained under backscatter electron (BEC) diffraction and secondary electron (SEI) modes*

At the forming temperature of 350°C, void sizes increased for all strain paths relative to 300°C (see Figs. 5.2.22 - 5.2.24) possibly due to reduced matrix/particle decohesion strength, further increase in matrix plasticity, and reduced fraction of particles due to particle dissolution at higher temperatures. Also, possible grain recrystallization (and consequent increase in matrix plasticity) could play a role as noted by others, Mikó et al. (2013), Zhou et al. (2014) and Guo et al. (2018). However, more definitive evidence of grain recrystallization is needed in polished and etched LT sections of fractured specimens to be confident. There are some rather large voids present in the plane strain and balanced biaxial tension samples possible due to the coalescing of smaller voids.

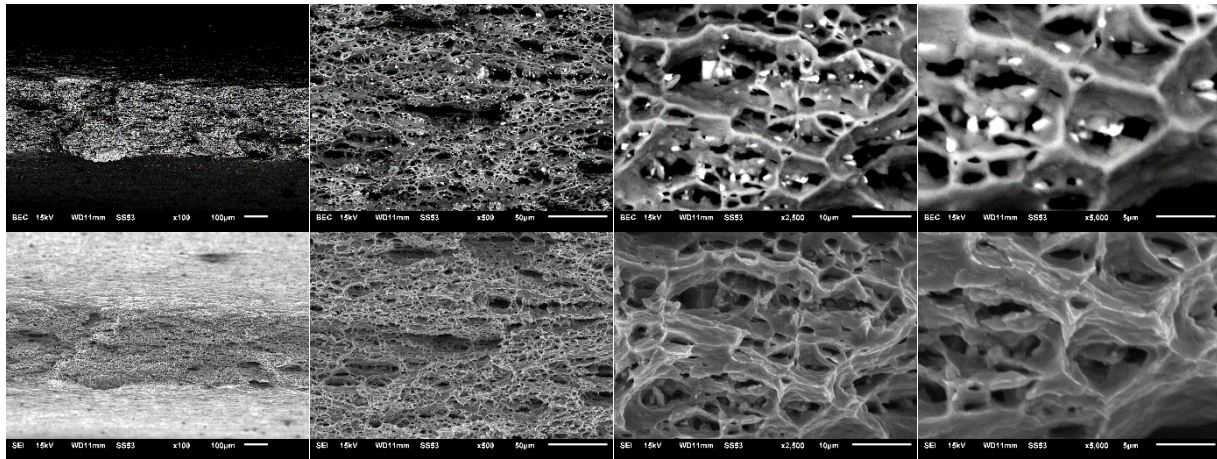


*Figure 5.2.22 0.5-inch width sample deformed at 350°C and observed at magnifications of x50, x500, x2,500 and x5,000 (left to right). Top and bottom rows of fractographic images of the same region were obtained under backscatter electron (BEC) diffraction and secondary electron (SEI) modes*

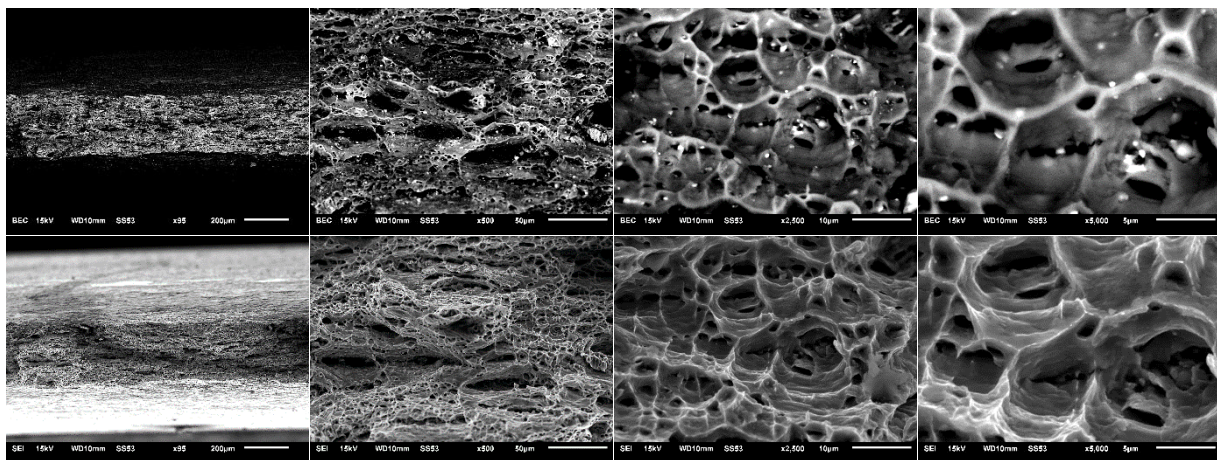


*Figure 5.2.23 3-inch width sample deformed at 350°C and observed at magnifications of x50, x500, x2,500 and x5,000 (left to right). Top and bottom rows of fractographic images of the same region were obtained under backscatter electron (BEC) diffraction and secondary electron (SEI) modes*

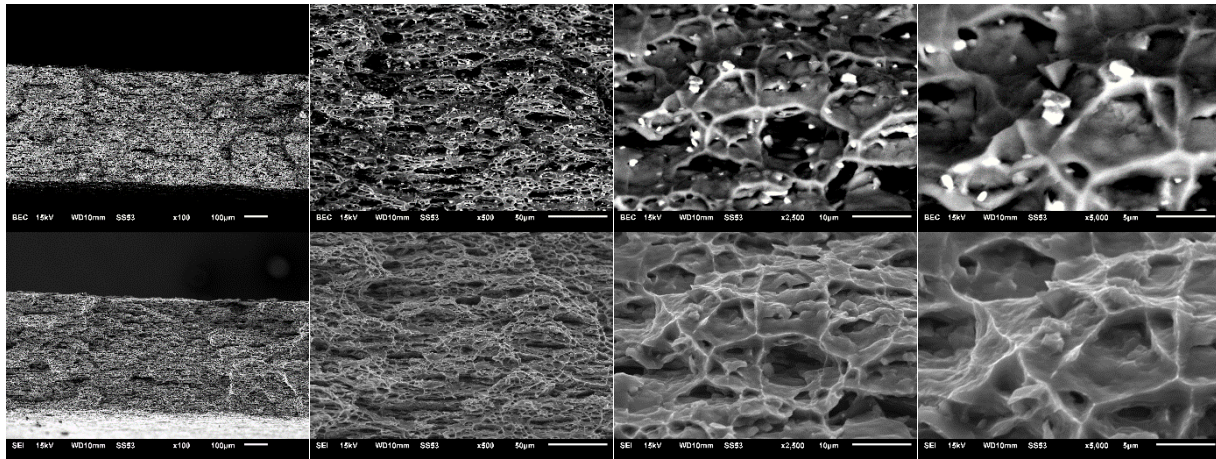


*Figure 5.2.24 7.5-inch diameter sample deformed at 350°C and observed at magnifications of x50, x500, x2,500 and x5,000 (left to right). Top and bottom rows of fractographic images of the same region were obtained under backscatter electron (BEC) diffraction and secondary electron (SEI) modes*

Figures 5.2.25 – 5.2.27 show fracture surfaces at 400°C for the same strain paths as earlier. Similar void formation and void coalescence damage mechanisms to that for 350°C tests are evident. In addition, some grain boundary failure is visible at low magnifications with different surface textures present at higher magnifications than the 350°C case. There is more extensive matrix plastic flow at lower flow stress, increased void formation and growth in the relatively particle-free matrix, and possibly earlier onset of fracture by fewer but larger voids that link through the thickness.

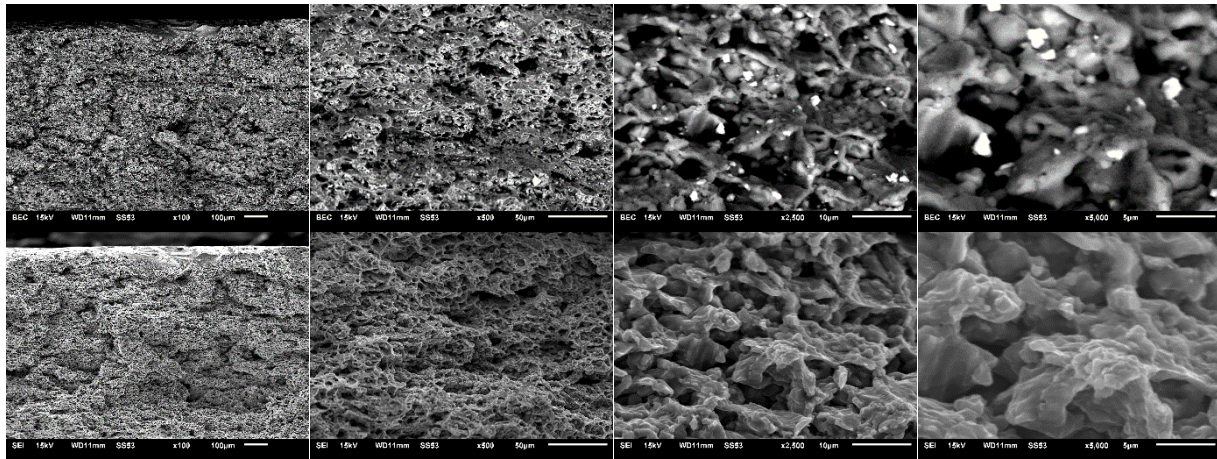


*Figure 5.2.25 0.5-inch width sample deformed at 400°C and observed at magnifications of x50, x500, x2,500 and x5,000 (left to right). Top and bottom rows of fractographic images of the same region were obtained under backscatter electron (BEC) diffraction and secondary electron (SEI) modes*

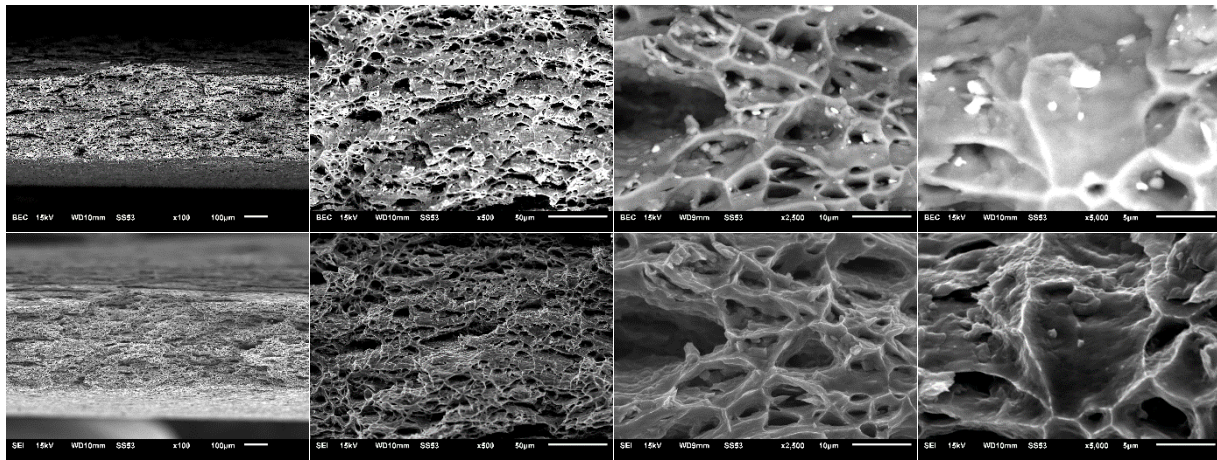


*Figure 5.2.26 3-inch width sample deformed at 400°C and observed at magnifications of x50, x500, x2,500 and x5,000 (left to right). Top and bottom rows of fractographic images of the same region were obtained under backscatter electron (BEC) diffraction and secondary electron (SEI) modes*

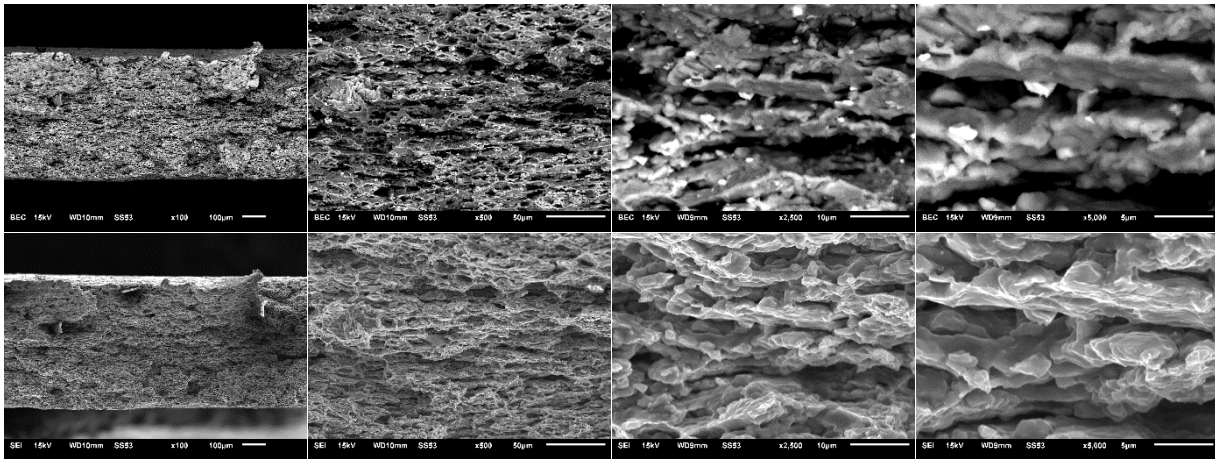


Figure 5.2.27 7.5-inch diameter sample deformed at 400°C and observed at magnifications of x50, x500, x2,500 and x5,000 (left to right). Top and bottom rows of fractographic images of the same region were obtained under backscatter electron (BEC) diffraction and secondary electron (SEI) modes

SEM - Fractographic observations presented in this sub-section will be later compared with SEM observations from the LT plane of fractured polished and specimens to further confirm some of the above findings about damage initiation, growth, linkage and final failure.

### 5.2.8 EDS Analysis of Precipitates in the Fractured Samples

Precipitates, constituent particles and dispersoids all play a role in plastic deformation and damage of high strength aluminum alloys. Since the F-temper material had a well-established precipitate structure from the rolling process it was considered useful to analyze that structure prior to testing. In order to analyze the composition of these precipitates on the fracture surfaces in AA7075 alloy, it was considered worthwhile to estimate the interaction volume the electrons have with the sample for interpreting the results. The interaction volume is helpful for EDS point analysis to interpret whether the results solely indicate precipitate composition or a combination of precipitate

and matrix depending on its size and make-up. The empirical expression for interaction radius proposed by Kanaya & Okayama (1972) is expressed as:

$$r(\mu m) = \frac{2.76 \times 10^{-2} \times A E_0^{1.67}}{\rho Z^{0.89}} \quad (5.1)$$

where A is the atomic mass (Al - 26.98 u, Zn - 65.38 u), Z the atomic number (Al - 13, Zn - 30), E<sub>0</sub> the accelerating voltage (20 keV), and ρ the density (Al - 2.70 g/cm<sup>3</sup>, Zn - 7.13 g/cm<sup>3</sup>). Substituting the properties of elements Al and Zn into Equation 5.1 reveals their respective interaction radii of 4.187 μm and 1.825 μm respectively.

Figure 5.2.28 shows an SEM micrograph of a fractured 0.5-inch wide sample deformed at room temperature. The EDS point analysis for 4 different regions of the microstructure are presented in Figure 5.2.29(a-d). Large white particles (see spectrum 5 in Figure 5.2.29(a)) correspond to elements Cu, Mg and Al and have voids associated with them as shown by dark regions around the particles. Zn-Cu-Mg-Al dispersoids appear to make up the rest of the smaller particles (see spectrum 6 in Figure 5.2.29(b)). The Al matrix also has some fine Mg-Zn dispersoids in it (see spectrum 8 in Figure 5.2.29(d)).

As discussed earlier, the interaction volumes, on the size of 2–4 μm are similar to size of the particles being examined. Therefore, it is difficult to say whether the Al seen in spectrums 1-3 is that of the matrix or precipitates. While the Zn-Mg seen in spectrum 4 may be from larger dispersoids present in the interaction volume but not visible and not that of the matrix make-up.

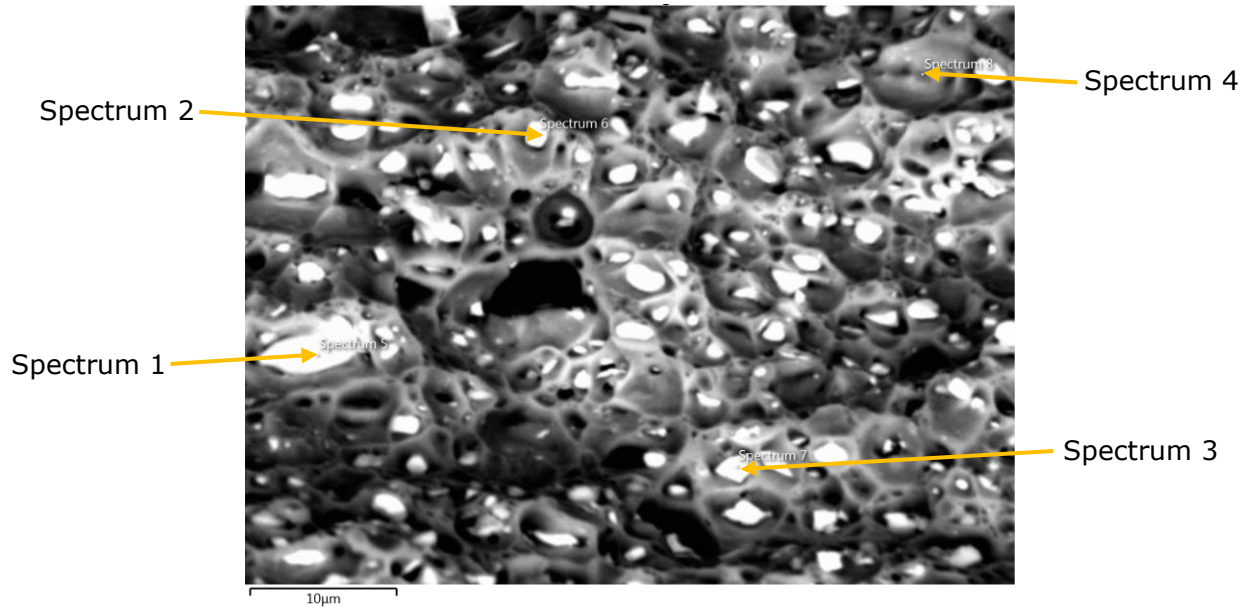


Figure 5.2.28 SEM fractographic image from fracture surface of 0.5-inch wide sample (uniaxial tension strain path) deformed at room temperature and marked with regions analyzed with EDS

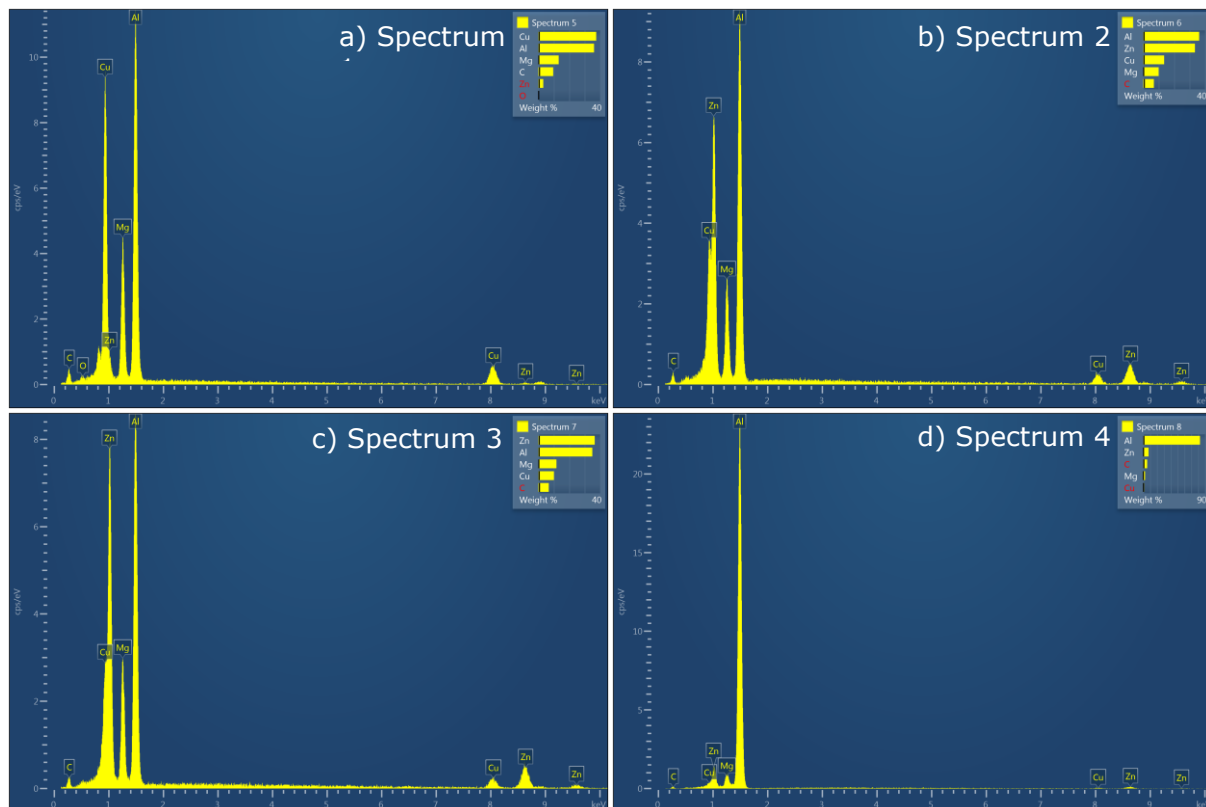
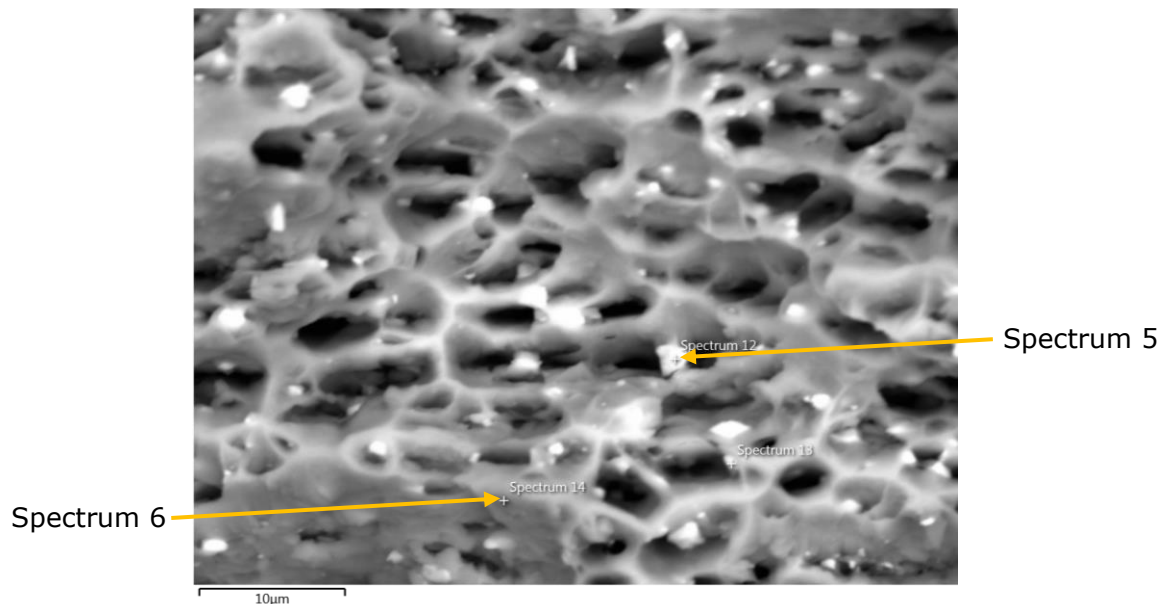


Figure 5.2.29 EDS point analysis of 0.5-inch sample tested at room temperature a) Spectrum 1 – Cu-Al-Mg precipitate b) Spectrum 2 -Al-Zn-Cu-Mg precipitate c) Spectrum 3 – Zn-Al-Mg-Cu d) Spectrum 4 – matrix make up, mainly consisting of Al with fine Zn-Mg precipitate make up

Figure 5.2.30 shows an SEM fractographic image of 7.5-inch diameter Marciniak sample (balanced biaxial tension path) deformed at 300°C. There is a decrease in the size as well as number of visible particles at the fracture surface compared to the room temperature test case earlier. The particles appear to contain Zn-Cu-Mg-Al as principal elements as per the EDS data shown in Figure 5.2.31 (spectrum 5). However, due to their smaller size, it is likely that EDS interaction volume ( $\sim 2 \mu\text{m}$  for Zn) includes not just the particles but also the composition of the matrix (see spectrum 6). The voids associated with the particles are larger in size and relatively uniformly distributed compared to the room temperature test case. It is not clear if the dispersoids are located at the grain boundaries.



*Figure 5.2.30 SEM fractographic image from fracture surface of 7.5-inch diameter sample (balanced biaxial tension strain path) deformed at 300°C and marked with regions analyzed with EDS*

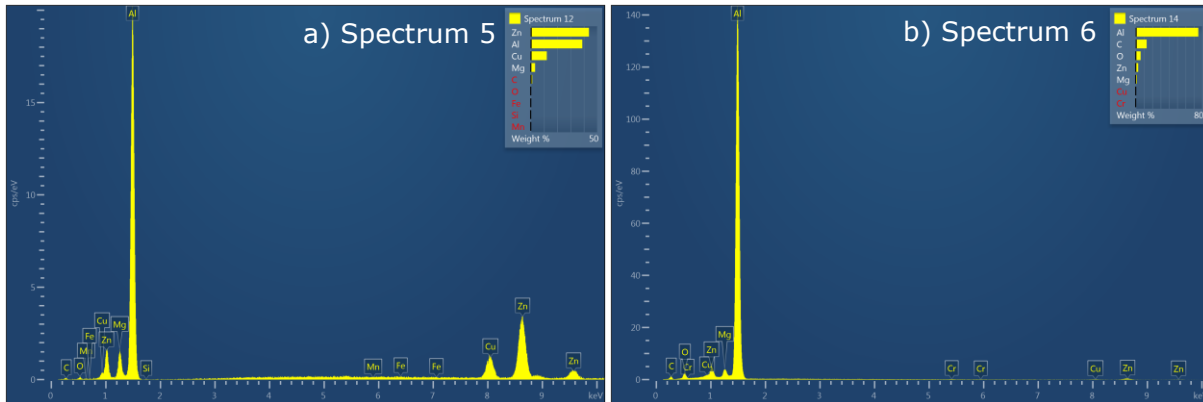


Figure 5.2.31 EDS point analysis of 7.5-inch diameter fractured sample tested at 300°C a) Spectrum 5 – Zn-Cu-Mg-Al precipitate, b) Spectrum 6 – Al matrix composition

Figures 5.2.32 and 5.2.33 show a SEM fractograph and EDS analysis of 7.5-inch sample at fracture for 350°C test respectively. The particles, as earlier for 300°C test case, contain Zn-Cu-Mg-Al as principal elements in their composition and appear to be about the same size as at 300°C. Also, many larger voids are visible compared to the 300°C case.

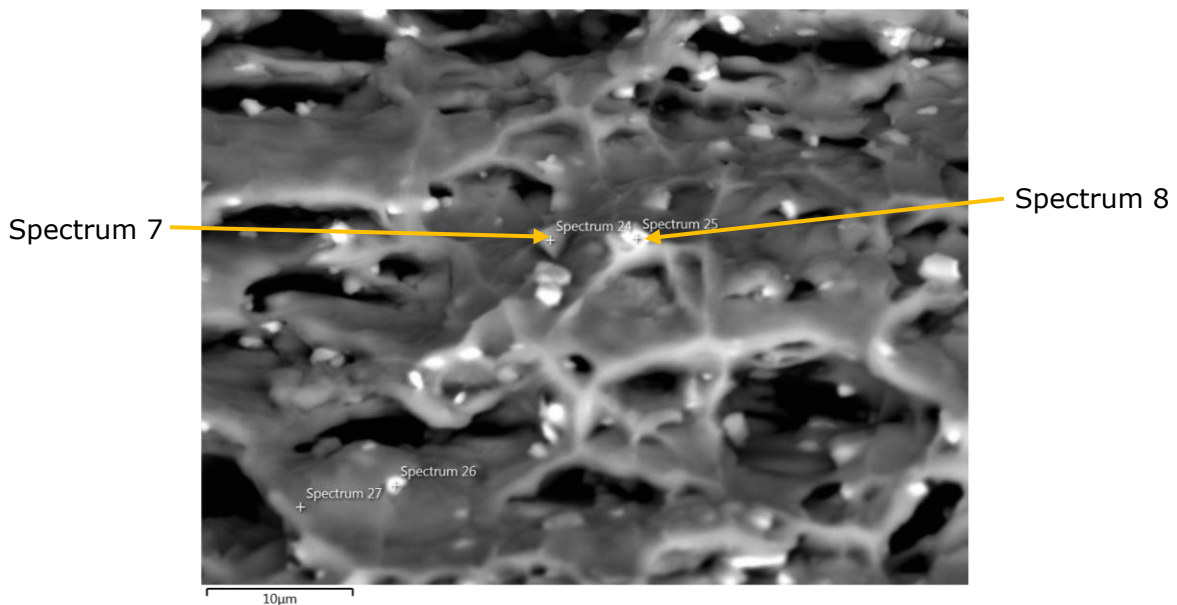


Figure 5.2.32 SEM fractographic image from fracture surface of 7.5-inch diameter sample (balanced biaxial tension strain path) deformed at 350°C and marked with regions analyzed with EDS

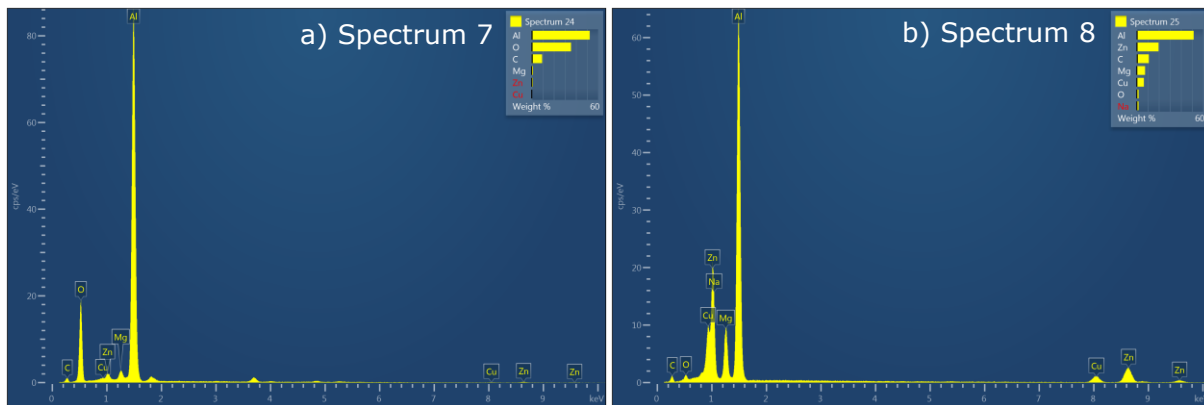


Figure 5.2.33 EDS point analysis of 7.5-inch diameter sample tested at 350°C a) Spectrum 7 – Al matrix b) Spectrum 8 – Zn-Mg-Cu-Al precipitate

Figures 5.2.34 and 5.2.35 show a SEM fractograph and EDS analysis of 7.5-inch diameter sample at fracture for 400°C test respectively. The microstructure in terms of both the precipitate content and its distribution and its relationship to void formation is different at this temperature compared to 300°C and 350°C. The voids are quite elongated and larger in size and seem to run along the grain boundaries with no distinct presence of particles. The few particles that are present appear to contain Zn-Cu-Al while the matrix contains Al with a high weight percent of Zn (see spectrum 9 in Figure 5.2.35).

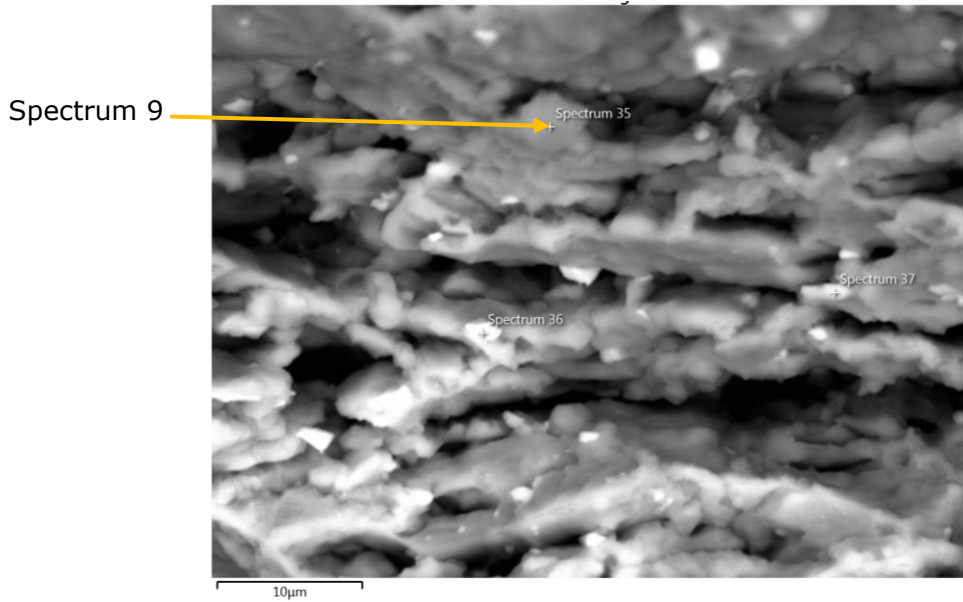


Figure 5.2.34 SEM fractographic image from fracture surface of 7.5-inch diameter sample (balanced biaxial tension strain path) deformed at 400°C and marked with regions analyzed with EDS

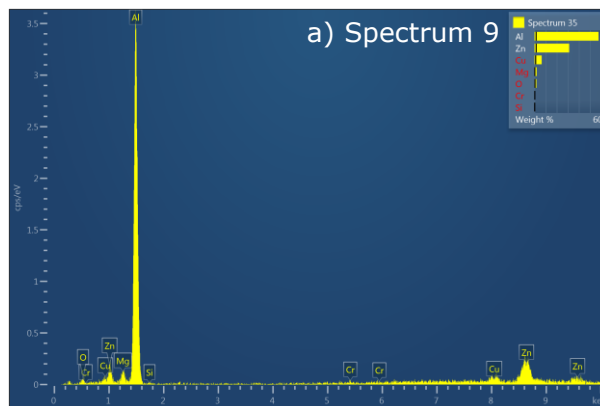


Figure 5.2.35 EDS point analysis of 7.5-inch diameter sample tested at 400°C a) Spectrum 9 – Al-Zn matrix

It is important to note that although the EDS analysis showed presence of carbon and oxygen in the composition analysis, they should be ignored. As part of SEM analysis, the samples had to be coated with carbon to allow for imaging and it is typical to pick up carbon in the alloy composition from this experimental step. The presence of oxygen, however, could be due to oxide

layer formation on the sample surfaces when they were in storage prior to microstructural work.

In summary, the SEM fractographic images of samples tested at the elevated temperature did not provide a fully satisfactory correlation of precipitates and void-induced damage and fracture characteristics when compared to the room temperature test. It was therefore decided to observe and analyze SEM images of fractured specimens in the vicinity of fracture from polished LT plane (i.e., through-thickness plane) for a better understanding of void formation and their association with specific particle compositions. These results are presented in the following section.

### **5.2.9 Neck and Fracture Characteristics**

Figures 5.2.36 – 5.2.47 show SEM micrographs from the polished LT section of fracture specimens. The images were taken in the vicinity of fracture to obtain damage characteristics prior to fracture for the uniaxial tension, plane strain, and equi-biaxial tension strain path cases at each of the three test temperatures, 300°C, 350°C and 400°C. Fracture specimens were prepared for microscopy studies as per the test procedure described earlier in sub-section 3.6.1. The SEM micrographs in each of the figures have been arranged in the order of increasing magnification (from left to right, top to bottom) and are taken in backscattered electron mode (BEC). This is the mode in which EDS analysis is carried out. The EDS results will be presented later in

a separate sub-section. Note that the direction of major principal tensile strain is indicated in all images.

Figure 5.2.36 shows the micrographs for the case of 0.5-inch width specimen (uniaxial tension strain path) deformed at 300°C. The first image at top left (column 1 and row 1), acquired at low magnification of 50X, exhibits a single through-thickness shear dominated fracture with some localized necking prior to fracture. Images acquired at progressively higher magnifications (200X, 2,500X and 5,000X) show highly deformed microstructure with many voids in the vicinity of fracture. Both precipitates (in white) and the associated voids (in black) are revealed with the background matrix material (in dark grey). Several long voids created via coalescence of smaller micro-voids along the major tensile loading direction can be seen in the BEC image at 200X (column 2, top row), and one such region at 2,500X and 5,000X is also shown in Figure 5.2.36 where many smaller particles are located at the top and bottom edges of the long void. The jagged edge of the fracture surface arises from similarly placed particle distribution through the sheet thickness. For example, BEC image at 2,500X (column 1, bottom row) indicates a large number of particles arranged vertically in the thickness direction along the right edge of the micrograph. Such a distribution of particles can indeed give rises to the jagged fracture edge observed in the specimen.

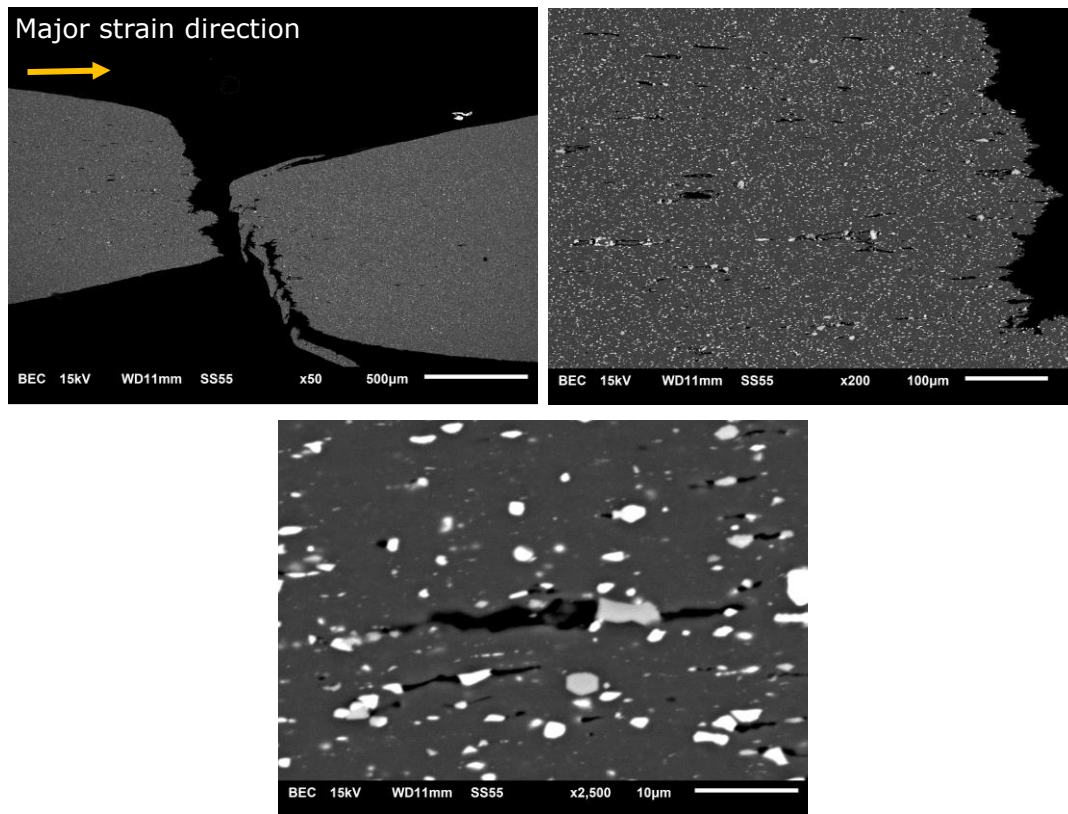


*Figure 5.2.36 SEM micrographs from polished LT section near fracture surface of 0.5-inch wide sample (uniaxial tension strain path) deformed at 300°C at magnifications of x50, x200 and x2,500. Backscatter electron mode (BEC)*

Figure 5.2.37 shows the micrographs for the case of 3-inch wide specimen (plane strain path) deformed at 300°C. The localized necking prior to fracture is more pronounced and the fracture surface can be generally described as cup and cone fracture. This type of fracture is more common when significant localized necking occurs in the material. Similar to the uniaxial tension case, void linkage leading to long single voids along the horizontal major tensile axis is evident in the higher magnification images. A few rather large Fe rich constituent particles and similarly sized voids associated with them are also noticeable in the image.

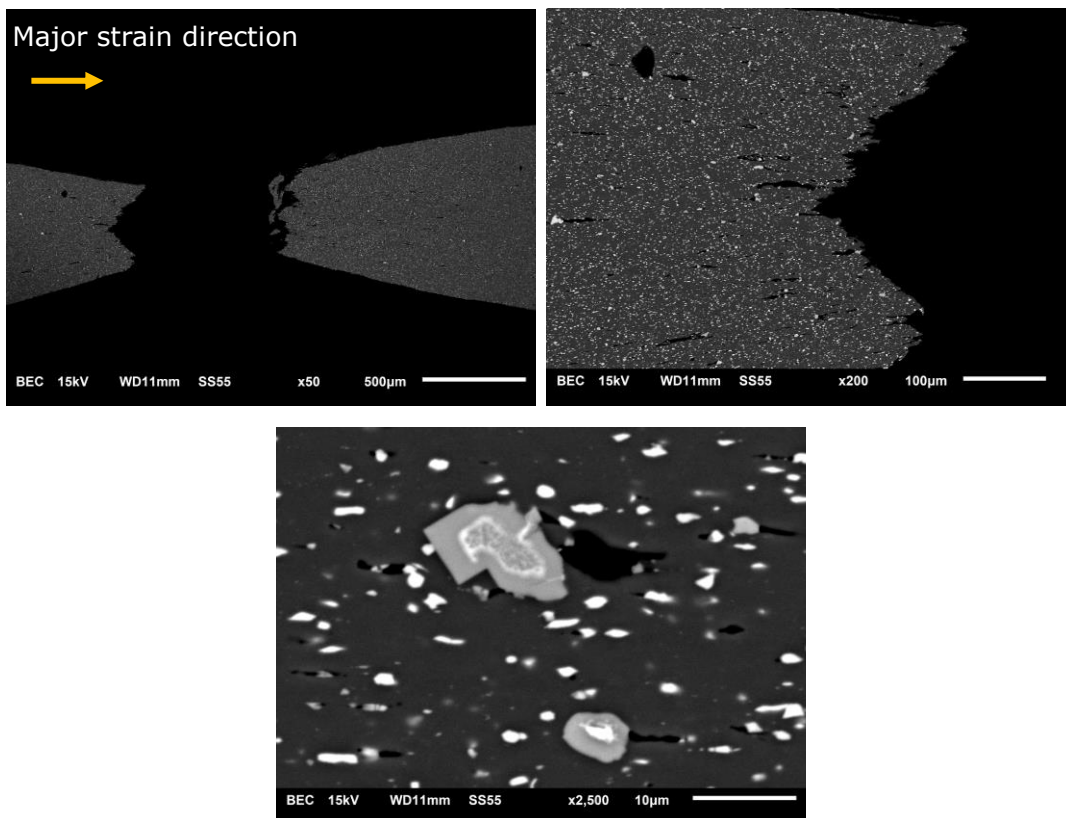


Figure 5.2.37 SEM micrographs from polished LT section near fracture surface of 3.0-inch wide sample (plane strain tension strain path) deformed at 300°C at magnifications of x50, x200 and x2,500. Backscatter electron mode (BEC)

Figure 5.2.38 shows the micrographs for the case of 7.5-inch diameter specimen (balanced biaxial tension strain path) deformed at 300°C. Void nucleation and growth occurred as seen in the other strain paths, however, the void linkage in the form of through thickness sheet (also referred to as void sheeting) was observed. The sample experienced minimal localized necking of the sheet indicating an early onset of fracture. Voids occurred more densely than either of the previous cases at 300°C and were dispersed evenly throughout the sample.

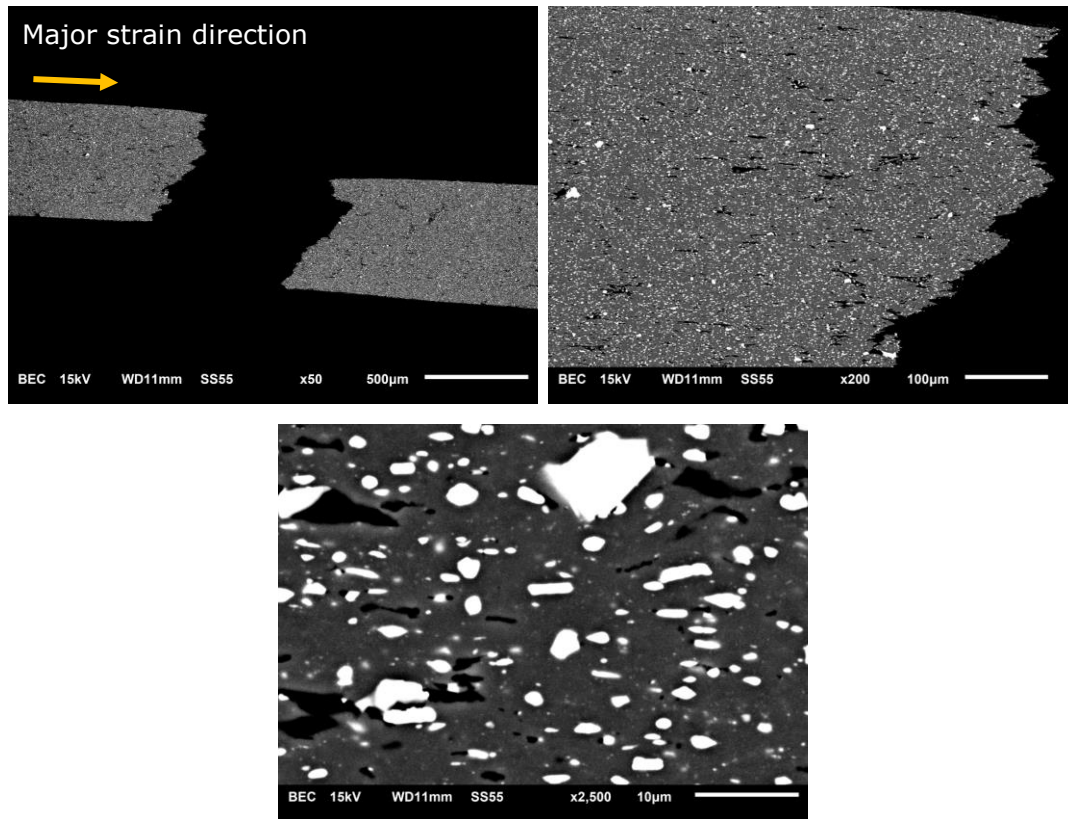
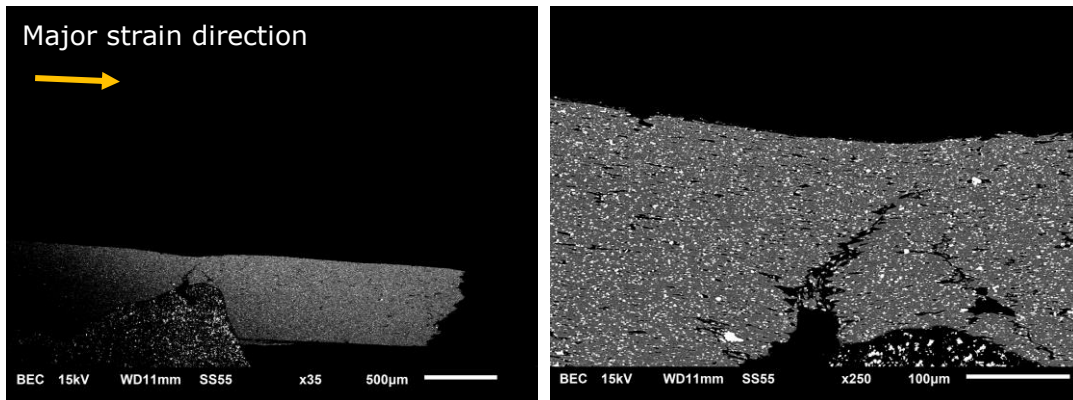


Figure 5.2.38 SEM micrographs from polished LT section near fracture surface of 7.5-inch diameter sample (balanced biaxial tension strain path) deformed at 300°C at magnifications of x50, x200 and x2,500. Backscatter electron mode (BEC)

Figure 5.2.39 shows, for the 7.5-inch wide sample, a partly covered nickel paint region  $\sim 2$  mm away from the fracture surface undergoing coalescence of voids into a secondary fracture region. Once again, a slant through-thickness shear failure path from the bottom surface is revealed. These types of failures from the bottom surface can occur in Marciniak test specimen as the bottom surface is unsupported (and not in contact with the punch), unlike the case of Nakazima test where the bottom surface is fully supported and has a compressive radial stress component.



*Figure 5.2.39 7.5-inch diameter sample secondary fracture region for 300°C at magnifications of x35 and x250. Backscatter electron mode (BEC)*

Figure 5.2.40 shows the micrographs for the case of 0.5-inch wide specimen (uniaxial tension strain path) deformed at 350°C. At this higher temperature the localized necking is even more pronounced leading to a cup and cone type of fracture. Observed extensive localized necking prior to fracture is consistent with the large separation between the FLD and FLCF points for uniaxial strain path as shown earlier in Figure 5.2.17. In addition to long voids along the major tensile axis arising from coalescence of micro-voids, break-up of larger constituent particles can also be observed. The resulting cracks from the break-up of particles are largely perpendicular to the major tensile axis.

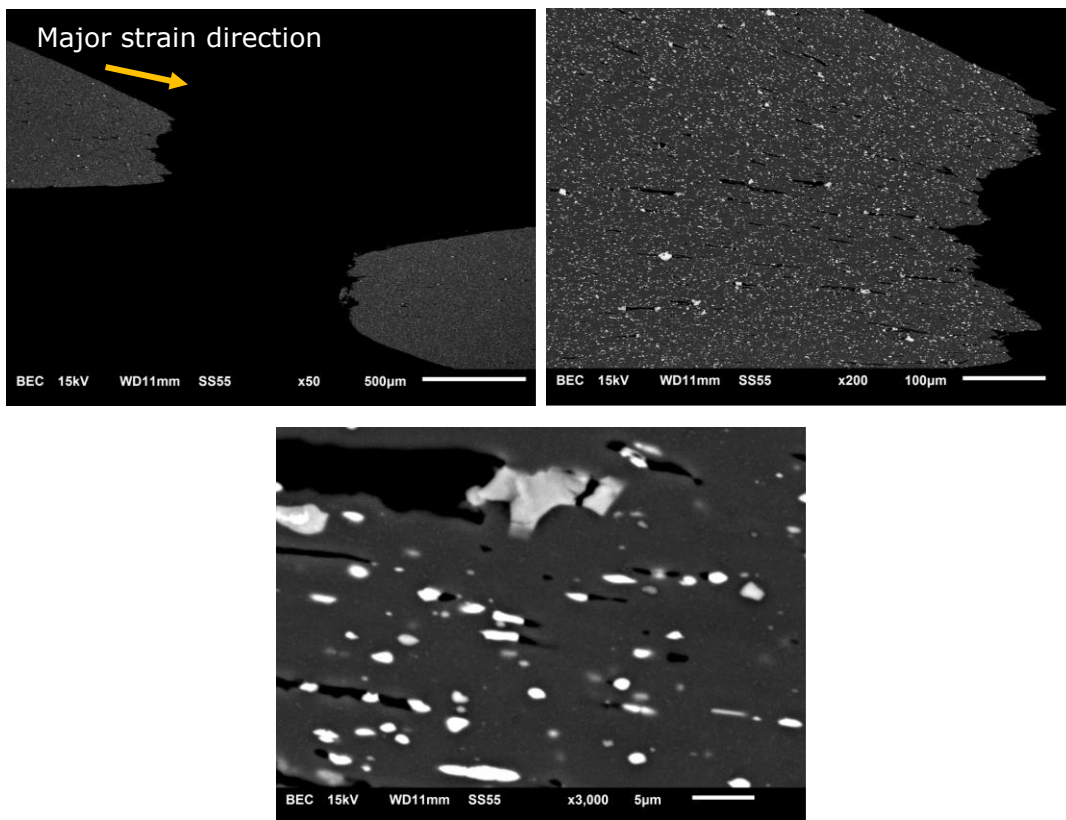


Figure 5.2.40 SEM micrographs from polished LT section near fracture surface of 0.5-inch wide sample (uniaxial tension strain path) deformed at 350°C at magnifications of x50, x200 and x2,500. Backscatter electron mode (BEC)

Figure 5.2.41 shows the micrographs for the case of 3-inch wide specimen (plane strain path) deformed at 350°C. Once again, extensive localized necking at 350°C leading to cup and cone fracture is clearly visible. In addition, significantly long voids of the order of 10  $\mu\text{m}$ , many of them without any precipitates, are visible along the shear planes in the localized neck region. Void damage is also present throughout the sample and more pronounced near the fracture surface. Void volume fraction data is presented later in this section.

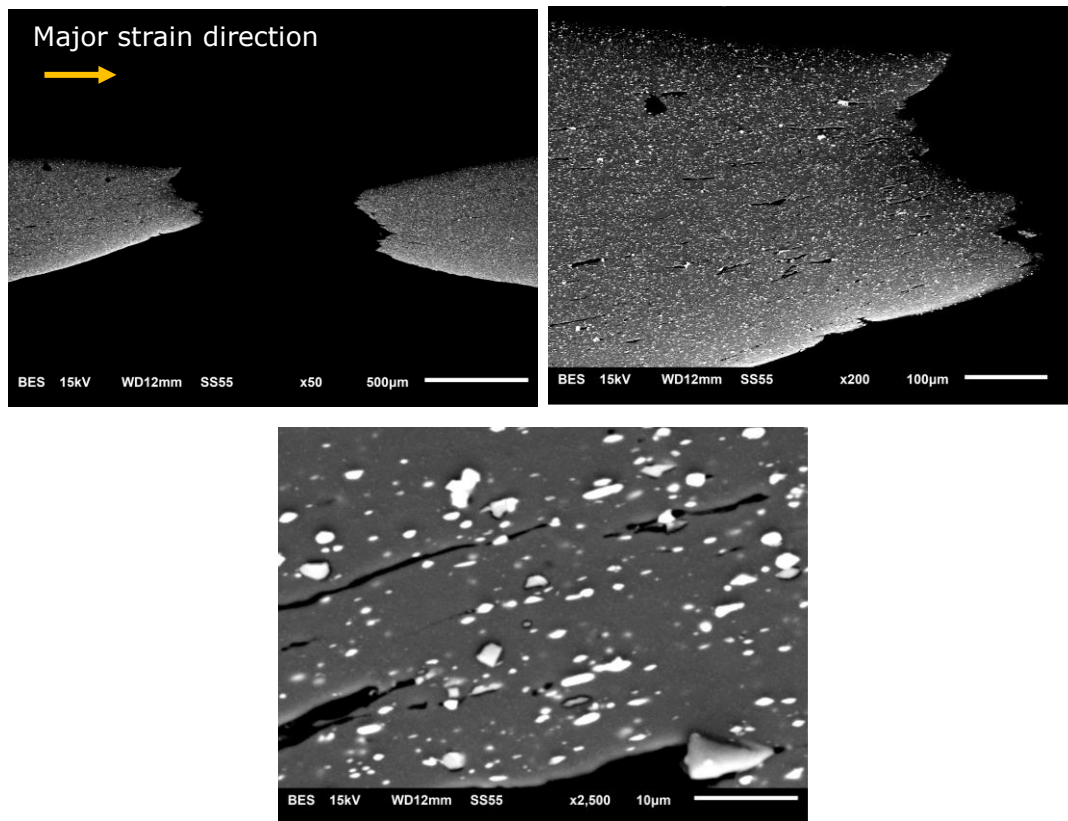
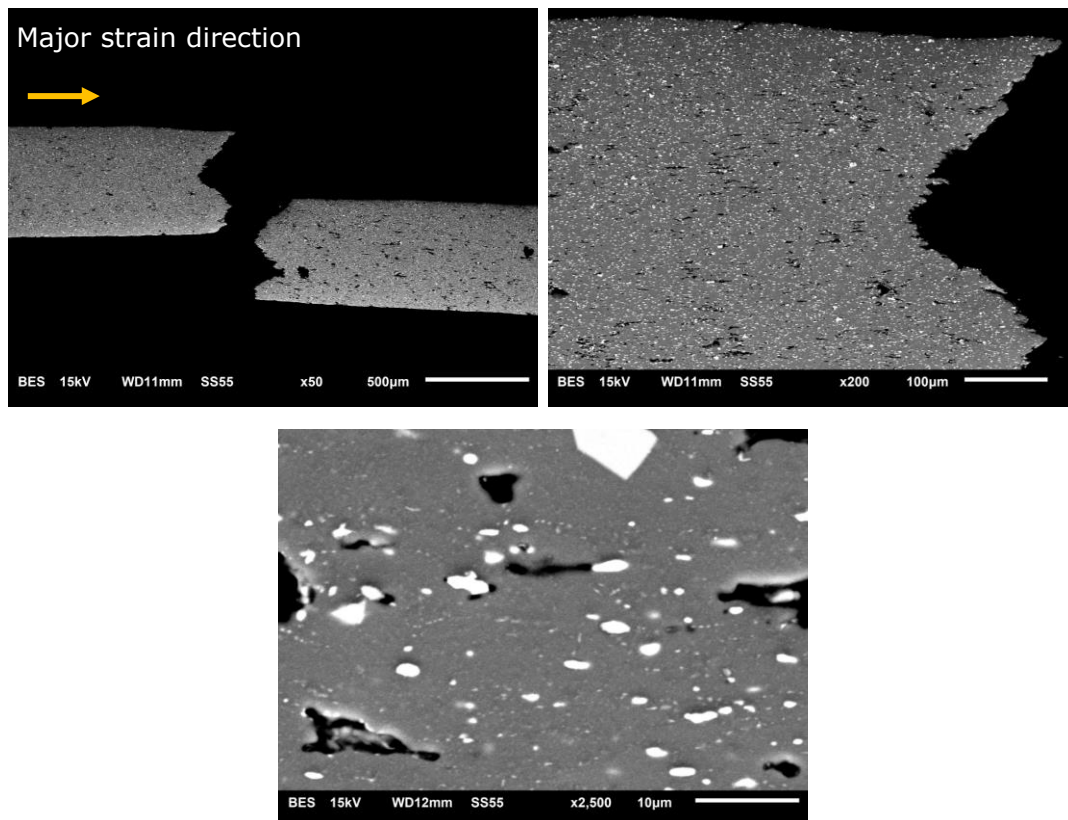


Figure 5.2.41 SEM micrographs from polished LT section near fracture surface of 3.0-inch wide sample (plane strain tension strain path) deformed at 350°C at magnifications of x50, x200 and x2,500. Backscatter electron mode (BEC)

Figure 5.2.42 shows the micrographs for the case of 7.5-inch diameter specimen (balanced biaxial tension strain path) deformed at 350°C. A zig-zag fracture at the microscale is observed perhaps from a combination of local through-thickness shear and more extensive void damage. Once again, as in the case of 300°C balanced biaxial strain path sample, there is minimal localized necking of the sample prior to fracture. The fracture has occurred along two preferential diagonal planes through the sheet thickness. Voids are present all over the sample with their length direction largely aligned normal to the plane of fracture.



*Figure 5.2.42 SEM micrographs from polished LT section near fracture surface of 7.5-inch diameter sample (balanced biaxial tension strain path) deformed at 350°C at magnifications of x50, x200 and x2,500. Backscatter electron mode (BEC)*

Figure 5.2.43 shows the micrographs for the case of 0.5-inch wide specimen (uniaxial tension strain path) deformed at 400°C. At this temperature, the void damage was most extensive for this strain path. Consequently, the extent of localized necking prior to fracture is small and the macroscopic fracture path appears to be dominated by void growth and coalescence.

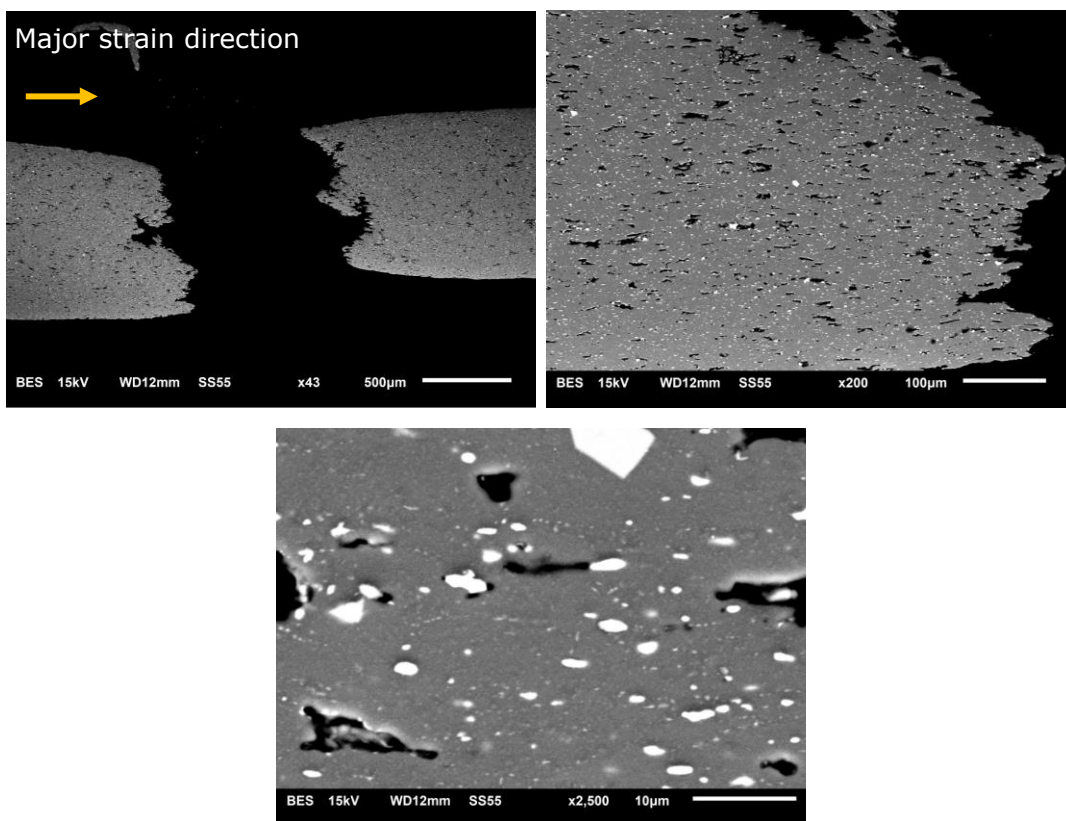


Figure 5.2.43 SEM micrographs from polished LT section near fracture surface of 0.5-inch wide sample (uniaxial tension strain path) deformed at 400°C at magnifications of x50, x200 and x2,500. Backscatter electron mode (BEC)

Figure 5.2.44 shows the micrographs for the case of 3-inch wide specimen (plane strain tension strain path) deformed at 400°C. The fracture surface appears to be a combination of localized necking, through-thickness shear along the top and bottom surfaces, and void-induced cup and cone fracture in the mid-thickness region. This is usually referred to as shear-ductile fracture with shearing of voids clearly evident in the earlier fractographic data (Figure 5.2.26). Lastly, there is extensive void linkage along the major strain axis leading long macroscopic voids that are spread throughout the sheet thickness, and especially near the fracture surface.

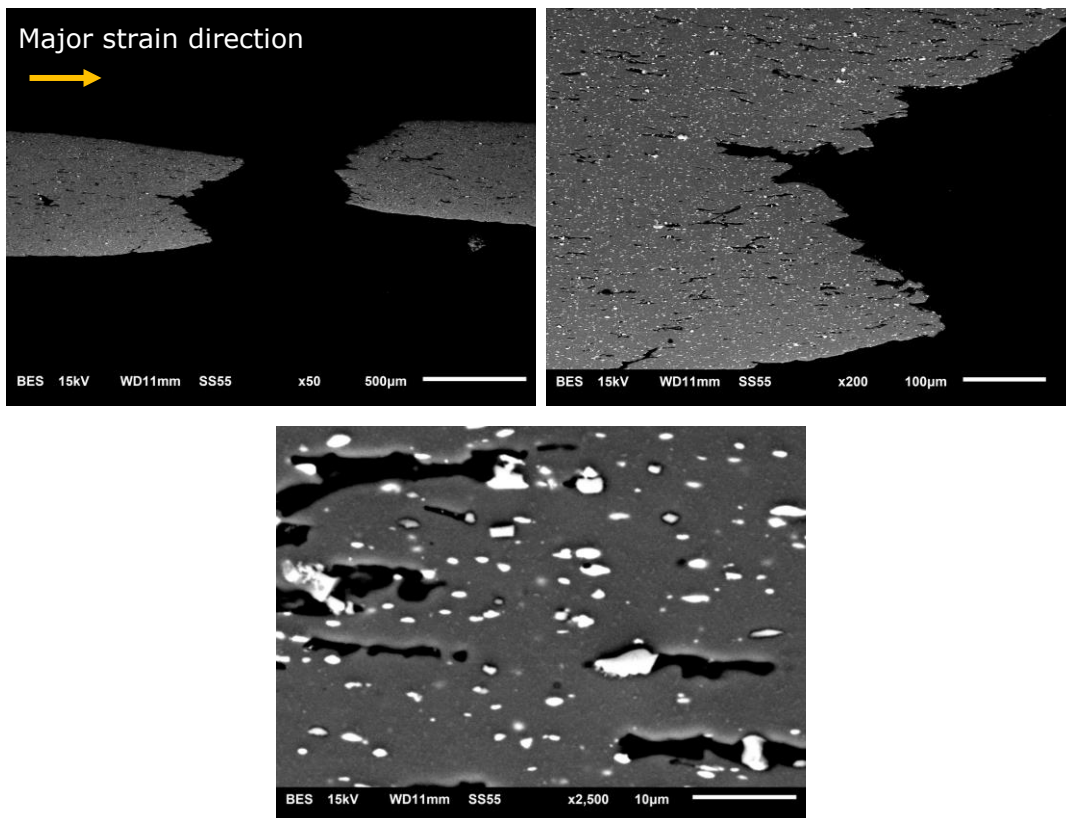
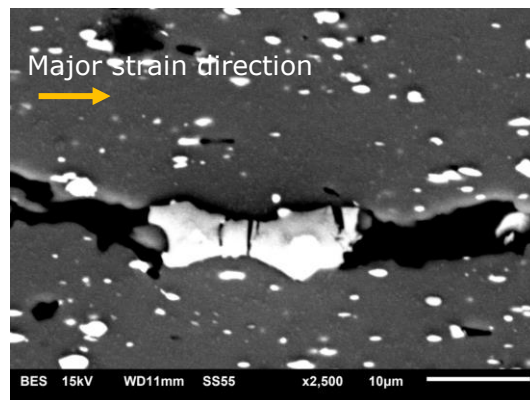


Figure 5.2.44 SEM micrographs from polished LT section near fracture surface of 3.0-inch wide sample (plane strain tension strain path) deformed at 400°C at magnifications of x50, x200 and x2,500. Backscatter electron mode (BEC)

Figure 5.2.45 shows an interesting break-up of a large Fe rich constituent particle in the 3-inch wide specimen deformed at 400°C. Multiple cracks are visible with complete separation of the particle at the minimum cross-section region and only partial cracking in the other regions with larger cross-sections. All crack directions are perpendicular to the major stress axis. Thus, the morphology of the particle appears to affect the local particle fracture. Also, this particle fracture does not appear to be the cause of void formation. This is also consistent with extensive evidence of void formation by matrix-particle decohesion and not by break-up of particles.



*Figure 5.2.45 3-inch wide sample secondary fracture region for 400°C at x2,500 magnification showing fractured particle. Backscatter electron mode (BEC)*

Lastly, Figure 5.2.46 shows the micrographs for case of 7.5-inch diameter specimen (balanced biaxial tension strain path) deformed at 400°C. This is the case of most extensive void growth observed in the vicinity of fracture in the present work. Some of the softening observed even in the uniaxial stress-strain curve past the maximum stress (see earlier Figure 5.1.2), past about a true strain of 0.6, may have been caused by significant

reduction in load carrying capacity of the material due to reduced cross-section of the sample. This was also evident in the drop in the punch load in the Marciniak punch load versus displacement curves for various specimen geometries (or strain paths) past the point of maximum load. Lastly, during balanced biaxial tension at 400°C the fracture appeared to be very stochastic and likely a function of local void distribution and not quite governed by localized shear associated with necking. In fact, an additional zig-zag fracture zone was evident ~2 mm from the fracture surface as shown in Figure 5.2.47. This occurred likely due to the massive amounts of voiding throughout the entire sample, allowing many fracture zones to initiate under high hydrostatic tension condition of the balanced biaxial tension loading.

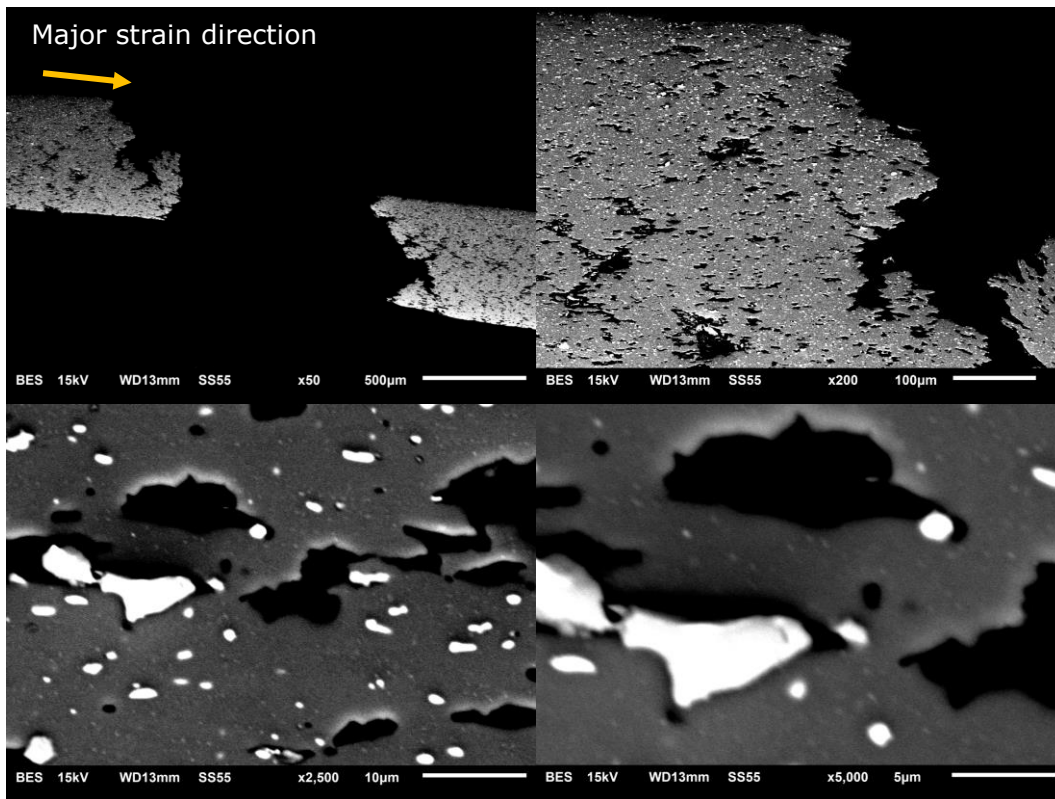


Figure 5.2.46 SEM micrographs from polished LT section near fracture surface of 7.5-inch diameter sample (balanced biaxial tension strain path) deformed at 400°C at magnifications of x50, x200, x2,500 and x5,000. Backscatter electron mode (BEC)

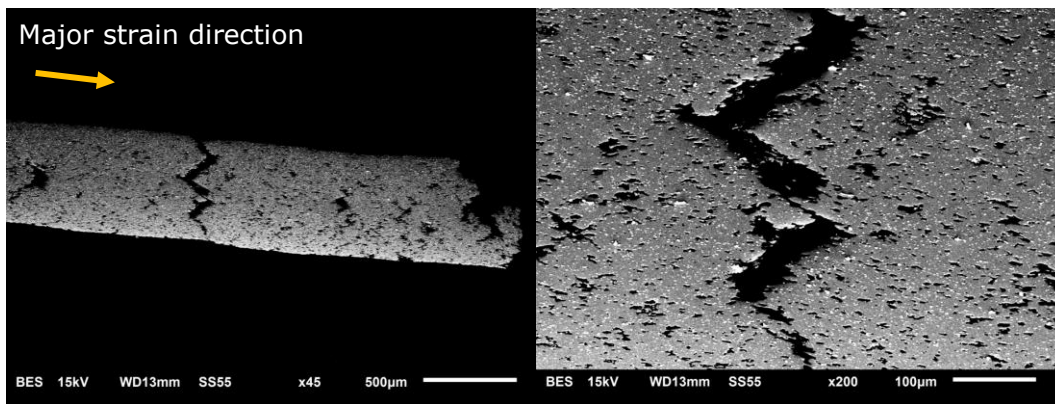


Figure 5.2.47 7.5-inch diameter sample secondary fracture region for 400°C test. Images acquired at magnifications of x45 (left) and x200 (right). Backscatter electron mode (BEC)

In conclusion, it is to be noted that matrix-particle decohesion of a large number of smaller particles was the predominant mechanism of void induced damage in all elevated temperature test samples irrespective of the strain

path and not the break-up of constituent particles which was only infrequently observed. This was clearly revealed in both SEM fractographic observations, and SEM micrographs from LT planes in the vicinity of fracture. A comparison of SEM fractographic with polished LT surfaces of fracture samples, good agreement was seen between particles observed on the surface. Although larger precipitates ( $\sim 50 \mu\text{m}$ ) in some cases tend to cause larger voids, these particles were typically not observed in the final fracture process. Fe-Cu-Al containing constituent particles of the size  $\sim 10 \mu\text{m}$  experienced matrix decohesion as well as particle fracture, where particle fracture rarely led to the formation of larger voids. The linking of voids to fracture typically occurred from decohesion between the matrix and Zn-Mg-Cu-Al dispersoids on the scale of  $2 \mu\text{m}$  with this mechanism being most common and thought to be the main cause of fracture.

As test temperature increased, the macroscopic fracture characteristics changed from shallow localized necking and single transverse or slanted shear (typical of room temperature test) to deeper localized necking and a cup and cone type fracture for uniaxial tension and plane strain tension strain paths at elevated temperatures. Fracture characteristics under balanced biaxial tension condition was relatively insensitive to temperature. There was through-thickness ductile-shear failure with minimum localized necking that led to zig-zag or even stochastic fracture surface that was highly dependent on the nature and extent of local through thickness void distribution and void

linkage with extensive damage as the temperature increased to 400°C. The number of voids tended to decrease with distance away from the fracture surface at all temperatures and strain paths due to reduced strains. However, at 300°C there were fewer voids in the vicinity of fracture, while at 350°C significant voids were present up to a distance of about 1.5 mm away from the fracture surface. At 400°C, while there was reduction in the number density of voids away from the fracture surface, significant voiding occurred throughout the sheet.

The regions near fracture were used to calculate void fractions which are typically associated with damage evolution. Figure 5.2.48 shows an example of image processing to calculate void fraction with the voids shown in red, where SEM backscatter images 0.5 mm away from the fracture surface with dimensions 0.25 mm x 0.25 mm were used as a base image for all calculations. Figure 5.2.49 shows a summary of void fraction data in terms of a correlation between equivalent strain values from DIC and void fraction. Void fraction increased with temperature and equivalent plastic strain as expected. As mentioned earlier, a substantial increase in void fraction occurred at 400°C under balanced biaxial tension, and perhaps exaggerated by inclusion of a large area of coalescing of voids in the image away from the fracture surface.

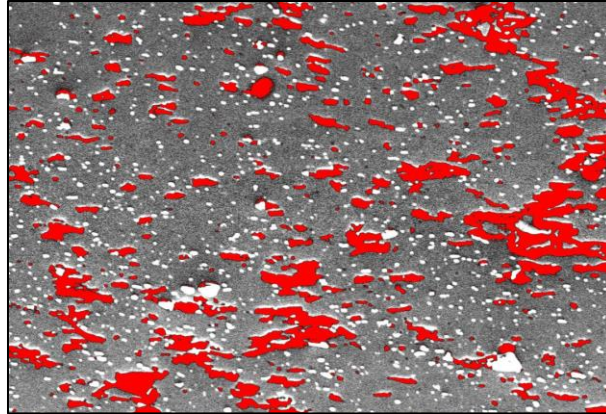


Figure 5.2.48 Fracture region of polished LT section of balanced biaxial tension sample tested at 400°C showing image processing for void fraction calculation where red regions indicate significant voids (14.2% void fraction)

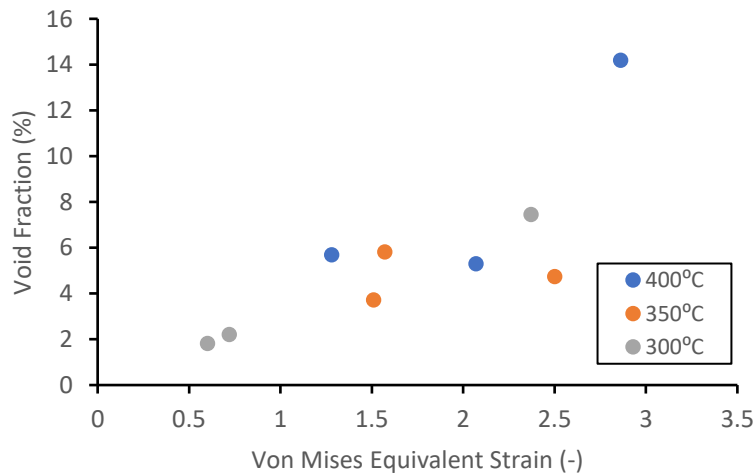


Figure 5.2.49 Relationship between void fraction, Von Mises equivalent strain, and temperature from uniaxial, plane strain, and balanced biaxial tension specimens

## 5.2.10 EDS Analysis of Precipitates from Neck and Fracture

### Regions of LT polished sections

EDS mapping was carried out on the polished LT samples in the localized neck region and in the vicinity of fracture to once again obtain an understanding of elemental composition of precipitate and constituent particles. EDS mapping of polished surfaces is superior to the earlier point

analysis on the fractographic surfaces since X-rays could be more readily captured with no surface topography. Figures 5.2.50 – 5.2.55 show damage regions near the fracture surface for a range of temperatures and the uniaxial strain path case. Again, a correlation can be seen between Fe-Al containing constituent particles and the formation of larger voids. Typically, these particles form voids along the major strain axis and in some cases experience brittle fracture perpendicular to the axis of applied force (Figures 5.2.50 and 5.2.52). At all temperatures Zn-Mg-Cu containing precipitates appear to be the main types of precipitates responsible for larger majority of void formation with fracture initiating due to linkage of smaller voids along shear planes. Additional EDS maps of the plane strain and equi-biaxial tension strain paths for each temperature are displayed in Appendix C as they exhibited similar trends to the uniaxial tension case, showing strain path appeared to have little effect on preferential particle decohesion.

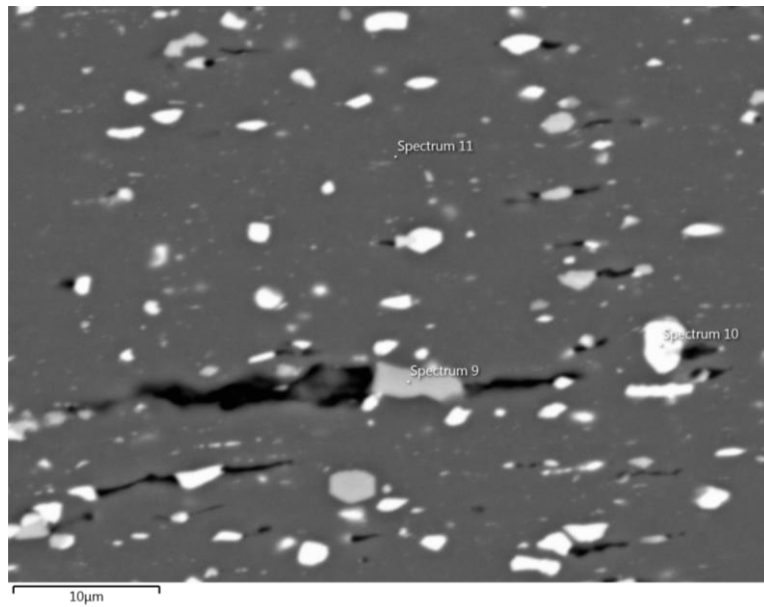


Figure 5.2.50 BSE image of fracture region for 0.5-inch wide sample tested at 300°C. This specimen region was chosen for EDS mapping data shown in Figure 5.2.51

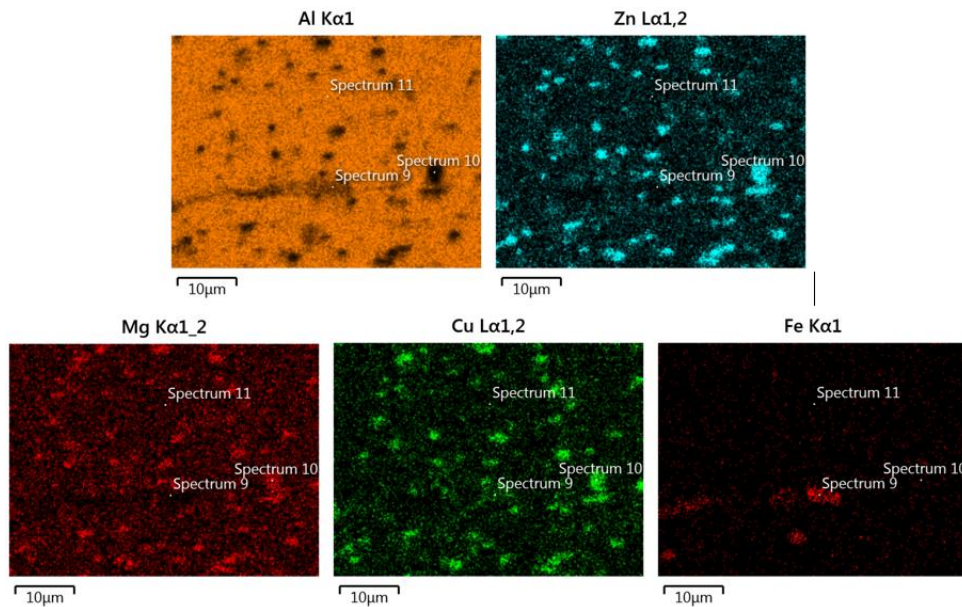


Figure 5.2.51 EDS maps of 0.5-inch wide sample at 300°C from BSE fracture region image

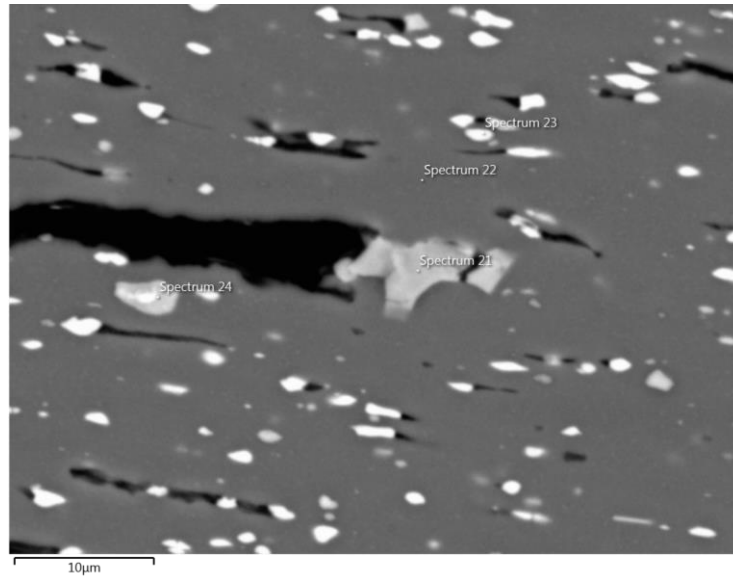


Figure 5.2.52 BSE image of fracture region for 0.5-inch wide sample at 350°C. This specimen region was chosen for EDS mapping data shown in Figure 5.2.53

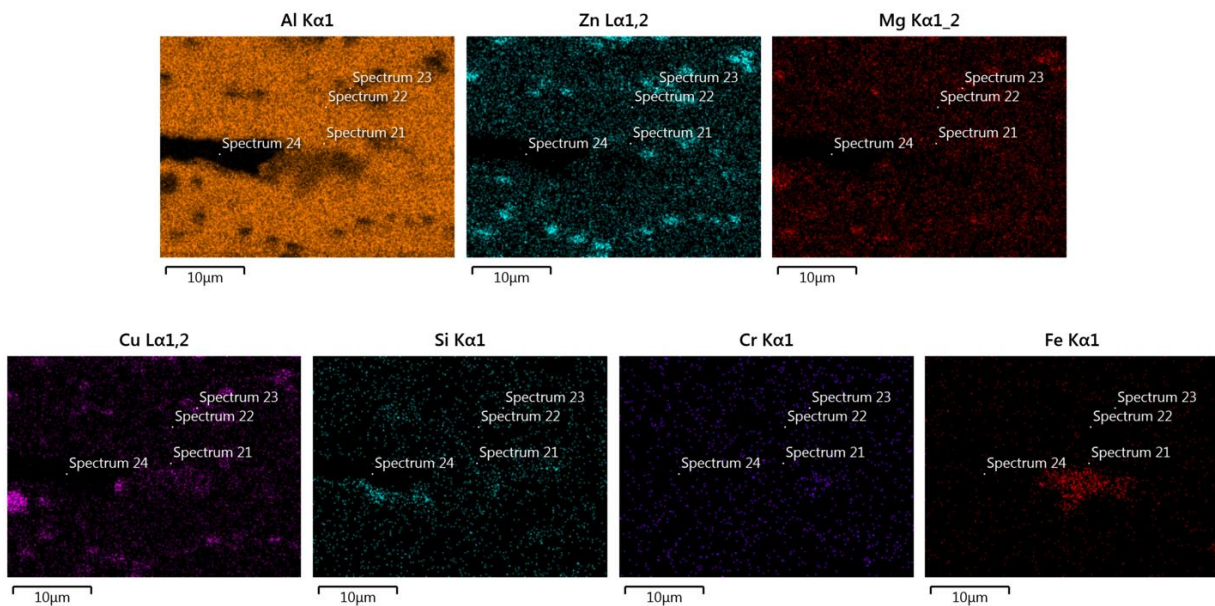


Figure 5.2.53 EDS maps of 0.5-inch wide sample at 350°C from BSE fracture region image

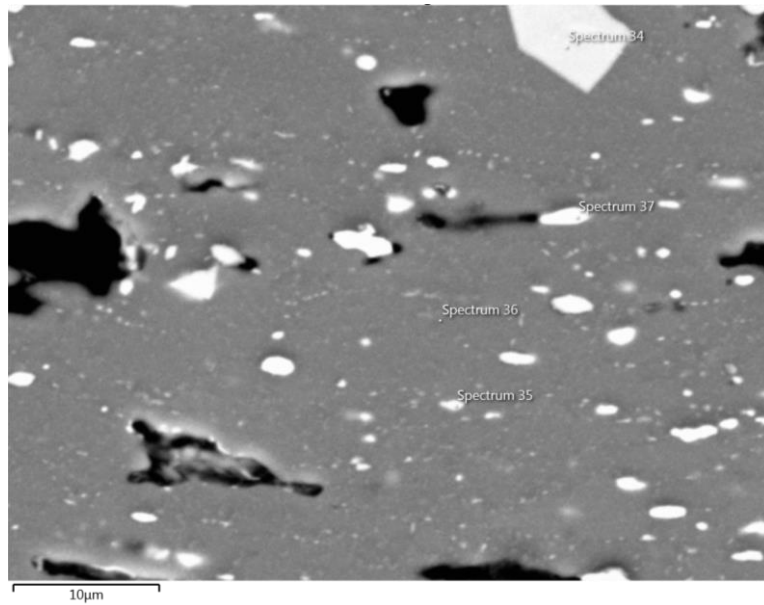


Figure 5.2.54 BSE image of fracture region for 0.5-inch wide sample at 400°C. This specimen region was chosen for EDS mapping data shown in Figure 5.2.55

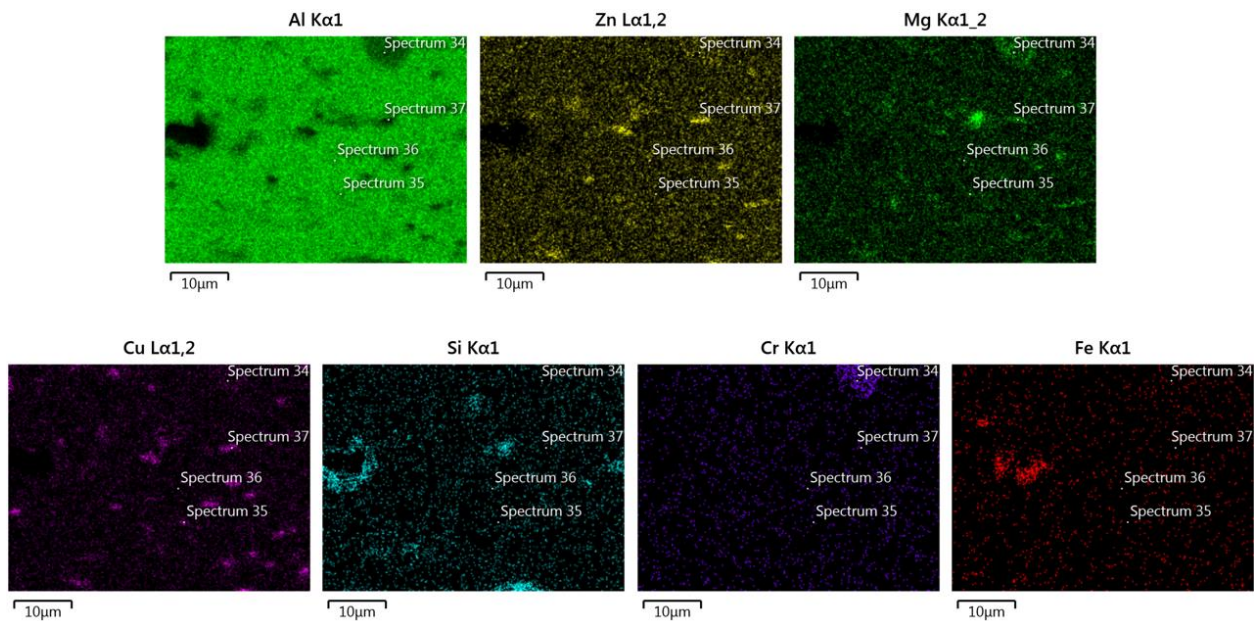


Figure 5.2.55 EDS maps of 0.5-inch wide sample at 400°C from BSE fracture region image

## **5.2.11 Surface Roughness Development in Deformed Specimens**

Surface roughness typically evolves with applied effective strain, strain path, grain size, microstructural inhomogeneity, crystallographic texture, material anisotropy, in-plane versus out-of-plane deformation, and solid or pressurized fluid contact of deformable sheet with a punch or a fluid pressure (Dai & Chiang, 1992). Hot or cold rolled sheets exhibit markings known as rolling lines result from similar imprints caused by plastic deformation of the sheet from the dressed rolls utilized to roll the sheet in the rolling mill. These marking can be seen with the naked eye and their direction corresponds with that of the rolling direction at which they were processed at the mill. At a microscopic level, these undulations are the roughening of the surface into peaks and valleys following this rolling direction. In extreme cases, excessive surface roughening can cause premature plastic strain localization in the valleys and premature failure of the part during stamping. In fact, there is evidence that increased initial sheet surface roughness can reduce the formability of the sheet (Fukui & Nakanishi, 1989). In contrast, by polishing or smoothing the surface of the sheet and the forming punch, the formability of the sheet can be enhanced. As noted earlier in Chapter 3, surface roughness evolution from elevated temperature forming of AA7075-F sheet was studied for its relationship to sheet formability in uniaxial tension, plane strain, and biaxial tension at three elevated temperatures. Deformed Marciniak test

samples were characterized for post-deformation surface roughness development. The results are summarized in Table 5.2.1 and in Figures 5.2.56 – 5.2.60 below.

The rolling direction from the as-received sheet, evident in Figure 5.2.56, was still apparent after subjecting the sheet to large strains under uniaxial tension strain paths at temperatures of 300°C (see Figure 5.2.57(a)). Given that typical average as-received surface roughness ( $R_a$ ) of AA7075-F sheet was approximately 0.3  $\mu\text{m}$ , significant surface roughening had occurred in all cases. However, the initial pattern of roll lines was significantly changed at higher temperatures of 350°C and 400°C (see Figure 5.2.57(b, c)) likely due to increased applied equivalent plastic strains. The roll lines were more diffuse transverse to the rolling direction. Also, the roll lines were broken up along the length of the lines. At 400°C, large scale surface undulations can also be noted. It is possible that some grain recrystallization occurred at higher temperatures of 400°C which resulted in both change in the crystallographic texture of the sheet which may have played a role in the surface roughness development. The surface roughness values in Table 5.2.1 are normalized by equivalent strain and shown as the last column. The results of this column indicate that the normalized roughness values are the highest for plane strain strain path at all temperatures. This is likely caused by the additional constraint placed on the movement of grains in the width direction.

Additionally, the data suggest that the strain path dependence of roughening is reduced with increased temperature.

Figure 5.2.58 presents similar surface roughness development results for straining under plane strain condition at the three test temperatures. There is an increase in the average surface roughness values in this case compared to the uniaxial case. Plane strain condition imposes larger strain in the thickness direction compared to the uniaxial tension strain path, for the same effective plastic strain, and that is expected to lead to a greater sensitivity of surface roughness to grain size differences in the thickness direction. As such, the surface layers of rolled sheet have a finer grain size compared to the grain interior. Once again, the initial pattern of roll lines is altered considerably at higher temperatures due to larger strains and static and dynamic (strain induced) grain recrystallization.

Figure 5.2.59 presents results for balanced biaxial tension strain path for tests at all temperatures. An interesting correlation between the voids present and surface undulations in balanced biaxial strain path at 400°C is observed. Large valleys of size 30  $\mu\text{m}$  corresponding to the same size as large voids apparent near the surface of the material as observed in polished samples via SEM (see Figure 5.2.47 earlier). In this case, collapse and coalescence of voids on the surface lead to surface undulations.

Table 5.2.1 Surface roughness measurements on deformed Marciniak samples in the vicinity of surface fracture (or crack)

Temperature	Strain path	Ra ( $\mu\text{m}$ )	Rq ( $\mu\text{m}$ )	Rz ( $\mu\text{m}$ )	$\bar{\epsilon}$ (-)	Ra/ $\bar{\epsilon}$
300°C	Uniaxial tension	0.536	0.666	2.371	0.72	0.74
	Plane strain	0.867	1.074	3.280	0.60	1.44
	Biaxial tension	0.704	0.854	2.638	2.37	0.29
350°C	Uniaxial tension	0.637	0.840	2.733	1.57	0.40
	Plane strain	0.874	1.057	3.349	1.51	0.57
	Biaxial tension	0.667	0.847	2.601	2.50	0.26
400°C	Uniaxial tension	0.469	0.574	1.982	1.28	0.36
	Plane strain	0.892	1.087	2.897	2.07	0.43
	Biaxial tension	1.182	1.482	4.819	2.86	0.41

**Note:** As-received AA7075 sheet at room temperature had a Ra value of 0.3  $\mu\text{m}$

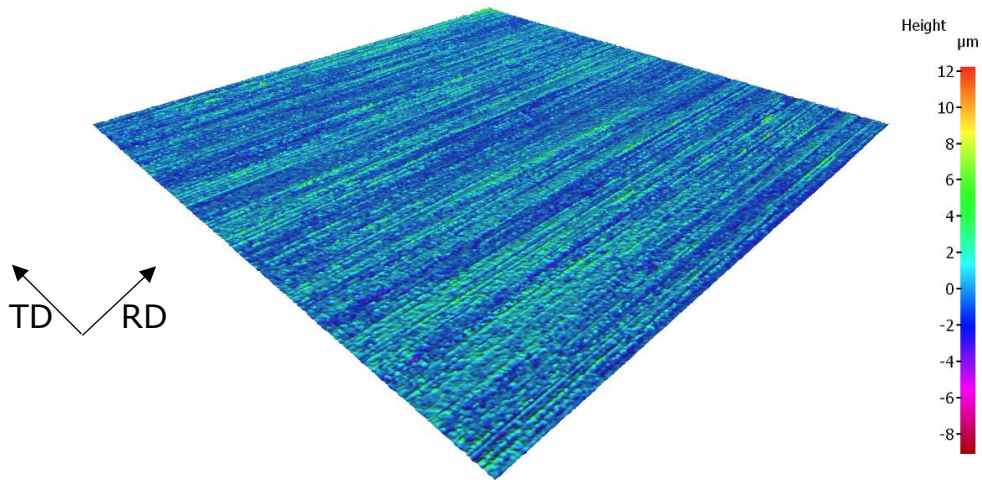


Figure 5.2.56 3D surface roughness graphs for as-received AA7075-F. Rolling direction (RD) and transverse direction (TD) shown. 1.6 x 1.6 mm

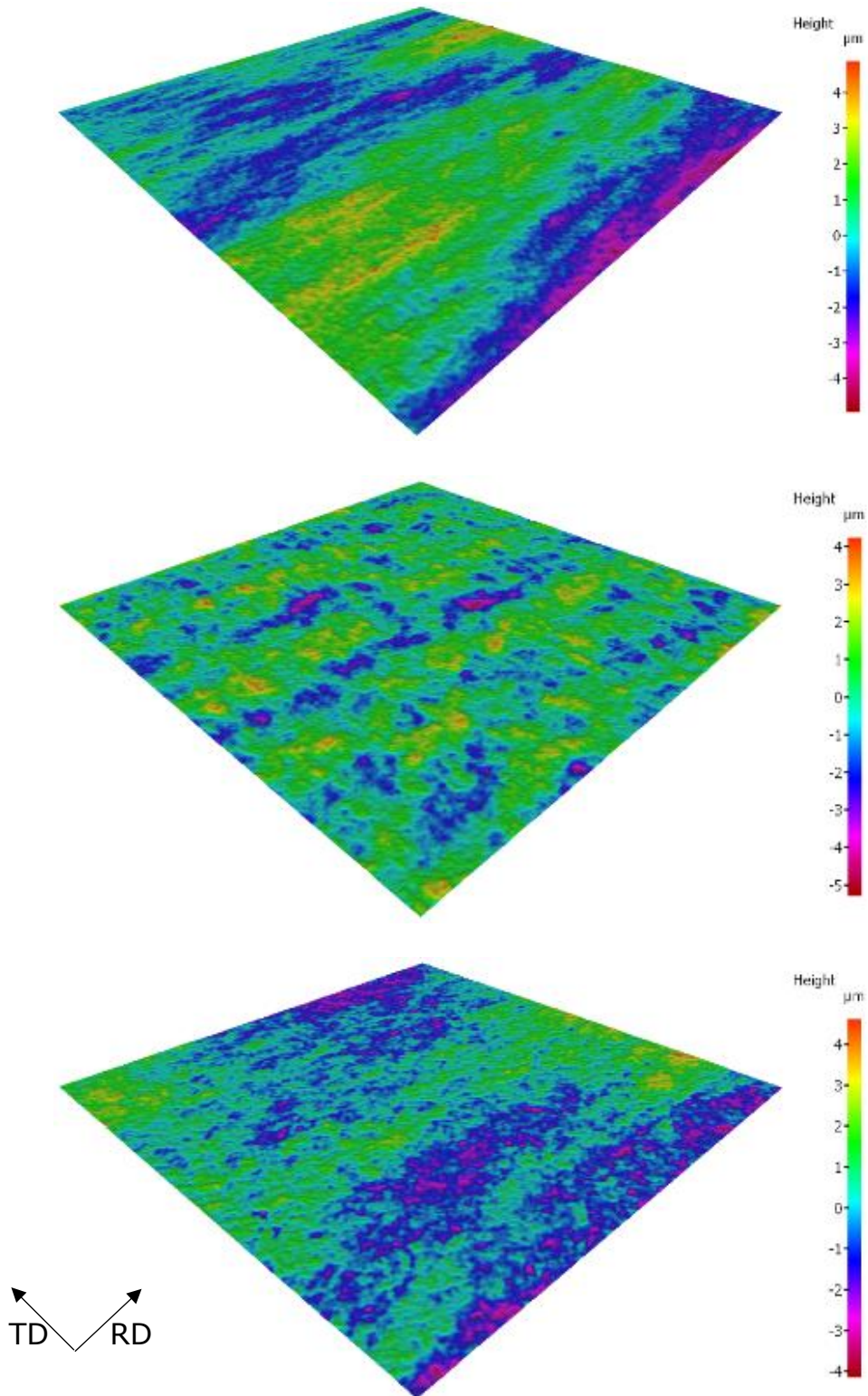


Figure 5.2.57 3D surface roughness graphs for uniaxial tension strain path at 300°C, 350°C, and 400°C (top to bottom). Direction of applied stress parallel to TD direction. 1.6 x 1.6 mm

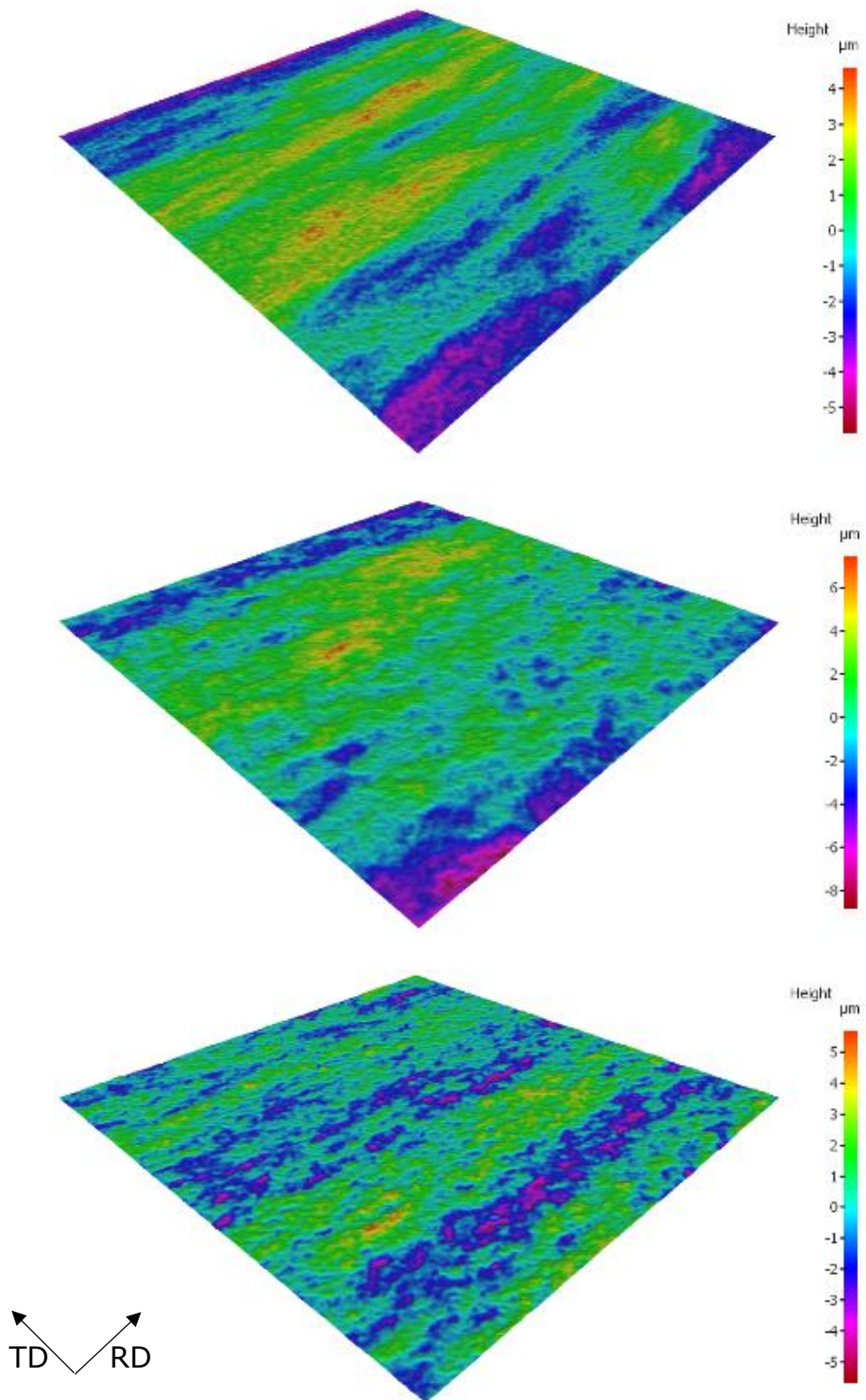


Figure 5.2.58 3D surface roughness graphs for plane strain path at 300°C, 350°C, and 400°C (top to bottom). Direction of applied stress parallel to TD direction. 1.6 x 1.6 mm

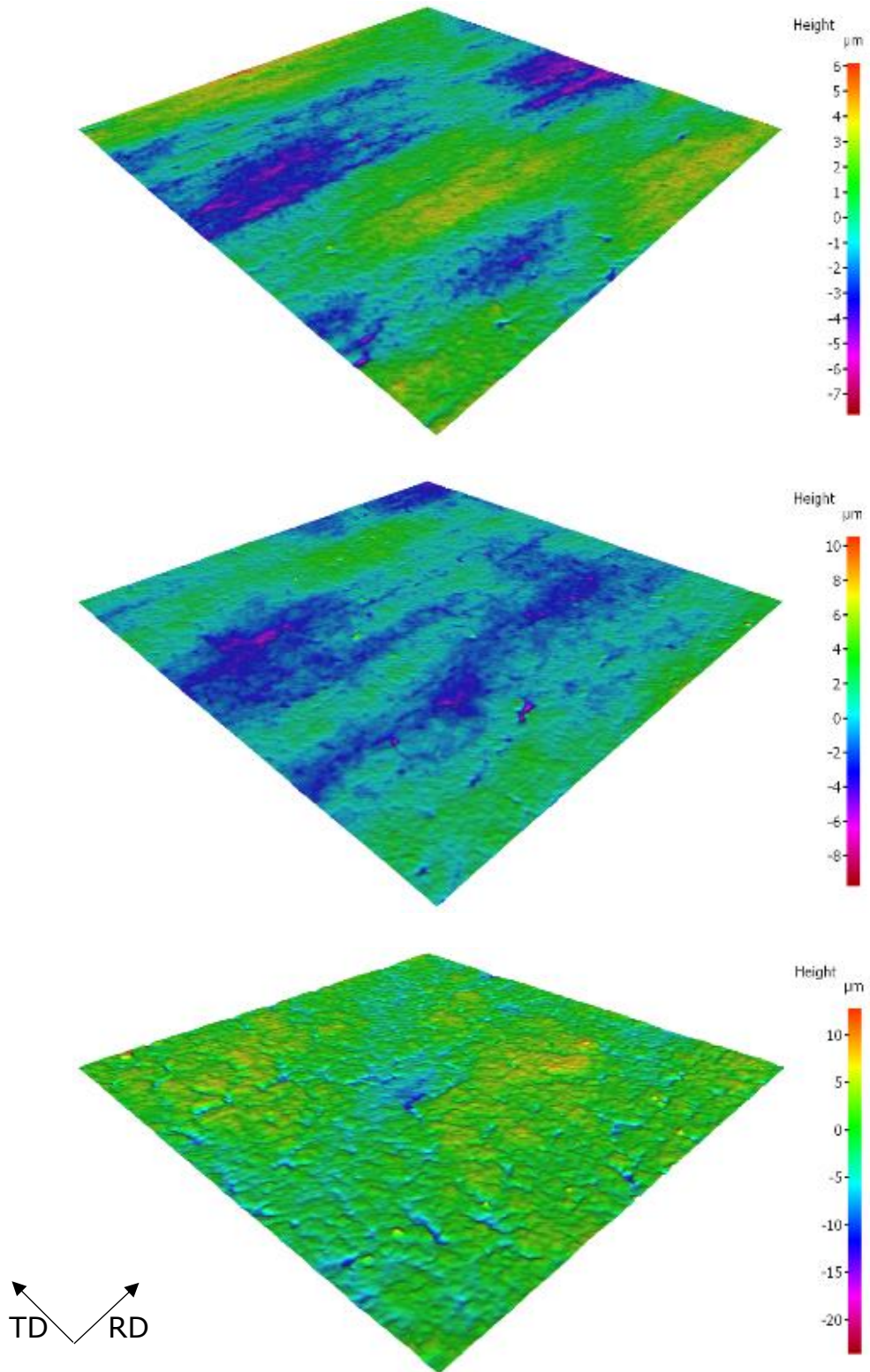


Figure 5.2.59 3D surface roughness graphs for balanced biaxial tension strain path at 300°C, 350°C, and 400°C (top to bottom). Direction of applied stress parallel to TD direction. 1.6 x 1.6 mm

Figure 5.2.60 shows an increasing relationship between average surface roughness and equivalent plastic strain and temperature compared to the as-received sheet. The scatter in data could be due to both low sample size as well as difficulty in accurately measuring equivalent strain at the point surface roughness was measured due to low resolution of the ARAMIS DIC grid.

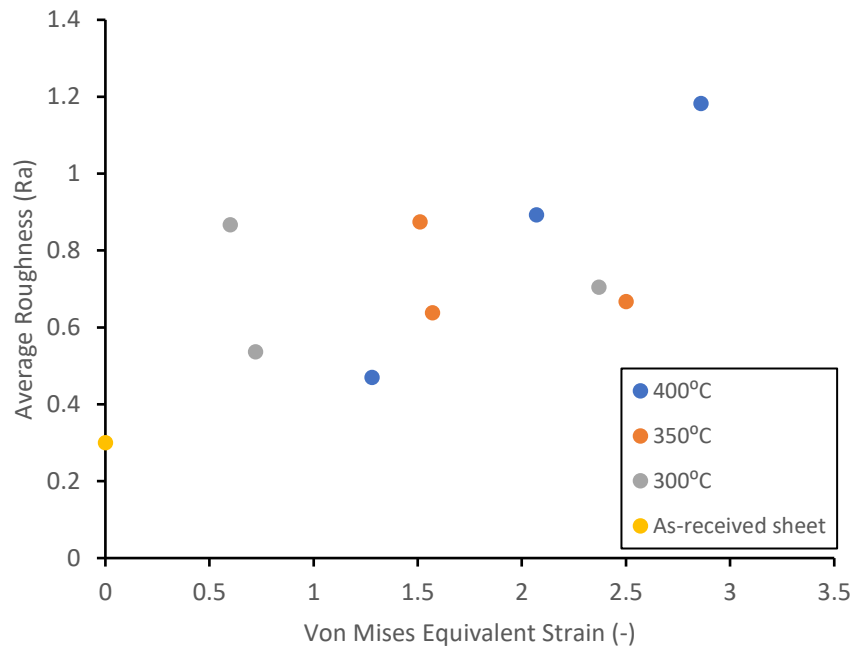


Figure 5.2.60 Relationship between average roughness (Ra), Von Mises equivalent technical strain, and temperature for as-received sheet as well as uniaxial, plane strain, and biaxial tension specimens

### 5.3 Marciniak Test FE Simulation Results

This section presents the results of FE model simulations of Marciniak tests at 400°C through 3 different specimen geometries consisting of 0.5-inch wide, 3-inch wide and 7.5-inch diameter samples. Multiple results from the

experimental and FE simulations of Marciniak testing are first used to assess general validity of the model. Then, model results are analyzed for FLC determination and comparison with the experimental FLCs. The model details were provided earlier in Chapter 4 including the details of the constitutive material model utilized in the simulations, elasto-plastic material data input into the model, and Coulomb friction coefficient values from the literature to handle contact and friction between the deformable sheet materials and between the tool and sheet.

### **5.3.1 Load versus Displacement Curves**

This macroscopic response of the experimental Marciniak test and model simulations can be compared by plotting the punch load versus punch displacement traces for specific test specimen geometries. Figure 5.3.1 shows such a comparison at 400°C for 0.5-inch width, 3.0-inch width and 7.5-inch diameter specimens. A reasonable agreement in terms of the general shapes of the curves can be observed for all specimen geometries. The punch load increases non-linearly to a maximum value and then drops gradually towards the end of the test. The model traces for 3.0-inch and 7.5-inch diameter specimens do exhibit some noise or oscillatory behavior towards the end of the test likely due to variations in contact conditions arising from mass scaling (“Abaqus/CAE User’s Guide”, 2016). For the 7.5-inch diameter blank, the maximum punch load from the simulation is significantly higher than in the experiments. The source of such variations are likely caused by constitutive

material model and the material and friction input data both are subjected to variation due to change in the stress state, model data extrapolation beyond the range of the experimental stress strain curve, and inability to accurately estimate the multiple high temperature friction conditions that prevail between the various sliding surfaces in the experiments (and should be utilized in the model simulations). The variation between the experimental and model load versus displacement traces is, however, considerably smaller for 0.5 and 3.0-inch wide specimen geometries possibly due to lower punch load and punch displacement values, and possibly reduced effect of mass scaling for these geometries.

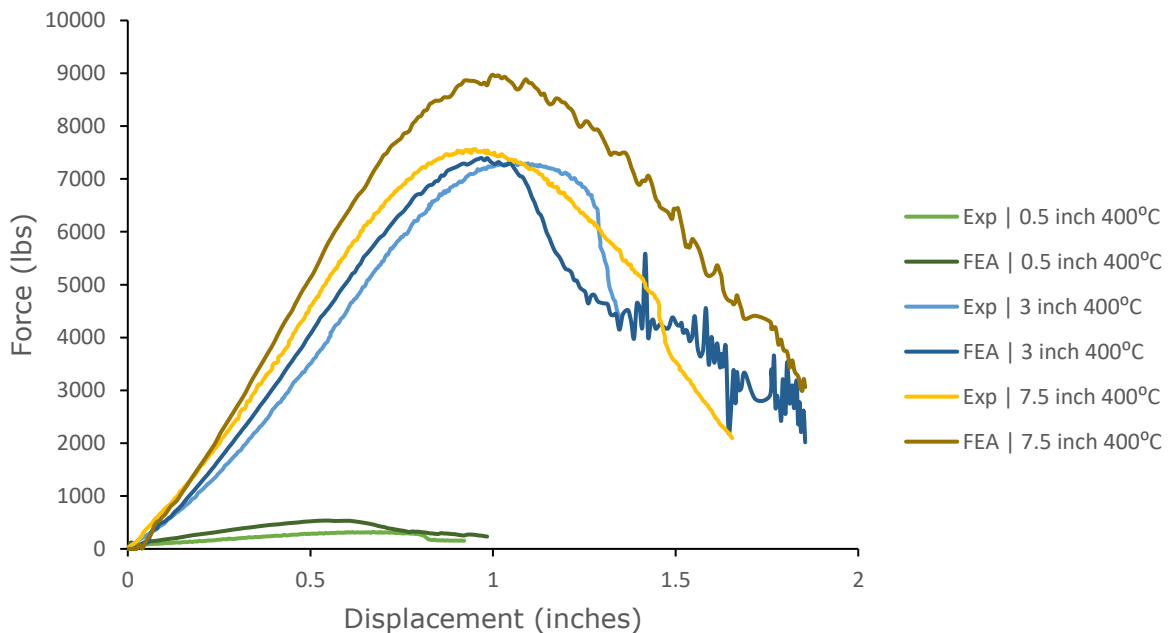


Figure 5.3.1 Force versus displacement curves comparing experimental and simulation test results for 0.5-, 3-, and 7.5-inch sample geometries at 400°C

### **5.3.2 Deformed Samples Characteristics and Strain Maps**

The simulations were carried out at 400°C test temperature only and for uniaxial tension, plane strain tension and balanced biaxial tension strain paths. Figures 5.3.2-5.3.4 show the simulation results in terms of major strain distribution over the surface of the test specimens at large strains close to localized necking or fracture of the specimens. In general, good agreement was observed in the two sets of major strain distributions and the locations of the largest strain values in each of the specimen even with a relatively simple material model that did not capture material softening at high strains. This would be further illustrated in terms of a comparison of the experimental and model strain paths for the three specimen geometries in the next section. Although the uniaxial tension and plane strain tension models showed localized necking occurring at similar strains and punch heights compared to experiments the model balanced biaxial strain path specimen was unable to capture the failure characteristic of the experimental test specimen. This is because no fracture model within the FE model was implemented in the present work. Fracture modeling would have required significant amount of development work as well as programming as a material subroutine within ABAQUS and was beyond the scope of the thesis.

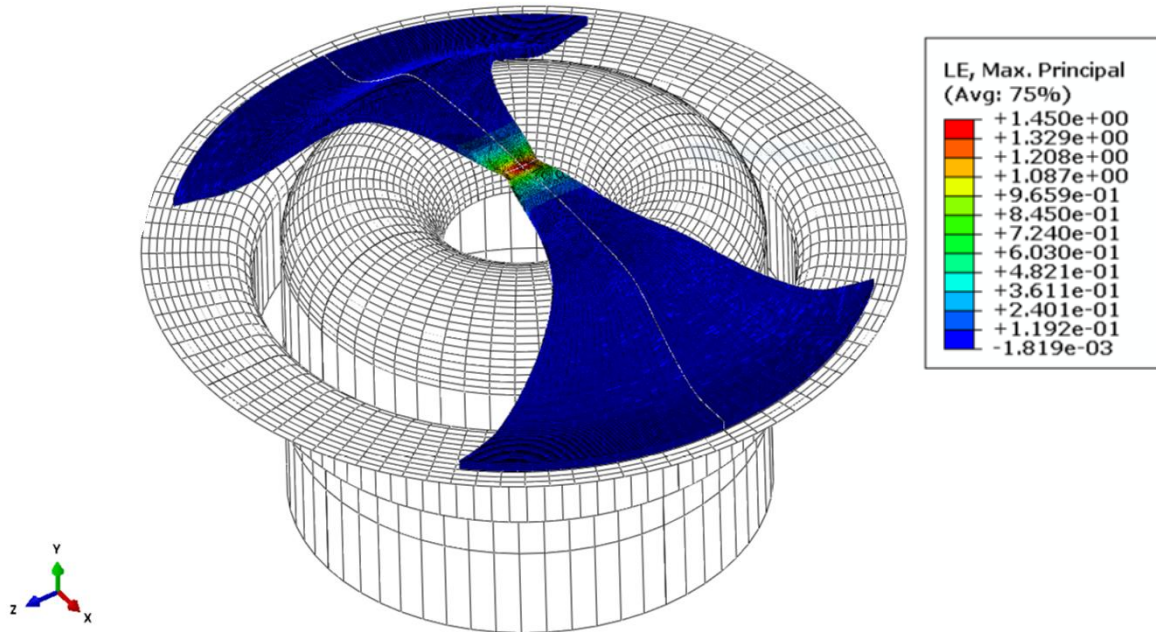


Figure 5.3.2 Simulated Marciniak uniaxial tension strain path test at 400°C showing the principal logarithmic strain for 0.5-inch wide geometry at punch displacement of 0.67-inches

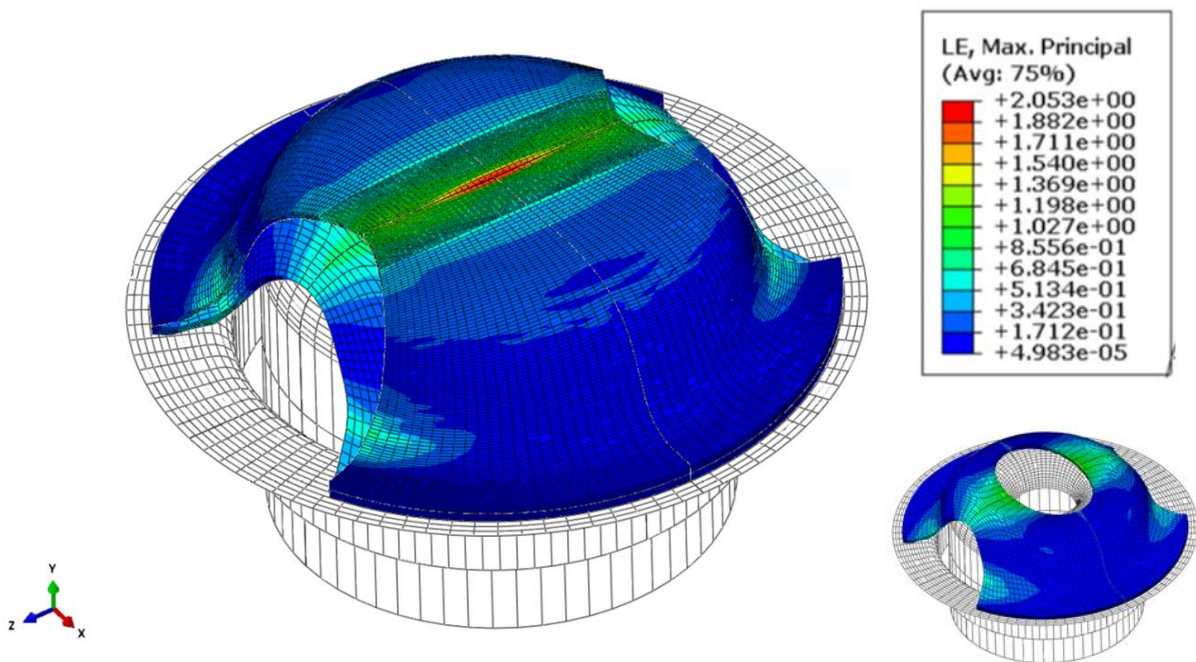


Figure 5.3.3 Simulated Marciniak plane strain tension strain path test at 400°C showing the principal logarithmic strain for 3.0-inch wide geometry at punch displacement of 1.21-inches. The strain distribution in the carrier blank is shown on the bottom right

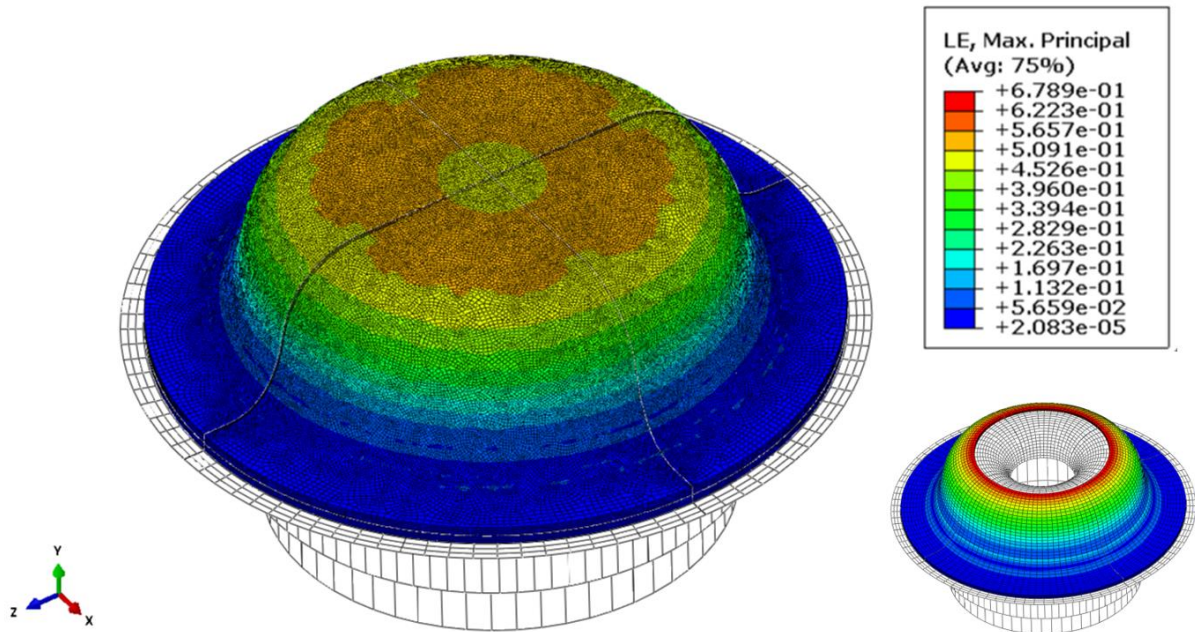
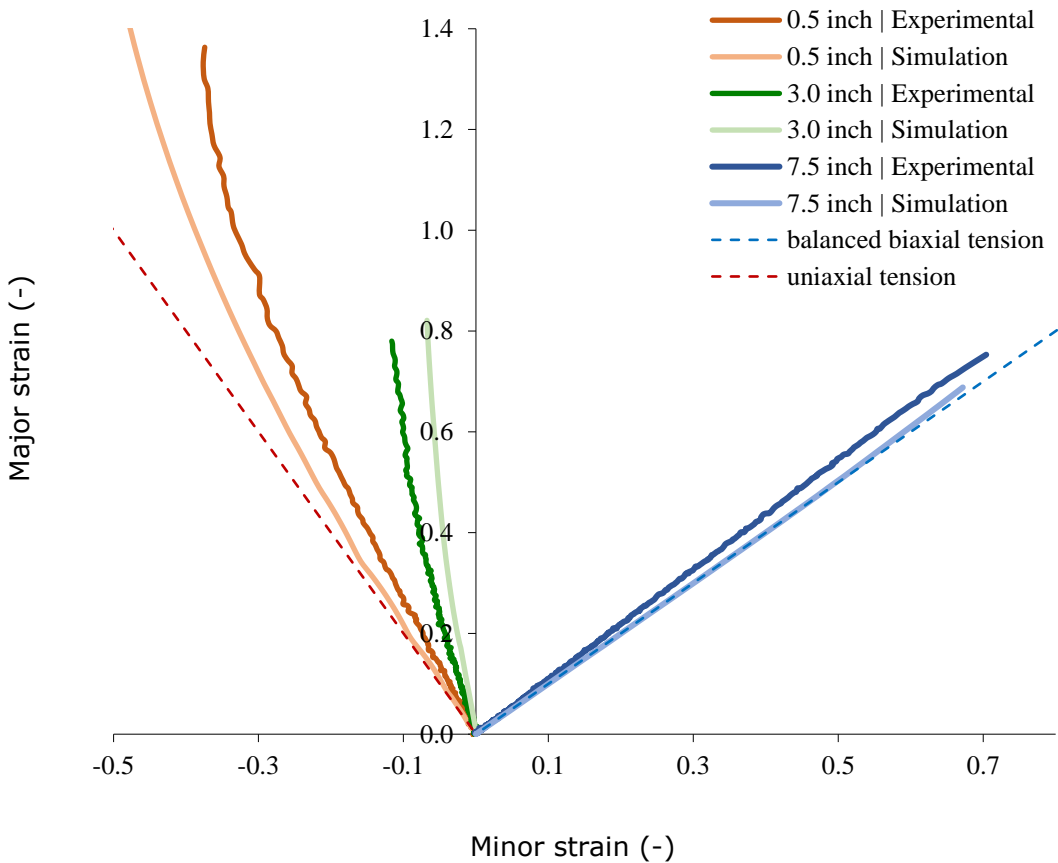


Figure 5.3.4 Simulated Marciniak balanced biaxial tension strain path test at 400°C showing the principal logarithmic strain for 3.0-inch wide geometry at a punch displacement of 1.39-inches. The strain distribution in the carrier blank is shown on the bottom right

### 5.3.3 Strain Paths and Necking Characteristics

Strain paths for cases of the experimental and simulated Marciniak tests for each of the 3 different strain paths at 400°C are presented in Figure 5.3.5. All simulated strain paths show a good agreement with experimental test cases. The simulated strain paths lie closer to the perfectly uniaxial tension and balanced biaxial tension strain paths in each case than experiments, where the 3.0-inch wide sample deviated more towards plane strain. These differences can be attributed to the highly idealized Coulomb friction model and friction coefficient values from literature, choice of the constitutive material model and use of isotropic Mises yield function.



*Figure 5.3.5 Marciniak sample strain paths at 400°C of a material point in the neck or highest strained region for both experimental and FE simulation*

As discussed, due to the nature of the FE model not incorporating a fracture criterion, limit strain was not obtained through the analysis method mentioned in ISO-12004-2:2008 as analysis was suggested to be done on the stage before fracture. Therefore, another criterion from literature, referred to as the time-dependent method (Martinez-Donaire et al., 2014) was utilized to establish the onset of localized necking and obtain the limit strain values as discussed below. According to this method, once necking was observed in the

model, the initial element outside of the necking region were used as limiting strain indicators. The elements in the neck region transitioned to a state of plane-strain while the major strain rate of those just outside the neck region showed a peak. Figures 5.3.6 and 5.3.7 show the progression of major strain rates for elements in and just outside of the necking region. As discussed, the time-dependent method determines limiting strain from an inflection in the major strain rate just outside of the neck region. The corresponding point inside the necking zone is deemed the limiting major and minor strain. Since no necking was observed in the biaxial case, only uniaxial and plane strain paths were able to define a limiting strain.

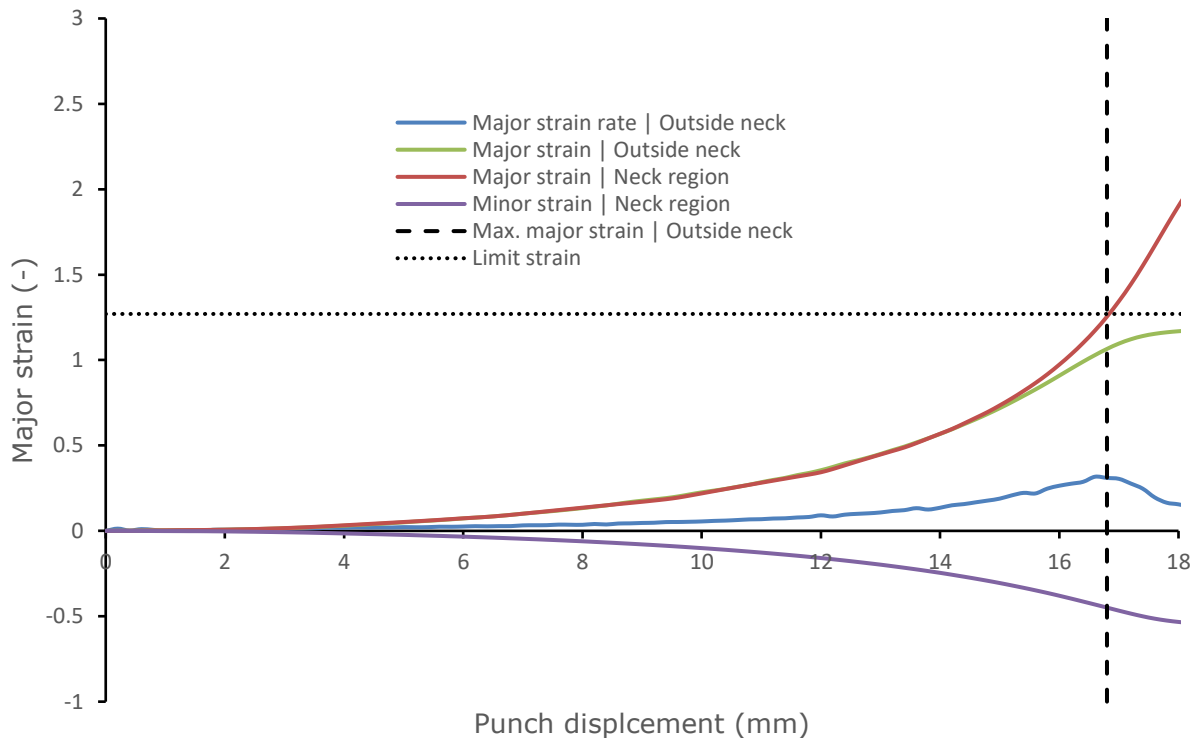


Figure 5.3.6 Time-dependent method (Martinez-Donaire et al., 2014) for calculating limiting strain for simulated Marciniak uniaxial strain path (0.5-inch geometry) at 400°C

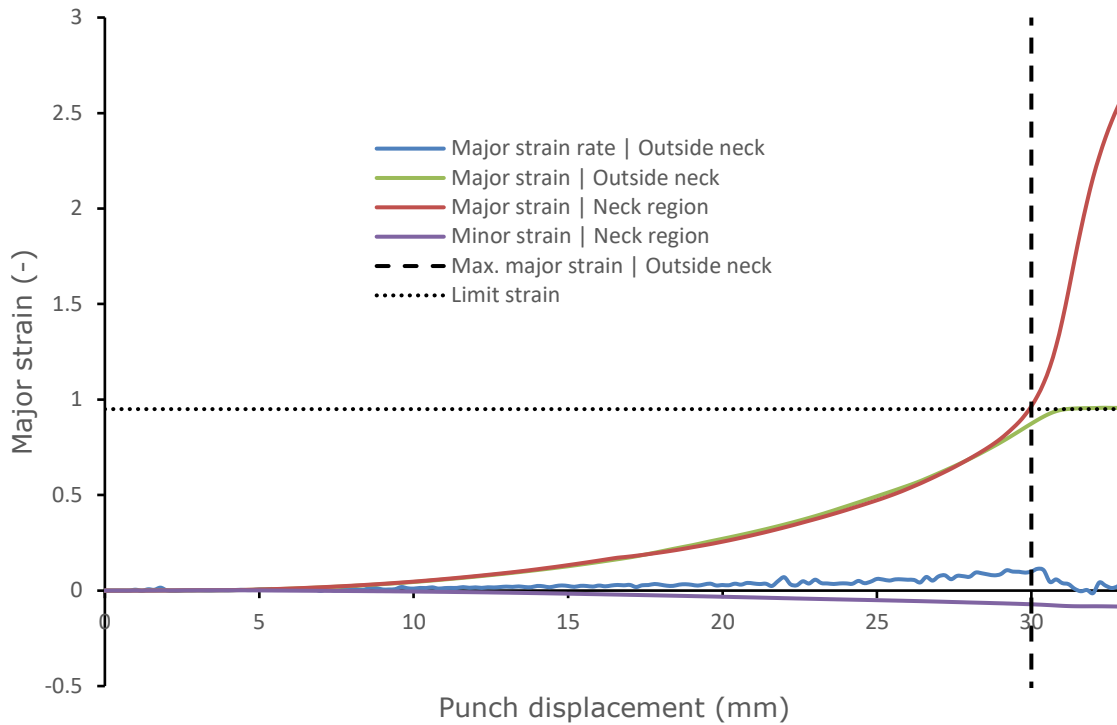


Figure 5.3.7 Time-dependent method (Martinez-Donaire et al., 2014) for calculating limiting strain for simulated Marciniak plane strain path (3-inch geometry) at 400°C

Figure 5.3.8 shows the full-field strain maps of experimental and simulated results for each of the previously stated strain paths/ sample geometries at 400°C. Experimental strain maps were taken the image before fracture and show reasonable correlation with FE results (taken at the same punch displacement) for both the uniaxial and plane strain tension cases. A deviation is observed between full-field strains of the balanced biaxial case with the experimental case showing strain localization occurring in the central region of the blank. However, the FE results showed no strain localization in the central region with a reduced strain profile in the center of the pole region. This could be explained due to the absence of an anisotropic yield criterion in

the model that may be able to capture the strain localization more accurately as well as influence of the initial imperfection in the modelled sheet.

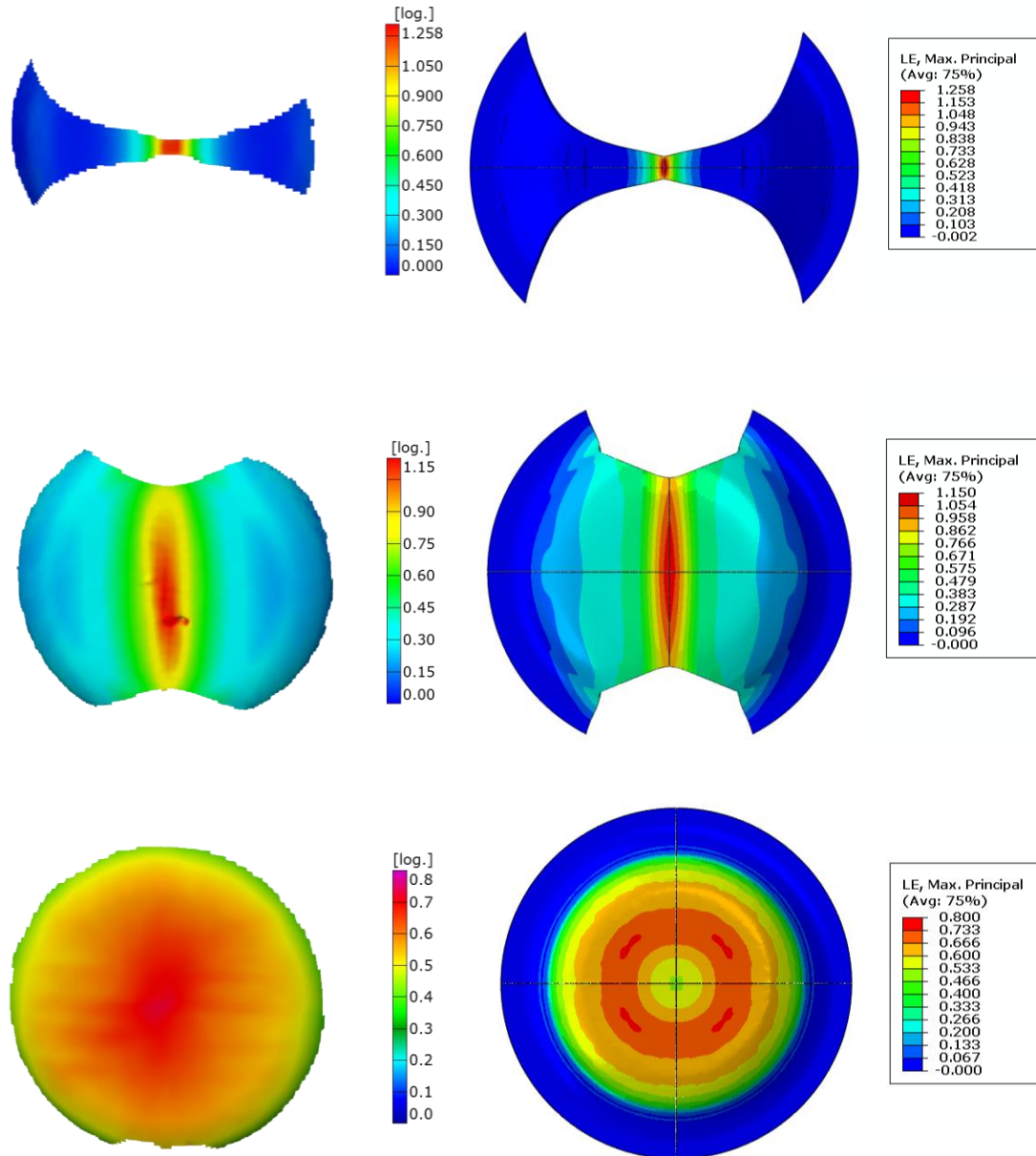


Figure 5.3.8 Full-field major strain maps of experimental (left column) and FE simulations (right column) for: (a) uniaxial tension, (b) plane strain, and (c) balanced biaxial tension strain paths at 400°C

### 5.3.4 Model FLD

Figure 5.3.9 shows experimental and FE simulation results of the forming limit curve at 400°C on the left-hand side. The model points in blue are based on just two simulations corresponding to 0.5-inch and 3.0-inch wide samples. The predictions based on FE simulation is close to values predicted in experiments even with the use of different FLD determination methods.

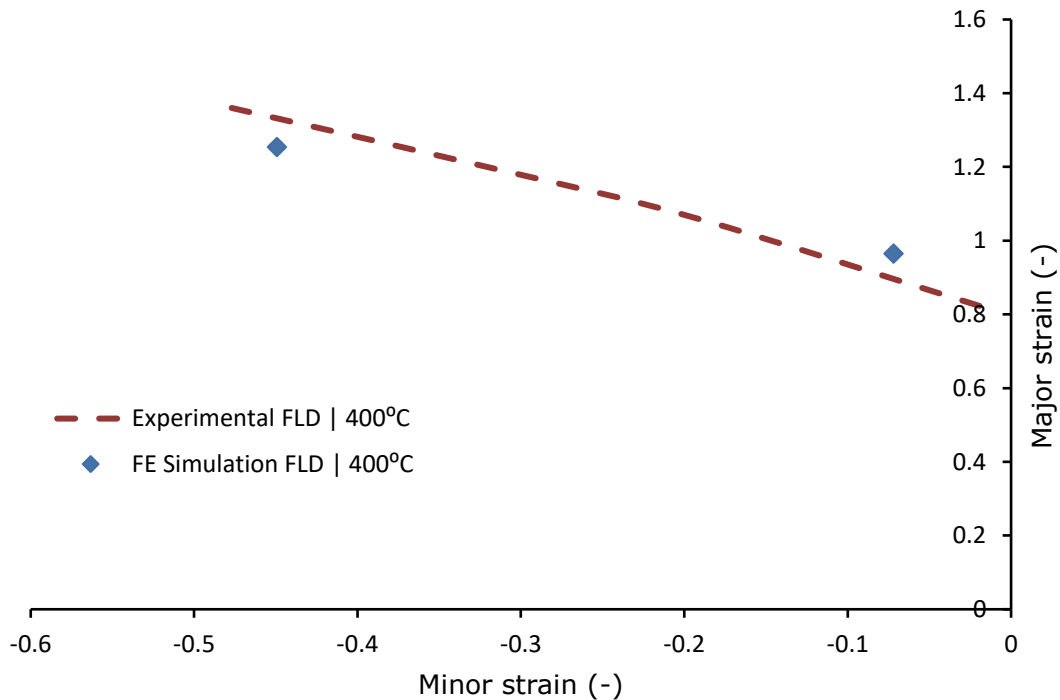


Figure 5.3.9 Experimental FLC in the tension-compression region and FE simulation based forming limit strains for uniaxial and plane strain paths at 400°C

### 5.4 Hot Stamping Results

The results related to hot stamping study of a hat-shaped part are presented in this section. As noted earlier, AA7075-F blank was heated in a separate furnace placed adjacent to the press, the blank was then manually

transferred to the press, clamped, formed into a hot shaped part, and then quenched by circulating water through the cooling channels in the die. The samples were then extracted from different regions of the formed part, artificially aged and tested in uniaxial tension to assess the feasibility of stamping AA7075-F sheet into the hat shaped part and possibility of obtaining properties close to the T6 strength of the original sheet.

### **5.4.1 Cooling Rates**

The cooling rates presented in Figure 5.4.1 show the cooling profiles of hot stamped parts. The temperature profiles correspond to each of the thermocouple ports as shown earlier in Figure 3.5.3 with position 1 starting on the left moving to position 5 on the opposite side. Therefore, there is a symmetry to the temperature measurement about the blank. This is evident in the temperature history of the curves as positions 1 and 5 and positions 2 and 4 have similar profiles. The blanks were solutionized by heating from room temperature to 480°C for 1 hour in a furnace and then transferred to the forming press and cold (room temperature) dies for forming. The temperature history curves begin when the furnace is opened, and transfer of the blank is initiated. The slow initial cooling rate from 0 to 5 seconds is a result of the transfer through air and primarily its cooling via convection, with very little radiative losses, as aluminum has a relatively low emissivity (Wen & Mudawar, 2004). From 5 to 10 seconds the cooling rate can be seen approximately doubling for positions 1 and 5 as the blank is set on the die surface where the

other positions are still in open air. The primary mode of heat loss at positions 1 and 5 is now primarily conduction. During this time, clamps are properly positioned on the press bed for blank clamping and the punch is raised to a position just below the clamped blank for forming. After 10 seconds the clamp is in place and the punch forms the part over a period of 2.25 seconds and is then held for 25 seconds and then released. The high contact pressures in the corner and clamping regions of the punch explain the increased cooling rates in positions 2 and 4. While positions 1 and 5 had an increased initial temperature loss, they exhibited a slower cooling rate later due to the lower clamping pressure in the walls of the part. Position 3 on top of the die saw little clamping until late in the process and was not clamped on both sides of the part which explained the smaller cooling rate. All temperature-time curves converged towards room temperature, progressing below 50°C, 25 seconds after blank transfer began. It is important to note that the critical temperatures range between 450°C-200°C was passed within 5 seconds in all regions of the formed part, avoiding unwanted quench induced precipitates (Sjolander et al., 2010)).

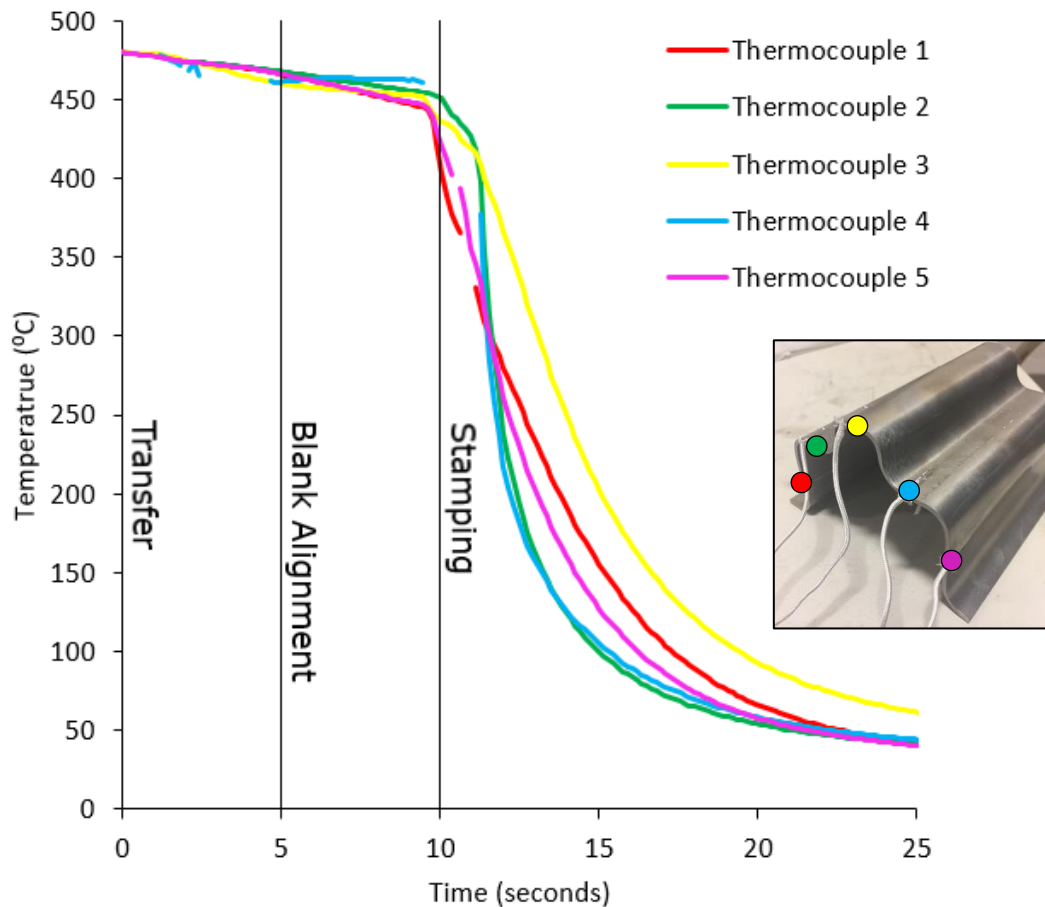


Figure 5.4.1 Cooling rate curves from 5 different positions in hot stamping blank during formation process

### 5.4.2 Post-ageing Strength

The uniaxial tensile test sample locations cut from the stamped part can be seen in Figure 5.4.2 with sample length into the page. The samples were aged to T6 temper for peak strength prior to testing. Three repeat tensile trials were completed with only a small variation in yield strength among the different regions of the formed part from where the tensile samples were extracted. The 0.2% offset yield strength was in the range 500 MPa - 550 MPa (see Figure 5.4.3). However, positions 1, 2, 6 and 7 which experienced less

clamping and a lower cooling rate were consistently among the samples with the lowest yield and ultimate strengths. Specimen positions in the part experiencing high pressure and rapid cooling such as positions 3 and 5 were among the top ultimate strength values for all repeated tests. This is consistent with the knowledge that AA7075 alloy gains its strength from the large amount of precipitates that form following the well-known precipitation sequence,  $SSSS \rightarrow GP \text{ zones} \rightarrow \eta' \rightarrow \eta$ . The lower strength could be attributed to a cooling rate slower than the critical cooling rate to avoid the nose of the CCT curve, and thus failing to maintain enough Zn and Mg in the SSSS to form the strengthening precipitates later in the age-hardening process.

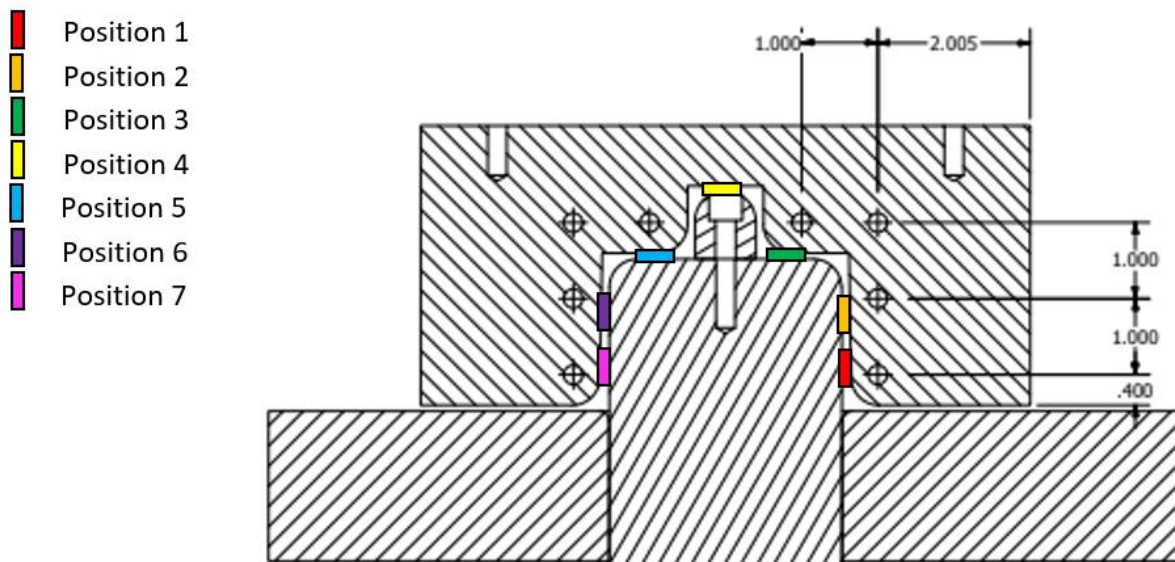


Figure 5.4.2 Locations of tensile samples taken from hot stamped part

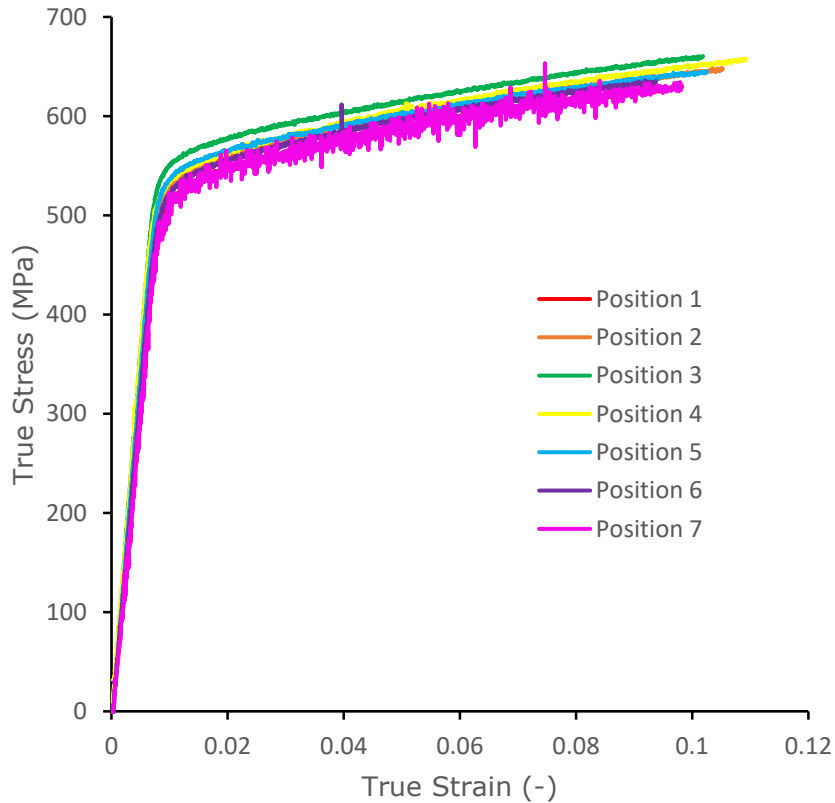
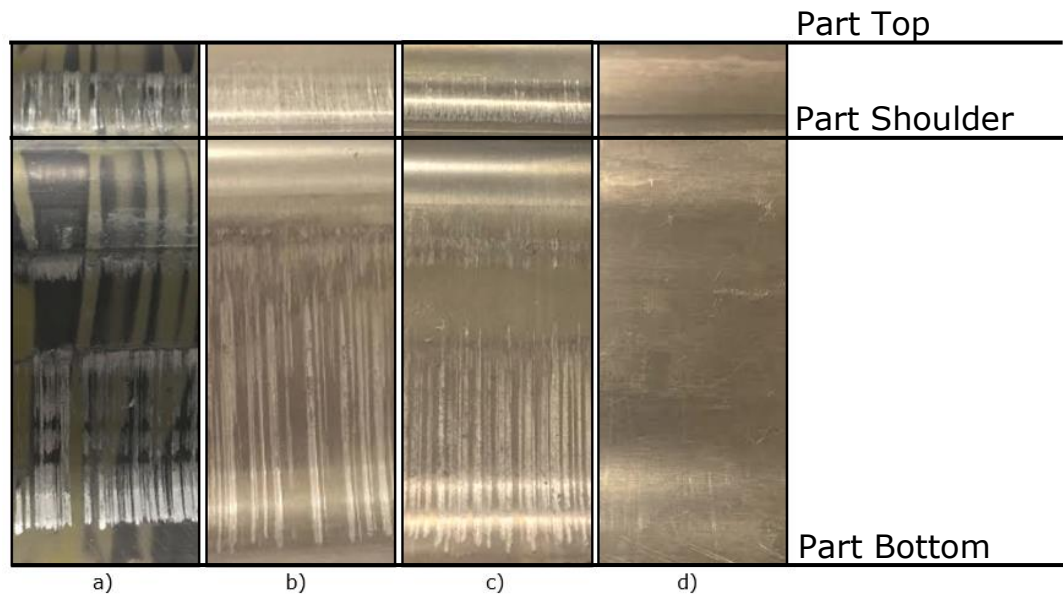


Figure 5.4.3 Post-artificial ageing stress versus strain curves from uniaxial tensile test samples cut from various regions along the hot stamped part

### 5.4.3 Part Surface Quality

The surface quality of parts is an important factor when considering high volume production parts for the automotive industry. Post-forming visual surface inspection was completed on all parts to check levels of galling and surface defects. Galling, a type of wear mechanism that occurs when binding of two materials takes place, can be detrimental to the stamping process. Material build-up on the hardened die surface can lead to part failure and downtime due to necessary die polishing steps. Several different lubricants were tried on the die surface to avoid this effect. Figure 5.4.4 shows the

surfaces after four different lubricants were applied to the die and/or blank surface. Application of Fuchs RENOFORM 10 ALWF applied to both the blank before heating and die surface before forming as well as silicon lubricant applied to the die showed part galling in all cases. Only application of Teflon film to the die showed part galling in all cases. Only application of Teflon film to the die prior to forming gave the ability to form a part without galling. The die design met standard criteria for die corner radius and was not believed to be a major cause for galling. However, it is possible that a die made of H13 or similar tool steel with a highly polished surface could have aided in reducing galling. Regardless, it is important to note that development or selection of proper high temperature lubricant for AA7075 hot stamping is necessary.



*Figure 5.4.4 Post hot stamping blank surface features for, a) Fuchs RENOFORM 10 ALWF applied to blank before heating, b) Fuchs RENOFORM 10 ALWF applied to die surface, c) Silicon lubricant applied to die surface, and d) Teflon film applied to die surface*

## 5.5 Supplementary Cooling Rate Study

To understand what quenching rates were necessary to maintain strength properties of AA7075 in the T6 temper a supplementary cooling rate study was carried out. In this study, uniaxial tensile samples were solutionized at 480°C for 1 hour and then quenched at several different quench rates. The samples were then aged to T6 temper by aging at 120°C for 24 hours and then tested in uniaxial tension to obtain T6 mechanical properties. Figure 5.5.1 shows the experimental temperature versus time traces from the cooling rate study. Five different cooling rates ranging from 3°C/s from air quenching up to a cooling rate of 800°C/s for water quenching were achieved. Tensile tests were carried out at an initial cross head velocity of 1 mm/s. The resulting engineering stress versus strain curves are shown in Figure 5.5.2. Analysis of the tensile test data showed that a tensile strength of 95 percent of T6 temper value of 600 MPa was maintained when a cooling rate of 40°C/s or above was maintained. On the other hand, a significant drop in tensile strength and strain at fracture was observed at cooling rates below 40°C/s. The above results related to part cooling rate and post-aged tensile strength for AA7075 sheet were similar to the results of Mackenzie et al. (2003) for hot stamping of AA7075 sheet, as shown in Figure 5.5.3.

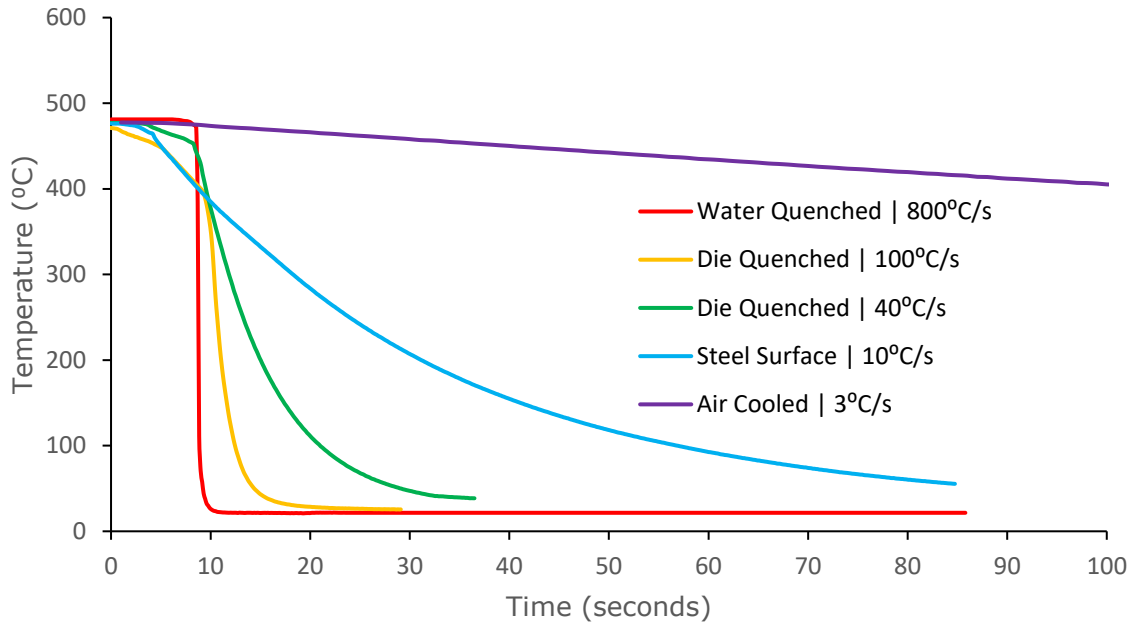


Figure 5.5.1 Tensile sample cooling rates after solutionizing samples for 1 hour and after post quench T6 tempering

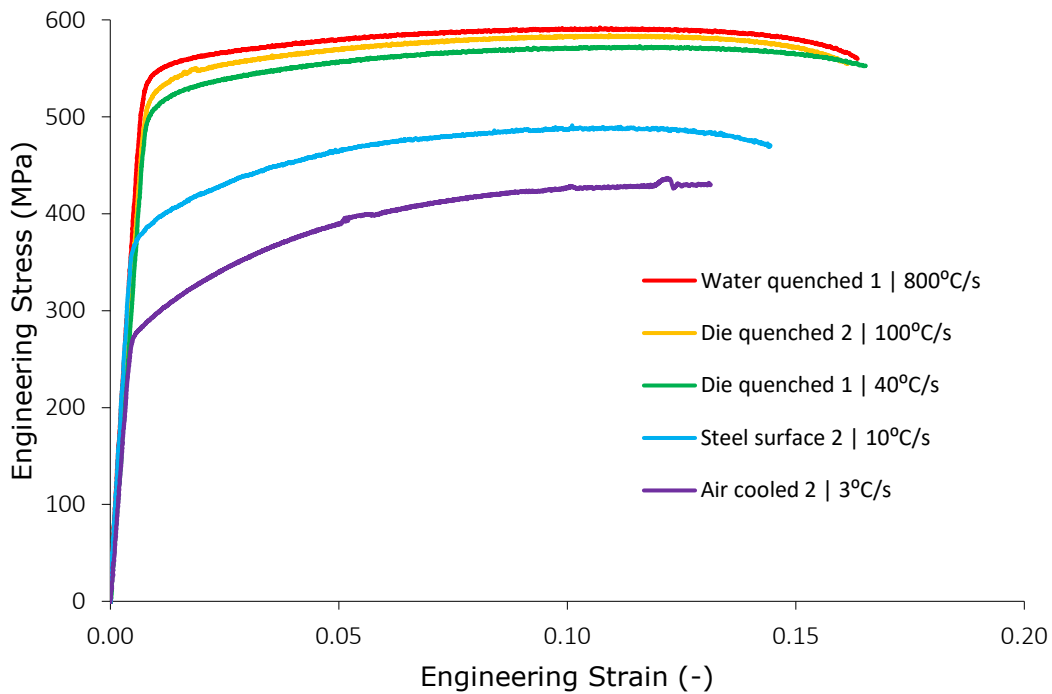


Figure 5.5.2 Engineering stress versus strain curves from uniaxial tensile test samples after solutionizing, quenching at various quench rates and artificial ageing to T6 temper state

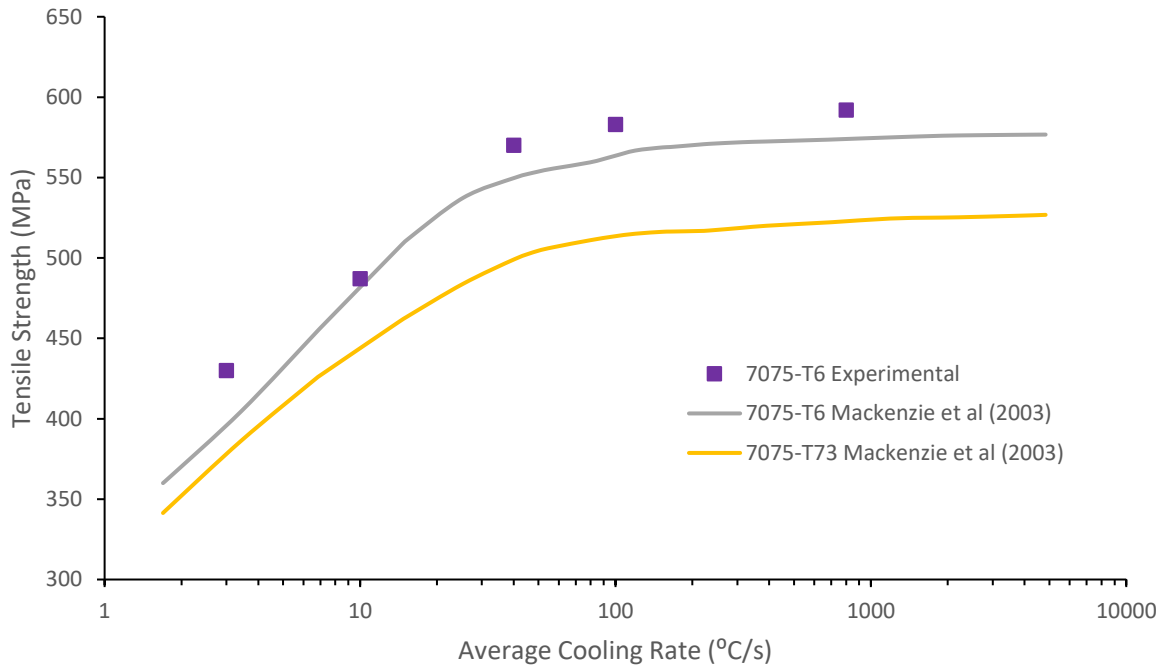


Figure 5.5.3 Effect of cooling rate on ultimate tensile strength (UTS) of AA7075

## 5.6 Summary

A high temperature Marciniak test die and blank design and aspects of the test procedure were developed to achieve good quality Marciniak test samples with necking in the unsupported region of the blank under different in-plane biaxial strain paths. Various elevated temperature mechanical and Marciniak formability test data related to elevated temperature forming of AA7075-F sheet was presented and analyzed to obtain forming and fracture limits at temperatures of 300°C, 350°C, and 400°C using online DIC strain measurement system. Very few researchers have been able to produce FLDs at elevated temperatures with AA7075 sheet above 250°C (Huang et al, 2010), where no known FLDs above these temperatures have been produced using the Marciniak test for AA7075-F. This detailed procedure should

therefore give an in depth understanding of the challenges encountered when developing elevated temperature FLDs for high strength aluminum alloys.

Complementary, microstructural studies were performed on test coupons extracted from the localized neck and fracture regions of Marciniak test samples to analyze the effect of strain path and test temperature on void-induced damage development, through-thickness fracture characteristics, and surface roughness evolution. Attempts were also made to relate elevated formability and fracture limits to the above microstructural and surface characteristics of AA7075-F sheet.

To support modeling work, additional experimental work consisted of elevated temperature uniaxial tensile testing to obtain material model parameters for the Ludwick model for use in FE models of laboratory-based elevated temperature Marciniak test. FE simulations were carried out on three different experimental specimen geometries consisting of uniaxial tension, plane strain tension, and balanced biaxial tension strain paths using ABAQUS-Explicit FE code. The modelling was useful in better understanding of the flow of material during Marciniak test and allowed for subsequent altering of the experiment test setup. Effort was also made to rigorously compare the experimental and model results related to the Marciniak test.

Lastly, hot stamping trials of AA7075 sheet were conducted using a hat-shaped in-house designed hot stamping die to understand the feasibility

of producing high strength AA7075 parts. Supplementary cooling rate, artificial ageing and post-ageing studies were also carried out to analyze the effect of cooling rate on final strength properties of the hot stamped part.

## Chapter 6

# Conclusions

The following are conclusions are drawn from this research:

1. Isothermal uniaxial tensile testing of AA7075-F sheet at elevated temperature of 300°C showed pronounced strain softening at higher initial strain rates of about  $0.2 \text{ s}^{-1}$  as well as a reduction in elongation. This softening was reduced at lower strain rates, and finally a material behavior closer to perfectly plastic state was observed. At temperatures of 400°C and 500°C slight softening was evident in all cases and showed little dependence on strain rate. The highest tested initial strain rate of  $0.2 \text{ s}^{-1}$  at 500°C showed similar flow stress to lowest strain rate of  $0.002 \text{ s}^{-1}$  at 400°C.
2. Elevated temperature Marciniak testing showed a decrease in forming force as temperature increased as well as an increase in Marciniak sample height with increasing temperature. This agreed well with the increase in forming limits and higher strains through full-field strain map analysis. Failure occurred in the unsupported pole region in a similar manner at all temperatures.
3. Strain paths during Marciniak testing showed linear proportional straining for the most part and tended towards plane strain during localized necking as reported in the literature for Marciniak testing. A

slight deviation was observed in strain path for the 4-inch geometry case due to use of an oversize carrier blank.

4. Elevated temperature FLCs at 300°C, 350°C, and 400°C showed an increase in formability on the tension-compression side of the FLD. In contrast, the FLCs on the tension-tension side tended to converge to the same point at all of the above temperatures. This can be explained in terms of extensive void-induced damage development under biaxial tension strain path which resulted in significant lowering of the fracture limit curves and led to the intersection of the fracture and forming limit curves.
5. Fracture limit curves showed an increase in formability from 300°C to 350°C mainly on the tension-compression side of the forming limit diagram. However, from 350°C to 400°C a decrease in fracture limit was observed due to significant increase in void induced damage in the formed sample at 400°C.
6. Ductile fracture with through thickness shear along the direction of void coalescence was observed at all temperatures and strain paths during elevated temperature Marciniak testing. Room temperature testing showed low elongation and fracture due to void coalescence around Al-Zn-Mg-Cu precipitates. At elevated temperature the precipitates were less pronounced at voids but were still believed to play a key role in fracture.

7. An increase in void fraction was observed with increase in temperature and stress biaxiality. Large voids were observed around Fe and Si containing constituent particles; however, they were not found to lead to extensive void coalescence and final fracture. It was the coalescence of the large numbers of smaller precipitates along shear lines that were responsible for final fracture.
8. The normalized roughness values were the highest for plane strain strain path at all temperatures. This is likely caused by the additional constraint placed on the movement of grains in the width direction. Additionally, the strain path dependence of roughening was reduced with increased temperature. Surface roughness features at 400°C biaxial tension strain appear to be related to the size of voids that formed on the sheet surface.
9. Although the FE material model employed was relatively simple, good general agreement was obtained between the experimental and model results such as punch load versus displacement, major strain distributions over the deformed specimen geometry, specific strain paths and forming limits. Prediction of forming limits on the tension-compression side of FLD at 400°C agreed well with experimental results. However, due to the absence of a fracture criterion in the FE model, forming limit prediction under balanced biaxial tension strain path was not possible.

10. Feasibility of hot stamping of AA7075-F sheet was assessed showing potential to produce quality parts using Teflon as a lubricant and a water-cooled die. Strength profiles in all areas of the part maintained 95% of T6 temper strength with a true strain of 0.10. Some effort is still necessary in the area of a suitable high temperature lubricant as some galling was evident in most test cases.
11. Supplementary cooling rate studies showed that part strength could maintained within 95% of T6 temper strength above cooling rates of 40°C/s. At lower cooling rates a rapid decrease in strength was observed.

## Chapter 7

### **Suggestion for Future Work**

The following suggestions for future work pertaining are worthy of consideration:

1. In typical industry hot stamping die quenching processes formation would take place after subsequent solutionizing. Therefore, it would be useful to investigate FLD determination at elevated temperature after solutionizing to investigate dissolution and precipitation effects on formability.
2. To ensure compatibility with industrial rates of forming, similar rates should be employed in the laboratory setting to determine elevated temperature FLDs of AA7075 sheet.
3. Marciniak test specimen design should be further optimized to reduce gaps in the strain paths on the right side and clustering of the strain paths on the left side of FLD.
4. High temperature friction tests to characterize coefficient of friction of various die materials in contact with AA7075 sheet and candidate lubricants should be developed to aid in the development of more accurate FE models.
5. More accurate temperature and strain rate dependent constitutive models of AA7075 sheet that accurately capture the shape of the stress-strain curves should be developed for use in FE modelling.

6. As shown in the corresponding works, cooling rates of 40°C/s and above appear to have little effect on material strength degradation. The effect of cooling rate of material microstructure should be more closely investigated.
7. As shown in the experimental hot stamping works the material surface features and galling can have detrimental effects on both the die surface and production as well as the part quality in the form of galling. Optimal die coatings, material coating, and lubricants could provide a wealth of information to fill this knowledge gap.
8. A key issue regarding the use of 7000-series aluminum alloys is the issue of SCC. This feature has been closely linked to cooling rates and precipitate formation. The effect of cooling rate on susceptibility to SCC should be explored.

## References

- Altenpohl, D.G. (1982). Aluminum Viewed from Within. Aluminum-Verlag. Dusseldorf
- ARAMIS. (2007). ARAMIS user manual, GOM mbH. 4 (14)
- Abachi, P., Nдавseri, P. S. Z., & Coyle, K. P. and T. W. (2016). Fracture Behavior Evaluation of High-Strength 7050 and 7075 Aluminum Alloys Using V-Notched Specimen. *Fracture Mechanics - Properties, Patterns and Behaviours*. <https://doi.org/10.5772/64463>
- Abaqus/CAE User's Guide (2016). (2016). Retrieved from <http://130.149.89.49:2080/v2016/books/usi/default.htm>
- Abovyan, T., Kridli, G. T., Friedman, P. A., & Ayoub, G. (2015). Formability prediction of aluminum sheet alloys under isothermal forming conditions. *Journal of Manufacturing Processes*, 20, 406–413. <https://doi.org/10.1016/j.jmapro.2014.08.003>
- Anderson, T. (2005). *Fracture Mechanics - Fundamentals and Applications* (3rd ed.). CRC Press Taylor and Francis Group.
- Arrieux, R., Bedrin, C. Boivin, M., 1982. Determination of an intrinsic forming limit stress diagram for isotropic metal sheets. In: proceedings of the 12<sup>th</sup> biennial Congress IDDRG, pp. 61-71
- Arzin, M., Backofen, (1970). W.A., Met. Trans, v. 1
- Affronti, E., Weidinger, M., & Merklein, M. (2018). Metallographic analysis of failure mechanisms during Nakajima tests for the evaluation of forming limits on a dual- phase steel, 8.
- Audi MediaCenter. (2017, April). Retrieved February 22, 2019, from <https://www.audi-mediacyenter.com:443/en/the-audi-q8-the-new-top-model-of-the-q-family-10412/body-10419>
- Bagheriasl, R. (2012). Formability of Aluminum Alloy Sheet at Elevated Temperature. University of Waterloo.
- Banabic, D., Comsa, S., Jurco, P., Cosovici, G., Paraianu, L., & julean, D. (2004). FLD theoretical model using a new anisotropic yield criterion, 157–158, 23–27.

Barata da Rocha, A., Barlat, F., & Jalinier, J. M. (1985). Prediction of the forming limit diagrams of anisotropic sheets in linear and non-linear loading. *Materials Science and Engineering*, 68(2), 151–164. [https://doi.org/10.1016/0025-5416\(85\)90404-5](https://doi.org/10.1016/0025-5416(85)90404-5)

Berman, B. (2015). Carbon Fiber Goes Into More Cars, but So Far, Just the Expensive Ones. *MIT Technology Review*. Retrieved from <https://www.technologyreview.com/s/539971/wheres-the-affordable-carbon-fiber-automobile/>

Beene, R., Dlouhy, J., & Lippert, J. (2018, April 2). EPA Moves to Cut Obama's Auto Mileage Rules. *Bloomberg.Com*. Retrieved from <https://www.bloomberg.com/news/articles/2018-04-02/trump-s-epa-moves-to-cut-obama-s-auto-mileage-rules-jfijl7vt>

Bragard, A., Barnet, J.C., & Bonnarens, H. (1972). A simplified technique to determine the FLD at the onset of necking. *Metall. Rep. CRM*.

Canada: Light duty: Fuel Consumption and GHG | Transport Policy. (2018). Retrieved July 18, 2018, from <https://www.transportpolicy.net/standard/canada-light-duty-fuel-consumption-and-ghg/>

Charpentier, P. L. (1975). Influence of punch curvature on the stretching limits of sheet steel. *Metallurgical Transactions A*, 6(8), 1665–1669. <https://doi.org/10.1007/BF02641986>

Chen, Z., & Fang, G. (2018). Determination of forming limit for aluminium alloy sheet eliminating the interferences of through-thickness stress and non-linear strain path. *IOP Conference Series: Materials Science and Engineering*, 418, 012051. <https://doi.org/10.1088/1757-899X/418/1/012051>

Chu, X., Leotoing, L., Guines, D., & Ragneau, E. (2014). Influence of temperature and strain rate on the formability of aluminium alloys: Comparison between experimental and predictive results. In CETIM (Ed.), *IDDRG2014* (pp. 91–96). Paris, France. Retrieved from <https://hal.archives-ouvertes.fr/hal-00999709>

Chung, K., Lee, C., & Kim, H. (2014). Forming limit criterion for ductile anisotropic sheets as a material property and its deformation path insensitivity, Part II: Boundary value problems. *International Journal of Plasticity*, 58, 35–65. <https://doi.org/10.1016/j.ijplas.2014.03.014>

Clark, R., Coughran, B., Traina, I., Hernandez, A., Scheck, T., Etuk, C., ... Es-Said, O. S. (2005). On the correlation of mechanical and physical properties of 7075-T6 Al alloy. *Engineering Failure Analysis*, 12(4), 520–526. <https://doi.org/10.1016/j.engfailanal.2004.09.005>

Considerere, A., Mrmoire sur l'emploi du fer et de l'acier dans les constructions, *Annales des Ponts et Chaussees*, Vol. 9 (1885) 574-775.

D'Amours, G., & Ilinich, A. (2018). Plasticity and Damage Modeling of the AA7075 Aluminium Alloy for Hot Stamping. *Metal Forming*, 12.

Dai, Y. Z., & Chiang, F. P. (1992). Strain path and surface roughness. *Mechanics of Materials*, 13(1), 55–57. [https://doi.org/10.1016/0167-6636\(92\)90035-C](https://doi.org/10.1016/0167-6636(92)90035-C)

Dicecco, S., Butcher, C., Worswick, M., Boettcher, E., Chu, E., & Shi, C. (2016). Determination of forming limit diagrams of AA6013-T6 aluminum alloy sheet using a time and position dependent localized necking criterion. *IOP Conference Series: Materials Science and Engineering*, 159, 012009. <https://doi.org/10.1088/1757-899X/159/1/012009>

Ding, J., Zhang, C., Chu, X., Zhao, G., Leotoing, L., & Guines, D. (2015). Investigation of the influence of the initial groove angle in the M–K model on limit strains and forming limit curves. *International Journal of Mechanical Sciences*, 98, 59–69. <https://doi.org/10.1016/j.ijmecsci.2015.04.011>

E28 Committee. (2013). *Test Methods for Tension Testing of Metallic Materials*. [https://doi.org/10.1520/E0008\\_E0008M-13A](https://doi.org/10.1520/E0008_E0008M-13A)

Fukui, Y., & Nakanishi, K., (1989) "A study on the formability of sheet steel", JSME (Japanese Society of Mechanical Engineering) International Journal, Series 1, Vol. 32, No. 1.

Gerold, V., (1979). Precipitation hardening. In: Nabarro, F.R.N. (Ed.), *Dislocations in Solids*. North-Holland, p. 222

Ghosh, A. K., & Hecker, S. S. (1974). Stretching limits in sheet metals: In-plane versus out-of-plane deformation. *Metallurgical Transactions*, 5(10), 2161–2164. <https://doi.org/10.1007/BF02643929>

Gurson, A. (1977). Continuum theory of ductile rupture by void nucleation and growth: Part I - Yield criteria and flow rules for porous ductile media. *Journal of Engineering Materials Technology*; 99:2.

Guo, Y., Zhou, M., Sun, X., Qian, L., Li, L., Xie, Y., ... Zhao, H. (2018). Effects of Temperature and Strain Rate on the Fracture Behaviors of an Al-Zn-Mg-Cu Alloy. *Materials*, 11(7). <https://doi.org/10.3390/ma11071233>

Gutierrez, D., Lara, A., Casellas, D., & Prado, J. M. (2010). Effect of Strain Paths on Formability Evaluation of TRIP Steels. *ResearchGate*, 89–91, 214–219.

Hashimoto, S. (1986). *Hot working of aluminum alloy 7075* (Thesis). Massachusetts Institute of Technology. Retrieved from <http://dspace.mit.edu/handle/1721.1/49572>

Hosford, W. F., & Caddell, R. M. (2011). *Metal Forming* (4th ed.). Cambridge.

Hsu, E., Carsley, J. E., & Verma, R. (2008). Development of Forming Limit Diagrams of Aluminum and Magnesium Sheet Alloys at Elevated Temperatures. *Journal of Materials Engineering and Performance*, 17(3), 288–296. <https://doi.org/10.1007/s11665-007-9196-y>

Hu, H., Zhen, L., Yang, L., Shao, W., & Zhang, B. (2007). Deformation behavior and microstructure evolution of 7050 aluminum alloy during high temperature deformation. *Materials Science and Engineering*, 64–71. <https://doi.org/10.1016/j.msea.2007.10.051>

Huang, H., LI, D.-y., & PENG, Y.-h. (2010). Experimental study on the forming limit diagrams (FLD) of 7075-T6 aluminum alloy sheet at warm state. *Journal of Plasticity Engineering*, 17(1), 93-97.

Hull, D. (1999). *Fractography: observing, measuring and interpreting fracture surface topography*. Cambridge: Cambridge University Press.

Jacumasso, S. C., Martins, J. de P., Carvalho, A. L. M. de, Jacumasso, S. C., Martins, J. de P., & Carvalho, A. L. M. de. (2016). Analysis of precipitate density of an aluminium alloy by TEM and AFM. *REM - International Engineering Journal*, 69(4), 451–457. <https://doi.org/10.1590/0370-44672016690019>

Jordon, J. B., Horstemeyer, M. F., Solanki, K., Bernard, J. D., Berry, J. T., & Williams, T. N. (2009). Damage characterization and modeling of a 7075-T651 aluminum plate. *Materials Science and Engineering: A*, 527(1), 169–178. <https://doi.org/10.1016/j.msea.2009.07.049>

J.R, Davis. (2001). Aluminum and Aluminum Alloys, 351–416. <https://doi.org/10.1361/autb2001p351>

Kanaya, K., & Okayama, S. (1972). Penetration and energy-loss theory of electrons in solid targets. *Journal of Physics D: Applied Physics*, 5(1), 43–58. <https://doi.org/10.1088/0022-3727/5/1/308>

Kotkunde, N., Deole, A. D., & Gupta, A. K. (2014). Prediction of Forming Limit Diagram for Ti-6Al-4V Alloy Using Artificial Neural Network. *Procedia Materials Science*, 6, 341-346. doi: 10.1016/j.mspro.2014.07.043

Kumar, S. D., Amjith, T. R., & Anjaneyulu, C. (2016). Forming Limit Diagram Generation of Aluminum Alloy AA2014 Using Nakazima Test Simulation Tool. *Procedia Technology*, 24, 386–393. <https://doi.org/10.1016/j.protcy.2016.05.053>

Leong, I. (2008). Aluminum 7075-T6 Cyclic fatigue testing at elevated temperatures. University of New South Wales.

Li, H., Bin, J., Zhao, Y., & Wang, X. (2011). Establishment of continuous cooling transformation diagrams of aluminum alloys using in situ voltage measurement. *Transactions of Nonferrous Metals Society of China*, 21(9), 1944–1949. [https://doi.org/10.1016/S1003-6326\(11\)60954-0](https://doi.org/10.1016/S1003-6326(11)60954-0)

Li, J., Peng, Z., Li, C., Jia, Z., Chen, W., & Zheng, Z. (2008). Mechanical properties, corrosion behaviors and microstructures of 7075 aluminium alloy with various aging treatments. *Transactions of Nonferrous Metals Society of China*, 18(4), 755–762. [https://doi.org/10.1016/S1003-6326\(08\)60130-2](https://doi.org/10.1016/S1003-6326(08)60130-2)

Liu, Y., Zhu, Z., Wang, Z., Zhu, B., Wang, Y., & Zhang, Y. (2017). Formability and lubrication of a B-pillar in hot stamping with 6061 and 7075 aluminum alloy sheets. *Procedia Engineering*, 207, 723–728. <https://doi.org/10.1016/j.proeng.2017.10.819>

Mackenzie, D., Totten, G., Eds. (2003) Handbook of Aluminum, Volume 1: Physical Metallurgy and Processes, CRC Press, pp. 103, 106, 108, 121-129, 882-885, 908, 1002.

Marciniak, Z., & Duncan, J. L. (1992). *The Mechanics of Sheet Metal Forming*. Edward Arnold. Retrieved from <https://books.google.ca/books?id=7mWYQgAACAAJ>

Marciniak, Z., Kuczynski, K., (1967). Limit Strains in the Processes of Stretch-Forming Sheet Metal. *International Journal of Mechanical Sciences* 9, 609-620.

Marciniak, Z., Kuczyński, K., & Pokora, T. (1973). Influence of the plastic properties of a material on the forming limit diagram for sheet metal in tension. *International Journal of Mechanical Sciences*, 15(10), 789–800. [https://doi.org/10.1016/0020-7403\(73\)90068-4](https://doi.org/10.1016/0020-7403(73)90068-4)

Martínez-Donaire, A., Garcia-Lomas, F. and Vallellano, C., (2014) New approaches to detect the onset of localised necking in sheets under through-thickness strain gradients," *Materials and Design*, 57, 135-45.

McClintock, F. (1968). A criterion of ductile fracture by growth of holes. *Journal of Applied Mechanics*; 35:363.

McDanel, D., & Hoffman, C. (1984). Microstructure and orientation effects on properties of discontinuous silicon carbide/aluminum composites (No. 2302). Cleveland, Ohio: Lewis Research Center.

Merklein, M., Lechler, J., (2008). Determination of material and process characteristics for hot stamping processes of quenchable ultra high strength steels with respect to a FE-based process design. SAE World Congress: Innovations in Steel and Applications of Advanced High Strength Steels for Automobile Structures, Paper No. 2008-0853.

Mikó, T., & Barkoczy, P. (2013). Determination of the Onset of the Dynamic Recrystallization of a 7075 Al Alloy. *Materials Science Forum*, 752, 105–114. <https://doi.org/10.4028/www.scientific.net/MSF.752.105>

Mohamed, M., Elatriby, S., Shi, Z., & Lin, J. G. (2016). Prediction of Forming Limit Diagram for AA5754 Using Artificial Neural Network Modelling. *Key Engineering Materials*, 716, 770–778. <https://doi.org/10.4028/www.scientific.net/KEM.716.770>

Olawale, O., Isadore, A., Aremo, B., Adeoye, M., & Shittu, M. (2012). Effect of Heat Treatment on Some Mechanical Properties of 7075 Aluminium Alloy. *Materials Research*. <https://doi.org/10.1590/S1516-14392012005000167>

Pepelnjak, T., Petek, A., & Kuzman, K. (2005). *Analyses of the forming limit diagram in digital environment* (Vol. 6, pp. 697-704). Trans Tech Publications.

Pepelnjak, T., & Kuzman, K. (2007). Numerical determination of the forming limit diagrams. *Journal of Achievements in Materials and Manufacturing Engineering*. Retrieved from [https://www.researchgate.net/publication/42253394\\_Numerical\\_determination\\_of\\_the\\_forming\\_limit\\_diagrams](https://www.researchgate.net/publication/42253394_Numerical_determination_of_the_forming_limit_diagrams)

Polmear, I. J. (2004). Aluminium Alloys – A Century of Age Hardening, 14.

Polmear, I.J., (2006). *Light Alloys; From Traditional Alloys to Nanocrystals*. Butterworth Heinemann, Oxford, pp. 43–69.

Rao, A. C. U., Vasu, V., Govindaraju, M., & Srinadh, K. V. S. (2014). Influence of Cold Rolling and Annealing on the Tensile Properties of Aluminum 7075 Alloy. *Procedia Materials Science*, 5, 86–95. <https://doi.org/10.1016/j.mspro.2014.07.245>

Safari, M., Hosseinipour, S. J., & Azodi, H. D. (2011). Experimental and Numerical Analysis of Forming Limit Diagram (FLD) and Forming Limit Stress Diagram (FLSD). *Materials Science and Applications*, 497–503.

Shao, Z., Bai, Q., Li, N., Lin, J., Shi, Z., Stanton, M., ... Dean, T. (2018). Experimental investigation of forming limit curves and deformation features in warm forming of an aluminium alloy. *Proceedings of the Institution of Mechanical Engineers, Part B: Journal of Engineering Manufacture*, 232(3), 465–474. <https://doi.org/10.1177/0954405416645776>

Sjolander, E., and Seifeddine, S. (2010), "The heat treatment of Al-Si-Cu-Mg casting alloys," *Journal of Materials Processing Technology*, vol. 210, pp. 1249-1259.

Steel Definitions | WorldAutoSteel. (2018). Retrieved February 21, 2019, from <https://www.worldautosteel.org/steel-basics/automotive-steel-definitions/>

Trefis Team. (2018). Trends in Steel Usage in The Automotive Industry. *Forbes*. Retrieved from <https://www.forbes.com/sites/greatspeculations/2015/05/20/trends-in-steel-usage-in-the-automotive-industry/>

Urbánek, M., Farahnak, P., Rund, M., & Džugan, J. (2018). Sheet Thickness Reduction Influence on Fracture Strain Determination. *Journal of Physics: Conference Series*, 1063, 012168. <https://doi.org/10.1088/1742-6596/1063/1/012168>

Wang, D., Ni, D. R., & Ma, Z. Y. (2008). Effect of pre-strain and two-step aging on microstructure and stress corrosion cracking of 7050 alloy. *Materials Science and Engineering: A*, 494(1), 360–366. <https://doi.org/10.1016/j.msea.2008.04.023>

Wen, C.-D., & Mudawar, I. (2004). Emissivity characteristics of roughened aluminum alloy surfaces and assessment of multispectral radiation thermometry (MRT) emissivity models. *International Journal of Heat and Mass*

*Transfer*, 47(17–18), 3591–3605.  
<https://doi.org/10.1016/j.ijheatmasstransfer.2004.04.025>

Yang, Z. (2018, March 20). Overview of Global Fuel Economy Policies. ICCT.

Yi, H. L., Sun, L., & Xiong, X. C. (2018). Challenges in the formability of the next generation of automotive steel sheets. *Materials Science and Technology*, 34(9), 1112–1117. <https://doi.org/10.1080/02670836.2018.1424383>

Zdravecky, D. (2007). Formability and Failure of Automotive Sheet Material AA5754. McMaster University.

Zhang, C., Chu, X., Guines, D., Leotoing, L., Ding, J., & Zhao, G. (2014). Effects of Temperature and Strain Rate on the Forming Limit Curves of AA5086 Sheet. *Procedia Engineering*, 81, 772–778.  
<https://doi.org/10.1016/j.proeng.2014.10.075>

Zhang, C., Leotoing, L., Guines, D., & Ragneau, E. (2009). Theoretical and numerical study of strain rate influence on AA5083 formability. *Journal of Materials Processing Technology*, 209(8), 3849–3858.  
<https://doi.org/10.1016/j.jmatprotec.2008.09.003>

Zhou, M., Lin, Y. C., Deng, J., & Jiang, Y.-Q. (2014). Hot tensile deformation behaviors and constitutive model of an AlZnMgCu alloy. *Materials and Design*, (59), 141–150. <https://doi.org/10.1016/j.matdes.2014.02.052>

## Appendix A

### Cooling Channel Optimization Calculations

As previously mentioned, during die design cooling channels were added to ensure a consistent die temperature was maintained as well as maximize cooling rates. These calculations utilized the chillers flow rate of 4.3 GPM as a boundary condition.

$$\text{Volumetric Flow Rate} = \dot{Q} = 4.3\text{GPM} = 4.3\text{GPM} \cdot \frac{\text{min}}{60\text{s}} \cdot \frac{1\text{m}^3}{264.172\text{ Gallons}} = 0.000271 \frac{\text{m}^3}{\text{s}}$$

Since heat transfer is maximized when fluids experience turbulent flow, therefore channel sizing was chosen based on geometry constraints on the overall die dimensions as well as fitting the maximum amount of channel that ensure turbulent flow. The estimated temperature of the working fluid (distilled water) was assumed to be 30°C which corresponds to:

$$\text{Density} = \rho = 996 \frac{\text{kg}}{\text{m}^3}$$

$$\text{Dynamic Viscosity} = \mu = 0.798 \times 10^{-3} \frac{\text{kg}}{\text{m}\cdot\text{s}}$$

To ensure maximum heat transfer, turbulent flow must be obtained, meaning Reynolds number (Re) must remain above 4,000 for circular pipes.

$$\text{Reynolds Number} = Re = \frac{4\dot{m}}{\pi D \mu}$$

Where:

$$\text{Mass Flow Rate } \left(\frac{kg}{s}\right) = \dot{m}$$

$$\text{Inner Diameter (m)} = D$$

Therefore, the mass flow rate of the chiller is:

$$\dot{m} = (\dot{Q})\rho$$

$$\dot{m}_{total} = (0.000271 \text{ m}^3/\text{s}) \cdot (996 \text{ kg/m}^3)$$

$$\dot{m}_{total} = 0.27 \text{ kg/s}$$

After analyzing the die geometry, a starting point of 10 channels was chosen to ensure that 1/8" NPT fittings could be installed with ease.

$$\dot{m} = \dot{m}_{total}/10$$

$$\dot{m} = 0.027 \text{ kg/s}$$

Back calculating for hole diameter with an assumed Reynolds number of 10,000 to ensure turbulence.

$$D = \frac{4\dot{m}}{\pi \cdot \mu \cdot Re}$$

$$D = \frac{4(0.027 \text{ kg/s})}{\pi \cdot 0.798 \times 10^{-3} \frac{\text{kg}}{\text{m} \cdot \text{s}} \cdot 10000}$$

$$D = 0.00431 \text{ m}$$

Although a nominal hole size of 1/8" is close to the results, drilling a hole through the die of this depth was decided against and calculations were repeated for the number of holes needed to ensure turbulence with a 1/4" hole.

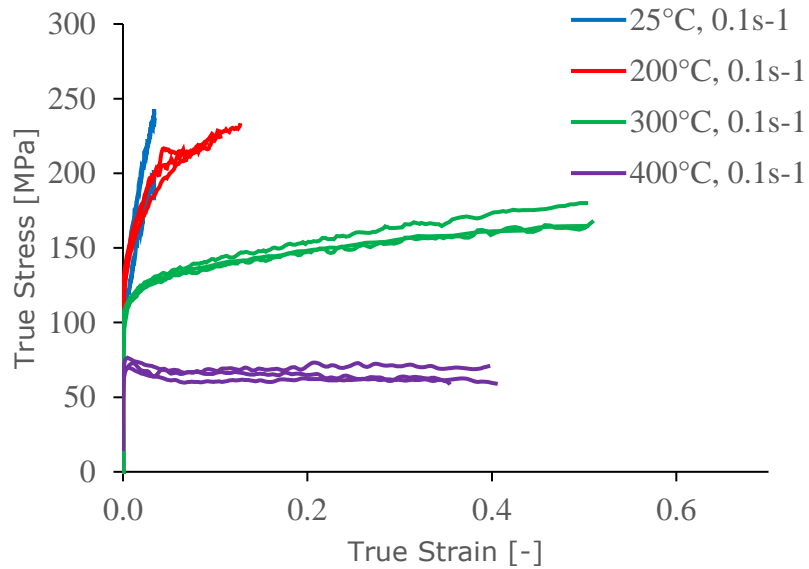
$$0.00635m = \frac{4\left(\frac{0.27kg}{s}\right)/(\text{Number of channels})}{\pi \cdot 0.798 \times 10^{-3} \frac{kg}{m \cdot s} \cdot 10000}$$

$$\text{Number of Channels} = 6.79$$

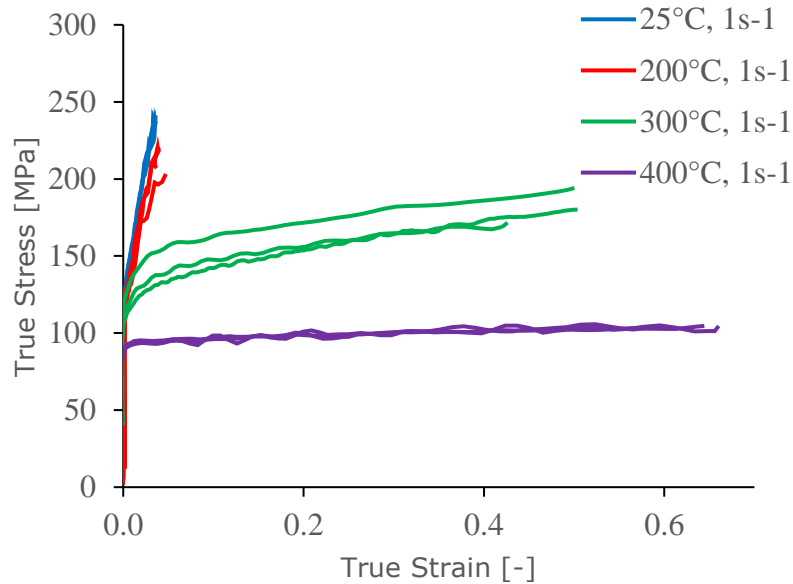
Selecting 8 cooling channels for symmetry and assembly purposes gives a Reynolds number of 8,485, well above the 2,900 target.

## Appendix B

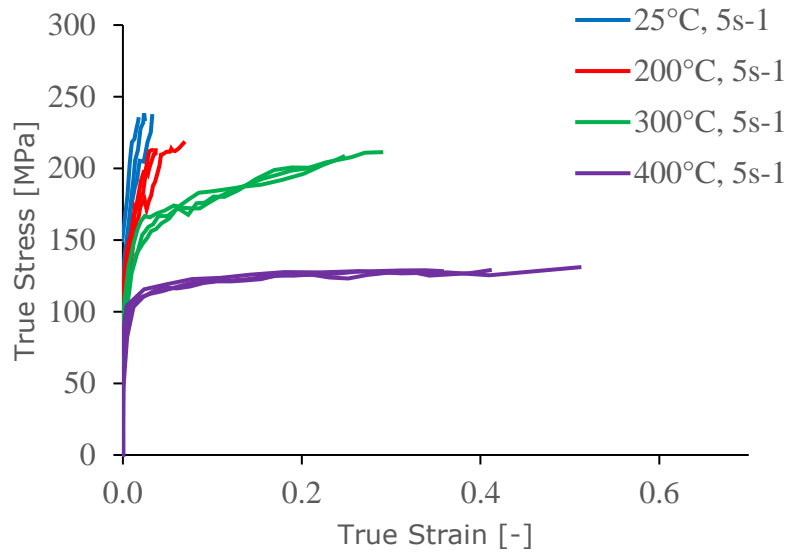
# Gleeble Tensile Testing Results for AA7075



*Effect of temperature on true stress versus true strain for AA7075-F tested at  $0.1s^{-1}$  using Gleeble® thermo-mechanical simulator*



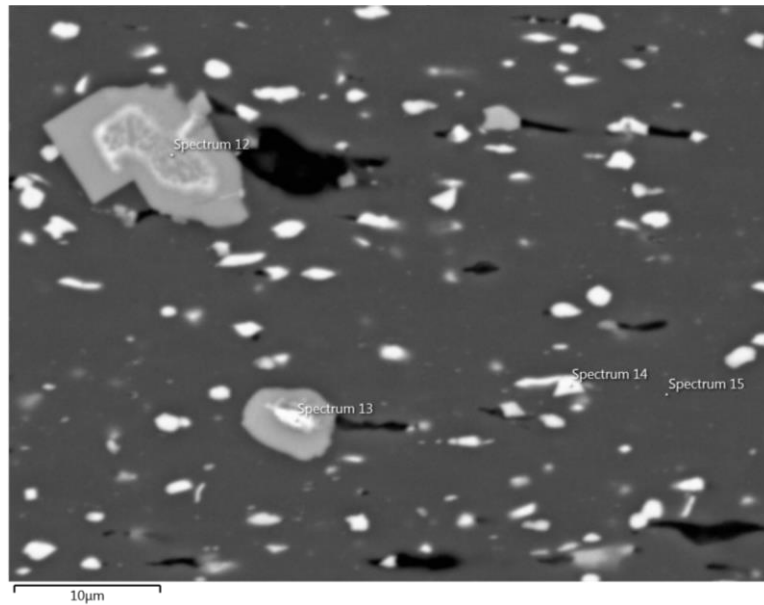
*Effect of temperature on true stress versus true strain for AA7075-F tested at  $1.0 s^{-1}$  using Gleeble® thermo-mechanical simulator*



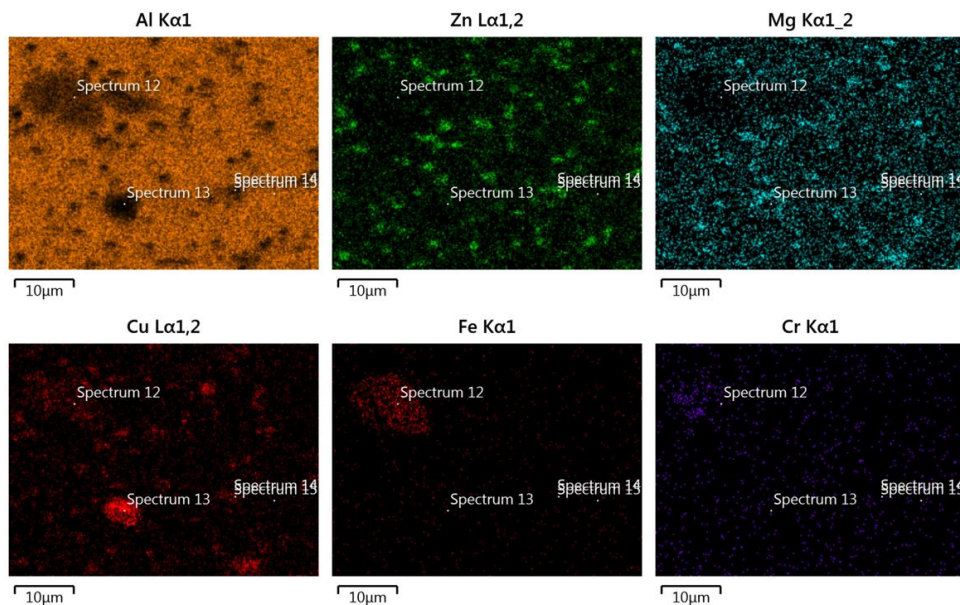
*Effect of temperature on true stress versus true strain for AA7075-F tested at 5.0 s<sup>-1</sup> using Gleeble® thermo-mechanical simulator*

## Appendix C

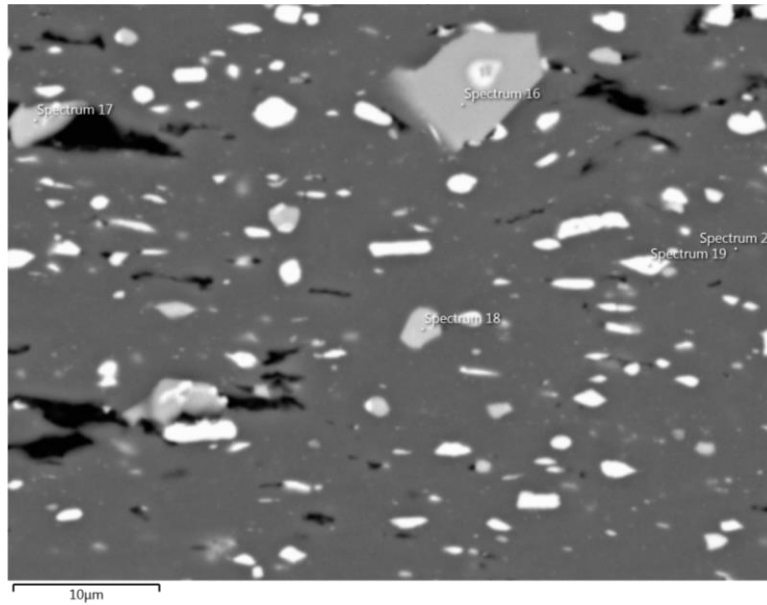
# EDS Mapping of Polished Fracture Samples



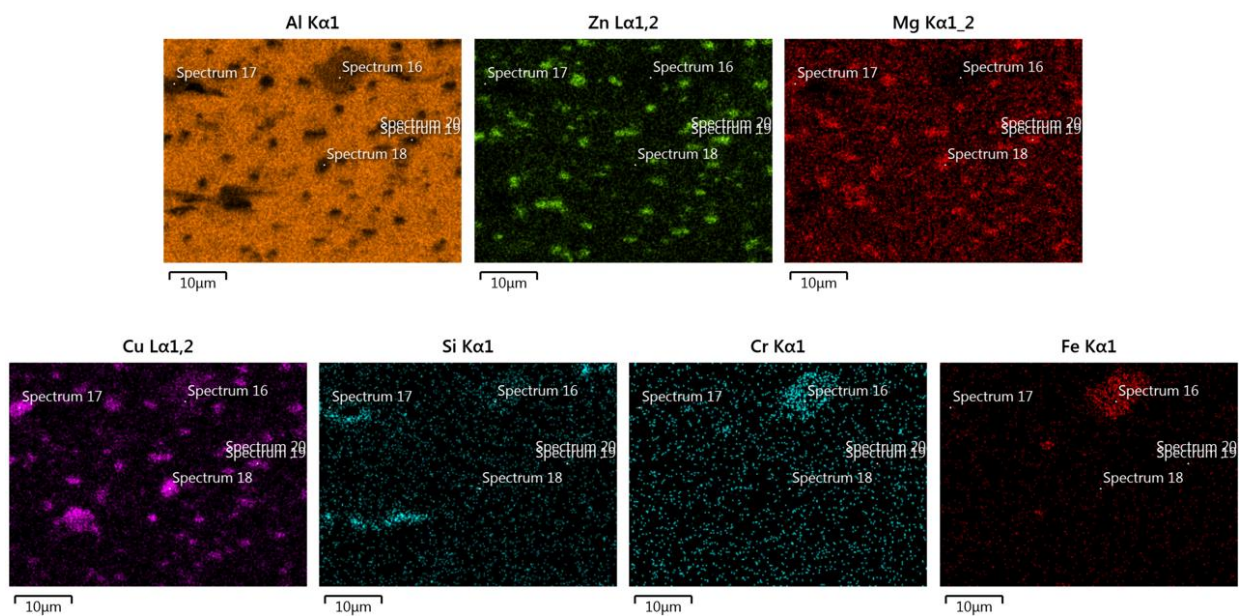
*BSE image of fracture region for 3-inch wide sample at 300°C*



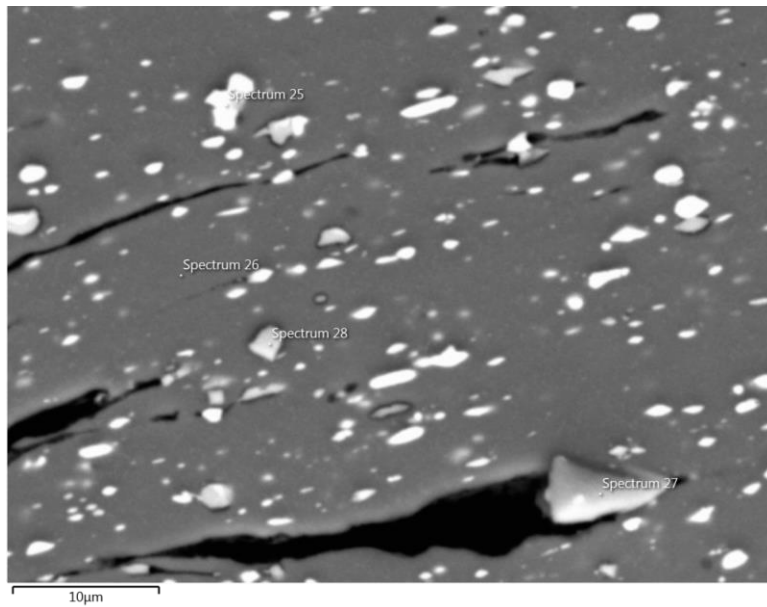
*EDS maps of 3-inch wide sample at 300°C from BSE fracture region image*



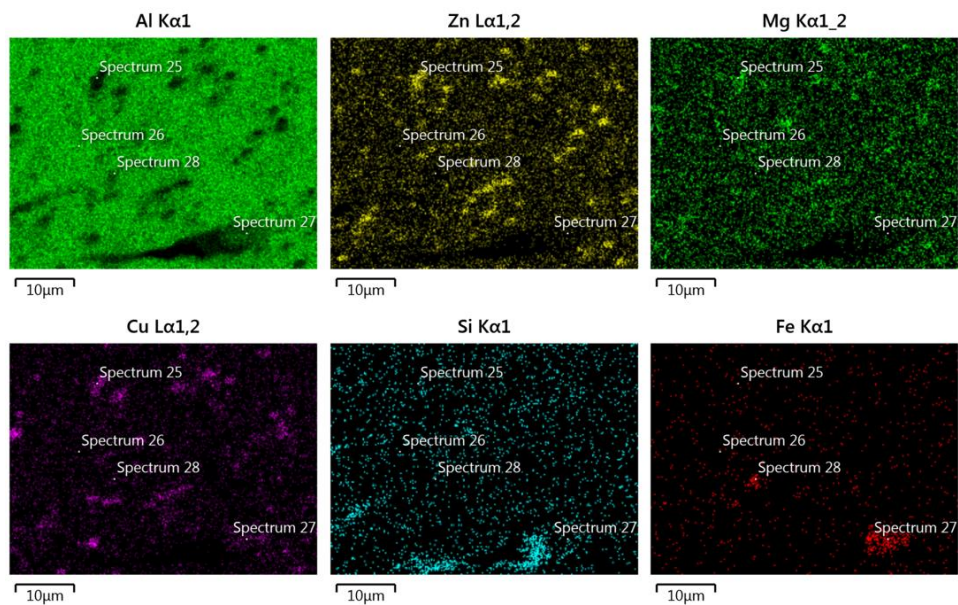
*BSE image of fracture region for 7.5-inch diameter sample at 300°C*



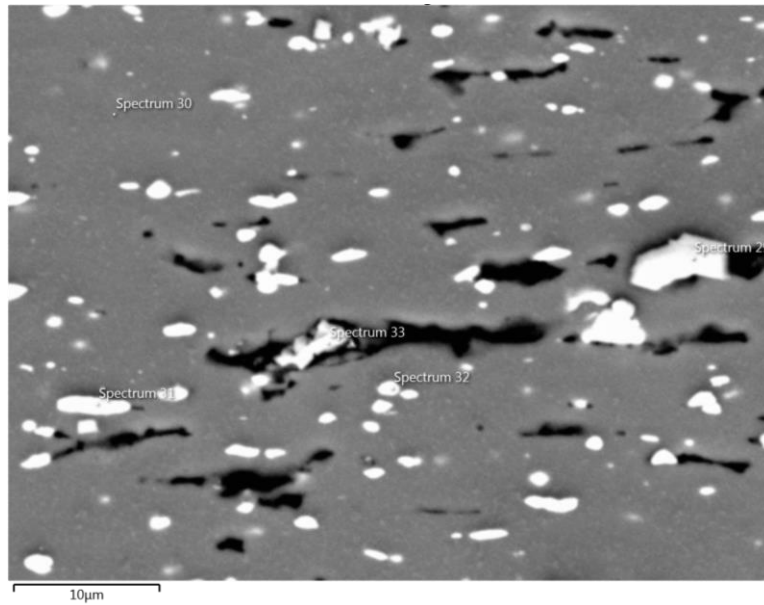
*EDS maps of 7.5-inch diameter sample at 300°C from BSE fracture region image*



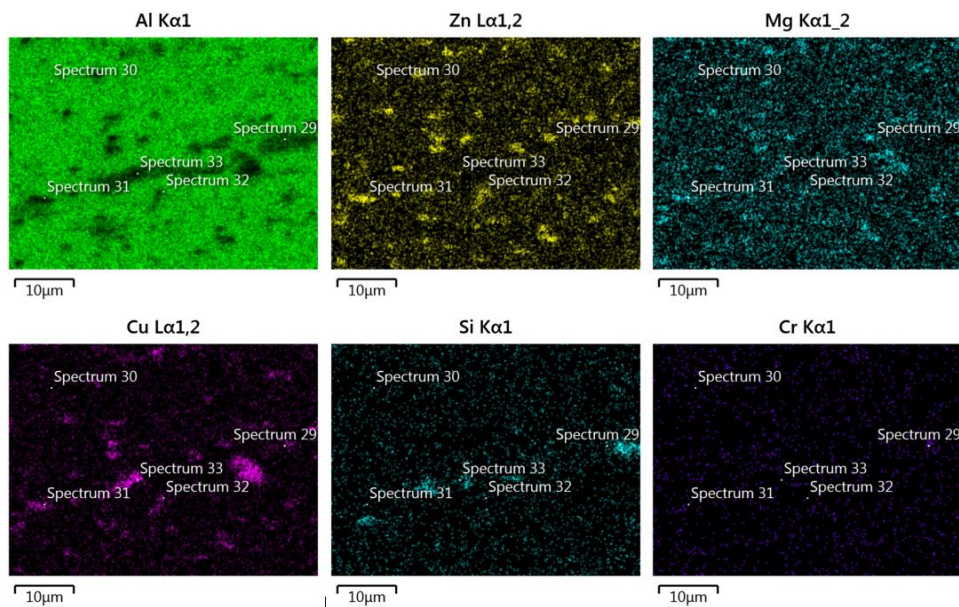
*BSE image of fracture region for 3-inch wide sample at 350°C*



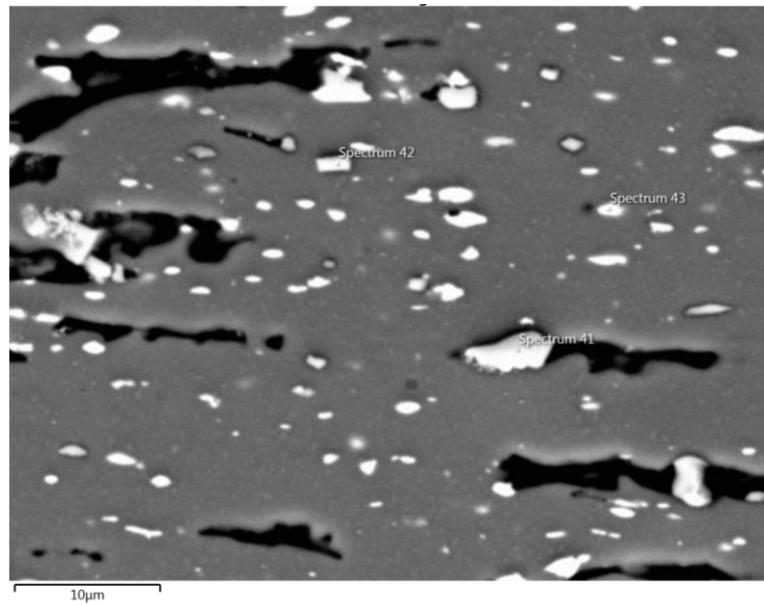
*EDS maps of 3-inch wide sample at 350°C from BSE fracture region image*



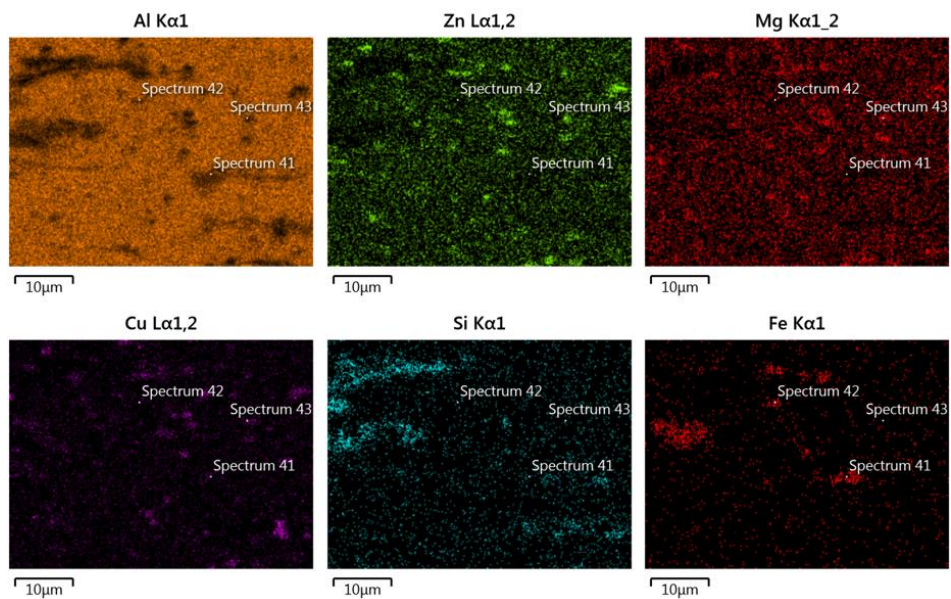
*BSE image of fracture region for 7.5-inch diameter sample at 350°C*



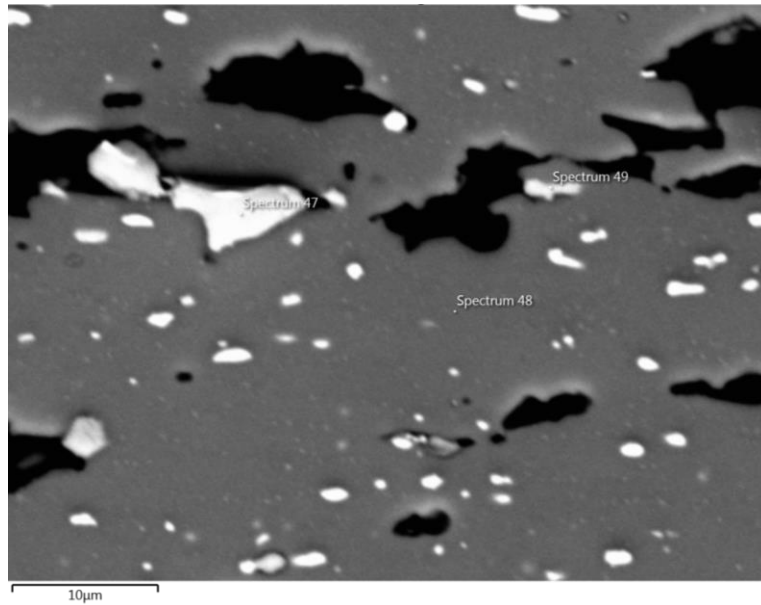
*EDS maps of 7.5-inch diameter sample at 350°C from BSE fracture region image*



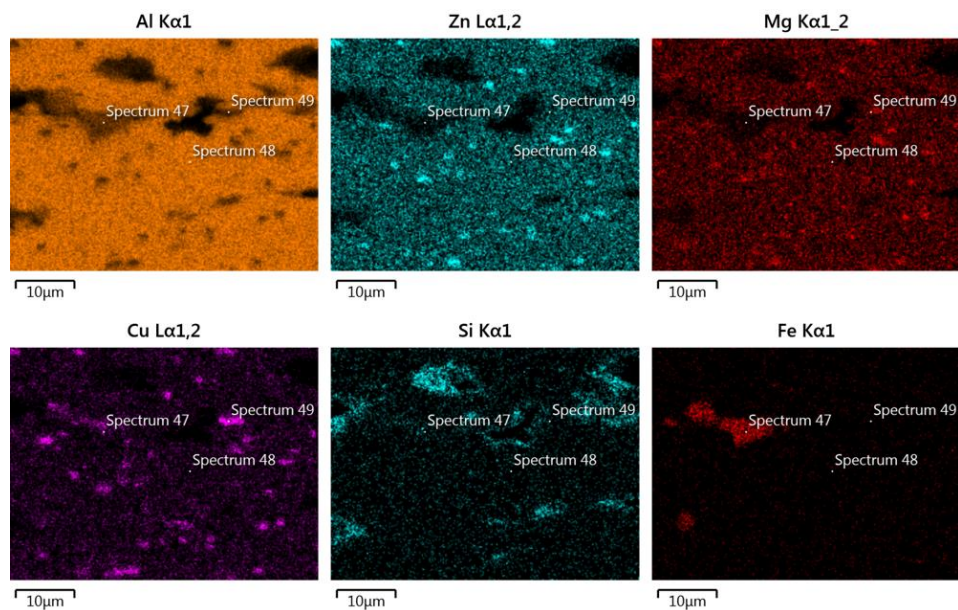
*BSE image of fracture region for 3-inch wide sample at 400°C*



*EDS maps of 3-inch wide sample at 400°C from BSE fracture region image*



*BSE image of fracture region for 7.5-inch diameter sample at 400°C*



*EDS maps of 7.5-inch diameter sample at 400°C from BSE fracture region image*